Ottava giornata di studio
Ettore Funaioli
18 luglio 2014

A cura di

Umberto Meneghetti, Alberto Maggiore e Vincenzo Parenti Castelli

Quaderni del **DIN – GMA**

Atti di giornate di studio – 8

A cura di:
U. Meneghetti , A. Maggiore , V. Parenti Castelli

Coordinatore di redazione:
Alessandro Zanarini

DIN
Dipartimento di Ingegneria Industriale
http://www.ingegneriaindustriale.unibo.it

GMA
Gruppo di Meccanica Applicata
http://wpage.unina.it/dellaval/GMA/GMA_homeold.htm

Accademia delle Scienze dell'Istituto di Bologna
http://www.accademiascienzebologna.it/AccademiaScienze/
default.htm

Ottava giornata di studio Ettore Funaioli

18 luglio 2014

A cura di:
Umberto Meneghetti, Alberto Maggiore e Vincenzo Parenti Castelli

Stampa a richiesta eseguita da:

INDICE

Prefazione

Prefazione

Questo volume raccoglie 20 delle 22 memorie presentate alla ottava "Giornata di studio Ettore Funaioli", svoltasi il 18 luglio 2014. Agli autori delle memorie qui raccolte e a tutti i partecipanti va il nostro più vivo ringraziamento per il permanente successo della manifestazione, legato al ricordo del Prof. Ettore Funaioli, che ricordiamo sempre con grande affetto e perenne gratitudine per l'appassionato insegnamento scientifico e la profonda umanità.

La numerosa e convinta adesione a queste Giornate di Studio conferma anche l'apprezzamento dei partecipanti per l'occasione di ritrovarsi fra colleghi ed amici, per scambiarsi idee sulle ricerche in corso e opinioni sui problemi generali della nostra comunità scientifica.

È come sempre motivo di grande soddisfazione per tutti, e ragione di orgoglio per i nostri Maestri, constatare l'elevata qualità scientifica dei lavori presentati e il costante impegno dei Ricercatori di Meccanica che hanno partecipato alla manifestazione.

Questa Giornata di studio si è svolta con il patrocinio dell'Accademia delle Scienze dell'Istituto di Bologna e del GMA – Gruppo di Meccanica Applicata. Di ciò ingraziamo vivamente il Presidente dell'Accademia delle Scienze, Prof. Emilio Pasquini e il Presidente del GMA, Prof. Federico Cheli.

La Giornata ha potuto svolgersi anche grazie alla collaborazione della Scuola di Ingegneria e Architettura e del DIN – Dipartimento di Ingegneria Industriale dell'Alma Mater Studiorum – Università di Bologna. Ringraziamo il Presidente della Scuola di Ingegneria e Architettura, Prof. Pier Paolo Diotallevi, e il Direttore del DIN, Prof. Gianni Caligiana, che hanno consentito queste collaborazioni e hanno voluto aprire la Giornata porgendo il loro saluto ai partecipanti.

Bologna, 25 giugno 2015

Umberto Meneghetti – Alberto Maggiore – Vincenzo Parenti Castelli

ARCHETYPE-BASED DESIGN OF MECHANICAL TRANSMISSIONS

Peroni Mariele
Dipartimento di Ingegneria "Enzo Ferrari",
Università degli Studi di Modena e Reggio Emilia
E-mail: mariele.peroni@unimore.it

Francesco Leali
Dipartimento di Ingegneria "Enzo Ferrari",
Università degli Studi di Modena e Reggio Emilia
E-mail: francesco.leali@unimore.it

Angelo O. Andrisano
Dipartimento di Ingegneria "Enzo Ferrari",
Università degli Studi di Modena e Reggio Emilia
E-mail: angelooreste.andrisano@unimore.it

Michele Forte
CNH Italia S.p.A.
E-mail: michele.forte@cnhind.com

Abstract
The knowledge management is essential for modern industries, since the turnover of the design teams and the retirement of senior engineers may cause a gradual loss of knowledge. The present paper introduces a method based on archetypes of mechanical systems. An archetype is defined as an engineering model for creating, organizing, standardizing and reusing information about mechanical systems, so that designers are guided in the design tasks. Starting from the analysis of existing and well-functioning systems, the method follows the systematic design and the reverse engineering guidelines, leading to modeling the archetype of the solution. The archetype catches the best design experience about specific systems and stores all the information needed for their dimensioning and modeling.

Keywords*: Engineering design, Archetype, Knowledge management, Systematic design, Reverse engineering*

1. INTRODUCTION

Operating Scenario
A good knowledge management is of crucial importance in professional organizations. Knowledge management is defined as the facilitation of the continuous process of creation,

dissemination and utilization of knowledge [1]. Mechanical design is a typical example of discipline that strongly depends on the knowledge coming from previous experience.

The loss of knowledge is a common problem for today's industries. The main factors that contribute to this phenomenon are the growing use of the outsourcing and the retirement or turnover of designers, often replaced by young and inexperienced engineers. As a consequence, no internal knowledge is created, or it is loss if nothing is made in order to capture and fix it. In other cases, the main problem is that there is not enough organization in the performed work, and the acquired information cannot be shared.

Furthermore, in many industries, designers face several times projects having the same or similar structure or design process, showing only small variants related to specific requirements. In these cases, the design process is necessary based on the previous knowledge and experiences.

This paper focus on the definition of a robust method to collect, share and reuse knowledge and experiences.

Scientific Background In Knowledge-based Methods For Engineering Design
Many authors investigated the problem of the knowledge creation and management, and proposed different approaches to face them.

Some authors focused mainly on the aspect of the knowledge creation and management.

According to [2], there are two kind of knowledge: explicit knowledge and tacit knowledge. Explicit knowledge can be expressed in words and numbers, and shared in the form of data, formulae and manuals. It can be readily transmitted between individuals. Tacit knowledge is personal and hard to formalize: insight and intuitions are part of this category. Knowledge creation is a spiraling process of interactions between explicit and tacit knowledge. The interaction between the explicit and tacit knowledge lead to the creation of new knowledge.

In [3], a model of the dynamics of knowledge creation in an engineering problem solving context is proposed. This model consists in a study based on interviews of men and women in engineering professions, asking each to recount more effective and less effective cases product-related problem solving and how engineering knowledge can be captured and disseminated in an organizational context. Some of the principal results were that problem solving is likely to be successful when there is easy access to needed resources and that the presence of mechanism for sharing information and knowledge is likely to facilitate effective problem solving and knowledge capture.

Guidelines are defined in [1] for knowledge management practitioners, defining two different perspectives of knowledge management and finding the strengths and the weakness of both. The authors argued that engineers should acknowledge both and switch between to effectively manage knowledge process. Thus, a set of rules is articulated, making use of the strength of both perspectives while mitigating their weakness.

Other authors focused, instead, on methods to share and reuse knowledge and take profit by it.

In [4] a method is proposed to carry out manufacturing and product engineering integrated with knowledge networking. It comprises the creation of a logic modeler by identifying elements of an engineering project and arranging them in a logic sequence based on engineering functions, ascertaining uniform meanings for elements and functions

to allow for interdisciplinary intercommunication, gathering existing knowledge pertinent to the project, reviewing of initial inputs to check rule or constraint violations of the gathered knowledge, interacting with the analysis to converge on acceptable or improved design functions.

In [5] the attention is focused on a knowledge-based system capable of optimizing its solution, using a set of data and a set of instructions. The method comprises the input of data from experts, the input of the instructions on how to operate and utilize the data, the definition of an application for the data and the instructions, the design of the product through an iterative calculation, using the initial data and instructions and, also, subsequent inputs by the user.

In [10] how to integrate a knowledge model and a design process model is shown, in order to facilitate the series mechanical product design. A driving knowledge library provides support for product design. The design process model drives the choice of parameters and realizes intelligent assembly synchronous with design processes.

Open Issues In Knowledge Creation And Management In Engineering Design
The studies analyzed above show two different aspect of the knowledge management: some of them focus on methods to create and manage knowledge, giving instructions and guidelines to collect and organize information in order to facilitate its sharing and utilization; some others show methods that apply the existing knowledge to the engineering design.

The aim of this work is to match the two approaches, defining a method that is able both to collect information and knowledge and to guide designers in every step of their activities. The solution proposed is based on the definition and use of archetypes of systems, or of components of a system. Archetypes, in fact, facilitate sharing knowledge and allow a high interoperability between information systems […] so that they are also a tool for guiding new staff [6]. In fact, an archetype can be defined as a method of problem-solving, a design strategy associated with the method and a collection of exemplar problems to which the method can be applied [7], and able to capitalize experiences and insight.

In the following sections we describe how to build an archetype of an engineering system, taking as example the mechanical transmission of an agriculture vehicle. Because of its complexity, the design of the mechanical transmission of a tractor requires a lot of knowledge and prior experience. As a consequence, it is a very significant example for the approach followed in this paper.

2. ARCHETYPE-BASED METODOLOGY FOR ENGINEERING DESIGN
Archetype-based Design
In this paper, an archetype is defined as a model that catches the best design experience of the mechanical system it represents. It is identified as a set of interactive drawings and 3D models of the system together with a technical documentation, supporting the design activity and catching the best design experiences for the system itself.

The technical documentation contains two levels of information: a ruled-based one and an experience-based one. The ruled-base information concerns the correct definition and dimensioning of the system. Thus, it guides the user in the definition of dimensions, choice of material, heat treatments, etc. The experience-based information collects the best

practices of existing systems and concerns the functionality of the system, such as machining, tolerances and all the technical choices carried out with the validation and operation of existing systems.

The CAD model must be parametric and automatic, guided from the parameters defined following the instructions given by the technical documentation.

It is necessary to identify a detailed methodology illustrating how to analyze an engineering problem in order to collect and organize all the knowledge regarding the specific system and needed for the archetype definition.

Knowledge Creation

The better method to collect information about a system is to start analyzing an existing and well-functioning system, trying to understand how it has been designed and the choices that have been made during the design process. In this context, reverse engineering and teardowns offer the better paradigm for design instruction, permitting a modern learning cycle of experiences, hypothesis, understanding and, then, execution [8].

Furthermore, it is necessary to identify a methodology as general and repeatable as possible, so that it can be applied to any engineering system, always following the same steps and giving homogeneous and comparable results. It is important to have a defined design procedure that finds good solutions. This procedure must be flexible and, at the same time, be capable of being planned, optimized and verified [9].

A systematic approach is the most effective way to rationalize the design and to provide solution that can be used again. Only in this way it is possible to: develop knowledge-based systems, use stored data and methods, link separate programs (e.g. geometric modelers with analysis programs), and ensure the continuity of data flow [9].

In agreement with the systematic approach, a design process can be divided in four main phases:

- Planning and task clarification: specification of information
- Conceptual design: specification of principal solution
- Embodiment design: specification of layout
- Detail design: specification of production

In [9], each of these phases is widely described and detailed in further main working steps.

We suggest again a matching of the two methodologies: starting from the existing system, each of the main phases and of the working steps is applied, but in the opposite sequence, starting from the analysis of the final product, splitting it up and simplifying it, identifying its main functions and properties and, finally, identifying how and why these functions and properties are related to the initial specifications.

Such a procedure is of crucial importance for the identification of archetypes of engineering systems. In fact, an archetype represents, by definition, a population of similar systems, catching the common properties of them. Then, a large number of systems must be analyzed, gathering those with the same functions and properties. But this is possible only if every system is analyzed following a specific and repeatable procedure.

Section 3 illustrates how to model an archetype of a mechanical system.

3. A METODOLOGY FOR ARCHETYPES DEFINITION

System definition

The mechanical transmission of an agriculture vehicle is taken as example to better
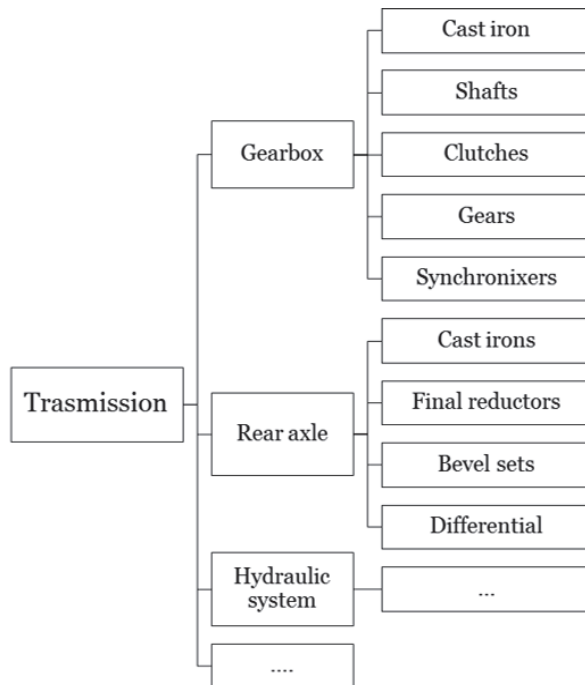
Figure 1. Hierarchical structure of a transmission.

illustrate the proposed methodology for the definition of an archetype. The mechanical transmission is a hierarchical system with a high level of complexity. Thus, it is impossible and useless to define an archetype of the entire system. It is then necessary to divide and simplify the problem until elementary and standalone systems are identified (Figure 1).

The process followed for this preliminary implementation is based on four main phases: data collection, data analysis, archetype definition, archetype modeling.

Data collection. Data and information can be found in the databases of existing systems. Important information are represented by requirement lists defining the driving parameter of the system, datasheet computing dimensions, rules and theories used in the past projects, product designs defining the fundamental features of the system or of parts of the system, schemes explaining the functionality of the system. Searching this kind of information relative to all the variants of the same system, a complete and exhaustive knowledge domain is available.

Data analysis. Through a structured analysis, information is processed and organized, and made suitable to guide the design process. If each variant is subjected to a precise functional analysis (Figure 2), specific functions are identified for each part of the system, and for each function a working principle is identified (Figure 3), explaining how the
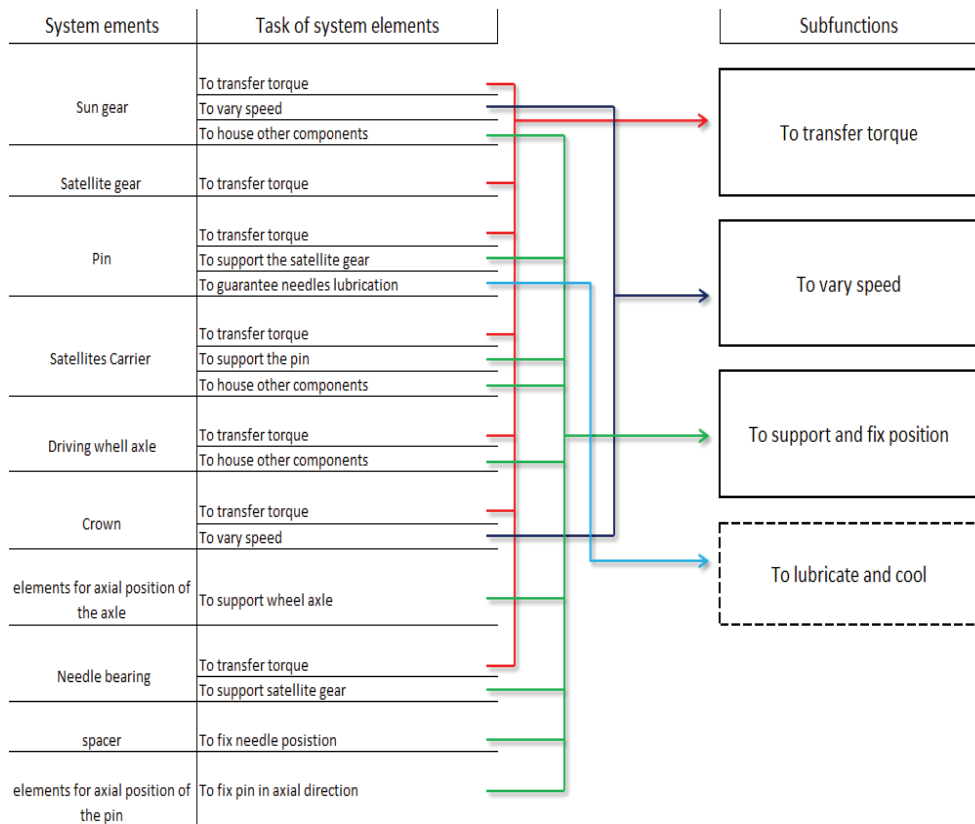
Figure 2. Functional analysis (Example of a final reductor).
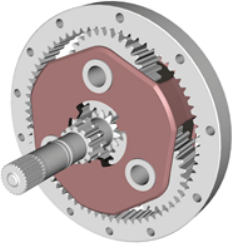
specific function are satisfied by the specific element. This is the better method to really understand the functionality of a system. If the functionality of the system is known, it is possible to define relations between the final geometry of components to the initial prerequisites. At the end, the mathematic model of the system is built.

Archetype definition. The criteria for the definition of the archetype have crucial importance. They must be founded on experience-based type knowledge because the main aim of the archetype is to represent the best design experience and minimize the possibility to make errors. So, the criteria for the choice of the best solution are defined during structured interviews with senior engineers, in which they are asked about their own specific experience in the design process of the system under study. The information collected allows to discard or approve solutions and to select the best one. Then, a final design review is necessary with the designers' team for the final approval of the proposed solution.

Archetype modeling. The archetype is built on the basis of the mathematic model and the design knowledge collected. Knowledge is structured and organized in a document that leads designers in the definition of driving parameters, constraints and assumptions. The

Final Drive								
Solution principles / Subfunctions				1	2	3	4	5
1	Transfer torque	Mechanical	Form connections	Gear drive	Shaft-hub	Shear-loaded	Preloaded spline	Riveted
2			Force connections	Friction Force	Force Field	Elastic Force		
3			Material connections	Welded	Adhesive			
4		Hydraulic		Hydrodynamics	Hydrostatic			
5		Elettric		Electric Motor				
6	Vary speed			Gear drive	Pulley			
7	Support and Position			bearing	axial location	guide	locking elements	Friction Force

Figure 3 - Working principles (example of a final reductor)

		Components	Sun	Planet	Ring	Carrier
			A	B	C	D
Functions Criteria				CNH1		
1	Archetype selection criteria		DC-1			
2	Mechanical Resistance		DC-2	DC-2	DC-9	DC-8
3	Correct coupling and assembly		DC-22	DC-20		DC-21
4	Manufacturability			DC-30	DC-31	DC-32
5	Proper Lubrication		DC-40	DC-40	DC-40	DC-40
6	Proper bearing choice			DC-50		
7	Cleanliness		DC-60			
8	Safety		DC-61			
9	Part classification and marking			DC-62		
	Apply adaptations for specific design, as required, on top of the base DQP		Purpose			

Figure 4 - Design Criteria (example of a final reductor)

document is structured as a correlation matrix in which components and their relative functions are reported and the specific Design Criteria (DC) are described in detail (Figure 4). One or more datasheets or algorithms are created to compute dimensions and fundamental parameters depending on the initial requirements. The CAD model is generated as a skeleton of the system and directly depends on the datasheet so that it
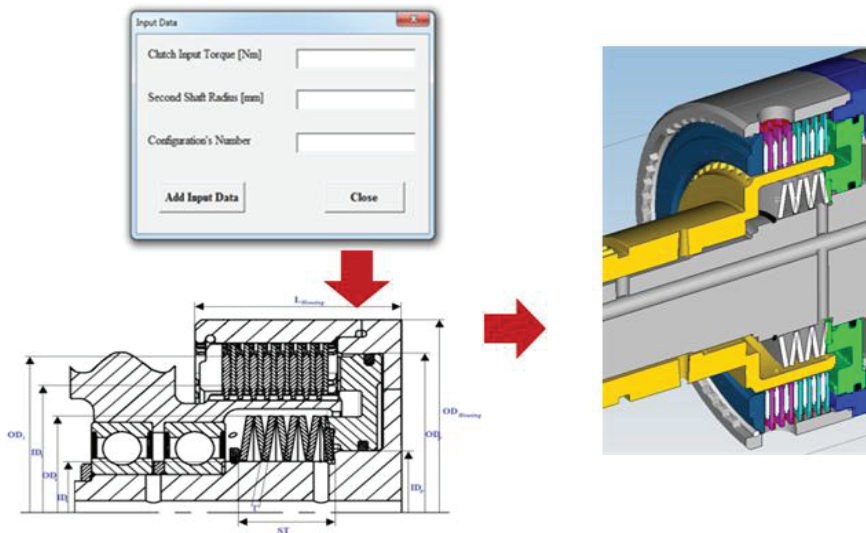
Figure 5 - Parametric CAD model (example of a hydraulic clutch).

automatically updates when requirements are changed (Figure 5). A user interface can be useful to facilitate the process of CAD regeneration.

4. CONCLUSIONS

A solution has been proposed to solve the problem of the gradual knowledge loss affecting companies. It consists in a procedure allowing the definition of archetypes of mechanical systems, intended as a tool helping engineers when they approach the project of a mechanical system. The procedure is based on the matching of the principles of reverse engineering and systematic approach to engineering design.

The archetype carried out by the proposed procedure consists of a set of interactive 3D models and 2D drawings and of a documentation collecting all the knowledge regarding the specific system. Both ruled-based information and experience-based information is considered, so that the final archetype can collect the best experiences of engineering design of a company.

The methodology was applied, until now, to two specific systems of the transmission: a hydraulic multiplate clutch and an epicyclic final reductor. The first three phases were successfully carried out and a proposal for the best solutions was made.

Future development we'll be considered after the final approval by the team of senior engineers. Then, the last step will be implemented and the final results will be, again, subjected to a design review for the final approval. The methodology will be finally applied to the remaining systems, in order to build a complete library of the systems contained in the transmission.

REFERENCES

[1] P.W.G. Bots, H. de Brujin, 2002, "Effective knowledge management in professional organizations: going by the rules", in Proc. of 35th Annual Hawaii International Conference on System Sciences.

[2] I. Nonaka, N. Konno, 1998, "The concept of 'ba': building foundation of knowledge creation", California management review, vol.40, no3, Spring.

[3] R. Itabashi-Campbell, S. Perelli, J. Gluesing, 2011 "Engineering problem solving and knowledge creation: an epistemological perspective", IEEE Int'l Technology management Conference.

[4] US Pat. 6230066, P.R. Sferro, G.J. Burek, S.B. O'Reilly, 2001, "Simultaneous manufacturing and product engineering integrated with knowledge networking".

[5] US Pat. 5799293, G.A. Kaepp, 1998, "Method for optimizing the design of a product using knowledge-based engineering techniques".

[6] J.T. Fernandez-Breis, M. Menarguez-Tortosa, C. Martinez-Costa, E Fernandez-Breis, J. Herrer-Sempere, D. Moner, J. Sanchez, R. Valencia-Garcia, M. Robles, 2008, "A semantic web-based system for managing clinical archetypes", 30th Annual international IEEE AMBS conference.

[7] K.M. Chandy, 1995, "Concurrent program archetypes", in Proc. of Scalable Parallel Libraries Conference.

[8] K.N. Otto, K.L. Wood, 2001, "Product design: techniques in reverse engineering and new product development", Prentice Hall.

[9] G. Pahl, W. Beitz, J. Feldhousen, K.H. Grote, "Engineering design. A systematic approach.", Third edition, Springer

[10] Yixiang F., Enfu L., Jiangyan J., Lanzhi G., Domain Knowledge Driving in Intelligent Design of Series Mechanical, 11th IEEE International Conference on Computer-Aided Design and Computer Graphics, pp. 422-428, Huangshan, CN, Aug 2009.

OTTIMIZZAZIONE DEI PERCORSI CNC PER LAVORAZIONI LASER DI SUPERFICI FREE FORM

F. Montanari
Dipartimento di Scienze e Metodi dell'ingegneria
Università degli studi di Modena e Reggio Emilia
E-Mail: montanari.reggio@gmail.com

M. Cocconcelli
Dipartimento di Scienze e Metodi dell'ingegneria
Università degli studi di Modena e Reggio Emilia
E-Mail: marco.cocconcelli@unimore.it

L. Orazi
Dipartimento di Scienze e Metodi dell'ingegneria
Università degli studi di Modena e Reggio Emilia
E-Mail: leonardo.orazi@unimore.it

R. Rubini
Dipartimento di Scienze e Metodi dell'ingegneria
Università degli studi di Modena e Reggio Emilia
E-Mail: riccardo.rubini@unimore.it

Abstract: *L'utilizzo della tecnologia Laser, in lavorazioni Laser Texturing ed Engraving, per la realizzazione di superfici free form è un'interessante alternativa alle lavorazioni EDM e di micro fresatura nella fabbricazione di stampi e matrici. Il tasso di rimozione del materiale di questo processo è tipicamente molto basso e la massima area di lavoro è limitata dal campo di spostamento massimo della testa di scansione galvanometrica ed anche dalla deformazione massima dello scanner o la curvatura della superficie. Di conseguenza, al fine di realizzare superfici free form o grandi, è necessario eseguire una serie di posizionamenti della testa laser rispetto al pezzo da lavorare, calcolati e controllati dal CNC. Il numero di questi posizionamenti può essere molto alto a causa della piccola quantità di materiale asportato in ciascuno di essi ed il tempo non operativo speso per spostare la testina di scansione può essere rilevante rispetto al tempo complessivo. In questo lavoro viene proposto un metodo basato sulla soluzione del problema del commesso viaggiatore, con lo scopo di ottimizzare il numero di spostamenti della testa di scansione e generalmente per ridurre il numero di movimenti degli assi a controllo numerico. Il metodo, che tenga conto sia l'architettura e le caratteristiche dinamiche del sistema CNC 5 assi, è stato implementato nel CALM software (Computer Aided Laser Manufacturing) utilizzato per programmare il percorso laser per parte texturing e applicata in casi industriali.*

Keywords: *TSP,CNC paths Optimization.*

1. INTRODUZIONE

L'applicazione della tecnologia laser nei processi di produzione è aumentato rapidamente negli ultimi anni. Molti processi termici come la saldatura, il taglio, la fresatura usano la sorgente laser come fonte di calore. La fabbricazione laser ha molti vantaggi rispetto le lavorazioni tradizionali: maggiore velocità e precisione sono garantiti grazie alle caratteristiche fisiche del fascio laser e al metodo di lavoro senza contatto. Tuttavia le differenze tra tecnologia laser e le lavorazioni convenzionali possono causare alcuni problemi peculiari e critici a causa della natura delle interazioni tra l'utensile e superficie grezza. In fresatura convenzionale il materiale viene rimosso per le forze di taglio generate tra utensile e grezzo. La tecnologia laser interagisce con il materiale per mezzo di un processo termico, che lo riscalda fino alla temperatura di evaporazione o superiore alla soglia di ablazione.

I difetti nelle lavorazioni Laser Texturing (LT) si verificano quando i percorsi laser si sovrappongono. In Fig. (1) è mostrato un tipico esempio di campo di lavoro sovrapposto e l'errore generato durante una lavorazione laser rispetto ad una lavorazione tradizionale.

Per risolvere il problema citato, l'area di lavorazione viene partizionata, ma ciò genera alcune ulteriori complicazioni per la gestione dei movimenti di spostamento del raggio laser (testa di scansione). Il numero di posizionamenti può essere elevato, dell'ordine di migliaia, e devono essere ripetuti per ogni piano di lavorazione. La soluzione del problema di sovrapposizione dei percorsi richiede un approccio strategico per prevedere e controllare il tempo di lavorazione generale.

Gli autori di questo articolo propongono di attuare il problema del commesso viaggiatore (TPS) allo scopo di minimizzare il tempo di trasmissione di un'operazione LT.

2. APPROCCI PRECEDENTI

Il TPS è un problema già noto nel campo della ricerca operativa. Una descrizione e formulazione di questo problema sarà descritta nei paragrafi successivi. Molti problemi riguardanti la minimizzazione dei percorsi, in termini di lunghezza o da altri coefficienti di interesse (ad esempio economici), possono essere risolti dagli algoritmi proposti per la risoluzione del problema TSP.

Inizialmente l'attenzione per l'ottimizzazione dei processi di fresatura tradizionali è stata focalizzata per migliorare i tempi di lavorazione, in questo modo la produttività è aumentata.
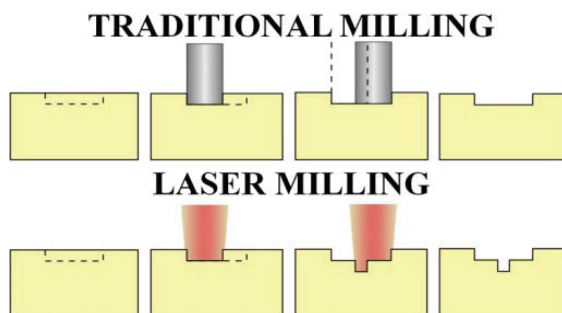

Figura 1. Errore generato dalla sovrapposizione delle aree di lavorazione.

Successivamente l'interesse per ridurre il tempo di lavorazione si è concentrata sul tempo di movimentazione: un tempo non produttivo che riduce l'efficienza e la resa del processo di lavorazione. Quest'ultimo caso è rilevante quando le aree di lavorazioni sono piccole ma il numero di punti da processare è elevato, come discusso in [1] da Castelino et al.

Una prima implementazione per ridurre il percorso durante il taglio laser è stato discusso da Han e Na [2]; i quali hanno sviluppato un semplice algoritmo per trovare la soluzione ottimale. Altre applicazioni di algoritmi allo scopo di ridurre i tempi di spostamento sono proposti da Oysu e Bingul [3] per mezzo di un algoritmo genetico ibrido, oppure Kolahan e Liang [4] che considerano non solo il tempo di spostamento, ma anche quello speso per il cambio utensile, valutandone anche usura e manutenzione.

Gli autori hanno testato la soluzione adottata su un oggetto di forma libera con una macchina CNC a cinque assi che verranno descritti nelle pagine seguenti. Nella letteratura scientifica diversi articoli affrontato le difficoltà generate della lavorazione di superfici free form utilizzando un CNC 5 assi. Ad esempio, nel lavoro di Lazoglu et al. [5] non solo è stato ottimizzata la lunghezza del percorso di lavorazione, ma anche la forza generata dal utensile. Un secondo articolo di Stanislav Makhanov [6] descrive l'ottimizzazione della traiettoria di una fresatrice 5 assi e in questo caso i movimenti degli utensili sono stati parzialmente risolti.

3. COMPUTER AIDED LASER MANUFACTURING SYSTEM

Gli Autori hanno già presentato in [8] il software di Computer Aided Laser Manufacturing, CALM. Si tratta di un software CAM progettato specificamente per la produzione laser (fresatura e texturing) per garantire una corretta elaborazione da parte di una macchina CNC 3 o 5 assi. Questo software è stato sviluppato in linguaggio C ++ e può essere utilizzato su diversi sistemi operativi disponibili sul mercato.

Un ulteriore strumento software è stato implementato in CALM per risolvere il problema TSP.

Triangoli di Piazzamento

CALM processa le superfici di ingresso e genera due triangolazioni, applicando il classico algoritmo proposto da Piegl in [7]. La prima triangolazione viene generata minimizzando l'errore cordale per approssimare con la miglior precisione la reale superficie grezza ed evitare errori durante la lavorazione; perciò la densità di triangoli risulta essere elevata per la prima triangolazione.

Una seconda triangolazione, che rappresenta i posizionamenti della testa di scansione laser, viene creata per partizionare l'area di lavoro e risolvere il problema descritto nella sezione precedente. Tali triangoli hanno un'area più grande rispetto ai primi, perché non hanno bisogno di approssimare al meglio la superficie del pezzo grezzo. I parametri che determinano la dimensione dell'area dei triangoli di posizionamento dipendono dalla capacità di focalizzazione della testa di lavorazione e dalla geometria della superficie free form. I parametri principali sono:
- Distanza di messa a fuoco;
- Spot laser;

- Curvatura della superficie grezza;
- Presenza di alta profondità in rapporto alla larghezza.

Un altro aspetto che deve essere considerato per generare le triangolazioni di piazzamento è il rateo di rimozione del materiale (MRR): solitamente è possibile rimuovere circa 1 micron di materiale per un singolo piazzamento. L'utilizzo della medesima triangolazione di posizionamento per ogni livello determina un errore ricorsivo, che è evidente nelle zone di bordo tra i triangoli della superficie lavorata. Per questo motivo la triangolazione viene variata per i diversi layer di lavorazione del grezzo al fine di garantire una migliore qualità superficiale della parte realizzata.

File di Output

CALM produce i seguenti file di output per tutti i dispositivi del sistema di fresatura laser:

- PROJECT.JOB contiene l'elenco dei file HPG nell'ordine in cui devono essere eseguiti.
- I file HPG per la testa di scansione contengono le coordinate geometriche su cui la sorgente deve accendersi o spegnersi e i movimenti dei due specchi galvanometrici.
- File PP.ISO descrivono il movimento degli assi del CNC in linguaggio G-code. La minimizzazione del numero di spostamenti riguarda il file PP.ISO.
- PARAM.PRO contengono i parametri di elaborazione per la sorgente laser.

4. TSP – PROBLEMA DEL COMMESSO VIAGGIATORE

CALM suddivide la geometria del pezzo grezzo in strati e ciascuno di essi è triangolato per risolvere il problema delle aree di sovrapposizione. Per ridurre al minimo il tempo di spostamento tra i triangoli gli autori hanno analizzato gli algoritmi proposti per la risoluzione del problema del commesso viaggiatore (TSP). Il TSP consiste nel visitare un insieme di clienti, una ed una sola volta, con l'obiettivo di ridurre al minimo la lunghezza del percorso (tempo di spostamento). I clienti di CALM sono i baricentri dei triangoli di piazzamento.

Descrizione Matematica

Dato un grafo (o un grafo completo[1]) $G = (V, E)$ dove $V = \{1, 2, .., n\}$ è l'insieme dei vertici (clienti) ed E è l'insieme dei bordi aventi un costo associato c_{ij} con $i, j \in V$, il problema consiste nel ricercare il circuito Hamiltoniano più breve (o di costo minimo), ossia un circuito chiuso che passa una ed una sola volta per tutti i vertici del grafo.

Il modello matematico può essere così rappresentato dal sistema di equazioni Eqn.(1), Eqn.(2), Eqn.(3), Eqn.(4), Eqn.(5), considerando la seguente definizione di x_{ij}

$$x_{ij} \begin{cases} 1, \text{se l'arco di percorrenza è scelto;} \\ 0, \text{altrimenti.} \end{cases}$$

$$Minimize \ \sum_{i=1}^{n} \sum_{j=1}^{n} c_{ij} x_{ij} \tag{1}$$

---

[1] Un grafo è completo se esiste per ogni coppia di vertici del grafo $(i; j) \in V, i \neq j$ un lato che li colleghi.

$$\sum_{i=1}^{n} x_{ij} = 1 \quad \forall j \in V \tag{2}$$

$$\sum_{i=1}^{n} x_{ji} = 1 \quad \forall j \in V \tag{3}$$

$$\sum_{j \in S} \sum_{i \in S} x_{ij} \leq |S| - 1 \quad \forall S \doteq V : |S| \leq |V| \tag{4}$$

$$x_{ij} \in 0,1 \; \forall i,j \in V \tag{5}$$

La funzione obiettivo (Eqn. (1)) minimizza il costo totale del circuito. L'equazione (2) descrive la necessità di entrare in ogni vertice $j \in V$. L'equazione (3) impone di uscire esattamente una volta dal vertice. In questo modo ogni vertice viene visitato una ed una sola volta. L'equazione (4) serve per eliminare possibili sub-tours ricorsivi.

Nella letteratura scientifica nell'ambito della ricerca operativa esistono altri modelli matematici per la rappresentazione dei vincoli del TSP, come le formulazioni MTZ (Miller-Truckler-Zemlin), one-commodity e multi-commodity. Tutte queste diverse espressioni sono state sviluppate al fine di semplificare il vincolo in Eqn. (4).

La procedura matematica trova sempre la soluzione ottimale, ma nei casi reali questa può essere difficile da trovare o comunque molto dispendiosa in termini di tempo di calcolo.

Complessità Computazionale

Il TSP, purtroppo, è un problema difficile da risolvere anche per le piccole istanze. Il numero di vincoli aumenta molto più velocemente rispetto alle dimensioni dell'istanza e non esistono algoritmi che possano trovare la soluzione ottimale in un tempo ragionevole.

La classe di questo tipo di problemi nella ricerca operativa è denominata "problemi NP-difficili, Polinomiali non-deterministici".

Gli approcci più utilizzati per ottenere una soluzione sono:
- Algoritmi Euristici, la maggior parte sono disponibili gratuitamente sulla rete.
- Algoritmi Genetici, che sono difficili da applicare a causa della numerosità dei parametri di configurazione.
- Ant Colony Optimization, descritto da Dorigo in [8] [9]. Algoritmo che rappresenta il comportamento delle formiche.

5. SOFTWARE CONCORDE

Concorde non è un algoritmo, ma un programma sviluppato in codice C-ANSI per risolvere i problemi TSP. Ha vinto numerosi premi per aver risolto grandi casi [13] e può essere considerato lo stato dell'arte tra i risolutori del TSP. Concorde solitamente trova una buona soluzione in pochi secondi per istanze con migliaia di vertici e presenta un piccolo gap rispetto la soluzione matematica ottimale.

Il software è gratuito per l'ambito della ricerca ed è disponibile come codice sorgente o come programma user-friendly. In questo lavoro è stato adottato il codice sorgente.

Concorde contiene più di 700 funzioni, in grado di risolvere diversi tipi di TSP e usa differenti algoritmi per trovare il più velocemente possibile la miglior soluzione.

Concorde è basato sull'algoritmo euristico chained Lin-Kernighan.

Chained Lin-Kernighan Heuristic (LKH)

CALM triangola ogni layer di lavorazione della superficie Free Form. L'algoritmo euristico LKH può risolvere in modo efficiente un 2D-TSP. Gli steps del LKH per un'istanza 2D possono essere riassunti nei seguenti punti:

- Creare un tour Hamiltoniano casuale.
- Calcolare il guadagno ottenuto dallo scambio dell'ordine di passaggio tra due o tre vertici del tour. LKH decide se scambiare due o tre vertici e utilizza la logica più redditizia di miglioramento.
- Scambiare il set più vantaggioso e ricominciare dal punto precedente.

Al fine di ottenere miglioramenti ulteriori, LKH accetta anche peggioramenti della soluzione, se non sono presenti guadagni positivi; questo per esplorare un dominio delle soluzioni più ampio.

Il ciclo continua fino a raggiungimento di un parametro, come: numero di iterazioni, percentuale di scarto, valore, etc.

Per evitare la possibilità di rimanere troppo a lungo in una regione del dominio delle soluzioni, LKH genera una tabulist nella quale i vertici troppo ricorrenti vengono penalizzati.

Una descrizione più dettagliata e completa di LKH è proposto in [13].

Questo algoritmo genera una soluzione molto buona quando il problema rispetta la seguente disuguaglianza, denominata *Triangle Inequality* Eqn.(6):

$$\forall\, i,j \in V, \nexists k \in V : c_{ik} + c_{kj} < c_{ij} \tag{6}$$

Questa richiesta è rispettata da CALM e dà a Concorde come input un file contenente una matrice in formato TSPLIB. TSPLIB è un linguaggio sviluppato appositamente per i problemi TSP. In questo file è contenuta la descrizione del problema da risolvere: il tipo TSP, il numero dei lati, il tipo di costo dei lati (distanza euclidea, coordinate geografiche, pesi espliciti). CALM calcola i costi (tempi) tra i baricentri dei triangoli, quindi i costi di bordo sono espliciti.

Integrazione CALM-Concorde

Durante l'elaborazione di un singolo layer, CALM seleziona i triangoli che devono essere elaborati, genera il file HPG e prima di scrivere il file PP.ISO, calcola i costi per collegare ogni coppia di triangoli. Concorde viene poi utilizzato per ottimizzare i costi. Gli indici dei triangoli e le relative distanze sono descritte in formato TSPLIB, file che CALM scambia con il programma Concorde. Infine Concorde restituisce a CALM il file con la sequenza ottimizzata dei triangoli. CALM scrive il file PP.ISO e passa allo strato successivo.

6. CALCOLO DELLA MATRICE DEI COSTI

Gli autori di questo articolo hanno concentrato la loro attenzione nel calcolare la matrice di costo operativi, valutando il costo come il tempo reale di movimentazione della macchina CNC.

Concorde è un risolutore molto efficiente, ma in questo articolo non verrà approfondito il metodo utilizzato per ottenere la soluzione.

Di seguito sono proposti tre percorsi diversi come soluzione, di cui gli ultimi due basati sull'applicazione della risoluzione del problema TSP:

- Percorso non ottimizzato;
- Percorso ottenuto considerando la matrice dei costi rappresentativa delle distanze euclidee 3D espresse in termini di tempo;
- Percorso realizzato considerando come costi i tempi reali di movimentazione della macchina a 5 Assi.

Soluzione Non Ottimizzata

In questo caso CALM generare il file PP.ISO senza ottimizzare la sequenza. Il percorso è generato seguendo la numerazione dei triangoli generata da CALM. Questo tipo di percorso è notevolmente dispendioso in termini di tempo.

Approccio Distanze Euclidee 3D

Nel file TSPLIB passato a Concorde, CALM calcola le distanze in mm considerando la lunghezza del segmento che collega il baricentro dei due triangoli, che verranno poi tradotte in tempi di percorrenza. La formula utilizzata è Eqn. (7):

$$d = \sqrt{(x_a^2 - x_b^2)^2 + (y_a^2 - y_b^2)^2 + (z_a^2 - z_b^2)^2} \tag{7}$$

Concorde calcola la soluzione che non rappresenta la movimentazione minima riferita all'intera superficie, ma il percorso minimo per il layer preso in considerazione (singola quota zeta).

Usando questo metodo su un sistema a 5 assi la soluzione può produrre una movimentazione non ottimizzata. La curvatura della superficie non è considerata e questo può produrre rotazioni inutili e grandi spostamenti della testa di scansione dovuta alla distanza di focalizzazione, che ha un range limitato e per questo la macchina deve essere correttamente posizionata.

Approccio Tempo Reale 5 Assi

L'approccio introduce il tempo reale di movimentazione degli assi nel codice di ottimizzazione. Questa operazione può essere fatta solo studiando le relazioni che l'architettura della macchina impone. In Fig. (2) è rappresentata l'architettura della macchina : gli assi di traslazione sono X, Y e Z; i loro valori sono riferiti alla posizione iniziale del sistema CNC, rappresentato dal sistema di riferimento O_G.

In figura è raffigurato un posizionamento della testa laser, punto Q, su un generico punto P.

Le rotazioni degli assi A e B sono indicati, rispettivamente, intorno agli assi X e Y.

CALM valuta la distanza di P rispetto al sistema di rifermento O_P, questo è ciò che accade nell'ottimizzazione Euclidea 3D, ma nell'ottimizzazione a 5 assi proposta devono essere valutati gli spostamenti della testa di lavorazione Q rispetto al sistema di riferimento O_G. Questo è possibile traducendo, in prima fase, la posizione della testa galvanometrica nel sistema di riferimento O_P.
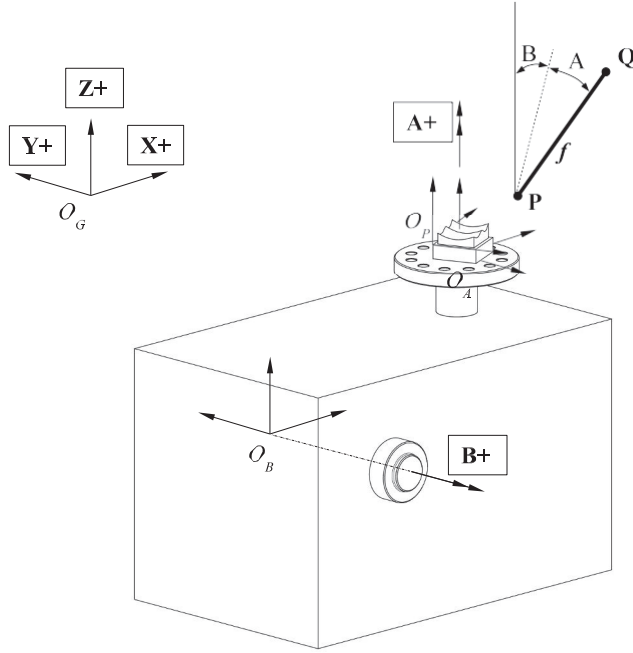
Figura 2. Architettura della macchina a 5 assi.

Vengono considerate quindi le rotazioni intorno agli assi X e Y, rispettivamente Eqn. (8) ed Eqn .(9):

$$R_X(\alpha) = \begin{bmatrix} 1 & 0 & 0 \\ 0 & \cos\alpha & -\sin\alpha \\ 0 & \sin\alpha & \cos\alpha \end{bmatrix} \qquad (8)$$

$$R_Y(\alpha) = \begin{bmatrix} \cos\beta & 0 & \sin\beta \\ 0 & 1 & 0 \\ -\sin\beta & 0 & \cos\beta \end{bmatrix} \qquad (9)$$

La componente di rotazione è quindi la seguente Eqn. (10):

$$R = \begin{bmatrix} \cos\beta & \sin\alpha\sin\beta & \sin\beta\cos\alpha \\ 0 & \cos\alpha & -\sin\alpha \\ -\sin\beta & \cos\beta\sin\alpha & \cos\alpha\cos\beta \end{bmatrix} \qquad (10)$$

Le coordinate di Q_p saranno così ottenute Eqn. (11), dove f è la distanza focale:

$$Q_p = \begin{bmatrix} \cos\beta & \sin\beta\sin\alpha & \sin\beta\cos\alpha \\ 0 & \cos\alpha & -\sin\alpha \\ -\sin\beta & \cos\beta\sin\alpha & \cos\beta\cos\alpha \end{bmatrix} * \begin{bmatrix} 0 \\ 0 \\ f \end{bmatrix} + \begin{bmatrix} X_P \\ Y_P \\ Z_P \end{bmatrix} = \begin{bmatrix} \sin\beta\cos\alpha * f + X_P \\ -\sin\alpha * f + Y_P \\ \cos\beta\cos\alpha * f + Z_P \end{bmatrix} \qquad (11)$$

Ciò che interessa è portare Q nel sistema O_G, pertanto è stato necessario ottenere la matrice di trasformazione dal sistema O_P al sistema O_G.

18

La matrice di trasformazione sarà data dalla seguente espressione:

$$T_P^G = T_B^G T_A^B T_P^A$$

Dove:

$$T_B^G = \begin{bmatrix} cos_B & 0 & sin_B & X_B \\ 0 & 1 & 0 & Y_B \\ -sin_B & 0 & cos_B & Z_B \\ 0 & 0 & 0 & 1 \end{bmatrix} \tag{12}$$

$$T_A^B = \begin{bmatrix} cos_A & -sin_A & 0 & X_A \\ sin_A & cos_A & 0 & Y_A \\ 0 & 0 & 1 & Z_A \\ 0 & 0 & 0 & 1 \end{bmatrix} \tag{13}$$

$$T_P^A = \begin{bmatrix} cos_P & -sin_P & 0 & X_P \\ sin_P & cos_P & 0 & Y_P \\ 0 & 0 & 1 & Z_P \\ 0 & 0 & 0 & 1 \end{bmatrix} \tag{14}$$

Dalle quali si ottiene Eqn. (15):

$$T_P^G = \begin{bmatrix} a_{00} & a_{01} & a_{02} & a_{03} \\ a_{10} & a_{11} & a_{12} & a_{13} \\ a_{20} & a_{21} & a_{22} & a_{23} \\ 0 & 0 & 0 & 1 \end{bmatrix} \tag{15}$$

Dove:

$a_{00} = cos_P cos_{AP}$;
$a_{01} = -cos_B sin_{AP}$;
$a_{02} = sin_B$;
$a_{03} = cos_B cos_A X_P - cos_B sin_A Y_P + cos_B X_A + sin_B Z_P + sin_B Z_A + X_B$;
$a_{10} = sin_{AP}$;
$a_{11} = cos_{AP}$;
$a_{12} = 0$;
$a_{13} = sin_A X_P + cos_A Y_P + Y_A + Y_B$;
$a_{20} = -sin_B cos_{AP}$;
$a_{21} = sin_B sin_{AP}$;
$a_{22} = cos_B$;
$a_{23} = -sin_B cos_A X_P + sin_B sin_A Y_P - sin_B X_A + cos_B Z_A + cos_B Z_A + Z_B$;

Applicando la matrice appena sviluppata Eqn. (15) al punto Q_p Eqn. (11) è possibile ottenere Eqn. (16) le coordinate di Q nel sistema di riferimento O_G:

$$
\begin{bmatrix} X_Q \\ Y_Q \\ Z_Q \\ 1 \end{bmatrix}^{G} = \begin{bmatrix} b_0 \\ b_1 \\ b_2 \\ 1 \end{bmatrix} \tag{16}
$$

In cui:

$b_0 =$
$cos_P cos_{AP} \cos \alpha \sin \beta \, f + cos_P cos_{AP} X_{P0} + cos_B sin_{AP} \sin \alpha \, f - cos_B sin_{AP} Y_{P0} + sin_B \cos \beta \cos \alpha \, f + sin_B Z_{P0} + + cos_B cos_A X_P - cos_B sin_A Y_P + cos_B X_A + sin_B Z_P + sin_B Z_A + X_B$

$b_1 = sin_{AP} \cos \alpha \sin \beta \, f + sin_{AP} X_{P0} - cos_{AP} \sin \alpha \, f + cos_{AP} Y_{P0} + sin_A X_P + cos_A Y_P + Y_A + Y_B;$

$b_2 =$
$-sin_B cos_{AP} \cos \alpha \sin \beta \, f - sin_B cos_{AP} X_{P0} - sin_B sin_{AP} \sin \alpha \, f + sin_B sin_{AP} Y_{P0} + cos_B \cos \beta \cos \alpha \, f + cos_B Z_{P0} - sin_B cos_A X_P + sin_B sin_A Y_P - sin_B X_A + cos_B Z_P + cos_B Z_A + Z_B$

La testa di lavorazione, per garantire una buona qualità superficiale, deve essere posizionata alla distanza focale f rispetto la superficie reale e parallelamente al vettore normale a quest'ultima. Il vincolo angolare può essere estrapolato dalla parte rotazionale dell'Eqn. (15) ed invertito siccome la trasformazione è inversa. L'espressione ricavata è la seguente Eqn. (17):

$$
\begin{bmatrix} cos_P cos_{AP} & sin_{AP} & -sin_B cos_{AP} \\ -cos_B sin_{AP} & cos_{AP} & sin_B sin_{AP} \\ sin_B & 0 & cos_B \end{bmatrix} \begin{bmatrix} 0 \\ 0 \\ 1 \end{bmatrix} = \begin{bmatrix} -sin_P cos_{AP} \\ sin_B sin_{AP} \\ cos_B \end{bmatrix} \tag{17}
$$

Poiché l'inclinazione dello strumento di lavoro Q si può esprimere utilizzando l'Eqn. (15), dove la posizione di P_0 è ininfluente cosi come la distanza focale f.
La relazione, ricavata riferendosi alle Eqn. (15) e Eqn. (17), è data dall' Eqn. (18):

$$
\begin{bmatrix} -sin_P cos_{AP} \\ sin_B sin_{AP} \\ cos_B \end{bmatrix} = \begin{bmatrix} \sin \beta \cos \alpha \\ -\sin \alpha \\ \cos \beta \cos \alpha \end{bmatrix} \tag{18}
$$

L'equazione (18) permette di ricavare la dipendenza di A e B in funzione di α e β, che saranno sostituite in Eqn. (16), le relazioni Eqn. (19), Eqn. (20), Eqn. (21) sono:

$$
cos_B = \cos \beta \cos \alpha \rightarrow B = \pm \cos^{-1}(\cos \beta \cos \alpha) \tag{19}
$$

Da cui:

$$
\begin{cases} cos_{AP} = -\dfrac{\sin \beta \cos \alpha}{sin_B} \\ sin_{AP} = -\dfrac{\sin \alpha}{sin_B} \end{cases} \quad se \; sin_B \neq 0 \tag{20}
$$

$$cos_B = 1 \ se \ sin_B = 0 \tag{21}$$

Esplicitando Eqn. (16) in funzione di P_0 supponendo che $sin_B \neq 0$ sostituendo in Eqn. (20) l'espressione Eqn.(22) risulta essere:

$$\begin{bmatrix} X_Q \\ Y_Q \\ Z_Q \\ 1 \end{bmatrix}^G = \begin{bmatrix} cos_P cos_{AP} & -cos_B sin_{AP} & sin_B & K_1 \\ sin_{AP} & cos_{AP} & 0 & K_2 \\ -sin_B cos_{AP} & sin_B sin_{AP} & cos_B & K_3 \\ 0 & 0 & 0 & 1 \end{bmatrix}_P^G \begin{bmatrix} X_{P0} \\ Y_{P0} \\ Z_{P0} \\ 1 \end{bmatrix}^P \tag{22}$$

I coefficienti possono essere esplicitati:

$K_1 = cos_P cos_{AP} \cos\alpha \sin\beta f + cos_B sin_{AP} \sin\alpha f + sin_B \cos\beta \cos\alpha f + cos_B cos_A X_P - cos_B sin_A Y_P + cos_B X_A + sin_B Z_P + sin_B Z_A + X_B$;

$K_2 = sin_{AP} \cos\alpha \sin\beta f - cos_{AP} \sin\alpha f + sin_A X_P + cos_A Y_P + Y_A + Y_B$;

$K_3 = -sin_B cos_{AP} \cos\alpha \sin\beta f - sin_B sin_{AP} \sin\alpha f + cos_B \cos\beta \cos\alpha f - sin_B cos_A X_P + sin_B sin_A Y_P - sin_B X_A + cos_B Z_P + cos_B Z_A + Z_B$;

L'equazione (16) nel caso Eqn. (21) si semplifica all'espressione Eqn.(23):

$$\begin{bmatrix} X_Q \\ Y_Q \\ Z_Q \\ 1 \end{bmatrix}^G = \begin{bmatrix} cos_{AP} & -sin_{AP} & 0 & K_1 \\ sin_{AP} & cos_{AP} & 0 & K_2 \\ 0 & 0 & 1 & K_3 \\ 0 & 0 & 0 & 1 \end{bmatrix}_P^G \begin{bmatrix} X_{P0} \\ Y_{P0} \\ Z_{P0} \\ 1 \end{bmatrix}^P \tag{23}$$

E i coefficienti risultano essere:

$K_1 = cos_P cos_{AP} \cos\alpha \sin\beta f + sin_{AP} \sin\alpha f + cos_A X_P - sin_A Y_P + X_A + X_B$;

$K_2 = sin_{AP} \cos\alpha \sin\beta f - cos_{AP} \sin\alpha f + sin_A X_P + cos_A Y_P + Y_A + Y_B$;

$K_3 = \cos\beta \cos\alpha f + Z_P + Z_A + Z_B$;

Al fine del calcolo della matrice dei costi è sufficiente ottenere dal controllo numerico i valori $X_{P0}, Y_{P0}, Z_{P0}, \alpha, \beta$ per risolvere il sistema di equazioni e ottenere la posizione di Q e i coefficienti A e B.

La matrice dei costi è ottenuta dividendo la distanza ricavata per la velocità dei singoli assi, tenendo in considerazione un transitorio di accelerazione di tipo lineare (rappresentato in Fig. (3). Il costo è pertanto determinato dall'asse di movimentazione che impiega più tempo a spostarsi dal baricentro corrente a quello successivo.
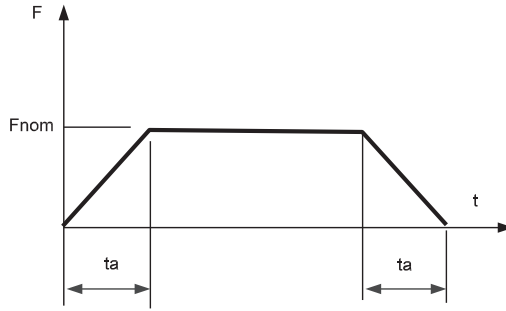
Figura 3. Rappresentazione del moto degli assi

Il tempo di percorrenza per uno spostamento s è dato dalle seguenti relazioni Eqn.(24):

$$t = \begin{cases} \frac{s}{F_{nom}} + t_a & se \;\; s > \frac{F_{nom} t_a}{2} \\ \sqrt{2 \frac{s}{F_{nom}} t_a} \,, & altrimenti \end{cases} \tag{24}$$

Le accelerazioni e decelerazioni nominali, misurate sul macchinario adottato per testare la soluzione proposta, sono riportate in Tab. 1.

Tabella 1. Leggi del moto ricavate sperimentalmente

Axes	F_{nom}	t_a
X	218 mm/s	0.239 s
Y	218 mm/s	0.246 s
Z	218 mm/s	0.245 s
A	2.12 rad/sec	0.207 s
B	0.87 rad/sec	0.156 s

7. RISULTATI SPERIMENTALI

Gli esperimenti sono stati condotti testando la soluzione su una superficie Free Form con proiezione piana circolare.

L'oggetto mostrato in Fig. (4) è composto da 980 milioni di triangoli rappresentanti la superficie e 3043 triangoli di piazzamento.

In Fig. (5) è rappresentato il percorso ottenuto seguendo la numerazione impostata da CALM, senza l'ottimizzazione.

Fig. (6) mostra il risultato della ottimizzazione della distanza euclidea 3D. La sequenza vista dall'alto è intuitivamente meno dispendiosa in termini di tempo rispetto alla precedente.

In Fig. (7) è riportata l'ottimizzazione tenendo in considerazione la cinematica della macchina 5 assi. La soluzione sembrerebbe essere peggiore rispetto le due precedenti ma ciò è dovuto al fatto che non è possibile raffigurare la movimentazione 5 assi in 2D. I risultati sperimentali, Tab. (2), confermano la bontà della soluzione.

Tabella 2. Risultati sperimentali

Metodo	Tempo Misurato [s]	Guadagno [%]
Non ottimizzato	**2775**	-
Euclidea 3D	**1939**	**30.1**
5Assi	**1715**	**38.2**
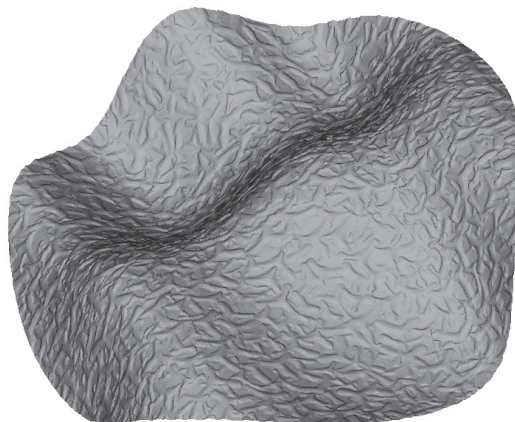
Figura 4. Superficie utilizzata.

Il tempo di calcolo per la risoluzione del TSP è dell'ordine di 2 minuti, che appaiono trascurabili rispetto ai tempi di movimentazione riportati in tabella, nonché rapportati ai tempi di lavorazione del CNC per la realizzazione della parte.
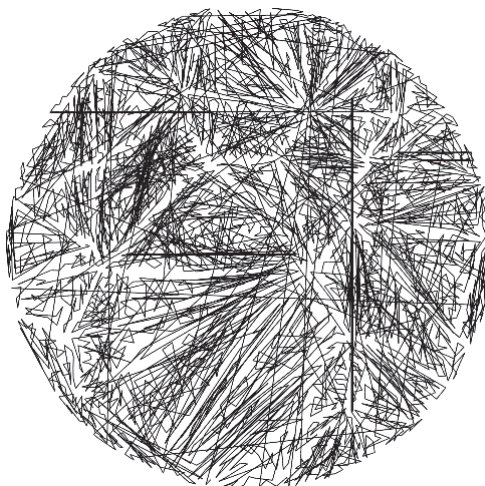
Figura 5. Percorso non ottimizzato
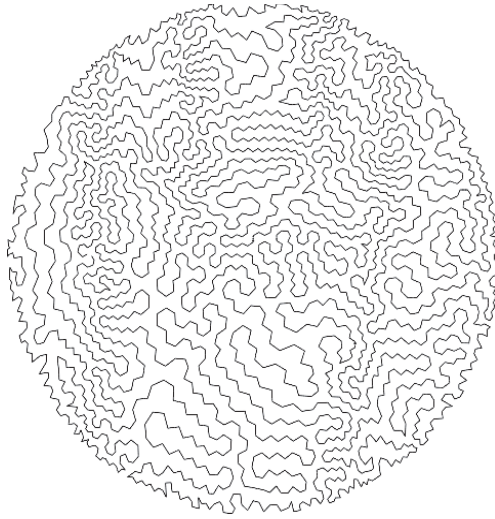
Figura 6. Percorso 3D con il metodo delle distanze euclidee
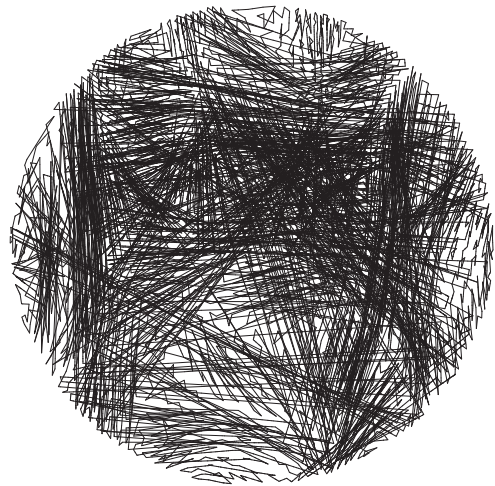
Figura 7. Percorso 3D con il metodo delle distanze "temporali"

8. CONCLUSIONI

Il problema proposto riguarda l'ottimizzazione della sequenza di piazzamento in un sistema di lavorazione laser a 5+2 assi. La sequenza originale è caratterizzata da un andamento casuale generato dall'algoritmo di triangolazione.

L'ottimizzazione del percorso è stata effettuata mediante una variante implementazione di un solutore euristico del problema del commesso viaggiatore è stata implementata introducendo al suo interno i parametri dinamici della macchina utensile utilizzata.

La riduzione dei tempi di processo risulta essere significativa, circa il 30%, a fronte di un aumento del tempo di calcolo quasi trascurabile, circa 120 secondi per un caso richiedente circa un'ora.

References

[1] Castelino K, D'Souza R, Wright PK, 2003, Toolpath Optimization for Minimizing Airtime during Machining. Journal of Manufacturing Systems 22(3):173–180.

[2] Guk-chan Han, Suck-joo Na, 1999. A study on torch path planning in laser cutting processes part 2: Cutting path optimization using simulated annealing. Journal of Manufacturing Systems, Volume 18, Issue 2, Supplement 1, Pages 62-70.

[3] Oysu, C., Bingul, Z. 2009, Application of Heuristic and Hybrid-GASA Algorithms to Tool–path Optimization Problem for Minimizing Airtime during Machining. Engineering Applications of Artificial Intelligence 22, 389–396.

[4] Kolahan F, Liang M. 2000, Optimization of hole-making operations: a tabusearch approach. International Journal of Machine Tools and Manufacture International Journal of Machine Tools and Manufacture, 40:1735-53.

[5] Lazoglu I, Manav C, Murtezaoglu Y. 2009, Tool path optimization for free form surface machining, CIRP Annals, 58:101-104.

[6] S. Makhanov : Optimization and correction of the tool path of the fiveaxis milling machine: part 1. spatial optimization. Mathematics and Computers in Simulation, 75, 2007, pp. 210–230 Applied Scientific Computing: Advanced Grid Generation, Approximation and Simulation.

[7] Piegl L.A, Tiller W, 1998, Geometry-based triangulation of trimmed NURBS surfaces. Computer Aided Design. 30(1):11-18.

[8] Cuccolini G., Orazi, L. and Fortunato, 2013, A. 5 Axes computer aided laser milling. Optics and Lasers in Engineering 51 (6):749-760.

[9] Tianjun Liao, Thomas Stützle, 2014, Marco Antonio Montes de Oca, and Marco Dorigo. A unified ant colony optimization algorithm for continuous optimization European Journal of Operational Research 234(3):597-609.

[10] Dorigo, M., Maniezzo, V., & Colorni, A. 1991. The ant system: An autocatalytic optimizing process. Tech. Rep. 91-016 Revised, Dipartimento di Elettronica, Politecnico di Milano, Italy.

[11] M. Dorigo, V. Maniezzo, A. Colorni, 1996, Ant system: Optimization by a colony of cooperating agents, IEEE Transactions on Systems, Man, and Cybernetics – Part B, 26 (1), pp. 29–41.

[12] M. Dorigo, T. Stützle, 2014, Ant colony optimization, MIT Press, Cambridge, London, England.

[13] Applegate D.L., Bixby R.E., Chvátal V., Cook W., Espinoza D.G., Goycoolea M., Helsgaun, K., 2009, Certification of an optimal TSP tour through 85,900 cities, Operations Research Letters, 37 (1), pp. 11-15.

[14] Applegate, D., Cook, W., Rohe, A. 2003, Chained Lin-Kernighan for large traveling salesman problems, INFORMS Journal on Computing, 15 (1), pp. 82

PROGETTAZIONE DI TRAIETTORIE ENERGETICAMENTE EFFICIENTI IN SERVOMECCANISMI PER MACCHINE AUTOMATICHE

Angelo Oreste Andrisano
Dipartimento di Ingegneria Enzo Ferrari,
Università degli Studi di Modena e Reggio Emilia, Italy
E-mail: angelooreste.andrisano@unimore.it

Federico Balugani
Dipartimento di Ingegneria Enzo Ferrari,
Università degli Studi di Modena e Reggio Emilia, Italy
E-mail: federico.balugani@unimore.it

Giovanni Berselli
Dipartimento di Ingegneria Meccanica, Energetica, Gestionale e dei Trasporti,
Università degli Studi di Genova, Italy
E-mail: giovanni.berselli@unige.it

Michele Gadaleta
Dipartimento di Ingegneria Enzo Ferrari,
Università degli Studi di Modena e Reggio Emilia, Italy
E-mail: michele.gadaleta@unimore.it

Marcello Pellicciari
Dipartimento di Ingegneria Enzo Ferrari,
Università degli Studi di Modena e Reggio Emilia, Italy
E-mail: marcello.pellicciari@unimore.it

Alberto Vergnano
Dipartimento di Ingegneria Enzo Ferrari,
Università degli Studi di Modena e Reggio Emilia, Italy
E-mail: alberto.vergnano@unimore.it

Abstract. *I Servomeccanismi (SM), anche detti camme elettroniche, sono sempre più utilizzati in sostituzione alle tradizionali camme meccaniche, al fine di incrementare la flessibilità e la ri-configurabilità delle moderne macchine automatiche. Nel tentativo di ottimizzare le prestazioni globali di un SM è necessario considerare vari fattori, tra cui le dinamiche di meccanismo a membri rigidi, motore elettrico e sistema di controllo, nonchè dalle leggi di moto richieste. In particolare, le traiettorie punto-punto (PP) vengono progettate sulla base di esigenze di processo e, allo stesso tempo, cercando di minimizzare opportuni indici di costo quali, ad esempio, la richiesta di coppia o potenza. Questa memoria presenta un metodo innovativo per generare traiettorie energeticamente efficienti, utilizzando spline cubiche o del quinto grado. Le funzioni costo sono calcolate utilizzando un prototipo virtuale del sistema che comprende la modellazione di tutti i principali sottosistemi di un SM. I risultati ottenuti sono affiancati a misure di validazione sperimentale ottenute su un prototipo fisico.*

Parole chiave: *Prototipazione Virtuale, Generazione di Traiettorie, Servomeccanismi*

1. INTRODUZIONE

Le moderne macchine automatiche vengono progettate e realizzate in modo da garantire, possibilmente, elevate flessibilità e possibilità di riconfigurazione, al fine di adattarsi alle svariate richieste produttive [1]. Per i suddetti motivi, in ambito automazione industriale, è sempre più frequente l'utilizzo di SM (detti anche camme elettroniche) in sostituzione alle tradizionali camme meccaniche, anche per movimentazioni caratterizzate da elevate velocità e richieste di precisione. L'adozione di SM permette infatti di utilizzare traiettorie ottimizzate per ogni modalità operativa (si pensi alle macchine che gestiscono differenti formati del prodotto). Per contro, i SM richiedono spesso una corposa fase di tuning, mirata al raggiungimento di errori di posizione accettabili [2].

Usualmente, le camme elettroniche vengono sviluppate con metodi e strumenti differenti e scarsamente integrati. Per esempio, la progettazione del cinematismo è di solito affidata agli ingegneri meccanici, che si preoccupano di ottenere una soluzione affidabile, compatta, rigida, leggera ed economica. In parallelo, la scelta dell'attuatore elettrico, della legge di moto ed il "tuning" del sistema di controllo spetta a figure professionali dedicate. Naturalmente, alcune parti della legge di moto non sono vincolate da particolari esigenze di processo e possono essere liberamente ottimizzate.

L'ottimizzazione off-line delle leggi di moto è un tema fortemente trattato dalla letteratura scientifica. Per esempio, [3] e [4] propongono rispettivamente un'ottimizzazione di tempo ciclo e jerk per robot seriali. Gli autori di [5] e [6] propongono algoritmi per la generazione di leggi di moto energeticamente efficienti, mentre in [7] viene minimizzata la variazione della coppia richiesta. Altri ricercatori hanno considerato strutture ridondanti [8] o ottimizzazioni multi-obiettivo, per esempio tempo-energia [9].

Indipendentemente dal tipo di ottimizzazione, ogni algoritmo richiede un modello del sistema che calcoli il valore della funzione costo. Per esempio, Saramago e Steffen [10] ottengono la richiesta di coppia degli assi del robot considerando solo il contributo dovuto alla dinamica dei corpi rigidi. Field e Stephanenko [11] calcolano il consumo energetico dei motori tenendo in considerazione le sole perdite resistive. In ogni caso, qualsiasi approccio

potrebbe fornire risultati non ottimali in mancanza di un corretto modello del sistema nel suo complesso.

Viste le precedenti considerazioni, l'obiettivo di questa memoria è innanzitutto quello di richiamare un dettagliato prototipo virtuale di un SM ad un grado di libertà (g.d.l.), precedentemente sviluppato dagli autori in [12]. Tale prototipo virtuale comprendente modelli di sistema meccanico, motore elettrico, controllore e convertitore di potenza. Le richieste di coppia e di potenza vengono così predette in modo accurato, differentemente da quanto potrebbe accadere trascurando uno o più sottosistemi. Viene poi descritto l'approccio utilizzato per la generazione di traiettorie energeticamente ottime. In particolare, le PP proposte utilizzano spline interpolanti una serie di punti virtuali, la cui posizione è variata dall'algoritmo di ottimizzazione. Vengono infine discussi risultati numerici e sperimentali.

2. MODELLAZIONE DEL SERVOMECCANISMO

Le applicazioni con camme elettroniche solitamente utilizzano motori sincroni a magneti permanenti (PMSM). Uno schematico del sistema è riportato in Fig. 1 e comprende il carico meccanico (in questo caso un manovellismo di spinta) movimentato da un PMSM, a sua volta alimentato da un "drive" di potenza connesso alla rete elettrica. Il drive comprende un raddrizzatore, un servo inverter ed un DC-bus con resistenza di drain. Come visibile nella stessa Fig. 1, il prototipo fisico del SM utilizzato è composto da un drive Beckhoff AX5112 e da un PMSM Beckhoff AM3072 connesso ad un manovellismo. Lo schema a blocchi del sistema di controllo (comprendente modello del motore elettrico e del carico meccanico) è visibile in Fig. 2, mentre Fig. 3 raffigura il modello del convertitore di potenza. Con ovvia notazione di simboli, u indica un generica variabile nel suo attuale valore, mentre u^* indica il valore desiderato per tale variabile (setpoint).
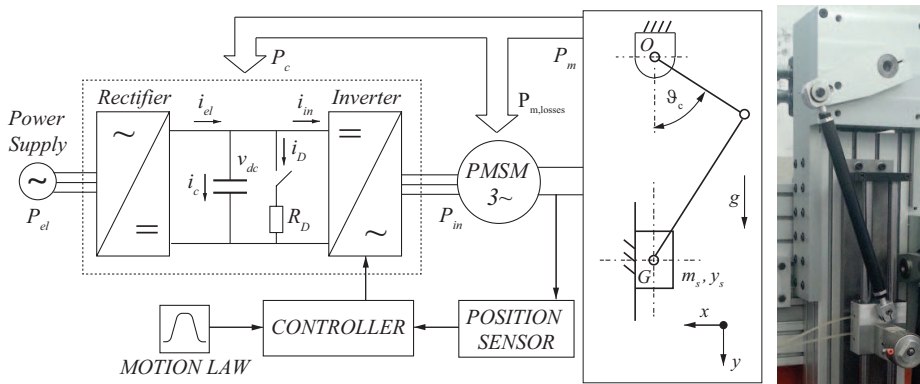

Figure 1. Schema di un SM ad un grado di libertà (sulla sinistra). I termini P_{el}, P_c, P_{in}, P_m rappresentano rispettivamente le potenze in ingresso al drive, al condensatore, all'inverter e al manovellismo. Sulla destra una foto del SM reale
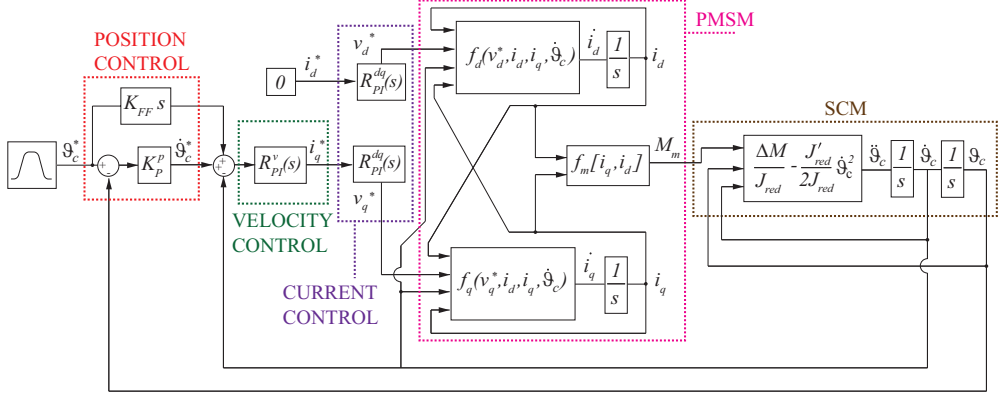
Figure 2. Diagramma a blocchi del controllore, dinamica del PMSM e del carico meccanico. Le funzioni f_d, f_q, e f_m sono definite nelle Eq. (2) e (4), mentre $\Delta M(\vartheta_c) = M_m - M_r(\vartheta_c) - dW_{pot}(\vartheta_c)/d\vartheta_c$, e $J'_{red} = dJ_{red}/d\vartheta_c$.
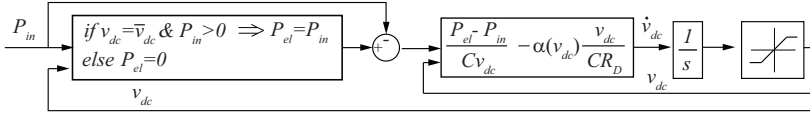
Figure 3. Diagramma a blocchi del modello del convertitore di potenza.

Modellazione del carico Meccanico

La dinamica del manovellismo di spinta può essere descritta utilizzando il concetto di momento d'inerzia ridotto [13]. In particolare, l'equazione del moto è semplicemente data da:

$$\ddot{\vartheta}_c = \frac{M_m - M_r - dW_{pot}/d\vartheta_c}{J_{red}} - \frac{dJ_{red}/d\vartheta_c}{2J_{red}} \dot{\vartheta}_c^2 \tag{1}$$

avendo definito ϑ_c come posizione angolare della manovella, M_m coppia di uscita del motore elettrico, M_r coppia resistente generalizzata, J_{red} momento d'inerzia ridotto all'albero motore, W_{pot} energia potenziale gravitazionale. In questo caso, la coppia M_r considera unicamente l'effetto degli attriti, mentre le altre forze non conservative si considerano trascurabili. Figura 4 riporta i valori di J_{red} e $dJ_{red}/d\vartheta_c$ in funzione di ϑ_c per il manovellismo di spinta considerato, evidenziando l'elevata variabilità di entrambe le grandezze. Noti i profili di moto desiderati $\vartheta_c^*(t)$, $\dot{\vartheta}_c^*(t)$, $\ddot{\vartheta}_c^*(t)$, Eq. (1) consente di calcolare l'ideale profilo di coppia richiesta dal carico meccanico.

Modellazione del PMSM

Similmente a [14] è possibile definire un modello accurato della dinamica del PMSM assumendo trascurabili le perdite per isteresi e per correnti parassite. Utilizzando la trasformata

Figure 4. Valori di J_{red}, $dJ_{red}/d\vartheta_c$ in funzione di ϑ_c.

$d - q$ [15] è possibile scrivere le equazioni di stato del sistema:

$$\frac{di_d}{dt} = L_d^{-1} \left[v_d^* - R_s i_d + p L_q i_q \dot{\vartheta}_c \right] = f_d(v_d^*, i_d, i_q, \dot{\vartheta}_c) \tag{2}$$

$$\frac{di_q}{dt} = L_q^{-1} \left[v_q^* - R_s i_q - p \dot{\vartheta}_c (L_d i_d + \lambda_m) \right] = f_q(v_q^*, i_d, i_q, \dot{\vartheta}_c)$$
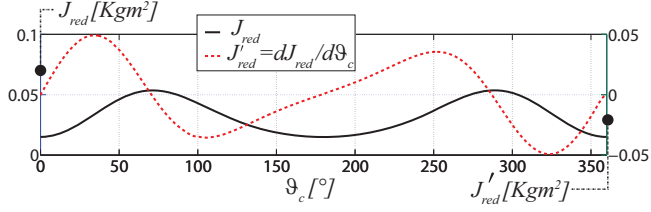
$$\lambda_m = \sqrt{2} K_t \Big/ 3p \tag{3}$$

con v_d^*, i_d, L_d tensione, corrente e induttanza dell'asse diretto (asse d), v_q^*, i_q, L_q tensione, corrente e induttanza dell'asse in quadratura (asse q), R_s resistenza statorica, p numero di paia poli, λ_m flusso rotorico e K_t costante di coppia. Risulta quindi possibile calcolare la coppia erogata dal PMSM come:

$$M_m = 3p \left[\lambda_m i_q + (L_d - L_q) i_d i_q \right] \Big/ 2 = f_M(i_q, i_d) \tag{4}$$

mentre la potenza richiesta dal PMSM vale:

$$P_{in} = 3 \left[v_q^* i_q + v_d^* i_d \right] \Big/ 2 \tag{5}$$

Modellazione del Controllore

Il controllore è basato su un controllo in cascata che comprende anelli di corrente, velocità e posizione. Con riferimento alla Fig. 2, $R_{PI}^{dq}(s)$ rappresenta il regolatore proporzionale integrale (PI) di corrente per gli assi d e q, $R_{PI}^{v}(s)$ rappresenta il regolatore PI di velocità, mentre K_P^p e K_{FF}^p indicano rispettivamente guadagno proporzionale e guadagno di feed-forward del controllore di posizione. Si precisa che il modello comprende gli effetti della discretizzazione dei segnali (dovuti al campionamento del controllore reale). Partendo dalla legge di moto desiderata (ovvero $\vartheta_c^*(t)$, $\dot{\vartheta}_c^*(t)$, $\ddot{\vartheta}_c^*(t)$) è possibile connettere modello del sistema di controllo con i modelli del carico meccanico e del PMSM al fine di ottenere una previsione di coppia più accurata rispetto a quanto si può ottenere considerando solo il carico meccanico.

Modellazione del Convertitore di Potenza

In Fig. 1 si notano i sottosistemi del convertitore di potenza ovvero il raddrizzatore, l'inverter ed il DC-bus. Ad oggi, generalmente, i drive sono equipaggiati con raddrizzatore passivi, i quali consentono alla potenza elettrica di fluire dalla rete al carico ma non viceversa (ovvero $P_{el} \geq 0$). Quindi, quando il PMSM funziona da generatore di potenza (durante le fasi di frenata rigenerativa), l'energia recuperata viene immagazzinata nel condensatore, C, facendo

alzare la tensione del DC-Bus. Nel caso in cui si raggiunga la soglia massima per la tensione del DC-Bus, viene automaticamente attivata la resistenza di drain, R_D, per dissipare l'energia rigenerata in eccesso. Con riferimento a Fig. 1, nel caso di corrente uscente dal raddrizzatore, è possibile scrivere l'equazione di nodo delle correnti:

$$i_{el} = i_{in} + C\frac{dv_{dc}}{dt} + \alpha i_D \tag{6}$$

con v_{dc} tensione del DC-Bus e α che può assumere valore pari a 0 o 1 in caso di resistenza di drain disattivata o attivata. Trascurando le perdite di inverter e raddrizzatore e nominando con $\bar{v}_{dc}$ la tensione massima raddrizzata (in uscita al raddrizzatore a vuoto), è possibile scrivere l'equazione di bilancio delle potenze in virtù dell'Eq. (6):

$$P_{el} - P_{in} = Cv_{dc}\frac{dv_{dc}}{dt} + \alpha v_{dc}^2/R_D \tag{7}$$

ed ottenere la richiesta di potenza prelevata dalla rete come:

$$P_{el} = \begin{cases} P_{in}, & \text{if } v_{dc} \leq \bar{v}_{dc} \text{ AND } P_{in} > 0 \\ 0, & \text{negli altri casi} \end{cases} \tag{8}$$

Tale modello è illustrato in Fig. 3.

3. OTTIMIZZAZIONE

Come visibile in Fig. 5, una generica legge di moto può essere suddivisa in zone di interazione prodotto (per esempio $\vartheta_c = h$) e zone meno rilevanti ai fini del processo. Queste ultime zone possono essere ottimizzate minimizzando specifiche funzioni costo. Si consideri una traiettoria PP, $\vartheta_c(t)$, con $t \in [0,T]$ avente $\dot{\vartheta}_c \geq 0$. Partendo da una legge polinomiale del quinto grado, che è la traiettoria che minimizza il jerk RMS [4], l'approccio proposto utilizza spline cubiche o del quinto grado che interpolano una serie di punti virtuali posizionati nell'intervallo $[0,T]$. La posizione di questi punti virtuali è variata dall'algoritmo di ottimizzazione per convergere verso una legge di moto ottima. In particolare, l'intervallo $[0,T]$ è diviso in n sotto-intervalli equi-spaziati (dove n è un numero intero scelto dall'utente, con l'unica condizione che $n > 3$). Il vettore degli istanti di tempo e le corrispondenti posizioni virtuali sono definite come:

$$\boldsymbol{\xi} = [\xi_i]^T = [iT/n]^T, \quad \mathbf{q} = [q_i]^T, \quad i = 0,\ldots,n \tag{9}$$
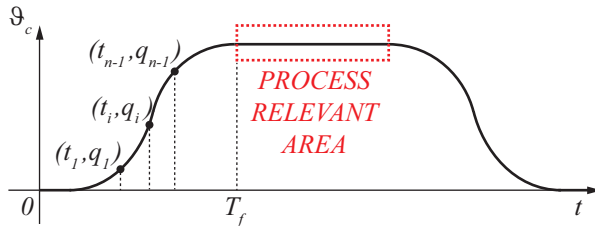

Figure 5. Generico profilo di Posizione.

Con $q_0 = \vartheta_c(0)$ e $q_n = \vartheta_c(T)$. La corrispondente legge polinomiale a tratti è definita come:

$$\vartheta_c(\mathbf{q},t) \equiv \left\{ \mathscr{P}_k(\mathbf{q},t) = \sum_{j=0}^{m} D_{j,k}(\mathbf{q})(t-\xi_k)^j, \ \xi_k \leq t \leq \xi_{k+1}, \ k = 0,\dots,n-1 \right\} \quad (10)$$

con $D_{j,k}$ coefficienti della polinomiale per ciascun tratto. L'Eq. (10) può descrivere sia una spline cubica con $4n$ coefficienti incogniti ($m = 3$) che una spline del quinto grado con $6n$ coefficienti incogniti ($m = 5$). Inoltre l'Eq. (10) diventa una singola polinomiale se $n = 1$.

Per le spline cubiche il numero di coefficienti incogniti può essere ridotto imponendo i seguenti vincoli:

1. $3(n-1)$ condizioni per la continuità di posizione, velocità e accelerazione nei punti intermedi:
$$\begin{aligned} \mathscr{P}_k(\mathbf{q},\xi_{k+1}) &= \mathscr{P}_{k+1}(\mathbf{q},\xi_{k+1}); \\ \dot{\mathscr{P}}_k(\mathbf{q},\xi_{k+1}) &= \dot{\mathscr{P}}_{k+1}(\mathbf{q},\xi_{k+1}); \\ \ddot{\mathscr{P}}_k(\mathbf{q},\xi_{k+1}) &= \ddot{\mathscr{P}}_{k+1}(\mathbf{q},\xi_{k+1}); \quad \text{for } k = 0\dots n-2 \end{aligned} \quad (11)$$

2. 6 condizioni per imporre posizione, velocità e accelerazione nei punti estremali:
$$\begin{aligned} \mathscr{P}_0(\mathbf{q},0) &= q_0; & \dot{\mathscr{P}}_0(\mathbf{q},0) &= 0; & \ddot{\mathscr{P}}_0(\mathbf{q},0) &= 0; \\ \mathscr{P}_{n-1}(\mathbf{q},T) &= q_n; & \dot{\mathscr{P}}_{n-1}(\mathbf{q},T) &= 0; & \ddot{\mathscr{P}}_{n-1}(\mathbf{q},T) &= 0; \end{aligned} \quad (12)$$

Per le spline del quinto grado il numero delle incognite può essere ridotto imponendo i seguenti vincoli:

1. $3(n-1)$ condizioni come in Eq. 11, più $2(n-1)$ condizioni per la continuità di jerk e quirk nei punti intermedi:
$$\begin{aligned} \dddot{\mathscr{P}}_k(\mathbf{q},\xi_{k+1}) &= \dddot{\mathscr{P}}_{k+1}(\mathbf{q},\xi_{k+1}); \\ \ddddot{\mathscr{P}}_k(\mathbf{q},\xi_{k+1}) &= \ddddot{\mathscr{P}}_{k+1}(\mathbf{q},\xi_{k+1}); \quad \text{for } k = 0\dots n-2 \end{aligned} \quad (13)$$

2. 6 condizioni come in Eq. 12, più 2 condizioni per imporre il jerk nei punti estremali:
$$\dddot{\mathscr{P}}_0(\mathbf{q},0) = 0; \quad \dddot{\mathscr{P}}_{n-1}(\mathbf{q},T) = 0; \quad (14)$$

Ne consegue che rimangono $n-3$ gradi di libertà, sia per le spline cubiche che per le per spline del quinto grado, cosicché solo un sottoinsieme del vettore $\mathbf{q}$ può essere utilizzato ai fini dell'ottimizzazione. Similmente a [17], la posizione dei punti q_1 e q_{n-1} è vincolata imponendo l'accelerazione nei punti estremali, per le spline cubiche, ed il jerk nei punti estremali per le spline del quinto grado. Siccome q_0 e q_n sono fissati, il vettore dei parametri di ottimizzazione risulta:
$$\mathbf{q}_{red} = [q_2,\dots,q_{n-2}]^T \subset \mathbf{q} \quad (15)$$

Il problema di ottimizzazione è formulato come minimizzazione della funzione costo $F(\mathbf{q}_{red})$ variando il vettore dei parametri di ottimizzazione $\mathbf{q}_{red}$:
$$\min_{\mathbf{q}_{red}} F(\mathbf{q}_{red}), \quad \text{sottoposta a:} \quad (16)$$

$$|\dot{\vartheta}_c(t)| < \dot{\vartheta}_c^{max} \quad |\ddot{\vartheta}_c(t)| < \ddot{\vartheta}_c^{max} \quad |\dddot{\vartheta}_c(t)| < \dddot{\vartheta}_c^{max} \quad (17)$$

$$|\tau_m(t)| < \tau_m^{max} \qquad (18)$$

$$\varepsilon(t) < \varepsilon^{max} \qquad (19)$$

Le equazioni (17) e (18) impongono che velocità, accelerazione, jerk e coppia rimangano al di sotto delle rispettive soglie limite $\dot{\vartheta}_c^{max}$, $\ddot{\vartheta}_c^{max}$, $\dddot{\vartheta}_c^{max}$, e τ_m^{max}. In modo simile, può essere imposta una soglia per il massimo errore di posizione, ε_{max}.

Per quanto riguarda la funzione costo $F(\mathbf{q}_{red})$, è possibile utilizzare direttamente l'energia richiesta ottenuta come integrale della potenza elettrica:

$$F(\mathbf{q}_{red}) = \int_0^T P_{el}(\mathbf{q}_{red}, t) dt \qquad (20)$$

Per quanto riguarda il set iniziale dei parametri di ottimizzazione, $\mathbf{q}_{red}^0$, è ottenuto fittando la polinomiale del quinto grado.

4. RISULTATI

L'ottimizzazione vincolata di Eq. (16) è stata risolta utilizzando l'algoritmo SQP implementato nella funzione *fmincon* dell'ambiente di programmazione Matlab, settando $n = 12$. I parametri del modello, utilizzati nelle simulazioni, sono riportati in Tab. 1, p_{samp}, v_{samp}, dq_{samp} sono i tempi di campionamento per gli anelli di posizione, velocità e corrente rispettivamente.

La traiettoria test utilizzata è del tipo *andata-sosta-ritorno*, ed è composta da una PP di andata, con $\vartheta_c \in [0°, 100°]$ e fase master $\vartheta_{ma} \in [0°, 360°]$, una sosta, caratterizzata da $\vartheta_c = 100°$ con fase master $\vartheta_{ma} \in [360°, 390°]$, e un movimento PP di ritorno con $\vartheta_c \in [100°, 0°]$ e fase master $\vartheta_{ma} \in [390°, 750°]$. La velocità dell'asse master virtuale è di 500 rpm quindi la durata totale della traiettoria è pari a 0.25s. Figura 6 riporta i profili ottimizzati (ottenuti con spline cubiche e del quinto grado) rispetto al profilo iniziale di riferimento (PP ottenute con delle polinomiali del quinto grado). Figura 7 mostra le curve di potenza della traiettoria iniziale e della migliore fra le traiettorie ottimizzate (ottenuta con spline cubica). In Fig. 7, con linea continua sono rappresentate le curve ottenute in simulazione, mentre in linea tratteggiata le curve di potenza sperimentale (misurate con un misuratore di potenza

Table 1. Model parameters.

$p = 5$	$R_s = .68\Omega$	$L_d = L_q = 10.35mH$
$K_t = 3.23Nm/A$	$M_{m,max} = 118.8Nm$	$C = 470\mu F$
$K_P^p = 45$	$K_{FF}^p = 1.20$	$K_P^v = 25$
$K_I^v = 1900$	$K_P^{dq} = 50$	$K_I^{dq} = 26000$
$p_{samp} = 250\mu s$	$v_{samp} = 125\mu s$	$dq_{samp} = 62.5\mu s$

Table 2. Optimization Results

	Energia (Simulazione) (J)	Energia (Sperimentale) (J)
Iniziale	46.3	48.9
Spline 3 Ottima	32.4	32.8
Spline 5 Ottima	33.2	33.5

Figure 6. Confronto Leggi di moto

(a) Traiettoria iniziale

(b) Spline cubica ottimizzata
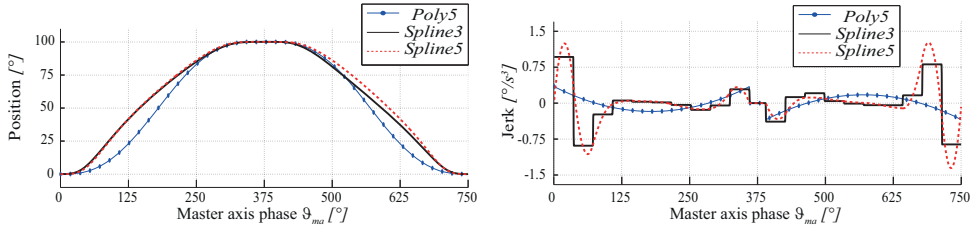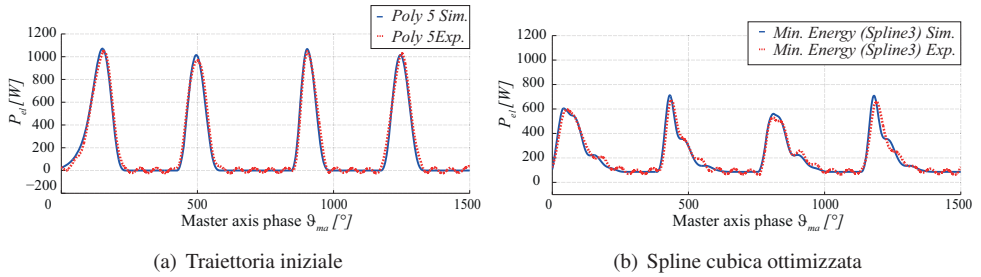
Figure 7. Curve simulate (Sim.) e sperimentali (Exp.) delle richieste di potenza elettrica per la traiettoria iniziale e la traiettoria ottimizzata con spline cubiche

professionale [18]). I risultati delle simulazioni vengono pienamente confermati da risultati sperimentali ottenuti su un prototipo fisico del sistema. In Tab. 2 sono riportati i valori numerici simulati e sperimentali di energia richiesta per ciclo. Dalla tabella si può notare una decisa diminuzione dell'energia richiesta di circa il 31.5% per le spline del quinto grado e del 32.9% per le spline cubiche. Tale risultato conferma che traiettorie più "dolci" (con un maggior numero di derivate continue) sono energeticamente meno efficienti.

5. CONCLUSIONI

Un nuovo metodo per l'ottimizzazione di leggi di moto PP è stato proposto e validato sperimentalmente. Tale metodo utilizza traiettorie spline che interpolano una serie di punti virtuali la cui posizione viene stabilita da un algoritmo di ottimizzazione. È stato proposto come caso studio un SM composto da un manovellismo di spinta controllato in posizione.

REFERENCES

[1] Heisel, U., and Meitzner, M., 2011. "Progress in reconfigurable manufacturing systems". *J. for Manufacturing Science and Production,* **6**, pp. 1–8.

[2] Pellicciari, M., Berselli, G., Ori, M., and Leali, F., 2013. "The role of co-simulation in the integrated design of high-dynamics servomechanisms: an experimental evaluation". *Applied Mechanics and Materials,* **278-280**, pp. 1758–1764.

[3] Bobrow, J., Dubowsky, S., and Gibson, J., 1985. "Time-optimal control of robotic manipulators along specified paths". *The International Journal of Robotics Research,* **4**(3), Sept., pp. 3–17.

[4] Flash, T., and Hogans, N., 1985. "The coordination of arm movements: An experimentally confirmed mathematical model". *Journal of Neuroscience,* **5**, pp. 1688–1703.

[5] Pellicciari, M., Berselli, G., Leali, F., and Vergnano, A., 2011.. "Object-oriented modeling of industrial manipulators with application to energy optimal trajectory scaling". *ASME IDETC 2011 International Design Engineering Technical Conferences, Washington DC, USA*, pp. 1–10.

[6] Huang, M.-S., and andRong Fong Fung, Y.-L. H., 2012. "Minimum-energy point-to-point trajectory planning for a motor-toggle servomechanism". *IEEE/ASME Transactions on Mechatronics,* **17**(2), april, pp. 337 –344.

[7] Uno, Y., Kawato, M., and Suzuki, R., 1989. "Formation and control of optimal trajectory in human multijoint arm movement". *Biological Cybernetics,* **61**(2), June, pp. 89–101.

[8] Hirakawa, A., and Kawamura, A., 1997. "Trajectory planning of redundant manipulators for minimum energy consumption without matrix inversion". In IEEE Int. Conf. on Robotics and Automation, Vol. 3, pp. 2415–2420.

[9] Jacobsen, D., Gershwin, S., and Lele, M., 1970. "Computation of optimal singular controls". *IEEE Transactions on Automatic Control,* **AC-15**(Issue 1), pp. 67–73.

[10] Saramago, S., and Jr, V. S., 1998. "Optimization of the trajectory planning of robot manipulators taking into account the dynamics of the system". *Mechanism and Machine Theory,* **33**(7), pp. 883 – 894.

[11] Field, G., and Stepanenko, Y., 1996. "Iterative dynamic programming: an approach to minimum energy trajectory planning for robotic manipulators". In IEEE Int. Conf. on Robotics and Automation, Vol. 3, pp. 2755–2760.

[12] Pellicciari, M., Berselli, G., and Balugani, F., 2014. "On Designing Optimal Trajectories for Servo-Actuated Mechanisms: Detailed Virtual Prototyping and Experimental Evaluation". *IEEE/ASME Transactions on Mechatronics,* **PP**(99), pp. 1–14.

[13] Dresig, H., and Holzweißig, F., 2010. *Dynamics of Machinery, Theory and Applications*. No. Springer.

[14] Pillay, P. andKrishnan, R., 1989. "Modeling,simulation, and analysis of permanent-magnet aotordrives: Part i. the permanent-magnet synchronous motor drive". *IEEE Transactions on Industry Applications,* **25**(2), pp. 265–273.

[15] Park, R. H., 1929. "Two-reaction theory of synchronous machines generalized method of analysispart i". *American Institute of Electrical Engineers, Transactions of the,* **48**(3), july, pp. 716 –727.

[16] Biagiotti, L., and Melchiorri, C., 2008. *Trajectory Planning for Automatic Machines and Robots*. Berlin, Germany: Springer-Verlag.

[17] Gasparetto, A., and Zanotto, V., 2008. "A technique for time-jerk optimal planning of robot trajectories". *Robotics and Computer-Integrated Manufacturing,* **24**(3), pp. 415–426.

[18] IRS S.r.l., 2014. @http://www.irsweb.it/MeetBOX.html.

STUDIO DELL'USURA E DEL MOMENTO RESISTENTE DI ANELLI DI TENUTA IN ELASTOMERO AL VARIARE DELLA RUGOSITÀ DELL'ALBERO

Edzeario Prati
Dipartimento di Ingegneria Industriale,
Università degli Studi di Parma
E-mail: edzeario.prati@unipr.it

Alessandro Tasora
Dipartimento di Ingegneria Industriale,
Università degli Studi di Parma
E-mail: alessandro.tasora@unipr.it

Silvia Longarini
Dipartimento di Ingegneria Industriale,
Università degli Studi di Parma
E-mail: silvia.longarini@unipr.it

Valentina Pollastri
Dipartimento di Ingegneria Industriale,
Università degli Studi di Parma
E-mail: valentina.pollastri@unipr.it

Abstract. *Nel presente lavoro si riportano i risultati di uno studio sperimentale in merito all'effetto della rugosità dell'albero sull'usura e sul momento resistente nel contatto fra albero e tenute a labbro.*

Parole chiave: *tenute radiali, rugosità, contatto, lubrificazione idrodinamica*

1. INTRODUZIONE

Gli anelli di tenuta a labbro svolgono un ruolo importante nell'industria meccanica, sia per confinare fluidi lubrificanti in prossimità di cuscinetti per alberi rotanti, sia per impedire l'ingresso di contaminanti nella macchina [1].

Le tipologie attuali di tenute a labbro fanno uso di elastomeri riconducibili principalmente a polimeri quali i fluoroelastomeri (FKM), le gomme nitrile-butadiene (NBR), i siliconi (VMQ) o il politetrafluoroetilene (PTFE), miscelati con pigmenti, antiossidanti, fillers e additivi di vario genere, secondo il tipo d'impiego [2, 3]. Nello studio attuale ci siamo concentrati su tenute in NBR in quanto sono quelle di più frequente impiego.

Nella maggior parte dei casi le tenute operano in presenza di olio lubrificante: durante
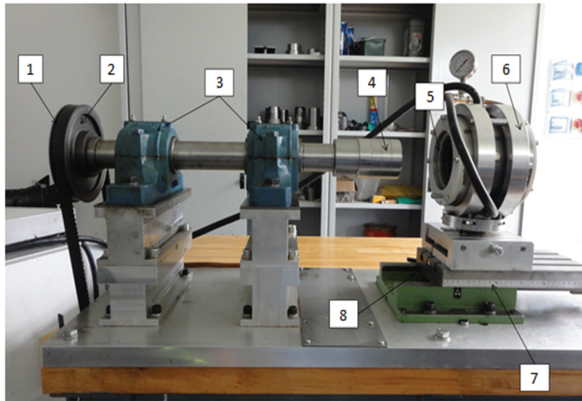
Figura 1. Banco prova. 1- cinghia; 2 puleggia ; 3- cuscinetti radiali; 4- provino; 5- alloggiamento; 6- camera dell'olio; 7- scala graduata; 8- slitta.

la rotazione dell'albero si forma un sottile film fluido fra labbro ed albero che impedisce il contato diretto fra i due materiali.

Per quanto le tenute di questo tipo siano impiegate da anni nell'industria, il fenomeno di lubrificazione è diventato oggetto di studi teorici, numerici e sperimentali solo di recente [4]. I primi studi sull'argomento sono riconducibili a [5].

Una correlazione fra la deformazione della superficie dell'elastomero, fenomeni d'attrito ed efficienza nella tenuta è stata analizzata in [6], mentre in [7] si sono proposte varie ipotesi sul tipo di lubrificazione fra labbro e tenuta. Nella maggior parte dei casi l'area di contatto è molto limitata in direzione assiale, tipicamente meno di 0.5 mm, e ciò ha reso molto difficile lo studio sperimentale della lubrificazione microscopica. Tuttavia solo in [8] si è giunti all'interpretazione corrente del fenomeno: ovvero si instaura una lubrificazione elasto-idrodinamica per effetto delle asperità dell'albero e dell'elastomero, che creano tanti

Figura 2. Albero con diverse rugosità. 1- $R_a = 0.44$; 2- $R_a = 0.34$; $R_a = 0.27$; $R_a = 0.24$

microscopici picchi di pressione all'interfaccia.

Ciò è confortato anche dall'esperienza empirica, secondo la quale è sconsigliabile montare alberi con rugosità eccessivamente bassa i prossimità delle tenute, contrariamente all'intuizione, in quanto si corre il rischio di far grippare il labbro sulla superficie a specchio.
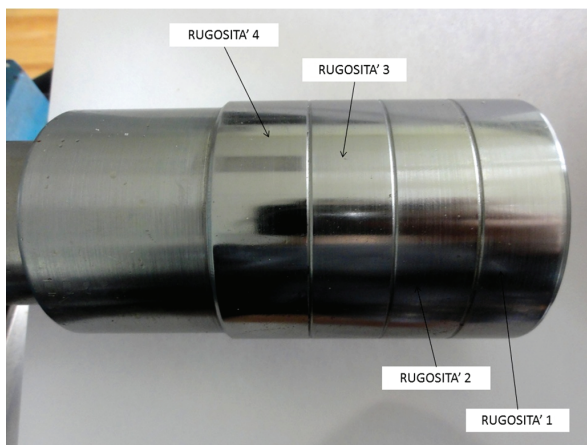
Studi successivi hanno approfondito l'argomento. In [9] si è usato un modello numerico per studiare la lubrificazione, ed in [10] si è evidenziato anche il ruolo della componente visco-elastica nello studio del fenomeno, specie in presenza di eccentricità.

Studi approfonditi sul ruolo delle asperità nella lubrificazione visco-elasto-idrodinamica in oggetto sono stati svolti da Salant et al. in [11–16]. Tali studi, di carattere principalmente numerico, hanno spiegato l'effetto benefico della presenza di micro-ondulazioni nelle superfici di contatto.

Studi compiuti in [17] hanno proposto una stima dell'usura basata su modelli numerici simili a quelli di Salant, mentre un'estensione della formulazione, che tenga in conto anche fenomeni termici, è stata proposta in [18]. Ulteriori avanzamenti sono reperibili in [19], [20], [21], [22].

In ambito sperimentale, il nostro gruppo ha svolto vari tipi di indagine, ad esempio sulla pressione di contatto [23]. In [24] abbiamo mostrato un apparato sperimentale in grado di misurare l'effetto della pressione dell'olio sulla pressione di contatto e, di conseguenza, anche sull'attrito e sul momento resistente. Altri lavori hanno mostrato l'influenza di altri parametri, ad esempio in [25] abbiamo mostrato anche l'effetto della temperatura.

Nel presente lavoro si è preso in esame l'effetto della rugosità dell'albero. Grazie ad un banco prova sviluppato appositamente per lo studio delle tenute a labbro, abbiamo svolto varie campagne sperimentali in grado di evidenziare come l'attrito, e quindi il momento resistente, cambi in funzione della rugosità dell'albero. Inoltre abbiamo svolto misurazioni sull'andamento della rugosità prima e dopo i test, evidenziando come si verifichi l'usura sulla superficie di contatto dell'albero.

2. BANCO PROVA

Il banco prova utilizzato per i test sperimentali è visibile in Fig.1.

Il banco è dotato di un sistema di controllo digitale Beckhoff con motore brushless, per monitorare la coppia resistente tramite la misura della corrente. Il momento è calcolato al netto della resistenza data da cuscinetti motore, trasmissione a cinghia, cuscinetti albero etc.

Le prove vengono svolte a velocità costante per un numero di ore prefissato.

La tenuta testata è della Angst-Pfister, conforme per esecuzione e dimensioni alla norma DIN 3760. La tenuta è in materiale NBR, con durezza 70 Shore A, di dimensioni 70x110x12, forma A. Il lubrificante è un Vanguard Gearing EP 220, con una densità a 20°C di 0,898 kg/dm^3; la sua viscosità è ISO 220 corrispondente alla classe SAE 90.

L'albero per le prove, in acciaio Fe360 non bonificato, è diviso in quattro zone a rugosità decrescente, come mostrato in Fig.2. Si è scelto un intervallo di rugosità non troppo lontano dai valori utilizzati solitamente per questi tipo di applicazioni nell'industria. Intervenendo sulla slitta 8 di Fig.1 prima dell'avvio del motore è possibile scegliere quale zona usare per i test. Ogni zona ha un'estensione in direzione assiale sufficiente per svolgere almeno quattro diversi test con la medesima rugosità.

Prima dello svolgimento dei test è stata misurata la rugosità dell'albero nelle quattro zone, usando un rugosimetro Mitutoyo, ed ottenendo i valori indicati in tabella 1.

	$R_a[\mu m]$	$R_z[\mu m]$	$R_t[\mu m]$	$R_{mr}[\mu m]$
Zona 1	0.44	3.73	5.54	78.54
Zona 2	0.34	3.06	4.10	87.44
Zona 3	0.27	2.50	3.29	93.80
Zona 4	0.24	1.89	2.33	97.81

Tabella 1. Rugosità dell'albero nelle quattro zone.

Figura 3. Superficie con $R_a = 0.44\mu m$ al microscopio elettronico.
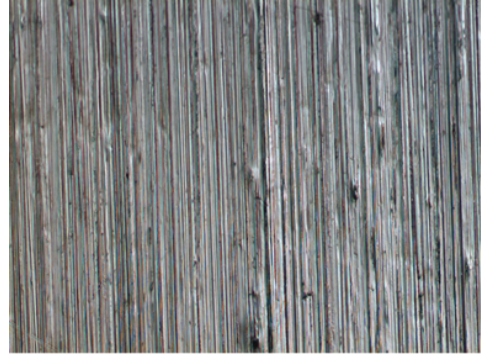
Figura 4. Superficie con $R_a = 0.34\mu m$ al microscopio elettronico.

Figura 5. Superficie con $R_a = 0.27\mu m$ al microscopio elettronico.
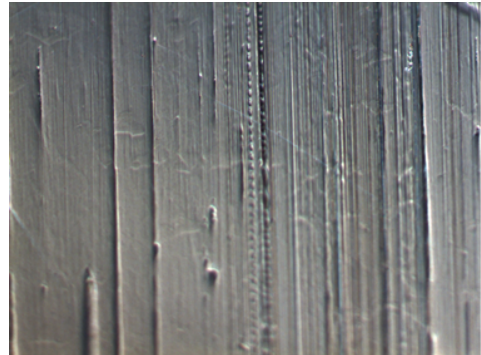
Figura 6. Superficie con $R_a = 0.24\mu m$ al microscopio elettronico.

Nelle figure 3,4,5 e 6 si mostra l'aspetto delle superfici osservate tramite microscopio elettronico SEM. Si noti che la rugosità è anisotropa, avendo seguito le indicazioni che richiedono la rettifica a tuffo; questa è una lavorazione tipica nel caso di alberi per tenute a labbro. Nelle figure, la direzione dell'asse dell'albero è orizzontale.

3. SVOLGIMENTO DELLE PROVE

Per ogni rugosità si sono svolte prove di durata variabile: rispettivamente da 1, 2, 4 e 6 ore a 2000 rpm. Ciò si è reso necessario dato che si voleva misurare l'andamento della rugosità

a diversi intervalli di tempo. Dato che sarebbe stato molto oneroso arrestare la macchina ad ogni intervallo di tempo, eseguire le misure di R_a e poi rimontare l'albero nella stessa posizione per riprendere il test, si è quindi pensato di svolgere le diverse durate su diverse sezioni dell'albero, ogni volta ricominciando da zero. In questo modo le misurazioni delle rugosità sono state svolte tutte in uno stesso momento, al termine di tutte le prove.

4. RISULTATI: MOMENTO RESISTENTE

Il momento resistente, al netto di effetti dovuti alla resistenza della trasmissione etc., è riportato nelle figure 7, 8, 9 e 10.

Si nota come il momento decresca rapidamente dopo un transitorio della durata di circa un'ora. Ciò è dovuto a varie ragioni, sia per un transitorio di assestamento termico nel quale il lubrificante ed il labbro hanno un localizzato incremento di temperatura, sia per il fatto (confermato dalle misurazioni riportate nella sezione successiva) che la rugosità iniziale viene levigata nel giro di una o due ore, portando ad un temporaneo aumento del lavoro delle forze d'attrito.

La figura 11 mostra il confronto fra le varie rugosità, evidenziando che il momento minore (e quindi la situazione ottimale di minor attrito) corrisponde ad una rugosità intermedia, e non alla rugosità più bassa come sarebbe intuitivo. Ciò è in accordo coi recenti risultati degli studi numerici e teorici sul fenomeno di micro-lubrificazione.
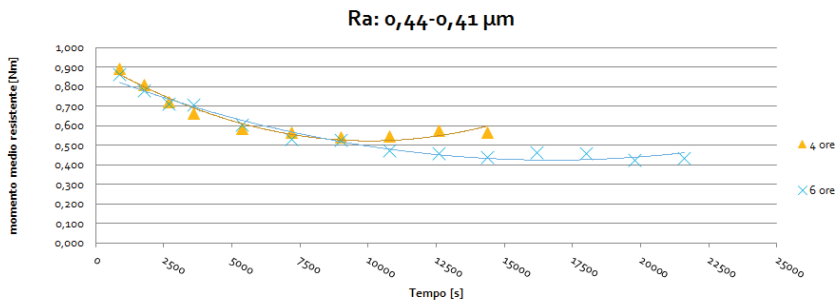
Figura 7. Andamento del momento resistente per due prove a $R_a = 0.44 \mu m$.
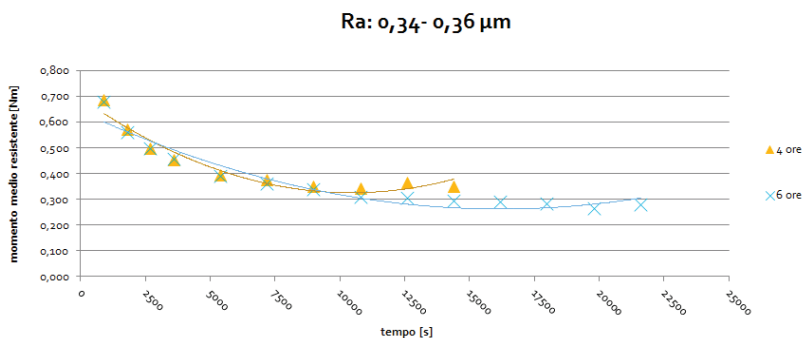
Figura 8. Andamento del momento resistente per due prove a $R_a = 0.34 \mu m$.
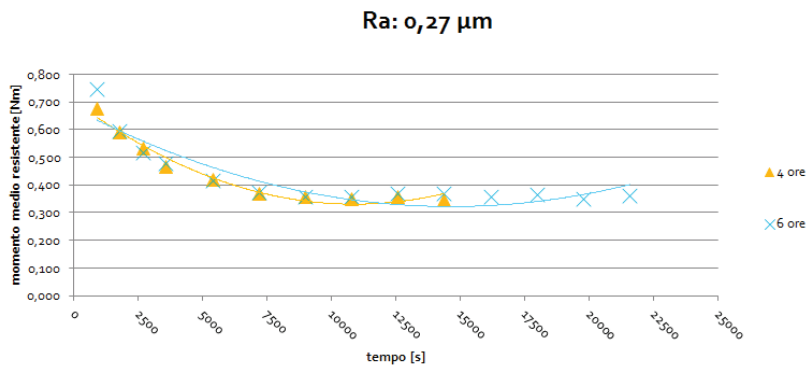
Figura 9. Andamento del momento resistente per due prove a $R_a = 0.27\mu m$.
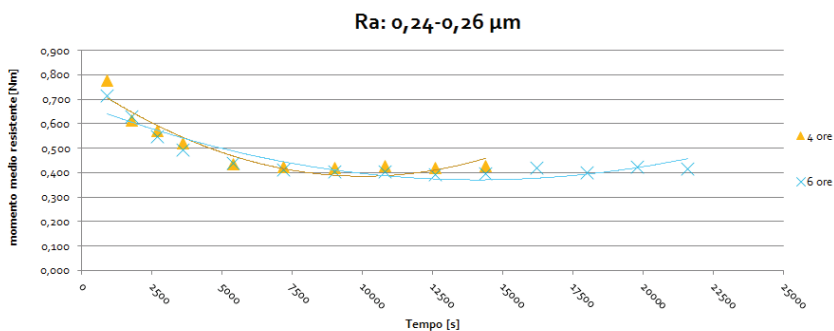
Figura 10. Andamento del momento resistente per due prove a $R_a = 0.24\mu m$.

5. USURA DELLE SUPERFICI

Al termine di ogni prova parziale il labbro è stato spostato su una successiva sezione dell'albero, ricominciando da T=0 la prova. In questo modo si sono svolti i test a tempi crescenti in un'unica sessione, smontando l'albero per i test sul rugosimetro solo alla fine di tutte le prove.

Il rugosimetro ha fornito i risultati riportati in Fig.12.

Si noti come la rugosità scenda nel volgere di una, massimo due ore, ed infine si assesti su un asintoto con valori generalmente nell'intervallo $R_a \in [0.20, 0.25]\mu m$. Ciò concorda con il fatto che il lavoro delle forze d'attrito nelle fasi iniziali è più intenso, come si evince dai precedenti grafici che mostrano l'andamento del momento resistente in funzione del tempo.

Nelle figure 13 e 14 si mostra, qualitativamente, l'effetto dell'usura del labbro di una tenuta dopo il transitorio di assestamento.

6. CONCLUSIONI

Nel presente lavoro si è condotto uno studio sperimentale sulle tenute a labbro, studiando l'usura degli alberi ed il momento resistente al variare della rugosità.

Figura 11. Andamento del momento resistente nel tempo, per diverse rugosità.

Figura 12. Andamento della rugosità nella zona di contatto fra albero e labbro di tenuta, al variare del tempo e al variare della rugosità iniziale.

Figura 13. Sezione della tenuta usurata dopo 6 ore, vista al microscopio ottico.
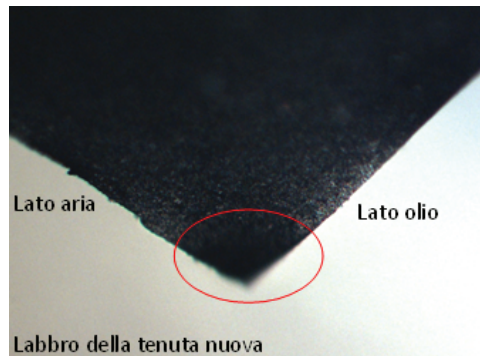
Figura 14. Superficie della tenuta nuova, vista al microscopio ottico.

Lo studio ha evidenziato come il momento resistente si presenti per un valore di rugosità intermedio (attorno a $R_a = 0.25\mu m$ nelle nostre prove) in quanto, come confermato da altri autori e dall'esperienza, una rugosità eccessivamente bassa non riesce ad innescare una lubrificazione microscopica ottimale a ridosso delle asperità.

Si è rilevato parimenti un livellamento delle asperità iniziali dopo un transitorio iniziale di poche ore. Si è provveduto a misurare l'andamento della rugosità nella zona di contatto e si sono riportati i valori ottenuti.

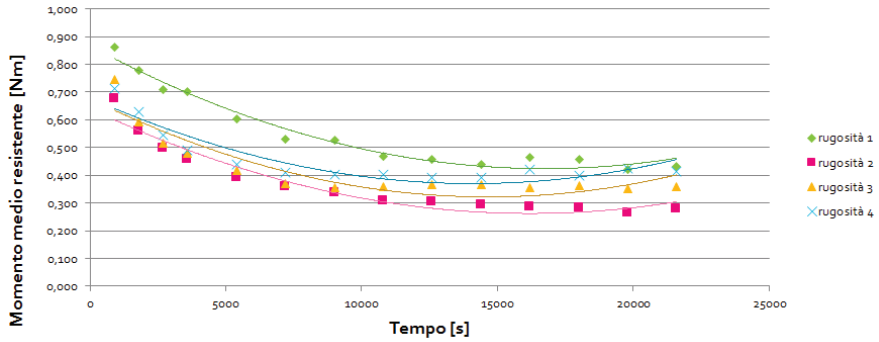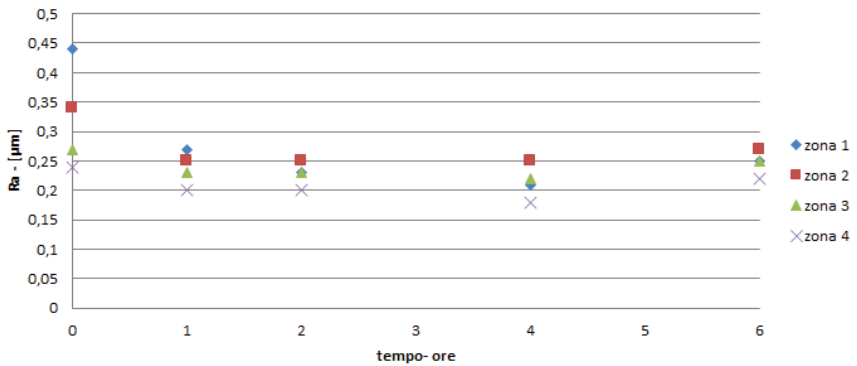La variazione della rugosità del labbro della tenuta e l'asportazione di elastomero dello stesso labbro sono fenomeni apprezzabili a livello qualitativo con i microscopi a nostra disposizione, ma una stima quantitativa precisa del materiale perso per l'attrito sarà oggetto di studi successivi.

REFERENCES

[1] Flitney, R. K., 2007. *Seals and Sealing Handbook (5th Ed.)*. Elsevier Science.

[2] Horve, L. A., 1996. *Shaft seals for dynamic applications*. CRC Press.

[3] Brown, R., 2006. *Physical Testing of Rubber*. Springer.

[4] Flitney, B., 2010. "Advances in understanding of polymer seals for rotating applications". *Sealing Technology,* **2010**(11), pp. 7 – 11.

[5] Jagger, E. T., 1957. "Rotary shaft seals: the sealing mechanism of synthetic rubber seals running at atmospheric pressure". *Proceedings of the Institution of Mechanical Engineers,* **171**, pp. 597–616.

[6] Kawahara, Y., Abe, M., and Hirabayashi, H., 1980. "An analysis of sealing characteristics of oil seals.". *ASLE TRANS.,* **23**(1), pp. 93–102.

[7] Müller, H., 1987. "Concepts of sealing mechanism of rubber lip type rotary shaft seals". In Proceedings of the 11th International Conference on Fluid Sealing, BHRA, pp. 698–709.

[8] Nakamura, K., 1987. "Sealing mechanism of rotary shaft lip-type seals". *Tribology International,* **20**(2), pp. 90–101.

[9] Stakenborg, M. J. L., van Leeuwen, H. J., and ten Hagen, E. A. M., 1990. "Visco-elastohydrodinamic (VEHD) lubrication in radial lip seals: Part 1 - steady state dynamic viscoelastic seal behavior". *Journal of Tribology,* **112**, pp. 578–583.

[10] van Leeuwen, H. J., and Stakenborg, M. J. L., 1990. "Visco-elastohydrodinamic (VEHD) lubrication in radial lip seals: Part 2 - fluid film formation". *Journal of Tribology,* **112**, pp. 584–591.

[11] Salant, R., 1992. "Numerical analysis of the flow field within lip seals containing microundulations". *Journal of Tribology,* **114**(3), pp. 485–492.

[12] Salant, R. F., and Flaherty, A. L., 1994. "Elastohydrodynamic analysis of reverse pumping in rotary lip seals with microundulations". *Journal of Tribology,* **116**(1), pp. 56–62.

[13] Salant, R. F., 1997. "Modelling rotary lip seals". *Wear,* **207**(1–2), pp. 92 – 99.

[14] Shi, F., and Salant, R. F., 2001. "Numerical study of a rotary lip seal with a quasi-random sealing surface". *Journal of Tribology,* **123**(3), pp. 517–524.

[15] Salant, R. F., and Rocke, A. H., 2004. "Hydrodynamic analysis of the flow in a rotary lip seal using flow factors". *Journal of Tribology,* **126**, pp. 156–161.

[16] Shen, D., and Salant, R. F., 2007. "An unsteady mixed soft EHL model, with application to a rotary lip seal". *Tribology International,* **40**, pp. 646–651.

[17] Sui, H., Pohl, H., Schomburg, U., Upper, G., and Heine, S., 1999. "Wear and friction of ptfe seals". *Wear,* **224**(2), pp. 175 – 182.

[18] Hajjam, M., and Bonneau, D., 2006. "Influence of the roughness model on the thermoelastohydrodynamic performances of lip seals". *Tribology International,* **39**, pp. 198–205.

[19] Maoui, A., Hajjam, M., and Bonneau, D., 2008. "Numerical analysis of thermoelastohydrodynamic behavior of elastomer radial lip seals". *Journal of Tribology,* **130**, pp. 021504–1–4.

[20] Maoui, A., Hajjam, M., and Bonneau, D., 2008. "Effect of 3d lip deformations on elastohydrodynamic lip seals behaviour". *Tribology International,* **41**, pp. 901–907.

[21] Gorriño, A., Angulo, C., and Canales, J., 2007. "Theoretical analysis of the pumping effect of rotary hydrodynamic seals with elastomeric lips". *Tribology International,* **40**, pp. 896–905.

[22] Hadinata, P. C., and Stephens, L. S., 2007. "Soft elastohydrodynamic analysis of radial lip seals with deterministic microasperities on the shaft". *Journal of Tribology,* **129**, pp. 851–859.

[23] Prati, E., and Strozzi, A., 1984. "A study of the elastohydrodynamic problem in rectangular elastomeric seals". *Journal of Tribology,* **106**(4), pp. 505–512.

[24] Silvestri, M., Prati, E., Tasora, A., and Marin, T., 2010. "Frictional behaviour of radial lip seals on varying exerted pressure". In Proceedings of the 14th Nordic Symposium on Tribology NordTrib - Storforsen, Sweden.

[25] Prati, E., Tasora, A., and Marin, T., 2011. "Influence of the temperature on the radial load in elastomeric seals". In Proceedings of the XX AIMETA Congress - Bologna, Italy.

FUNCTIONAL DESIGN OF A NEW FINGER EXOSKELETON BASED ON A STEPHENSON TYPE MECHANISM

Claudio Mazzotti
Department of Engineering for Industry,
University of Bologna, Italy
E-mail: claudio.mazzotti4@unibo.it

Marco Troncossi
Department of Engineering for Industry,
University of Bologna, Italy
E-mail: marco.troncossi@ unibo.it

Vincenzo Parenti-Castelli
Department of Engineering for Industry,
University of Bologna, Italy
E-mail: vincenzo.parenti@unibo.it

Abstract*. This paper deals with the design of a single degree-of-freedom Stephenson type mechanism for a finger exoskeleton. The finger exoskeleton, fastened to the second phalange of the human finger and to the palm, guides the flexion/extension of the finger while generating desired grasping trajectories. In this paper preliminary results and a 3D printed prototype of the proposed finger exoskeleton are reported. The results obtained showed that the proposed finger exoskeleton can be successfully adopted for the motion guidance of the fingers of a hand exoskeleton.*

Keywords*: Finger Exoskeleton, Rehabilitation, Six-Link Mechanism, Dimensional Synthesis.*

1. INTRODUCTION

In Italy stroke affects about 200,000 people per year and it is the leading cause of disability and the third leading cause of mortality [1]. The 35% of the persons affected by stroke suffers from brain-damage-related disabilities, e.g. lack of control of the arm and/or the hand. Traditional rehabilitation with a therapist is nowadays the more common way to rehabilitate stroke patients. The results obtained from the rehabilitation therapy are better, since the rehabilitation training is more intensive and continuous in time [2]. However traditional rehabilitation requires manual interaction of the therapist with the patient, consequently raising times and costs. These drawbacks, in addition to the lack of quantitative evaluations of patient improvements during the rehabilitation process, make the traditional rehabilitation approach not completely satisfying and successful. In the last decades, robotic rehabilitation gained a great interest as a useful tool to assist therapists during the rehabilitation of stroke patients [3]. The possibility to provide repetitive

trainings, to assist-as-needed the patients [4] during exercises and to quantitatively evaluate the improvements reached by the patients during the rehabilitation therapy represent the main advantages of the robotic rehabilitation. Exoskeletons can be efficiently used as rehabilitation systems. In this paper the focus is on hand exoskeleton rehabilitation systems.

Recently many prototypes of hand exoskeletons have been proposed in the literature [2,5]. The solutions proposed to guide the motion of each finger are varied. Many solutions exploit the use of mechanisms coupled to the human fingers to guide the motion of the fingers themselves. Usually, the adopted mechanisms, have more than 1 degree of freedom (DoF) then they use more than one actuator to guide the motion of each finger, resulting in complex and bulky multi-DoF hand exoskeletons which consequently increase the final cost of the devices. Several authors have pursued different design strategies proposing hand exoskeletons with simple architectures and a lower number of actuators. In particular we highlight the hand device of the Gentle-G [6] that uses one actuator for the thumb and two actuators for the four finger together, the robot proposed in [7] that allows finger and thumb extension to be controlled by the same single DoF, the HWARD [8] that has one actuator for the four fingers together, the active hand orthosis in [9] that uses a 1-DoF four bar linkage mechanism that actuate the four fingers together. In addition, in [10] an eight-link 1-DoF mechanism is designed for finger rehabilitation, in [11] a six-link spatial 1-DoF mechanism is designed for the thumb motion guidance. Finally in [12,13] the hand exoskeleton presented uses 1-DoF planar twelve-link mechanisms for each finger using one actuator for the thumb motion guidance and another actuator for the simultaneous motion guidance of the four fingers together.

The final goal of our research activity is to design a new hand exoskeleton for rehabilitation purposes, which could possibly represent a good trade-off among simplicity, functionality and cost. In particular, the rehabilitation target is to drive finger motion in order to execute a classical post stroke rehabilitation task, that is the power grasping of cylindrical objects. This task was chosen as reference task because rehabilitation of power grasping is, in general, one of the main manipulation ability that stroke patients need to recover first. To achieve this goal, several preliminary choices have to be taken by the designer. For instance in [12] a systematic analysis of principles ruling the design process of hand exoskeletons is reported. Generally speaking, the design of a hand exoskeleton must face a wide range of choices, such as: the solution used for the motion guidance of each finger, the number of actuators, the motion transmission system, the control scheme, etc. The *best possible device* has probably not been invented yet and a trade-off must be found. In this paper it is shown that, for the power grasping rehabilitation task, a good trade-off for the motion guidance of the five fingers could be found by adopting the following strategies: (*i*) the use of a 1-DoF mechanism to guide the motion of each finger, (*ii*) to place the mechanism above the finger in order to avoid interferences between the hand exoskeleton and the cylinder to grasp (*iii*) the use of two actuators only, one to actuate the thumb motion and the other one to actuate the four finger simultaneously. As a final result the hand exoskeleton device should be a good compromise among simplicity, functionality and costs.

According to a conventional model, the human hand has 20 DoFs [14,15]. Each finger is usually modeled as a serial manipulator, which comprises 4 revolute joints and five links, i.e. a 4-dof serial manipulator. The first DoF exploits the abduction/adduction of the first phalanx with respect to the hand metacarpus, whereas the other three DoFs exploit the flexion/extension of the three phalanges of each finger. As universally accepted, a simplification of the complex motion of the hand is to consider the three flexion/extension revolute axis as parallel lines.

This paper presents a 1-DoF planar mechanism (which adopts the above considerations) that is useful for the motion guidance of the fingers for a hand exoskeletons. The proposed mechanism, based on a Stephenson type mechanism, is intended to use in a new version of the hand exoskeleton proposed in [12,13]. Section 2 explains the design process followed, Section 3 presents the synthesis of the proposed mechanism, Section 4 presents some concluding remarks.

2. FUNCTIONAL DESIGN

The design of the finger exoskeleton is reported in this section; it is divided in three steps, the first step concerns the choice of a hand grasping model, the second step concerns the choice of the mechanism used to guide the motion of the finger, whereas the third step concerns the synthesis of the selected mechanism.

The human hand model

In this paper the grasping model proposed in [16,17] is used. In [14] the human hand is modeled by considering the phalanges as rigid links and the relative motion of two adjacent phalanges is considered as a rotation about an axis passing through the MCP, the PIP and the DIP human joints respectively. The MCP joint is the metacarpal joint, i.e. the joint among the metacarpal phalange of the hand and the first phalanx of the finger, whereas the PIP (DIP) joint is the joint among the first (second) phalange and the second (third) phalange. With reference to Figure 1 and according to [14] the length l_i, $i = 0,..,3$, of each finger phalanx and the position of each human joint (MCP, PIP and DIP) is correlated to the length (L) and to the width (W) of the human hand. The position of each human joint (MCP, PIP and DIP) is given with respect to the system of coordinates (with axes x, y, z and origin O_w) fixed to the wrist, Figure 1. In Table 1 average values taken from [18] of L and W of European males and corresponding to the 5th percentile, 50th percentile and 95th percentile are reported.

Table 1. Average hand lengths (L) and hand width (W)
of an European male, [18].

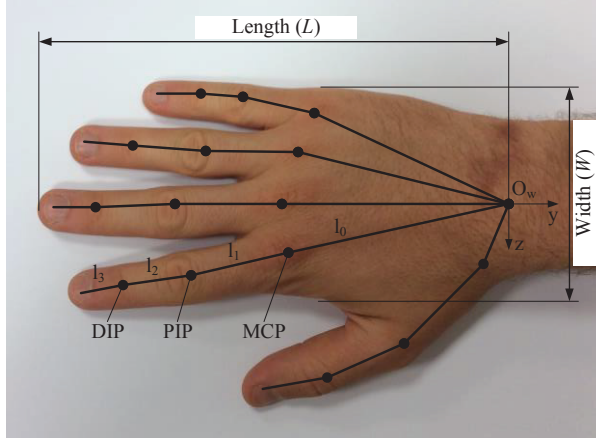| Percentile	L (mm)	W (mm)
5th	173	78
50th	189	87
95th	205	95

Figure 1. The hand model in [14].

The model used in this paper for the grasping of a cylindrical object of diameter d is reported in Figure 2. The model considers a planar motion of the human finger, neglects the abduction/adduction of the first phalange of the finger and considers the contact between the finger and the cylinder to grasp occurring at the MCP, PIP and DIP human joints and at the fingertip [16,17]. It provides the configuration of the human finger, i.e. the flexion angles ${}^h\beta_i$ ($i = 1,2,3$) where the superscript h refers to the hand model. The contact among the human joints and the grasped cylinder is modeled as circles whose diameter coincides with the width of the human joint, placed in contact with the surface of the grasped cylinder. With reference to Figure 2, a_1 is the distance from the center of the wrist and the cylinder to grasp measured along the direction identified by the vector $\mathbf{O_wC_c}$, where C_c is the trace of the axis of the grasped cylinder in the plane defined by the xy axis of the wrist, whereas a_i ($i=2,..,5$) are the radii of the contact circles. The grasping model assumes $a_5 = a_4 / 2$ as a good approximation of the fingertip contact.

To the author's knowledge, average measures of the human joints width are not reported in the literature. We measured the human joints of the index finger of ten people of average age of 32 years old. In Table 2, the mean values (m) and the standard deviation (sd) of the measured human joints are reported. We define as *slim finger,* a finger having the joints width a_i equal to $a_i = m\text{-}sd$, similarly we define as *medium finger* and *large finger* fingers having the joint widths equal to $a_i = m$ and $a_i = m+sd$ respectively.

Table 2. The anthropometric data measured.
Measures reported in mm.

	a_1	a_2	a_3	a_4
m	70.9	17.3	12.5	27.3
sd	4.79	1.56	1.17	2.35
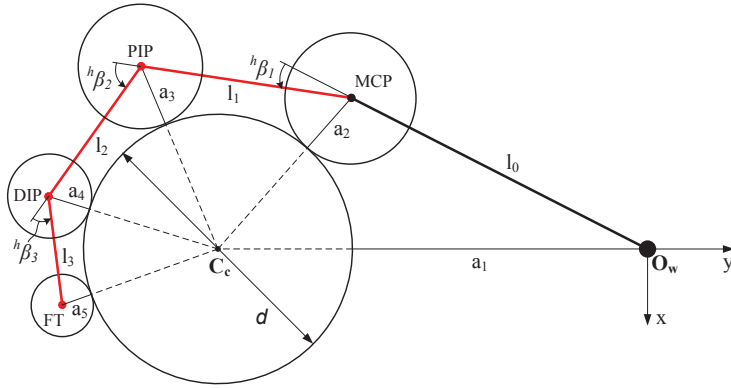
Figure 2. The hand model used.

The six-link mechanism

The feasibility study of a planar 1-DoF mechanism, whose topology is conceived as suitable for all the fingers is the target of this first design step. Some basic consideration for the synthesis of the targeted 1-DoF planar mechanism can be done, starting from the Grubler's formula for planar mechanisms:

$$l = 3(n-1) - 2c_1 - 2c_2 \qquad (1)$$

where l is the number of DoFs of the mechanism, n is the number of links and c_1 and c_2 are the number of lower pairs (revolute and prismatic joints) and higher pairs (cam-follower type joints) respectively. Usually, cam-follower type joints are not adopted in hand exoskeletons for many reasons, e.g. complex design of a bilateral constraint, likelihood of high friction forces, etc. Considering mechanisms with lower pairs only and assuming $l=1$, the mechanism topologies exploiting this features are reported in Table 3.

In this paper the focus is on the six-link mechanisms. Planar six link mechanisms comprise seven links and six revolute joints and have two well-known topologically distinct configurations, called the Watt and the Stephenson six-bar chains.

Depending on which link is considered as the frame link, the Watt and the Stephenson chain yields to the Watt I, Watt II, Stephenson I, Stephenson II and Stephenson III linkages respectively. The Stephenson III mechanism was selected as a possible candidate for the motion guidance of the human finger.

Table 3. Mechanism topology to exploit 1-DoF planar motion with lower pairs.

n	4	6	8	10	12	…
c_1	4	7	10	13	16	…
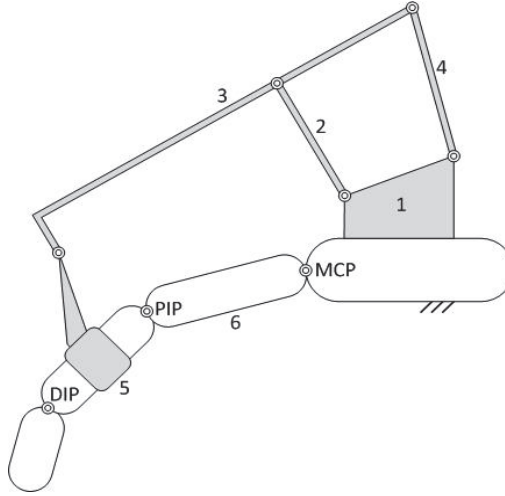
Figure 3. The finger exoskeleton based on a Stephenson III mechanism.

In Figure 3, the resulting exoskeleton based on this mechanism is reported. The first and the second phalanges are considered as parts of the mechanism, in particular link 5 of the mechanism comprises the second phalanx, whereas link 1 comprises the palm. The link 1 is the frame link, whereas link 2 is the moving link. The exoskeleton couples the flexion/extension movements of the first two phalanges through a number of poses (position and orientation) corresponding to the grasp of a number of different cylindrical objects, and entails a natural motion of the finger along the grasping trajectory. The third phalange is free, i.e. its motion is not guided.

The six-link mechanism is composed by two loops as shown in Figure 4. The closure equations of the Stephenson mechanism are:

$$\begin{cases} \boldsymbol{O_2D} + \boldsymbol{DE} + \boldsymbol{EO_3} + \boldsymbol{O_3O_2} = \boldsymbol{0} \\ \boldsymbol{O_2D} + \boldsymbol{DC} + \boldsymbol{CG} + \boldsymbol{GO_1} + \boldsymbol{O_1O_2} = \boldsymbol{0} \end{cases} \tag{2}$$

By manipulating Eqs (2), relationships between the phalanges configuration angles β_1, β_2 and the input angle θ_2 are obtained. These equations are not reported for the sake of conciseness. The mechanism singularity occurs when the links described by the vectors **CG** and **GO₁**, and the links described by the vectors **DE** and **EO₃** are aligned.

The synthesis problem here to tackle is to find the mechanism capable to guide the human phalanges so as they reach positions compatible with the selected power-grasping task while avoiding singularities of the mechanism during the grasping trajectory.
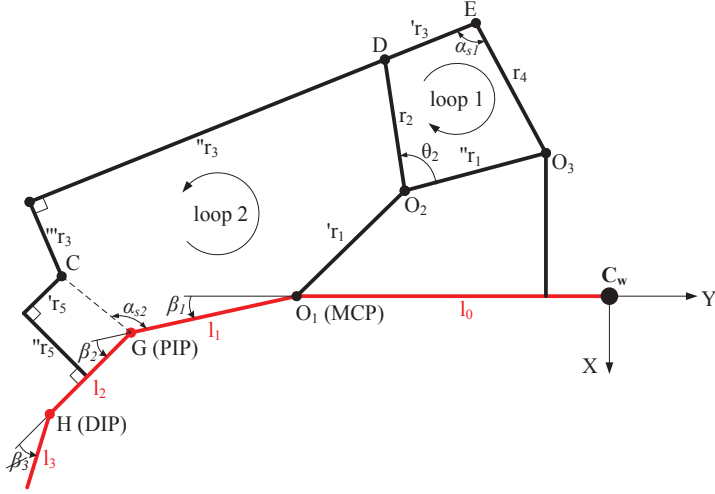
Figure 4. The Stephenson mechanism.

The dimensional Synthesis

A numerical procedure is used to find a solution $\mathbf{x}$, namely a vector containing the link lengths $'r_1, ''r_1, r_2, 'r_3, ''r_3, '''r_3, r_4, 'r_5$ *and* $''r_5$ by solving a constrained minimization problem specified as follows:

$$\min f_c(\mathbf{x}) \text{ such that } \begin{cases} c(\mathbf{x}) \leq \mathbf{0} \\ l_b \leq \mathbf{x} \leq u_b \end{cases} \tag{3}$$

where the function $f_c(\mathbf{x})$, defined in details below, is the cost function that must be minimized; the vector $c(\mathbf{x})$, also defined in details below, contains the constraints of the problem; the vectors l_b and u_b contain the lower and upper bounds of the solution vector $\mathbf{x}$, respectively. The function $f_c(\mathbf{x})$ is defined as follows. Being the lengths l_i, $i = 0,..,3$, corresponding to the hand sizes reported in Table 1 and for a *medium finger* size of the finger, six finger configuration are considered. In particular five finger configurations corresponding to the grasp of five different cylindrical objects of diameters d, equals to 90, 80, 70, 60, 50 mm, respectively, and another configuration corresponding to the finger fully-extended are considered. For a generic vector $\mathbf{x}$ and considering a rotation of the moving angle θ_2 from 0 to 2π, the actual values $^a\beta_1$, $^a\beta_2$ are computed and the cost function is defined for each one of the six configurations for which $^a\beta_1 \equiv {}^h\beta_1$, thus the cost function $f_c(\mathbf{x})$ is:

$$f_c(\mathbf{x}) = \sum_{i=1}^{6} \frac{\left({}^a\beta_{2,i} - {}^h\beta_{2,i} \right)^2}{6} \tag{4}$$

Figure 5. Errors e_{tot} for the different hand sizes tested. Blue lines refer to the *slim fingers*, green lines refer to the medium finger, whereas red lines refer to *large finger*.

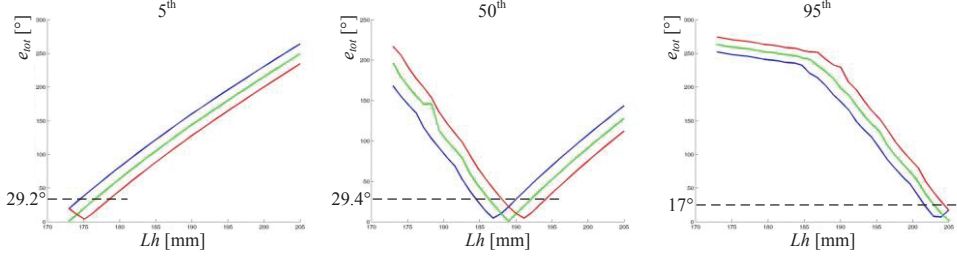where the index $i = 1,..,6$ refers to the six targeted finger configurations; the superscript a is referred to the actual mechanism; whereas the superscript h is referred to the hand grasping model. The vector $c(x)$ is defined as:

$$c(x) = \begin{pmatrix} |\alpha_{s1} - \overline{\alpha}_{s1}| \\ |\alpha_{s2} - \overline{\alpha}_{s2}| \end{pmatrix} \tag{5}$$

where α_{sk}, $k = 1,2$, are the values of the angle between the two links described by the vectors **CG** and **GO₁** and the vectors **DE** and **EO₃** respectively, whereas $\overline{\alpha}_{sk}$ are the maximum threshold values of the angle α_{sk}. To keep $c(x) \leq 0$ means to avoid the mechanism singularities through all the desired trajectory. The optimization, performed by using a Genetic algorithm, was done for the three hand lengths reported in Table 1, thus three different Stephenson mechanisms were found.

3. SIMULATIONS

Several simulations on the synthesized mechanism were conducted. The aim of the simulations is to evaluate the kinematic and the kinetostatic behavior of the three exoskeletons found when they are used to guide the motion of a finger having a generic size. Considering a linear interpolation of the three hand sizes reported in Table 1 thirty one different hand sizes were extrapolated, moreover for each resulting hand size the index finger is considered to have *slim*, *medium* and *large* size, thus finally ninety three different index fingers are considered for these simulations. For the kinetostatic analysis of the mechanisms the force needed to grasp a cylinder is modeled as a force F = 15 N applied in the middle of the second phalange and having direction perpendicular to the phalange itself. The counter torque M applied to the moving link 2 and the MCP and the PIP joint reaction forces, here called R_{MCP} and R_{PIP} respectively, are computed. The angular error e_i, $i=1,..,6$, that occurred in reaching each of the six prescribed finger configurations is computed. The error e_i is defined as $e_i = \left| {}^a\beta_{2,i} - {}^h\beta_{2,i} \right|$ for the configuration where ${}^a\beta_1 \equiv {}^h\beta_1$.
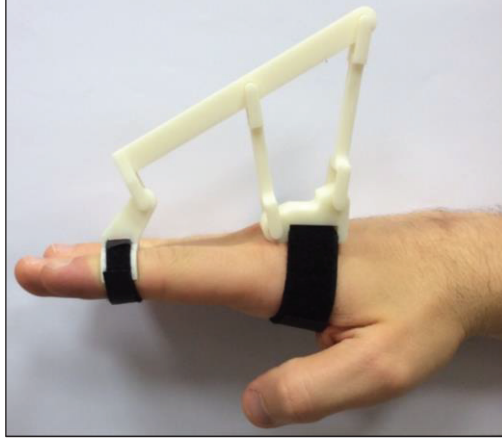
Figure 5. A 3D printed preliminary prototype of the proposed finger exoskeleton.

Moreover, the total angular error e_{tot} in reaching all the six prescribed finger configurations is defined as $e_{tot} = \sum_{i=1}^{6} \left| {}^a\beta_{2,i} - {}^h\beta_{2,i} \right|$, where the index i, $i = 1,..,6$, refers to the six configurations that the finger must reach. Each one of the ninety three mechanisms tested is considered as useful for the motion guidance of the finger, if: each errors $e_i \leq 10°$, the error $e_{tot} \leq 30°$ (i.e. an average acceptable angular error of 5° for each one of the six configurations is admitted), and the maximum magnitude of the reaction forces R_{MCP} and R_{PIP} are less than 50 N. These thresholds were set by the authors as deemed common sense values. Results of the simulations are summarized in Table 4, whereas in Figure 4 the total angular error e_{tot} is reported with respect to the different hand sizes considered. The finger exoskeletons found by considering the hand size corresponding to the 5th, 50th and 95th percentile can be satisfactorily used for six, nine and three hands respectively. Results suggests that the synthesized finger exoskeletons can be used mainly for hand sizes close to the hand for which they are found. However, the results are good considering that in general the mechanisms usually achieve good performances just for the reference task to which they are designed and small changes in the link lengths could provide low performances.

A 3D printed prototype of the finger exoskeleton was built. The link lengths of the prototype correspond to the link lengths of the mechanism found for an hand size corresponding to the 50th percentile.

Table 4. Results of the simulations.

Percentile	5th	50th	95th
W x L [mm]	173x78	189x87	205x95
e_{tot} [°]	29.2°	29.4°	17°
e_i [°]	8.3°	6.8°	3.6°
max(R_{MCP},R_{PIP}) [N]	13.8	15.6	28.5
satisfying test	6 / 93	9 / 93	3 / 93

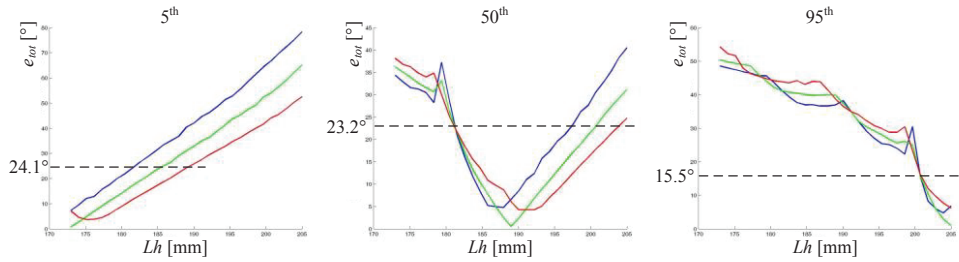**Figure 6**. Errors e_{tot} for the different hand sizes tested considering as adjustable the position of the revolute joint identified by the point C. Blue lines refer to the *slim fingers*, green lines refer to the medium finger, whereas red lines refer to *large finger*.

Preliminary qualitative tests of such a prototype showed, as expected, a very good behavior of the exoskeleton for hand sizes close to the 50th percentile.

In order to improve the number of hand sizes to which the exoskeleton can be fit, other simulations were conducted. The possibility to use adjustable link length is investigated. In particular, interesting results were found by admitting to adjust the position of the revolute joint centered in the point C along a direction parallel to the second phalange (i.e. to adjust the length $'r_5$). A threshold deemed acceptable for the variability of the link length $'r_5$ is $\pm$ 10 mm. Results of the simulations, summarized in Table 5 and reported in Figure 6, showed that the finger exoskeletons found by considering the hand size corresponding to the 5th, 50th and 95th percentile can be satisfactorily used for twenty seven, forty five and fifteen hands respectively. Results showed that by admitting to adjust the link length $'r_5$, the synthesized finger exoskeletons can be used for an extend range of hand sizes, in particular the most interesting results are obtained for the mechanism corresponding to the 50th percentile hand sizes.

Finally, other four mechanisms to guide the motion of finger having size corresponding to the 50th percentile were synthesized and analyzed. The results of the simulations are reported in Table 6 and revealed that a mechanism designed for an hand having $L = 187.9$ mm and $W = 86.4$ mm could be satisfactorily used on a large number of hands by admitting a reasonable variability of the link $'r_5$.

Table 5. Results of the simulations for an adjustable length $'r_5$.

Percentile	5th	50th	95th
$W \times L$ [mm]	173x78	189x87	205x95
e_{tot} [°]	24.1°	23.2°	15.5°
e_i [°]	9.6°	9.6°	7.7°
max(R_{MCP},R_{PIP}) [N]	15.9	16	35.2
adjustable length [mm]	-1.2 ÷ 7.2	-5.6 ÷ 8	-3.7 ÷ 1
acceptable cases	27 / 93	45 / 93	15 / 93

Table 6. Results of the simulations considering the use of an adjustable link length.

Percentile	-	-	50th	-	-
W x L [mm]	186.6x85.8	187.9x86.4	189x87	190.06x87.5	191.1x88.06
e_i [°]	9.3°	9.9°	9.6°	9.5°	9.7°
e_{tot} [°]	27.7°	23.1°	23.2°	27.2°	25.1°
max(R_{MCP},R_{PIP}) [N]	14.5	17.9	16	23.2	17.1
adjustable length [mm]	-7 ÷ 7.8	-5.6 ÷ 6.9	-5.6 ÷ 8	-4.2 ÷ 7.3	-5.5 ÷ 4.5
acceptable cases	51 / 93	48 / 93	45 / 93	42 / 93	45 / 93

3. CONCLUSIONS

In this paper the design of a new single degree-of-freedom Stephenson type mechanism for a finger exoskeleton is presented. The finger exoskeleton, fastened to the second phalange of the human finger and to the palm, guides the flexion/extension of the finger while generating a desired grasping trajectory. Several mechanisms ad hoc designed for the motion guidance of different finger sizes were found. Several simulations with the aim to evaluate the behavior of the exoskeletons once fit on hands having a generic size are conducted. The simulations reveal encouraging results suggesting that the proposed finger exoskeleton can be successfully adopted for the motion guidance of the fingers for a hand exoskeleton. Finally a 3D printed prototype of the proposed finger exoskeleton was built to show the effectiveness of the proposed solution.

References

[1] Consoli D., de Falco F. A., Lenzi G. L., Micieli G., Palumbo F., Rosati G., Simonetti G., Stanzione P., Ugenti R., Zangrillo A., 2010. "Organizzazione dell'assistenza all'ictus: le Stroke Unit." Italian Ministry of Health.

[2] Heo P., Min Gu G., Lee S.-J., Rhee K., Kim J., 2012. "Current hand exoskeleton technologies for rehabilitation and assistive engineering." International Journal of Precision Engineering and Manufacturing 13.5: 807-824.

[3] Chang W. H., Kim Y.-H., 2013. "Robot-assisted therapy in stroke rehabilitation." Journal of stroke 15.3: 174-181.

[4] Marchal-Crespo L., Reinkensmeyer D. J., 2009. "Review of control strategies for robotic movement training after neurologic injury." Journal of neuroengineering and rehabilitation, **6**:20.

[5] M. Mozaffari-Foumashi, M. Troncossi, V. Parenti-Castelli, 2011. "State-of-the-art of hand exoskeleton systems." Internal Report, DIEM, Università di Bologna.

[6] Loureiro R. C. V., Harwin W. S., 2007. "Reach & grasp therapy: design and control of a 9-DOF robotic neuro-rehabilitation system." IEEE International Conference on Rehabilitation Robotics (ICORR 2007), Twente, The Netherlands.

[7] Masia, L., Krebs H. I., Cappa P., Hogan N., 2007. "Design and characterization of hand module for whole-arm rehabilitation following stroke." Mechatronics, IEEE/ASME Transactions on 12.4: 399-407.

[8] Takahashi Craig D., Der-Yeghiaian L., Le V., Motiwala R. R., Cramer S. C., 2008. "Robot-based hand motor therapy after stroke." Brain 131.2: 425-437.

[9] Rosati G., Cenci S., Boschetti G., Zanotto D., Masiero S., 2009. "Design of a single-dof active hand orthosis for neurorehabilitation." IEEE International Conference on Rehabilitation Robotics (ICORR 2009), Kyoto, Japan.

[10] Wolbrecht E. T., Reinkensmeyer D. J., Perez-Gracia A., 2011. "Single degree-of-freedom exoskeleton mechanism design for finger rehabilitation." IEEE International Conference on Rehabilitation Robotics (ICORR 2011), Zurich, Switzerland.

[11] Yihun Y., Miklos R., Perez-Gracia A., Reinkensmeyer D. J., Denney K., Wolbrecht E. T., 2012. "Single Degree-of-Freedom Exoskeleton Mechanism Design for Thumb Rehabilitation." Engineering in Medicine and Biology Society (EMBC 2012). Annual International Conference of the IEEE, San Diego, USA.

[12] Troncossi M., Mozaffari Foumashi M., Carricato M., Parenti-Castelli V., 2012. "Feasibility study of a hand exoskeleton for rehabilitation of post-stroke patients." ASME 2012 11th Biennial Conference on Engineering Systems Design and Analysis (ESDA 2012), Nantes, France.

[13] Mozaffari Foumashi M., Troncossi M., Parenti-Castelli V., 2013. "Design of a new hand exoskeleton for rehabilitation of post-stroke patients." Romansy 19–Robot Design, Dynamics and Control. Vienna, Austria, 159-166.

[14] Buchholz B., Armstrong T. J., Goldstein S. A., 1992. "Anthropometric data for describing the kinematics of the human hand." Ergonomics 35.3: 261-273

[15] Kapandji I. A., 1982. "Physiology of the Joints: Upper Limb - Volume 1. " Edinburgh: Churchill Livingstone.

[16] Burton T. M. W., Vaidyanathan R., 2010. "A parameterized kinematic model of the human hand." *Towards Autonomous Robotic Systems (TAROS), Plymouth*: 34-40.

[17] Burton T. M. W., Vaidyanathan R, Burgess S. C., Turton A. J., Melhuish C., 2011. "Development of a parametric kinematic model of the human hand and a novel robotic exoskeleton." *IEEE International Conference on Rehabilitation Robotics (ICORR)*.

[18] Pheasant S., Haslegrave C. M., 2003. "Bodyspace: Anthropometry, Ergonomics And The Design Of Work. Second Edition" Taylor & Francis e-Library.

MEASURE AND ANALYSIS OF MOTION AND MUSCLE FORCES AT THE HUMAN KNEE DURING DYNAMIC MOTION TASKS

Michele Conconi
Department of Industrial Engineering,
Health Sciences and Technologies Interdepartmental Centre for Industrial Research (HST-ICIR)
University of Bologna, Italy
E-mail: michele.conconi@unibo.it

Nicola Sancisi
Department of Industrial Engineering,
Health Sciences and Technologies Interdepartmental Centre for Industrial Research (HST-ICIR)
University of Bologna, Italy
E-mail: nicola.sancis@ unibo.it

Magherita Forlani
Department of Industrial Engineering,
Health Sciences and Technologies Interdepartmental Centre for Industrial Research (HST-ICIR)
University of Bologna, Italy
E-mail: margherita.forlani@ unibo.it

Vincenzo Parenti Castelli
Department of Industrial Engineering
Health Sciences and Technologies Interdepartmental Centre for Industrial Research (HST-ICIR)
University of Bologna, Italy
E-mail: vincenzo.parenti@ unibo.it

Abstract. *The characterization of the joint behaviour under physiological loading condition is a necessary step to come to the definition of significant joint models, which open the way to the identification of better treatments and prosthesis and orthosis designs. A test rig has been recently developed, capable to replicate a generic loading condition while measuring the relative motion of the bones participating to the articulation and estimating the associated muscular forces. In this paper, the rig architecture and functioning will be briefly recalled. Then, the result of its application on a knee joint will be presented.*

Keywords: *Motion Analysis, Static Analysis, Dynamic Analysis, Joint Characterization, Test Rig, Knee.*

1. INTRODUZIONE

La caratterizzazione del comportamento cinematico e dinamico delle articolazioni umane è un passaggio fondamentale per la definizione e la validazione di modelli biomeccanici. Tali modelli sono di grande importanza, ad esempio per la progettazione di protesi efficienti e per la definizione di tecniche chirurgiche e strategie riabilitative [1,8].

La misura del comportamento sotto carico di una articolazione può essere effettuata in vivo o in vitro. Nel primo caso, è possibile valutare il moto dei segmenti ossei che partecipano all'articolazione insieme al pattern di attivazione dei muscoli. Tuttavia, per ottenere misure di moto precise sono necessarie tecniche invasive (fluorosocopia o perni intracorticali); in alternativa si può ricorrere all'uso dei meno invasivi marker cutanei, che tuttavia aggiungono alla misura il rumore associato al moto dei tessuti molli [7]. D'altro canto, i test in vitro permettono di misurare con grande precisione il moto dei diversi segmenti ossei grazie a tracker che possono essere fissati direttamente alle ossa. In questi casi però, è necessario misurare preventivamente in vivo (ad esempio mediante pedane di forza) le condizioni di carico associate al task motorio che si vuole analizzare, condizioni che devono poi essere accuratamente replicate in vitro. Inoltre, il contributo muscolare è particolarmente complesso da replicare in vitro.

Negli ultimi anni sono state presentate diverse attrezzature per lo studio delle articolazioni sotto carico, con particolare attenzione al ginocchio che, insieme all'anca, è una delle articolazioni più soggette ad infortuni e quindi a trattamento chirurgico. Si possono individuare due tipologie principali per tali attrezzature, ovvero quelle basate sull'architettura dell' Oxford Knee Rig (OKR) [11] e quelle che utilizzano sistemi robotici più tradizionali [9]. In entrambi i casi, il moto relativo tra femore e tibia possiede 6 gradi di libertà (gdl) durante l'applicazione dei carichi esterni. Tuttavia, a causa della sua particolare architettura che vuole replicare le articolazioni di anca e caviglia nell'ancorare il preparato al telaio, l'OKR non è in grado di generare carichi esterni generici. Per questo motivo, negli ultimi anni hanno preso piede attrezzature di carico di tipo robotico, ad architettura sia seriale che parallela. In questi casi, una delle due ossa di tibia o femore viene mantenuta fissa, mentre l'altra viene movimentata tramite un controllo che può essere in posizione [2], in forza o di tipo misto [9]. La maggior parte di tali attrezzature utilizza robot commerciali, che non sono stati pensati per i range di moto e di carico tipici delle articolazioni umane e che hanno costi considerevoli. Inoltre, il controllo in forza di tali robot è in generale complesso, aumentando i costi dell'attrezzatura e riducendone in genere l'accuratezza.

Per superare tali limitazioni, è stata recentemente proposta un'innovativa attrezzatura di carico [12], la cui architettura si basa su un robot parallelo a cavi. Tale attrezzatura permette lo studio del comportamento del ginocchio sia nel suo moto naturale che sotto l'azione di un carico generico, che può essere variato con continuità su un ampio range di flessione. L'articolazione è sempre libera di raggiungere l'equilibrio sotto l'azione delle sole forze esterne e delle azioni esercitate dalle strutture interne all'articolazione: come risultato, il moto è guidato dalla sola geometria articolare e può essere misurato ad esempio con un sistema optoelettronico. L'attrezzatura permette inoltre di simulare l'azione dei principali gruppi di muscoli flessori ed estensori, permettendo il calcolo della forza muscolare necessaria ad equilibrare l'articolazione sotto carico.

In questo lavoro, dopo aver richiamato il funzionamento dell'attrezzatura di carico proposta, verranno presentati i risultati di una sua applicazione su una articolazione di ginocchio durante una prova sperimentale.
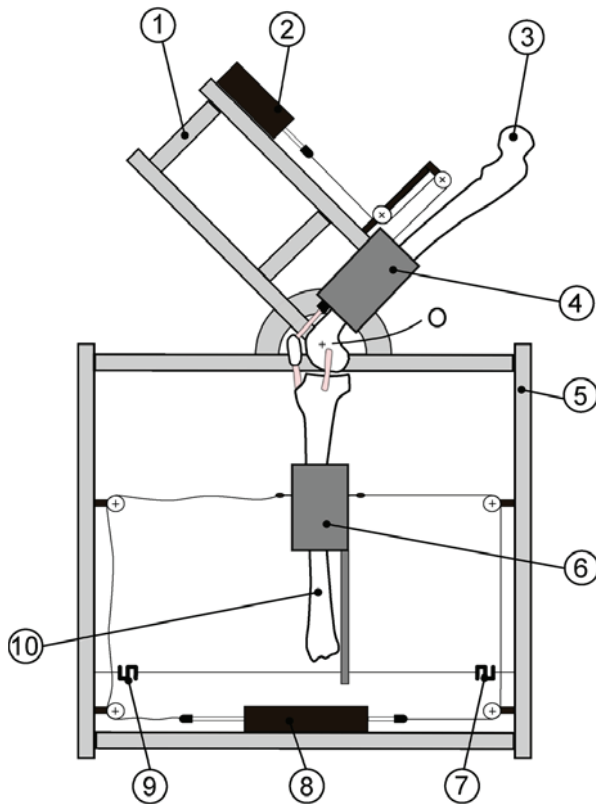
Figura 1: Struttura dell'attrezzatura di carico

2. FUNZIONAMENTO DELL'ATTREZZATURA DI CARICO

In [12] è possibile trovare una trattazione dettagliata dei principi di funzionamento dell'attrezzatura in tutte le sue parti. Di seguito verrà illustrato il suo funzionamento di massima.

L'attrezzatura (Fig. 1) si compone di due parti: una base fissa (5) e un portale (1) libero di ruotare attorno ad un perno (O).

Il femore (3) è collegato al portale tramite un afferraggio (4) che permette di aggiustarne il posizionamento in relazione all'attrezzatura con 6 gdl. Trovata la posizione corretta, questa può essere bloccata, rendendo rigido il riferimento tra osso e portale. Il sistema di afferraggio permette inoltre di smontare il femore, garantendone un successivo preciso riposizionamento.

Un anello (6), fissato alla tibia (10), permette l'applicazione di carichi esterni (forze e coppie) del tutto generici, grazie ad un sistema di 12 cavi che, a due a due, costituiscono 6 circuiti chiusi, in ciascuno dei quali è inserito un pistone pneumatico (8), fisso a telaio. L'attuatore presente in ogni circuito può mettere in tensione uno solo dei due cavi, permettendo l'applicazione di una sola forza. Nel complesso, quindi, sei forze indipendenti

vengono esercitate sull'anello (5). E' possibile suddividere i sei attuatori in tre gruppi, ciascuno dei quali genera una componente di forza e una di coppia, per un totale di tre forze e tre coppie tra loro ortogonali. Grazie alla particolare configurazione dei cavi e delle connessioni, il sistema di carico risultante risulta quasi perfettamente disaccoppiato, semplificando il controllo della macchina e migliorandone l'efficienza della trasmissione delle forze.

Tale sistema di carico non vincola il moto della tibia, che è libera di raggiungere una configurazione di equilibrio sotto l'azione delle sole forze esterne e dei vincoli prodotti dalle strutture articolari del ginocchio. Le massime forze e coppie applicabili si attestano a 2400 N e 100 Nm in ogni direzione, mentre il femore è libero di flettere fino a 135°: tale combinazione permette di simulare la maggioranza dei compiti motori quotidiani.

L'attrezzatura comprende anche un sistema che premette di stimare sperimentalmente le azioni dei principali gruppi di muscoli flessori ed estensori, invece di imporle a priori. Due celle di carico (7) e (9) sono connesse distalmente all'anello di tibia tramite cavi. Tali celle permettono una misura indiretta del momento generato dai carichi esterni sul ginocchio. Nel caso tale momento tenda a flettere il ginocchio, il controllo aziona un martinetto (2), fissato al portale e collegato al tendine del quadricipite di cui pertanto simula l'azione, fino al ripristino dell'equilibrio. Qualora invece il momento risulti estensore, il controllo calcola l'azione dei flessori necessaria all'equilibrio del ginocchio e la applica alla tibia tramite l'anello di carico, in sovrapposizione ai carichi esterni. In questo caso, la co-contrazione dei muscoli antagonisti non è considerata poiché non determinabile sperimentalmente.

3. PROCEDURA SPERIMENTALE

La caratterizzazione funzionale di un'articolazione di ginocchio incomincia con l'analisi da parte di un chirurgo che ne verifica le eventuali patologie e quindi procede alla rimozione del piede e dei tessuti molli, lasciando intatta la capsula articolare. Il preparato anatomico viene quindi munito di traker ottici (Fig. 2.a) che possono essere rilevati da un sistema fotogrammetrico (Vicon Motion Systems Ltd., accuratezza nominale 0.5 mm/0.5°, Fig. 2.b) e che consentono la misura del moto relativo fra i segmenti ossei di tibia, femore e rotula.
Il preparato anatomico viene quindi connesso all'attrezzatura tramite l'afferraggio femorale. Si esegue quindi una prima misurazione del moto naturale del ginocchio, ovvero del moto relativo tra i segmenti ossei in assenza di carichi esterni, flettendo il femore tramite il portale e lasciando la tibia libera di raggiungere la posizione di equilibrio. Durante quest'operazione, un precarico pari a 5N è applicato dal martinetto (2) per stabilizzare la posizione della rotula. La tibia viene quindi collegata all'anello di carico e si passa allo studio dei compiti funzionali, in questo caso lo squat e l'alzata dalla sedia. I carichi esterni corrispondenti sono stati presi dalla letteratura [1,5,6]. I moti relativi così ottenuti vengono poi espressi nella convenzione di Grood e Suntay [4]. Per ogni prova sperimentale vengono eseguite più ripetizioni.

4. RISULTATI

Il confronto fra i tre compiti può essere effettuato attraverso la componente del moto relativo tra tibia e femore che presenta la maggior variazione durante la flessione del ginocchio, ovvero l'intra-extra rotazione della tibia. In figura 3 si possono confrontare le traiettorie medie di intra-extra rotazione della tibia al variare dell'angolo di flessione per i tre compiti motori considerati.
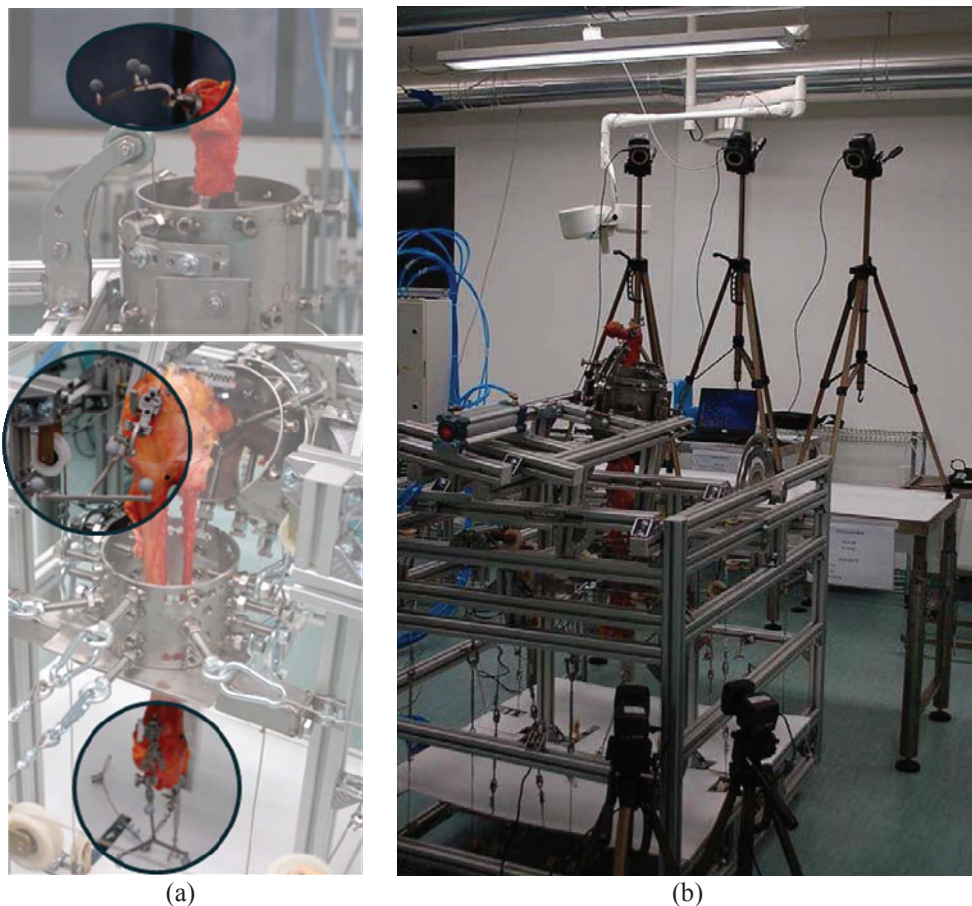
Figure 2. Configurazione sperimentale: marker ottici posizionati su femore, rotula e tibia per la determinazione dei moti relativi (a); sistema fotogrammetrico per il rilievo dei moti relativi tra i segmenti ossei del ginocchio (b).

Tabella 1: Deviazione standard media per le cinque componenti dipendenti del moto relativo femoro-tibiale per i tre compiti considerati.

	Ab-Add (°)	Intra-Extra (°)	Ant-Post (mm)	Prox-Dist (mm)	Med-Lat (mm)
Moto passivo	0.05	0.09	0.19	0.13	0.15
Squat	0.13	0.41	0.42	0.15	0.22
Sedia	0.24	0.38	2.76	0.41	2.05

La tabella 1 mostra la deviazione standard media per ciascuna delle componenti dipendenti del moto femoro-tibiale (ovvero intra-extra rotazione, ab-adduzione, traslazione antero-posteriore, medio-laterale e prossimo-distale), valutata per ciascun compito.

Infine, in figura 4 viene mostrata la forza muscolare netta come misurata dall'attrezzatura (valori positivi corrispondono all'attivazione dei muscoli estensori, mentre valori negativi sono associati all'attivazione dei flessori).

Figure 3. Intra-extra rotazione della tibia al variare dell'angolo di flessione per i tre compiti motori considerati.

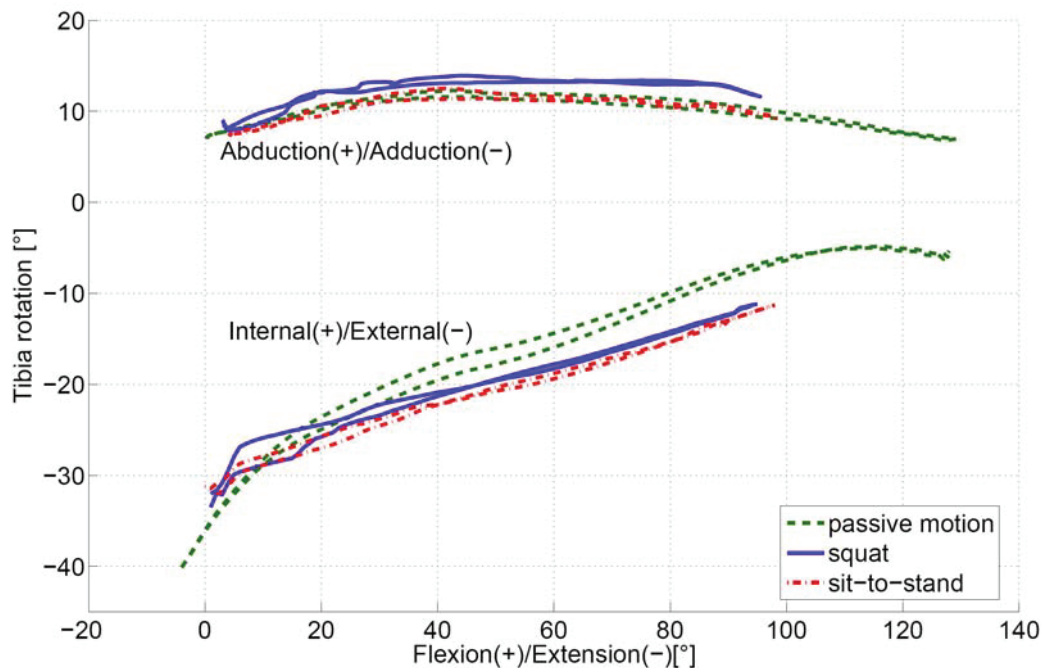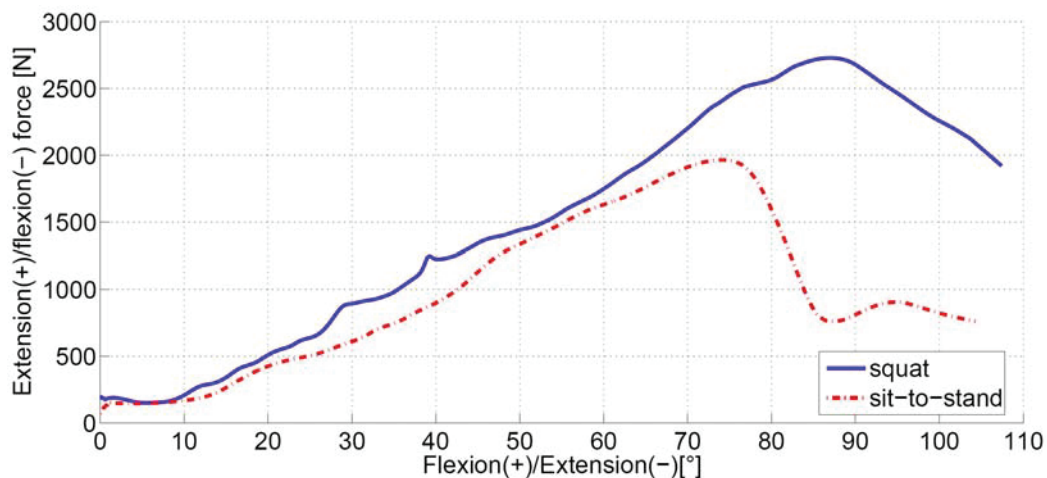**Figure 4.** Forza muscolare netta calcolata per i compiti motori caricati presi in esame.

5. DISCUSSIONE

L'accuratezza dell'attrezzatura può essere valutata confrontando fra loro le traiettorie ottenute per le varie componenti di moto relativo femoro-tibiale al variare del compito motorio. In tutti i casi analizzati, l'accuratezza dell'attrezzatura permette di osservare un comportamento isteretico, ben visibile in figura 3. I ridotti valori ottenuti per la deviazione standard media (Tab. 1) forniscono un'indicazione della ripetibilità dell'attrezzatura. Partendo da queste osservazioni, è possibile ritenere attendibili i risultati prodotti dalla procedura sperimentale qui riportata.

L'analisi svolta su una articolazione di ginocchio ha evidenziato come anche compiti motori tra loro simili, quali lo squat e l'alzata dalla sedia, producono variazioni nel moto relativo tra i segmenti ossei del ginocchio (Fig. 3) che, seppur piccole, possono essere apprezzate con la metodologia sperimentale presentata in questo lavoro.

Per quanto riguarda le azioni muscolari, il sistema di controllo evidenzia correttamente come il contributo dei muscoli estensori superi quello dei flessori in ambo i compiti caricati (Fig. 4). Ancora, sebbene i due compiti motori caricati siano tra loro simili, è possibile apprezzare una significativa differenza tra i due che evidenzia correttamente come lo squat sia il compito più oneroso dal punto di vista muscolare.

6. CONCLUSIONI

Nonostante la semplicità costruttiva e di controllo dell'attrezzatura impiegata, l'analisi effettuata ha mostrato buona accuratezza e ripetibilità durante i compiti motori considerati. Inoltre, la procedura qui presentata è stata in grado di evidenziare le differenze anche in compiti motori tra loro simili, provando la sua validità per la caratterizzazione funzionale dell'articolazione del ginocchio.

Sebbene in questo lavoro non sia stata considerata la co-contrazione dei muscoli antagonisti, tale effetto può essere facilmente incluso nella strategia di controllo una volta che siano stati forniti gli opportuni riscontri sperimentali.

Le attività future mireranno a validare ulteriormente l'attrezzatura, testandone l'efficacia su ulteriori preparati anatomici e possibilmente anche su altre articolazioni, quali la caviglia.

REFERENCES

[1] F. C. Anderson and M. G. Pandy, 2001. "Dynamic optimization of human walking". *Journal of Biomechanical Engineering,* **123**(5):381–390.

[2] B. Ding, R. M. Stanley, B. S. Cazzolato, and J. J. Costi, 2011. "Real-time fpga control of a hexapod robot for 6-dof biomechanical testing". In Proceedings of *IECON 2011-37th Annual Conference on IEEE Industrial Electronics Society*, pages 252–257.

[3] E. S. Grood, S. F. Stowers, and F. R. Noyes, 1988. "Limits of movement in the human knee". *The Journal of Bone and Joint Surgery*, **70**-A(1):88–97.

[4]. E. S. Grood and W. J. Suntay. "A joint coordinate system for the clinical description of three-dimensional motions: application to the knee". *Journal of Biomechanical Engineering*, **105**:136–144.

[5] T. M. Guess and A. Stylianou, 2012. "Simulation of anterior cruciate ligament deficiency in a musculoskeletal model with anatomical knees". *The open biomedical engineering journal*, **6**:23–32.

[6] H. Hirschfeld, M. Thorsteinsdottir, and E. Olsson, 1999. "Coordinated ground forces exerted by buttocks and feet are adequately programmed for weight transfer during sit-to-stand". *Journal of neurophysiology*, **82**(6):3021–3029.

[7] A. Leardini, L. Chiari, U. D. Croce, and A. Cappozzo, 2005. "Human movement analysis using stereophotogrammetry: Part 3. soft tissue artifact assessment and compensation". *Gait & posture*, **21**(2):212–225.

[8] N. Sancisi, D. Zannoli, V. Parenti-Castelli, C. Belvedere, and A. Leardini, 2011. "A one-degree-of-freedom spherical mechanism for human knee joint modelling". *Proceedings of the Institution of Mechanical Engineers, Part H: Journal of Engineering in Medicine*, **225**(8):725–735.

[9] K. M. Varadarajan, R. E. Harry, T. Johnson, and G. Li, 2009. "Can in vitro systems capture the characteristic differences between the flexionextension kinematics of the healthy and tka knee?" *Medical engineering and physics*, **31**(11):899–906.

[10] D. Zannoli, N. Sancisi, and V. Parenti Castelli, 2012. "A simple rig for precise measurements of the knee and ankle joint motion under static loading conditions". In Proceedings of *Sesta Giornata di Studio Ettore Funaioli*, 160–165.

[11] A. B. Zavatsky, 1997. "A kinematic-freedom analysis of a flexed-knee-stance testing rig". *Journal of biomechanics*, **30**(3):277–280.

[12] M. Forlani, N. Sancisi, M. Conconi, and V. Parenti-Castelli, in press. "A new test rig for static and dynamic evaluation of knee motion based on a cable-driven parallel manipulator loading system", *Meccanica*, DOI 10.1007/s11012-015-0124-1.

GRAVITY COMPENSATION OF THE *ORTHOGLIDE 5-AXIS* PARALLEL KINEMATICS MACHINE

Alberto Martini
Department of Engineering for Industry,
University of Bologna, Italy
E-mail: alberto.martini6@unibo.it

Marco Troncossi
Department of Engineering for Industry,
University of Bologna, Italy
E-mail: marco.troncossi@unibo.it

Marco Carricato
Department of Engineering for Industry,
University of Bologna, Italy
E-mail: marco.carricato@unibo.it

Alessandro Rivola
Department of Engineering for Industry,
University of Bologna, Italy
E-mail: alessandro.rivola@unibo.it

Abstract. *This study deals with the compensation of gravity loads in the Orthoglide 5-axis, a prototypal parallel robot with Linear-Delta architecture for machining operations. Static balancing is analytically achieved by using an approach based on constant-force generators. A feasible solution, based on tension springs and a simple additional linkage, is presented to implement gravity compensation in practice. Both the robustness and the effectiveness of the proposed balancing strategy are confirmed by numerical analyses. In particular, the simulation results prove that the balancing device can provide an appreciable enhancement of the mechanism working performance in terms of improved energy efficiency.*

Keywords: *static balancing, gravity compensation, parallel kinematics machine, linear-delta robot*

1. INTRODUCTION

A mechanism is *statically balanced* (or *gravity compensated*) if the actuators are not required to exert any action for sustaining the weight of its members, for any admitted motion. The compensation of gravity loads in serial manipulators is essential and it is therefore normally performed. Conversely, static balancing of closed-loop mechanism is not a common practice, even if this topic has been widely studied and several different approaches have been proposed [1-10]. Indeed their use in industrial applications is mostly
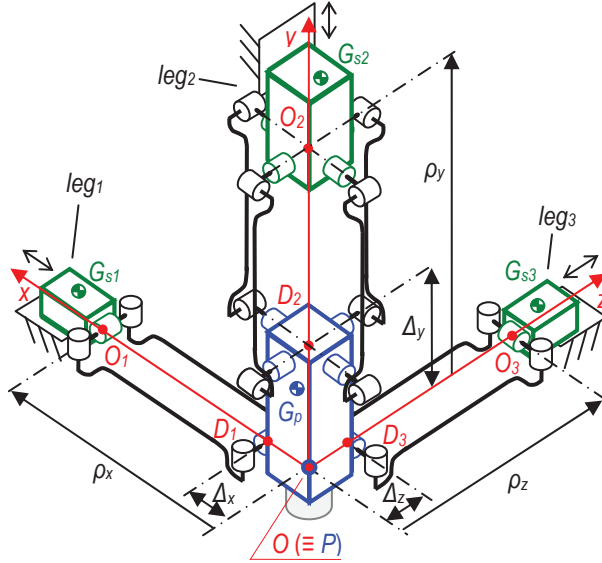
Figure 1. *Orthoglide 5-axis* kinematic scheme.

related to high-speed manipulation (such as pick and place tasks), with dynamic loads being largely preponderant. Nonetheless, applications which adopt parallel robots for different purposes, e.g. robotic surgical systems or Parallel Kinematics Machines (PKMs) for machining operations, are constantly increasing. These systems generally feature a heavy moving platform and working conditions characterized by both long time intervals at rest and operation at low/moderate dynamics. Such features cause gravity loads to significantly affect the required motor actions, thus static balancing appearing potentially profitable [11-15]. In particular, an appreciable improvement of their working performance in terms of energy efficiency and safety is reasonably expected, provided that the pros and cons (e.g. possible detrimental elastodynamic effects related to balancing devices) are carefully assessed [16-19].

This work investigates a prototypal spatial PKM for machining applications, namely the *Orthoglide 5-axis* [20]. This 5-DOF mechanism features a serial-parallel hybrid design (Fig. 1). A closed-loop chain, made up of three legs arranged in a *Linear-Delta* scheme, provides the platform (carrying the spindle) with 3 translational DOFs. The axes of the actuated prismatic joints are mutually orthogonal, with one being vertical. An actuated 2-DOF spherical wrist is located on the platform and controls the spindle orientation. Firstly, static balancing of the *Orthoghlide 5-axis* is analytically carried out. Then a feasible solution for implementing gravity compensation in practice is presented. Finally, actual benefits and potential drawbacks of the proposed balancing device are assessed by means of numerical simulations.

2. STATIC BALANCING OF THE MECHANISM

A general method for balancing parallel manipulators (formerly proposed by Carricato and Gosselin [9] and exploiting the concept of *constant-force generators* [21]) is adopted. Firstly, a set of constant forces, acting on the platform and satisfying its neutral equilibrium, is determined. The introduction of proper balancing devices (namely counterweights and
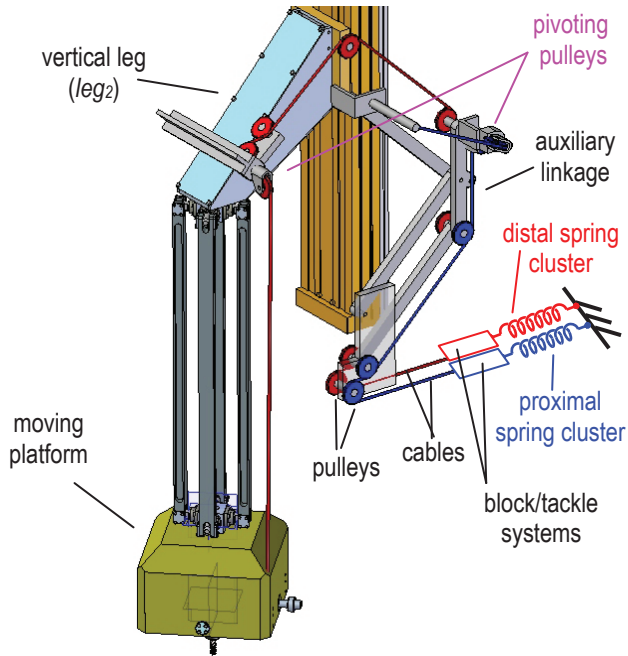
Figure 2. Preliminary representation of the balancing device attached to the vertical leg.
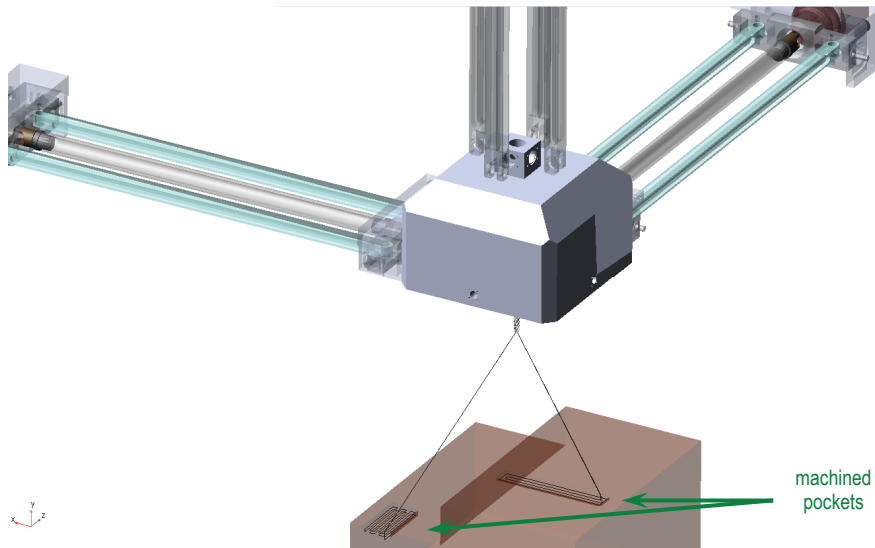
Figure 3. Tool path of the simulated milling (roughing) task.

springs) makes the legs generate the computed forces. The design parameters of such devices are determined by imposing the invariance of the total potential energy of each leg.

In the case of the *Orthoglide 5-axis*, gravity compensation can be achieved by acting only on the vertical leg, and without using counterweights [22]. The proposed balancing

device consists of two zero free-length springs (acting on the platform and on the vertical slider, respectively) and a simple auxiliary linkage (that connects the vertical slider to the fixed base). A feasible solution for the practical implementation of this balancing device is shown in Fig. 2. A set of cables and pulley is arranged for properly transmitting the elastic forces, thus allowing the adoption of common extension springs installed on the fixed base.

3. NUMERICAL SIMULATIONS

Models and analyses

The numerical rigid-body models of the unbalanced *Orthoglide 5-axis* and its balanced variant are implemented and simulated inside a multibody environment.

A sensitivity analysis is carried out for studying the influence on the compensation effectiveness of possible inaccuracies affecting the actual implementation of the proposed balancing device. The residual static loads acting on the actuators are monitored, across the complete workspace, for variations of several parameters (e.g. the platform mass or the spring rates) with respect to their nominal values.

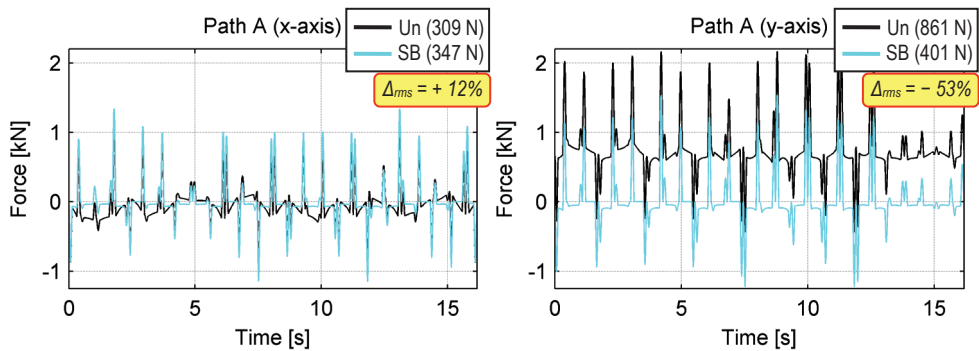**Figure 4.** Rapid tool positioning along reference *Path A*, motor loads of the unbalanced (Un) and the balanced (SB) robot along the x- and y-axis.
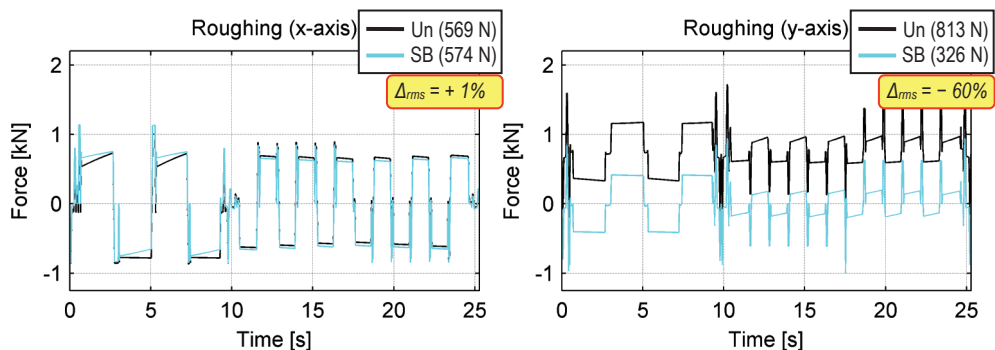

Figure 5. Milling task (roughing), motor loads of the unbalanced (Un) and the balanced (SB) robot along the x- and y-axis.

Inverse dynamics analysis is performed to investigate the dynamic operation of both mechanisms. The working performances of the unbalanced and the balanced systems are compared for different functioning conditions, and in particular for both rapid positioning operations and ordinary machining tasks, e.g. milling of rectangular pockets on horizontal surfaces of a hypothetical workpiece (Fig. 3). The effects of cutting forces are simply taken into account in the simulations as a resistant force proportional to the feed velocity. The required motor actions are analyzed and their rms values are computed for evaluating the global energy consumption of the working cycles.

Simulation results

The sensitivity analysis prove that the effectiveness of the balancing device is weakly influenced by possible inaccuracies affecting the design parameters, thus allowing design tolerances to be relieved.

The comparison between the motor loads of the unbalanced mechanism and its balanced variant for two tested conditions (computed through inverse dynamics analysis) is reported in Figs. 4 and 5, where the trends of the forces along the x- and the y-axis (chosen as examples) are plotted as functions of time. The corresponding rms values are provided inside the parentheses. For all tested working conditions the simulation results show that gravity compensation brings about a remarkable reduction in the vertical actuator force (in terms of both rms and peak values), while the motor loads of the horizontal legs are marginally affected by the introduction of the balancing devices. Therefore a significant reduction in the overall motor loads, as well as a more uniform loading of the actuators, can be achieved through gravity compensation.

4. CONCLUSIONS

The presented balancing device achieves gravity compensation with minor modifications of the original system and a small increment of the mass and inertia of the moving links. Its robustness and effectiveness are proven satisfactory by the simulation results. In particular, an appreciable global reduction of the motor loads required for performing common operations and standard machining tasks is observed, resulting in a profitable improvement of the system energy efficiency. Hence, the proposed balancing device appears as a suitable solution.

Even if this study focuses on the *Orthoglide 5-axis*, the approach for gravity compensation may be extended to other applications characterized by a linear-delta architecture.

Finally, gravity compensation is confirmed as a viable strategy for enhancing the operation of PKMs for machining applications, thus further investigation appearing worthy of interest.

REFERENCES

[1] Lowen, G. G., Tepper, F. R., and Berkof, R. S., 1983. "Balancing of linkages—an update". *Mechanism and Machine Theory*, **18**(3), pp. 213–220.

[2] Streit, D. A., and Shin, E., 1993. "Equilibrators for planar linkages". *ASME Journal of Mechanical Design*, **115**(3), pp. 604–611.

[3]   Wongratanaphisan, T., and Cole, M. O. T., 2008. "Analysis of a gravity compensated four-bar linkage mechanism with linear spring suspension". *ASME Journal of Mechanical Design*, **130**(1: 011006), pp. 1−8.

[4]   Deepak, S. R., and Ananthasuresh, G. K., 2012. "Static balancing of a four-bar linkage and its cognates". *Mechanism and Machine Theory*, **48**, pp. 62−80.

[5]   Laliberté, T., and Gosselin, C. M., 1999. "Static balancing of 3-DOF planar parallel mechanisms". *IEEE/ASME Transactions on Mechatronics*, **4**(4), pp. 363−377.

[6]   Wang, J., and Gosselin, C. M., 2000. "Static balancing of spatial four-degree-of-freedom parallel mechanisms". *Mechanism and Machine Theory*, **35**(4), pp. 563−592.

[7]   Gosselin, C. M., and Wang, J., 2000. "Static balancing of spatial six degree-of-freedom parallel mechanisms with revolute actuators". *Journal of Robotic Systems*, **17**(3), pp. 159−170.

[8]   Russo, A., Sinatra, R., and Xi, F., 2005. "Static balancing of parallel robots". *Mechanism and Machine Theory*, **40**(2), pp. 191−202.

[9]   Carricato, M., and Gosselin, C. M., 2009. "A statically balanced Gough/Stewart-type platform: conception, design, and simulation". *ASME Journal of Mechanisms and Robotics*, **1**(3: 031005), pp. 1−16.

[10]   Ebert-Uphoff, I., Gosselin, C. M., and Laliberté, T., 2000. "Static balancing of spatial parallel platform mechanisms—revisited". *ASME Journal of Mechanical Design*, **122**(1), pp. 43−51.

[11]   Baradat, C., Arakelian, V., Briot, S., and Guegan, S., 2008. "Design and prototyping of a new balancing mechanism for spatial parallel manipulators". *ASME Journal of Mechanical Design*, **130**(7: 072305), pp. 1−13.

[12]   Li, Y., Wang, J., Liu, X.-J., and Wang, L.-P., 2010. "Dynamic performance comparison and counterweight optimization of two 3-DOF parallel manipulators for a new hybrid machine tool". *Mechanism and Machine Theory*, **45**(11), pp. 1668−1680.

[13]   Stan, G., Ciobanu, R., and Pal, A., 2011. "Balancing-compensation system for the vertically moving elements of the machine tools with numerical control". *Meccanica*, **46**(4), pp. 755−769.

[14]   Lessard, S., Bigras, P., and Bonev, I. A., 2007. "A new medical parallel robot and its static balancing optimization". *ASME Journal of Medical Devices*, **1**(4), pp. 272−278.

[15]   Dehkordi, M. B., Frisoli, A., Sotgiu, E., and Bergamasco, M., 2012. "Modelling and experimental evaluation of a static balancing technique for a new horizontally mounted 3-UPU parallel mechanism". *International Journal of Advanced Robotic Systems*, **9**(193), pp. 1−12.

[16]   Raghu, E., and Balasubramonian, A., 1990. "Experimental study on the elastodynamic behavior of the unbalanced and the counterweighted four bar mechanisms". *ASME Journal of Mechanical Design*, **112**(3), pp. 271−277.

[17]   Walker, M. J., and Haines, R. S., 1982. "An experimental study of the effects of counterweights on a six-bar chain". *Mechanism and Machine Theory*, **17**(6), pp. 355−360.

[18]   Martini, A., Troncossi, M., Carricato, M., and Rivola, A., 2014. "Elastodynamic behavior of balanced closed-loop mechanisms: numerical analysis of a four-bar linkage". *Meccanica*, **49**(3), pp. 601−614.

[19]   Martini, A., Troncossi, M., and Rivola, A., 2013. "Elastodynamic effects of mass-balancing: experimental investigation of a four-bar linkage". *Advances in Mechanical Engineering*, http://dx.doi.org/10.1155/2013/949457, pp. 1−10.

[20] In Proceedings, Ur-Rehman, R., Caro, S., Chablat, D., and Wenger, P., 2008. "Kinematic and dynamic analyses of the Orthoglide 5-axis". *In Proceedings of the 7th France–Japan, 5th Europe–Asia Congress on Mechatronics*, Le Grand Bornand, France, May 21-23.

[21] Nathan, R. H., 1985. "A constant force generation mechanism". *ASME Journal of Mechanisms, Transmissions, and Automation in Design*, **107**(4), pp. 508–512.

[22] Martini, A., Troncossi, M., Carricato, M., and Rivola, A., 2015. "Static balancing of a parallel kinematics machine with *Linear-Delta* architecture: theory, design and numerical investigation". *Mechanism and Machine Theory*, **90**, pp. 128–141.

MODELLING AND VALIDATION OF A CONTINUOUS ROTARY MOTOR COMBINING SHAPE MEMORY WIRES AND OVERRUNNING CLUTCHES

Giovanni Scirè Mammano
Department of Engineering Sciences and Methods,
University of Modena and Reggio Emilia, Italy
E-mail: giovanni.sciremammano@unimore.it

Eugenio Dragoni
Department of Engineering Sciences and Methods,
University of Modena and Reggio Emilia, Italy
E-mail: eugenio.dragoni@unimore.it

Abstract. *This paper presents the conceptual design, modelling, prototyping and testing of a novel rotary motor featuring shape memory alloy (SMA) wires and overrunning clutches. The device comprises a SMA wire wound around a low-friction cylindrical drum contrasted by a backup beam spring and fitted to the output shaft through an overrunning clutch. Electrical heating produces a contraction of the wire, hence a rotation of the drum which is transferred to the shaft. Thanks to the overrunning clutch, during the recoiling phase the drum rotates backward while the shaft does not move. Spurious backward movements of the shaft are contrasted by a second overrunning clutch linking the shaft to the frame. The paper develops a model for the quasi-static simulation of the motor and the experimental characterization of a prototype device featuring three active drums, a rotary sensor and an angular brake to apply the external load. Despite the low degree of optimization, the tested motor performs well in terms of specific stroke, specific output torque and specific output work per cycle. Winding of the wire on the drum impairs somewhat the fatigue life with respect to publish data on straight wires, a drawback which calls for further design refinements.*

Keywords: Shape memory alloys, Wires, Rotary motor, Overrunning clutches

1. INTRODUCTION

High power density, smooth and silent operation, mechanical simplicity, compatibility with aggressive environments are but a few from a long list of advantages that make shape memory alloy (SMA) actuators strong competitors to conventional drives in many industrial applications. A relatively unexplored field for the exploitation of the shape memory technology is the area of rotary actuators, especially for generating large rotations (multiple revolutions). Shape memory torsion tubes are the favourite concept for rotary shape memory actuators [1-3] due to their simple geometry and high output torque. However, unless unrealistically long tubes or additional multiplying gear trains are used, the effective rotation is generally low (less than one revolution).

The simplest, strongest and most efficient SMA elements that can be used in practice are the drawn wires, commercially available in a wide range of diameters and physical properties. The main issue in using SMA wires for rotary actuation is the need to convert the linear motion, intrinsic to the wires, into an angular movement. Marketed rotary actuators make this conversion either by means of antagonistic wires wound onto a rotating shaft [4] or by coupling a linear shape memory actuator with a spring-loaded, cam-action rotary output [5]. Jansen and coworkers [6] developed an integrated positioning actuator using two SMA wires wound antagonistically onto an output shaft. A brake-assisted mechanism activated by a third SMA wire and released by a fourth SMA wire was provided to ensure stability of intermediate positions. A modular architecture comprising several units was envisioned to adapt the concept to a wider field of applications. A modular approach was adopted also in [7] where the basic module contained a moving rotor actuated tangentially by four shape memory springs. The solution in [7] contains also a first instance of elastic compensation performed by means of an elastic spring that reduced the torque ripple of the single module. Lan at al. [8] presented the design and implementation of a rotary manipulator combining SMA wires and flexural beams. Both one-way and two-way wheel-like manipulators were validated, in which the outer rim of the wheel was connected by three compliant sprockets to the centre shaft. Tangential forces were provided by SMA wires connecting the midpoints of each sprocket to the outer rim. Upon deactivation of the wires, the internal elastic force returned the sprockets to their original positions. Though mechanically simple, the above concepts [4-8] have severe limitations in the output rotation (60° is the maximum claimed rotary stroke) and cannot by any means provide unlimited angular motion.

In the early 2000s Yoshida [9] proposed a continuous rotary actuator formed by an inner disc rotating around a main shaft. The inner drum was connected to an outer casing through two spiral springs, which were wound in opposite directions and could unwind to recoil when electrically heated. Ratchet gears were provided between drum and casing to allow continuous motion. The merits of ratchet architectures for producing large strokes from compact packages in SMA actuators were recently addressed by Kim and coworkers [10] in a fairly general way. Scalable bi-directional rotary actuators were designed in [11] using SMA wires with diameter of about 100 micron. Based on this bi-directional actuator, SMA ratchet mechanisms with minimum feature sizes of about 200 micron were developed transform the alternated angular motion to continuously rotating motion. Pöhlau and Meier [12] suggested a high torque drive powered by six pairs of SMA actuators positioned radially inside a flexible gear wheel with external teeth. The flexible wheel was meshed with an outer gear wheel with internal teeth. Activating the pairs of SMA wires sequentially produced a strain wave in the internal wheel which induced continuous rotation of the external wheel much in the way a harmonic drive does. The conceptual design, mathematical modelling and experimental testing of an SMA Poly Phase motor was presented in [13]. Three identical SMA wires in series with identical elastic springs (forming the three phases of the motor) were fixed to the end point of a crank and the other ends of the springs were connected to fixed points, spaced 120° apart. By activating the SMA wires sequentially, a bi-directional continuous rotation of the crank could be achieved with net output torque. Zhang and Yan [14] modelled and characterized a low-speed, high-torque continuous rotary motor actuated by multiple segments of SMA wires. The requirements of continuous rotation was met by coupling in series five unidirectional rotary actuators, actuated sequentially. Each actuator achieved the unidirectional rotation

by exploiting the irreversibility of motion between a ratchet wheel and two friction pawls, one used to receive the tangential force of the SMA wires and the other used as stalling device. Hwang and Higuchi [15, 16] proposed a cycloidal wobble motor driven by SMA wires. The applied driving mechanism consisted of a pin/roller based annular gear as a wobbler, a cycloidal disc as a rotor, and crankshafts to guide the eccentric wobbling motion. The wobbling motion of the annular gear was generated by sequential activation of radially-placed SMA wires backed up by elastic springs. The cycloidal disc was rotated by rolling-contact-based cycloidal gearing placed between the wobbler and the rotor. Though continuous and sometimes characterized by high torque output, the above SMA motors [9-16] are marred by the complexity of the mechanisms used to convert the reciprocating elongation of the wires into unlimited angular rotation.

To overcome the limitations of the published solutions, this paper presents the conceptual design, modelling and prototyping of a novel rotary motor based on shape memory alloy wires, coiling drums and overrunning clutches. The basic module of the device capitalizes on a SMA wire wound around a low-friction cylindrical drum according to a concept originally proposed by Song [17]. The drum is coupled with a set of overrunning clutches as explained in the following Section. This combination of elements produces a rotary actuator with high output torque and virtually infinite angular stroke (motor). The model developed and the proof-of-concept described in this paper demonstrate the potential of this idea to be converted into a compact, robust and efficient rotary motor with unlimited output stroke.

2. ARCHITECTURE OF THE ROTARY MOTOR

The rotary motor described in this paper merges wire-on-drum actuators [17, 18] with overrunning clutches [19] to exploit the advantages of both devices.

Figure 1 shows the concept of a wire-on-drum actuator. The SMA wire W is wound onto the low-friction drum D and is fixed in c to the drum itself and in e to the frame F. The drum can rotate freely about the axis a-b so that the tension force in the wire is contrasted by the compression force in the elastic spring S, also attached between drum and frame. Upon activation/deactivation of the wire, the wire slips over the drum and the inner attachment point c reciprocates between the positions c and c' so that the drum oscillates by the angle $\Delta\alpha$.

An overrunning clutch is a device in a transmission that disengages the driveshaft from the driven shaft when the driven shaft rotates faster than the driveshaft. Among the many practical instances available from the market [19], Fig. 2a exemplifies one particular type of overrunning clutch based on the sphere-socket concept. Figure 2b shows the symbolic representation of the device which will be adopted in the following description of the motor, regardless of the specific way to realize the device.

Figure 3 shows the conceptual architecture of the motor. The main shaft, S, is coupled to the frame, F, by means of the overrunning clutch, C_1, which allows only clockwise rotations of the shaft. The other end of the shaft is fitted with a second overrunning clutch, C_2, mounted with the same orientation as C_1 (if the outer ring of C_2 is held stationary, the shaft can rotate only clockwise). A low-friction drum D, fixed to the outer ring of C_2, receives several tightly-wound turns of the pre-stretched SMA wire, W, the ends of which are attached to the drum, D, and frame, F. The winding orientation of the SMA wire is such that, upon contraction of the wire (activation of the motor), a clockwise torque is applied to the drum, D.
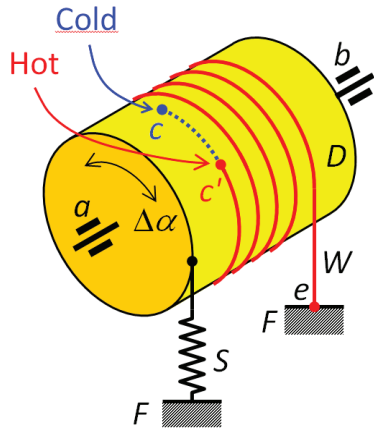
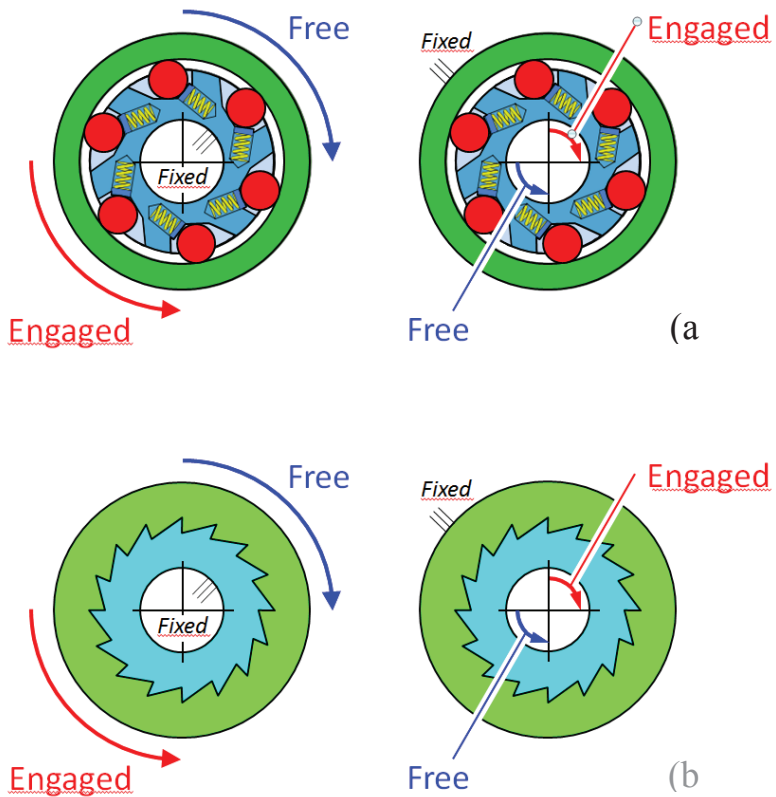**Figure 1.** Concept of the reciprocating wire-on-drum actuator [18].

Figure 2. Embodyment of an overrunning clutch wit fixed inner or outer ring (a) and corresponding symbolic representation of the device (b).
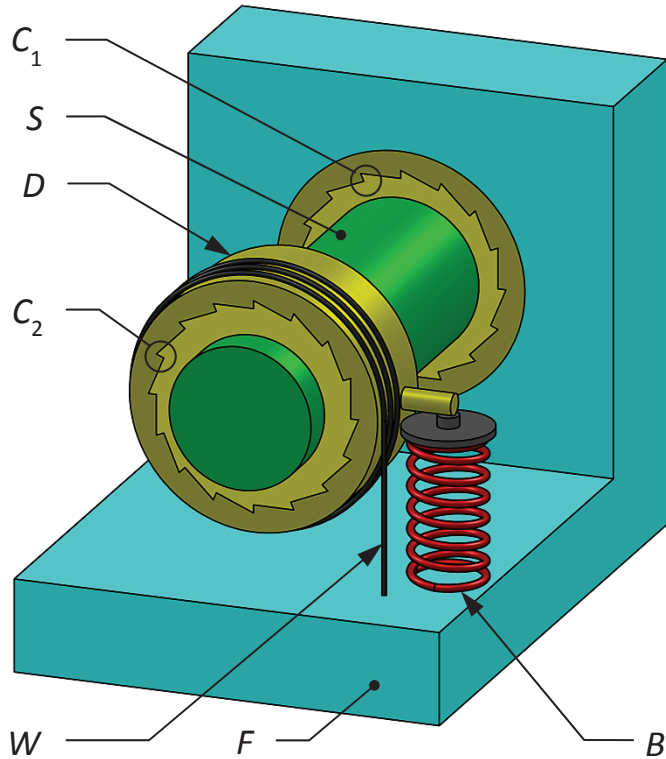
Figure 3. Concept of the rotary motor.

Thanks to the engaged overrunning clutch, C_2, the clockwise torque is ultimately transferred to the shaft, S, which is free to rotate because of the particular orientation of the first overrunning clutch, C_1. Tangentially on the drum, D, is also acting the elastic compression spring, B, which applies a counterclockwise backup torque to the system. The torque applied by the spring B must be large enough to overcome the torque of the martensite wire when it is in the cool, deactivated state. If this is the case, the counterclockwise rotation of the drum is allowed by the overrunning clutch C_2, while the clutch C_1 prevents any spurious counter-rotation of the shaft with respect to the frame.

In summary, once the pre-stretched wire has been tightly wound on the drum, the unidirectional clockwise rotation of the shaft is obtained by repeating two-step cycles of alternated heating and cooling of the wire. During heating, which is conveniently achieved by Joule effect through electric current supply, the wire contracts and effectively rotates the drum and the shaft clockwise. During cooling, which is improved by direct contact of the wire with the drum, the backup spring rotates the drum counterclockwise, thus elongating the memory wire while the shaft remains still. At the end of cooling step, the motor is ready to perform another cycle.

The sub-system comprising the SMA wire, W, the backup spring, B, the drum, D, and the overrunning clutch, C_2, represents the unit power module of the motor. The shaft, S,

embodies the output port of the motor. Of course, several unit modules can be arranged on a single output shaft, as shown in Fig. 4 for a three-stage motor, and activated in several possible ways. Serial activation of the modules (i.e. by cycling them one after the other) results in a smoother rotation of the output shaft with respect to a single-stage motor. Similarly, parallel activation of the modules (cycling them simultaneously) increases the output torque while conserving the step-wise rotation of the unit stage. If the number of modules is large (three or more), it is also possible to combine serial and parallel activation of subsets of modules and also partially overlap the cycle time of the modules within each subset. This produces concurrent increase of output torque and improved regularity of the rotation.

3. MODELLING OF THE UNIT MODULE

This section presents the analytical model of the unit module of the motor (dashed box in Fig. 4) in terms of angular displacements produced by activating the SMA wire for any given externally applied torque. The model is based on the theory developed by the authors [18] for the case of a SMA wire wound on a low-friction cylindrical drum and contrasted by a constant force. That theory is applied here to the unit module by assuming that the backup spring, (B in Fig. 3) generates a constant force and, consequently, the drum D receives a constant external torque. As widely recognized [20], the constant backup force (zero backup stiffness) improves the performance of the actuator with respect to a linear backup force (constant stiffness). For this application, a nearly zero-stiffness condition is achieved by using a thin beam loaded axially beyond its buckling limit [21].

The wire-on-drum model presented in [18] assumes a linear elastic stress-strain response of the shape memory wire in the austenite state and a bilinear response in the martensite state as shown in Fig. 5 (see [20] for details on this simple yet realistic material model).
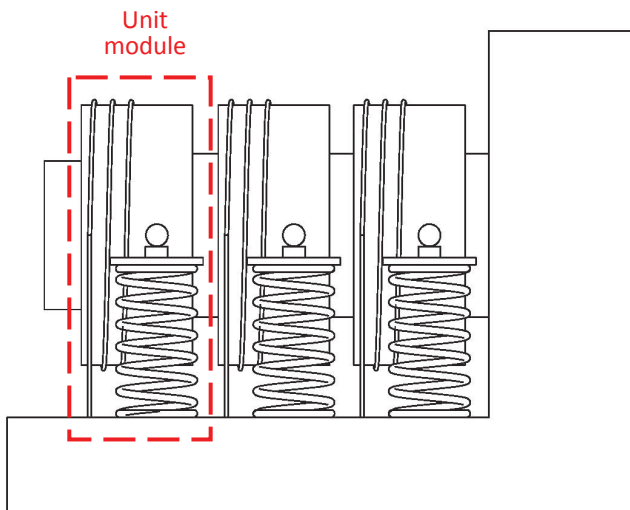

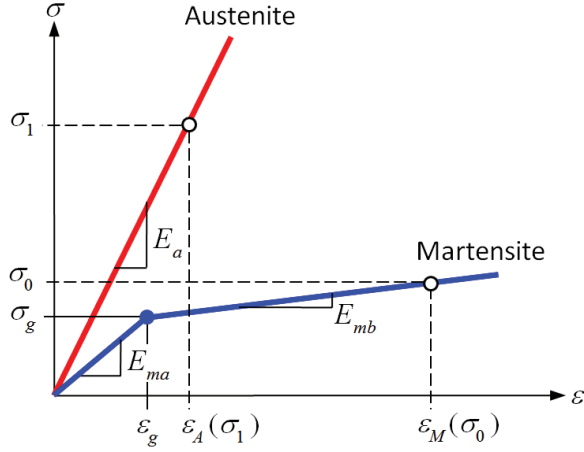**Figure 4.** Example of a three-stage rotary motor.

Figure 5. Material model of the SMA wire in austenitic and martensitic states.

The relationship between applied torque and angular rotation of the drum following this assumption is based on the differential elongation of the wire in the two limit states of fully transformed austenite and fully transformed martensite. The behavior of the device for partial degrees of transformation is not taken into consideration.

Central to the determination of the austenite and martensite elongations of the wire is the stress acting in the wire due to the torques acting on the drum in the two material states. Upon activation, the stress in the austenite wire, σ_1, is (see Fig. 3):

$$\sigma_1 = \frac{T_b + T_L + T_1}{R \cdot A_w} \tag{1}$$

where R is the winding radius of the wire, Aw is the cross-sectional area of the wire, T1 is the friction torque of the overrunning clutch C_1, T_L is the externally-applied torque and $T_b = F_b r_b$ is the restoring torque generated by the backup spring B (F_b is the constant backup force and r_b is the arm of F_b with respect to the axis of rotation of the drum).

Upon deactivation, the stress σ_0 in the martensitic wire is:

$$\sigma_0 = \frac{T_b - T_2}{R \cdot A_w} \tag{2}$$

where T_2 is the friction torque of the overrunning clutch C_2. Both stresses σ_1 and σ_0 are measured in the free wire length comprised between the frame and the drum in Fig. 3.

Following [18], the elongation ΔL_m of the martensite wire in contact with the drum produced by the stress σ_0 is:

$$\Delta L_m = \frac{R\sigma_0}{f E_{ma}} \left\{ \left(1 - e^{-f\alpha_A}\right) + \left(\frac{s_m - 1}{s_m}\right) \left[e^{-f\alpha_g} + \left(zf\alpha_g - 1\right) \right] \langle 0 \leq \alpha_g \rangle \right\} \tag{3}$$

in which E_{ma} is the elastic modulus of the martensite, $s_m = E_{mb}/E_{ma}$ is the characteristic ratio between pseudoplastic and elastic martensitic moduli, f is the frictional coefficient between wire and drum, $z = \sigma_g/\sigma_0$ is the ratio between the martensite yield stress and the overall stress in the wire, α_A is the winding angle and α_g is the portion of α_A over which the wire is stressed beyond σ_g (yielded wire). Angle α_g has the following expression:

$$\alpha_g = \min \left\{ \frac{-\ln z}{f} \langle z < 1 \rangle , \; \alpha_A \right\} \tag{4}$$

In equations (1) and (2) and in the remainder of the paper, the Boolean operator $\langle expression \rangle$ is used, which assumes the values 1 or 0 according to whether expression is true or false.

When the wire is activated and the alloy transforms from martensite to austenite, the stress in the free wire switches from σ_0 to σ_1 and the stress in the wound wire, σ_c, increases with the winding angle α according to the following exponential law:

$$\sigma_c(\alpha) = \sigma_1 e^{f\alpha} \tag{5}$$

The model in [18] shows that the net rotation angle of the drum, $\Delta\alpha$, following recovery of the strain upon martensite to austenite transformation is given by either of the following two values $\Delta\alpha_1$ and $\Delta\alpha_2$:

$$\Delta\alpha_1 = \frac{1}{f E_a} \left\{ \sigma_1 \left(1 - e^{f\alpha_{lim1}}\right) + \frac{s_1 \sigma_0}{s_m} \left[\left(1 - e^{-f\alpha_{lim1}}\right) + zf\left(s_m - 1\right)\alpha_{lim1} \right] \right\} \tag{6}$$

$$\Delta\alpha_2 = \frac{1}{f E_a} \cdot$$
$$\cdot \left\{ \sigma_1 \left(1 - e^{f\alpha_{lim2}}\right) + s_1 \sigma_0 \left(1 - e^{-f\alpha_{lim2}}\right) - \frac{s_1 \sigma_0}{s_m} \left(s_m - 1\right) \left[1 + z\left(\ln z - 1\right) \right] \langle 0 \leq \alpha_g \rangle \right\} \tag{7}$$

where:

$$\alpha_{lim1} = \min \left\{ \begin{array}{l} \dfrac{1}{f} \ln \left\{ \dfrac{1}{2 s_m \sigma_1} \left[z s_1 \sigma_0 \left(s_m - 1 \right) + \sqrt{ s_1 \sigma_0 \left[4 s_m \sigma_1 + z^2 s_1 \sigma_0 \left(s_m - 1 \right)^2 \right] } \right] \right\} \\ \alpha_A \end{array} \right. \tag{8}$$

and:

$$\alpha_{lim\,2} = \min \left\{ \dfrac{1}{2f} \ln \left(\dfrac{s_1 \sigma_0}{\sigma_1} \right), \alpha_A \right\} \tag{9}$$
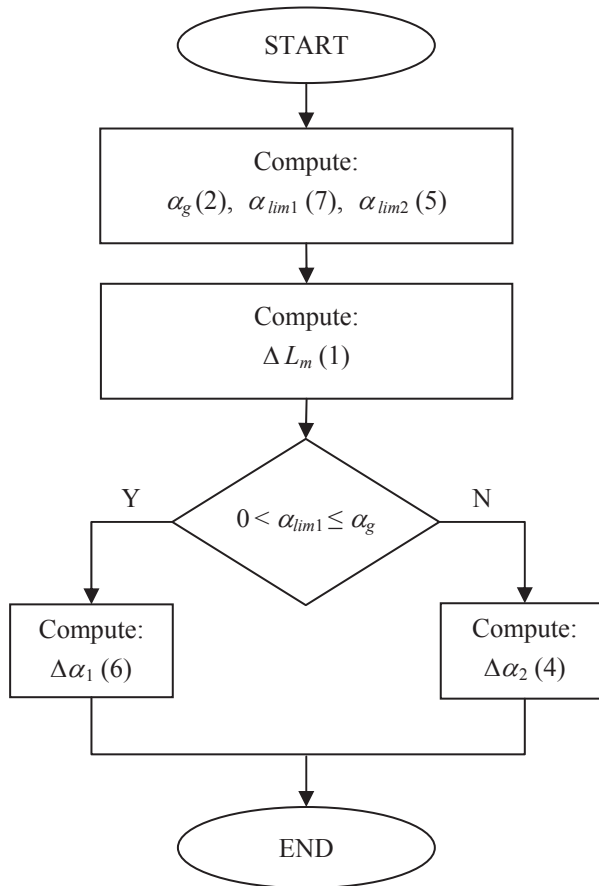

Figure 6. Flow-chart of the logical steps for calculating the angular stroke of the motor.
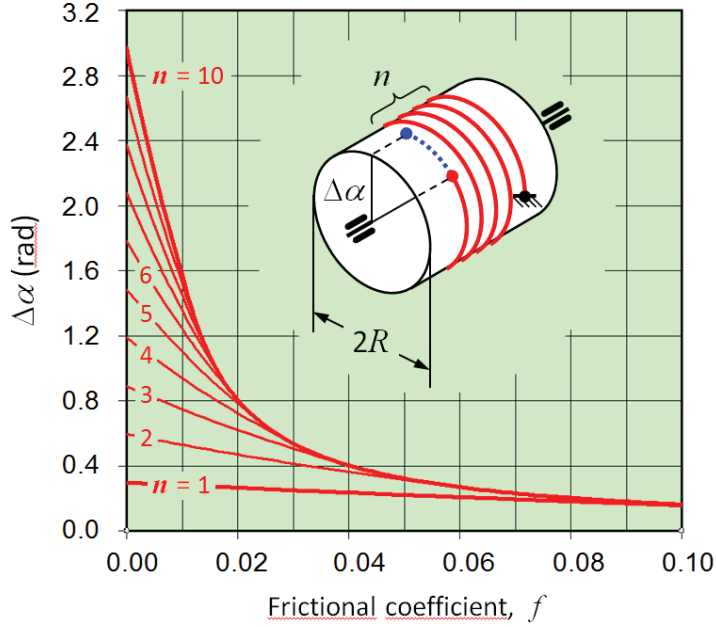
Figure 7. Net rotation of the wire-on-drum actuator for a martensite strain $\varepsilon_M = 5\%$.

are alternative winding angles over which the strain in the wire is actually recovered, E_a is the elastic modulus of the austenite wire and $s_1 = E_a/E_{ma}$ is a characteristic elastic ratio of the alloy. The flowchart in Fig. 6 summarizes the procedure used to calculate the maximum wire elongation and the effective rotation of the motor from the equations presented above. Figure 7 plots the net rotation of the drum, $\Delta\alpha$, as a function of the frictional coefficient and the number of wound coils, n, for a wire stretched with an initial martensite strain of $\varepsilon_M = 5\%$ (see Fig. 5). It is seen that the efficiency of the device increases exponentially as the coefficient of friction approaches zero.

4. DESIGN OF PROTOTYPE AND TEST BENCH

Motor architecture

For the prototype motor the architecture with three unit modules shown in Fig. 4 was chosen. The modules were operated sequentially to increase the regularity and the mean speed of the output shaft. A sensor for measuring the output rotation and a brake for applying the external torque were added to the design to allow final characterization. Figure 8 shows the CAD model of the motor mounted on the test bench.
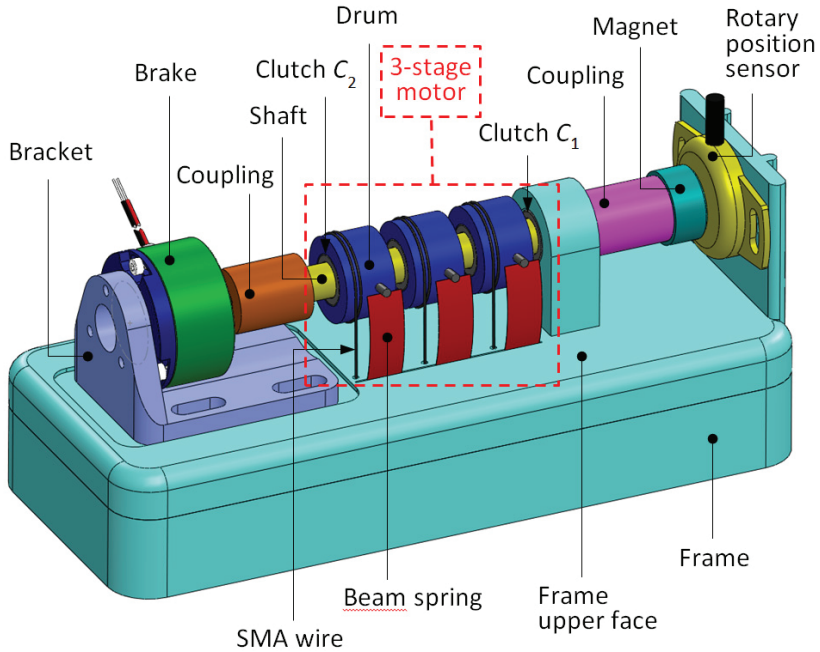
Figure 8. 3D CAD model of the prototype motor mounted on the test bed.

The SMA wires of the prototype were powered through a custom electronic board implementing a current-loop control. The desired supply current was set by means of a proportional voltage (gain = 1 A/V) generated by a National Instrument USB 6251 card. The USB 6251 card handled the operation and the data acquisition for the entire system by means of a custom program developed in the LabVIEW environment.

The three SMA wires were electrically connected in parallel. Each wire was supplied through an N-MOS transistor operated in the saturated region and acting as a switch for the corresponding wire. The three transistors were driven by the USB 6251 card through a voltage signal ranging from 0 to 5 V. Despite the parallel hardware connection, the wires were supplied sequentially so as to be activate one at a time.

Design of the unit module

The three basic elements of the unit module in Fig. 3 are the wound SMA wire, the overrunning clutch C_2 and the backup spring B. As SMA element, the 0.15 mm NiTi SmartFlex wire manufactured by SAES Getters was chosen (A_w = 0.0177 mm^2, A_s = 86°C A_f = 94°C, M_s =65°C , M_f = 57°C). From the quasi-static martensite and austenite stress-strain curves shown in Fig. 9, the following parameters were calculated: E_{ma} = 8 GPa, σ_g = 35 MPa, s_l = 5.62, s_m = 0.4 . Each of the three SMA wires in Fig. 8 was wound for 1.5 turns on a 20 mm drum, giving a winding length of about 94 mm. One end of the wire was attached to the drum by means of an electric ferrule inserted into a radial hole in the drum.
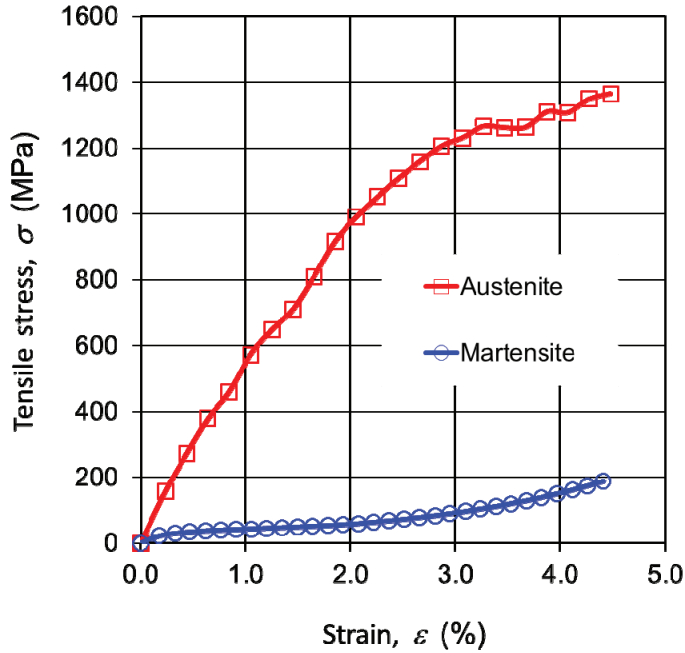
Figure 9. Martensitic and austenitic stress-strain curves for the 0.15 mm
SmartFlex® wire used in the prototype motor.

The other end of the wire was also provided with an electric ferrule and was fastened to the frame by means of a screw. The total length of the wire, including the unwound portion, was about 120 mm.

The overrunning clutches for the three unit modules (C_2 in Fig. 3) and for the support of the shaft (C_1) were made using NBS clutches, model HF0812, with a bore of 8 mm, an outside diameter of 12 mm and a width of 12 mm. This particular model of clutches comes without centering roller bearing, which are recommended when the radial loads are particularly high. The friction torque of the clutches, either with or without external load, was not provided by the manufacturer. All four overrunning clutches were coupled by interference fit to a ground aluminium shaft of 8 mm in diameter. Each clutch of type C_2 was encased in a PTFE drum with external radius $R = 10$ mm.

The three backup springs of the prototype (B in Fig. 3) were embodied by axially-loaded flat beam springs made by cutting straight laminae from a spring steel sheet. The laminae were inserted vertically into a socket cut into the frame (see Fig. 8) and engaged with the corresponding drum through a radial steel pin jutting out from the drum surface. Both ends of the laminae engaged with "V" sockets provided by frame and pin. This solution promoted stability of the contact and reproduced pinned-pinned constraining conditions in the plane of flexure of the beams. The arm of the beam springs with respect to the shaft axis was $r_b = 10.25$ mm. When loaded beyond the buckling limit, the axial beam springs bend transversely at almost constant force (nearly zero stiffness). The combination of relatively large buckling forces with virtually zero post-buckling stiffness make of these

elements an ideal backup element for SMA-activated devices. Another practical advantage of this spring solution is the ease with which laminae with the designed mechanical properties can be manufactured inexpensively from steel sheets using simple shears or other standard cutting tools.

Reference [21] describes the detailed beam design procedure, which leads to the material, length and cross section of the lamina starting from the required buckling load and total deflection. For the prototype motor, the stress needed to stretch the martensite SMA by $\varepsilon_M = 4\%$ is $\sigma_0 = \sigma(\varepsilon = \varepsilon_M = 4\%) \approx 155$ MPa. The force of the lamina able to generate this stress is $P_0 = \sigma_0 A_w R / r_b = 155 \times 0.0177 \times 10 / 10.25 \approx 2.65$ N. The overall elongation of the martensitic wire, ΔL, equals the elongation of the wound wire, $\Delta L_m = 3.56$ mm from (1), plus the elongation of the free $\Delta L_{Free} = 0.04 \times (120 - 94) = 1.04$ mm. This gives $\Delta L = 4.6$ mm, which was rounded up to $\Delta L = 5$ mm. The length, l, of the vertical spring beams, was chosen so that the midpoint of the deflection $\Delta L = 5$ mm was placed approximately at the same height as the motor axis (about 20 mm) from the upper face of the frame (see Fig. 8). This condition yielded $l \approx 23$ mm.

The prototype laminae were cut from standard high-carbon steel sheets with elastic modulus $E = 190.7$ GPa, allowable stress $\sigma_{adm} \approx 1\,400$ MPa and thickness ranging from 0.05 mm to 0.15 mm in steps of 0.05 mm. Entering the above values into the procedure [21] led to a beam spring with free length $l = 23$ mm, thickness of 0.1 mm and width of 8.46 mm. The actual stiffness of the spring was $k_0 = 0.061$ N/mm, which means that the force increase after the elongation $\Delta L = 5$ mm was about 0.3 N, a mere 11% greater than the nominal force $P_0 = 2.65$ N. Figure 10 shows the force-deflection curve of the single beam spring measured experimentally. The force $P_0 = 2.65$ N (dashed horizontal line) is achieved approximately at midspan of the nominal deflection of 5 mm (hollow circle).

Test bench

The 3D CAD model of in Fig. 8 includes the sensor and the brake used for experimental characterization.

The contactless rotary position sensor (Penny+Giles NRH280DP) is seen on the right, with the stator fixed to the frame and the polarized magnet (rotor) connected to the shaft by means of a polymer joint.

The reading of the sensor was acquired by the USB 6251 card and processed by the custom LabVIEW program. At the left end of the frame in Fig. 8 is the magnetic hysteresis brake (MOBAC HB3M-2) featuring a two-way torque capacity up to 20 Nmm. The rotor of the brake is connected to the motor shaft while the brake casing is fixed to the frame. Advantages of the magnetic hysteresis technology are the very low friction torque and the precise linear relationship between applied voltage and braking torque. As for the rotary sensor, also the brake was connected electrically to the USB card and managed logically by the LabVIEW interface.
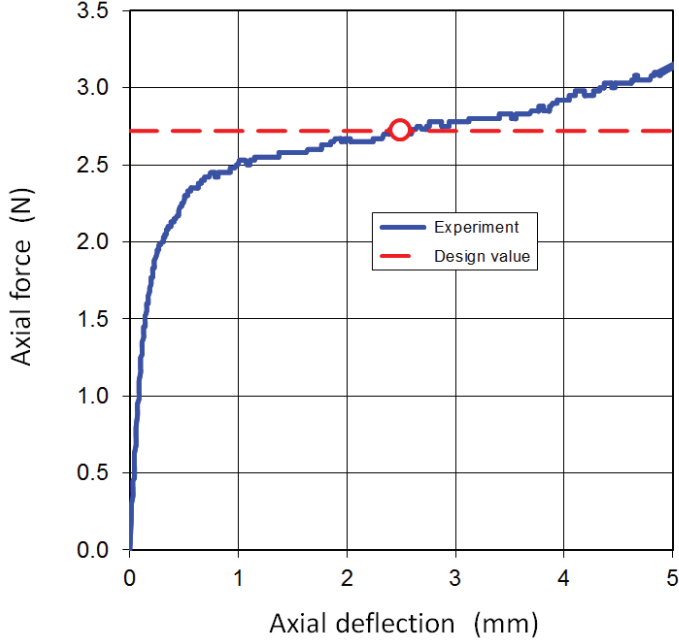
Figure 10. Experimental force-deflection curve for the beam spring used in the prototype motor.

5. PROTOTYPE TESTING AND MODEL VALIDATION

The prototype motor is shown in Fig. 11. The drums, beam springs, SMA wires are easily recognizable, together with the rotary sensor and the brake. The frame was manufactured by rapid prototyping using a 3D printer based on FDM technology. Testing of the prototype in Fig. 11 was performed in three stages, with two stages involving the single module and two stages involving the motor as a whole.

In the first test stage, the net stroke of the unit module was measured for five levels of braking torque: 0, 5, 10, 15 and 20 Nmm. The measurements were performed starting with the wire in the martensite state and then supplying the wire with a constant current of 800 mA up to complete austenite transformation. The experimental points of this first stage of testing are shown in Fig. 12 with solid circles and compared with the analytical predictions (hollow squares) for the net rotation defined as:

$$\Delta\alpha_{Tot} = \Delta\alpha + \Delta\alpha_{Free} \tag{10}$$

where $\Delta\alpha$ is the theoretical rotation calculated using the procedure in Fig. 6 and and $\Delta\alpha_{Free}$ is the shaft rotation associated with the strain recovery in the free wire length between frame and drum. Based on the martensite and austenite strains, ε_M and ε_A, highlighted in Fig. 5, the free rotation $\Delta\alpha_{Free}$ can be calculated as:
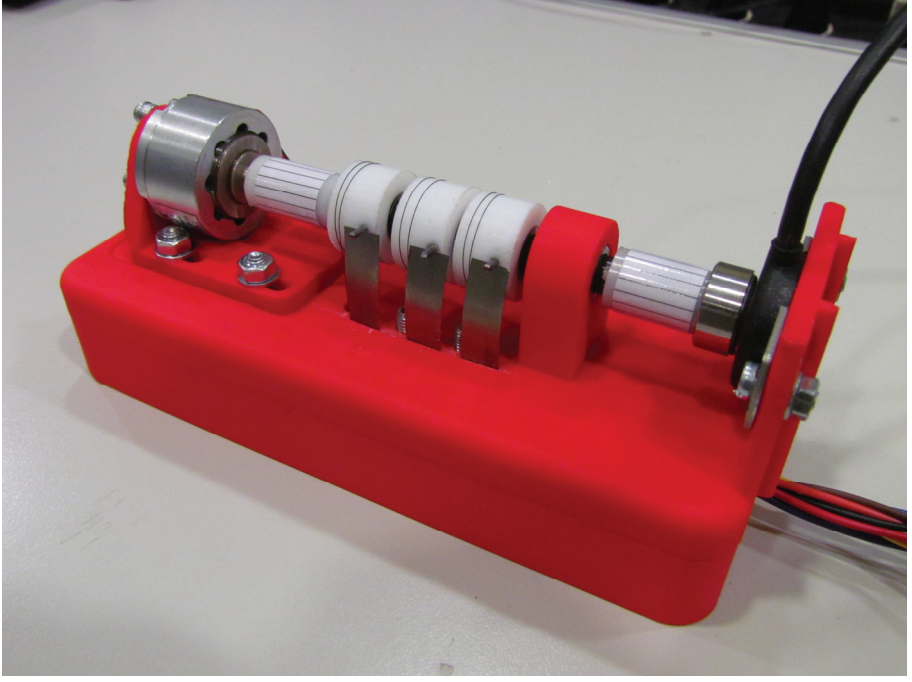
Figure 11. Close-up of the prototype motor in testing arrangement.

$$\Delta\alpha_{Free} = \frac{L_{Free}}{R}\Big[\varepsilon_M\left(\sigma_0\right) - \varepsilon_A\left(\sigma_1\right)\Big] =$$
$$= \frac{L_{Free}}{E_{ma}R}\left\{\sigma_0\left[1 + \left(\frac{1-s_m}{s_m}\right)(1-z)\big\langle\sigma_0 \geq \sigma_g\big\rangle\right] - \frac{\sigma_1}{s_1}\right\} \qquad (11)$$

where $L_{Free} \approx 26$ mm and the stresses σ_0 and σ_1 are calculated from (1) and (2) with T1 = T2 = 0.

In the second test stage, the transient output rotation of the unit module was measured under five levels of braking torques (0, 5, 10, 15 and 20 Nmm) upon application of a supply current stepping instantly from 0 to 800 mA. The results of this test, which was aimed at quantifying the intrinsic dynamics of the motor, are shown in Fig. 13.

In the third test stage, the mean velocity of the entire motor was measured for several braking torques (again 0, 5, 10, 15 and 20 Nmm) and by varying the supply time, t_{phase}, of the modules. During each single test, a constant current of 800 mA was supplied sequentially to the modules for a time equal to t_{phase}, giving a cooling time equal to 2 t_{phase} before being powered again. The mean angular velocity was calculated as the inverse of the time (in minutes) taken by the motor shaft to perform one complete rotation starting from the condition of all the modules at room temperature (martensite state). The results of these tests are presented in Fig. 14.
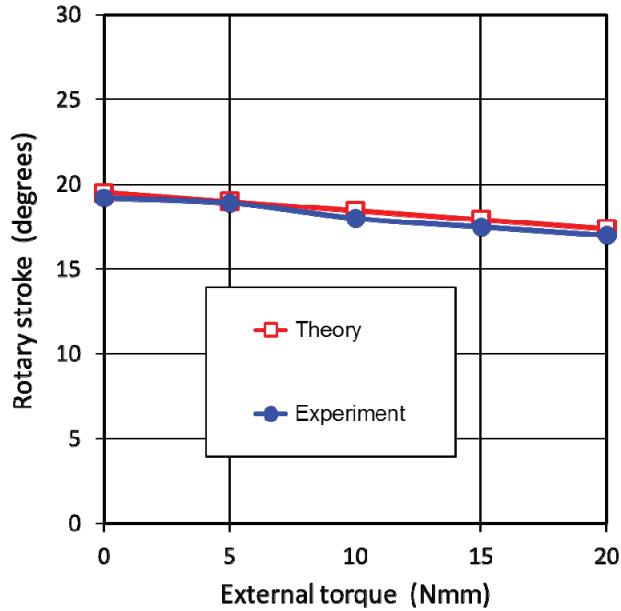
Figure 12. Experimental and analytical output rotation of the unit module as a function of the external torque.

The fourth and final test stage was and endurance test, carried out with the chief aim to investigate the fatigue life of the SMA wires in the actual working conditions of the motor. The modules were actuated sequentially with the following test parameters: supply current = 900 mA, supply time t_{phase} = 1.0 s, cooling time = 2.0 s, external torque T_L = 10 Nmm (implying a maximum wire stress of 227 MPa). The results of the endurance tests are shown in Fig. 15 for two runs performed on two distinct sets of wires. The rotation reported along the vertical axis in Fig. 15 represents the overall rotation of the shaft upon completion of an entire supply cycle (all three stages have been activated and deactivated).

6. DISCUSSION

From an engineering standpoint, the main advantage of the design presented is the modularity of the concept. The assembly of any number of unit modules (overrunning clutch, SMA wire and backup spring) on the same shaft, as shown in Figs. 4, 8 and 11, can easily lead to series, parallel or series-parallel working modes by choosing the proper scheme of electrical power management. Sequential supply of the modules (series mode) improves the regularity of the motion. Simultaneous supply (parallel mode) increases the output torque. Overlapping of the supply times between modules (series-parallel mode) enhances both regularity and output torque.
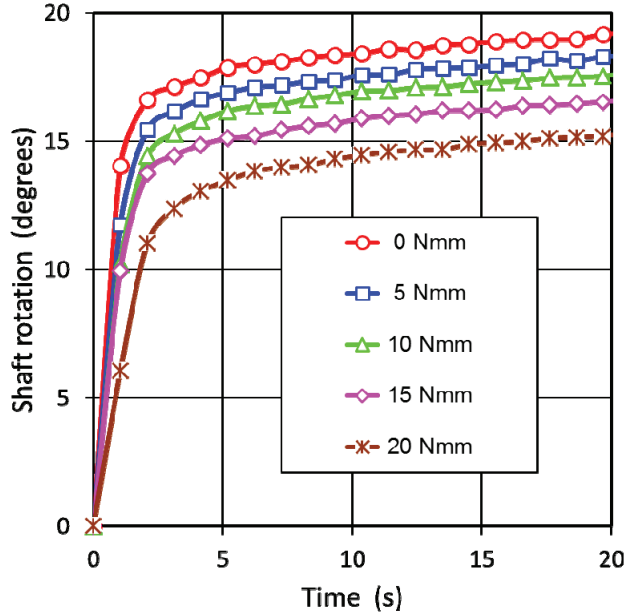
Figure 13. Transient of the shaft rotation (unit module) under a current step of 800 mA for several external torques.

Another asset of the construction is represented by the particular type of backup spring used to recoil the SMA wire upon de-activation of the modules. Besides being compact, the flat beam springs provide remarkable deflections at nearly-constant force. Figure 10 shows that the variation of the actual force is within $\pm$ 15% of the nominal force (red dashed line) in the range of deflections 0.5−5 mm. Furthermore, the flat beams are easily manufactured to any design, a production flexibility which is particularly important for prototype or custom constructions.

The good uniformity of the force generated by the backup spring made it possible to use the analytical model developed in [18] to describe the torque-stroke behaviour of the unit module (see also Fig. 7). Figure 12 shows that, although the restoring force of the backup spring is not precisely constant as assumed in [18], the analytical predictions (hollow squares) fit very closely the experimental data (solid circles). The error between theory and experiment is never greater than 2.5% for all the torques applied to the module.

It is seen that the analytical predictions are always in excess of the test data. This is probably due to having dropped from the model the friction torque in the clutches (C_1 and C_2 in Figs. 3 and 8) because this piece of information was not available from the supplier.

The dynamics of the unit module emerging from Fig. 13 (transient rotations following a stepped current supply) can be considered satisfactory.
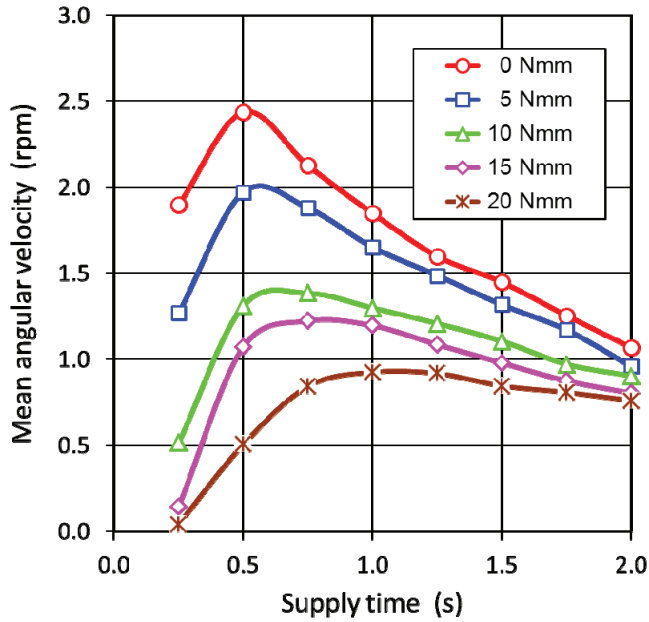
Figure 14. Mean angular velocity of the output shaft (three-stage motor) as a function of the supply time tphase of the modules for several external torques (supply current = 800 mA).

The time needed to achieve 50% of the full stroke (values in Fig. 12) ranges from 0.7 s to 1.3 s as the external torque increases from 0 to 20 Nmm.

These promising response times can probably be further reduced by increasing the supply current or adopting optimized supply schemes. For example, pulse-width modulation (PWM) supply is becoming more and more popular in the field of SMA actuation [22] because it increases the heating efficiency without impairing the fatigue life of the material [23].

The relevance of the supply scheme on the dynamic behaviour of the motor as a whole is clearly visible also in Fig. 14. The key variable in Fig. 14 is the supply time (t_{phase}) of each module within a sequential supply scheme across the modules. Due to the sequential activation, the heating time of the single module affects also the cooling time of the same module, which equals the time needed to supply the remainders (for the present case of three modules, the cooling time is 2 t_{phase}). Figure 14 shows that, regardless of the applied torque, the mean velocity of the motor initially increases then decreases with the supply time. For very short supply time, the wire has not enough time (2 t_{phase}) to cool down and recover the strain before the next supply cycle starts again. For relatively longer supply times, the modules remain idle even after they have cooled down and the strain in the wire has been completely recovered. The curves in Fig. 14 show that the peak angular velocity decreases with the applied torque while the supply time needed to achieve the peaks increases with the torque.
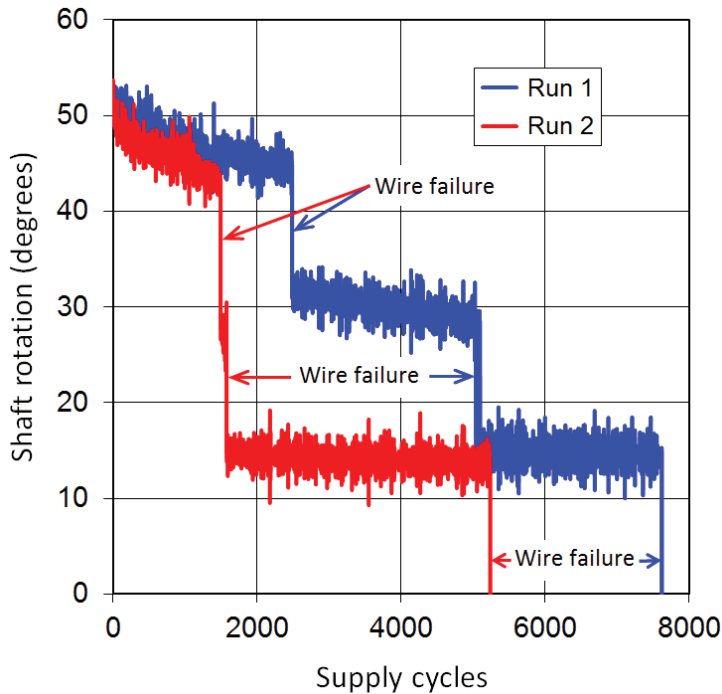
Figure 15. Endurance test results for two sets of SMA wires

Both results are coherent with Fig. 13 (lesser strokes and longer transient times for larger torques) and are explained by the increase of the transformation temperature of the SMA promoted by the higher stresses in the wire. Since the supply current was always the same (800 mA), the higher transformation temperatures require more time for complete transformation, leading to poorer dynamics for the higher loads.

The cycles to failure of the wires during cyclic operation of the motor (Fig. 15) range from about 1,500 to about 7,500, with an overall mean of about 3,900 cycles. The applied stress during the activation of each motor stage was almost constant, ranging from 227 MPa to 234 MPa. During deactivation, the only force applied to the wire was due to the beam spring, which was designed for inducing a martensite strain of 4%. For a similar combination of applied stress and maximum martensite strain (235 MPa and 4%, respectively), the laboratory tests in [24, 25] gave an average life of about 7,900 cycles (with a standard deviation of 965 cycles). The lower fatigue life with respect to publish data [24, 25] is presumably due to the bending overstresses consequent upon winding of the SMA wires on the drum. This drawback could be reduced by using many thinner wires on each drum instead of a single thick wire. This solution would conserve the area of the wire cross section (thus preserving the output torque) while reducing the bending stresses due to the lesser ratio of wire diameter to drum diameter.

Another drawback of the wire-on-drum solution, already reported in [18] with possible detrimental effects on the fatigue life, is the steady increase of the temperature of the PTFE drum during cyclic activation of the wire. This is because the low-friction drum material has also a relatively low thermal conductivity. A possible solution to this problem could be limiting to a minimum the thickness of the PTFE ring covering the overrunning clutch. Better still, using modern coating techniques [26] the outer ring of the clutch could be cladded with a thin layer of antifriction material to let the steel body of the clutch function as a heat sink.

The prototype motor was tested under externally applied torques up to 20 Nmm because this was the maximum torque capacity of the available brake. For the torque of 20 Nmm the stress in the SMA wire averages 260 MPa through the activation cycle. Though this stress level is not low, this particular alloy could certainly withstand higher stresses, resulting in higher output torques. This of course would be achieved for ever-decreasing rotary strokes, mean angular velocities and useful fatigue life.

The overall dimensions of the prototype in Fig. 11 are $L \times W \times H = 168 \times 70 \times 65$ mm, inclusive of frame, brake and position sensor. By excluding brake and sensor (which belong to the test apparatus) and optimizing the frame, the net dimensions of the present system could be easily reduced to $60 \times 20 \times 35$ mm. With reference to the parameters defined in the comprehensive comparison by Nespoli et al. [27], this reduced motor would present the following properties: specific angular stroke = S_R = 0.014 deg/mm^3, specific output torque = T_R = 0.8·10^{-3} Nmm/mm^3, specific work per cycle = W_R = 0.3·10^{-5} J/mm^3, which place this solution in the high end of all actuators known so far. In particular, the specific output work per cycle, W_R, is about three times the highest value reported in [27].

7. CONCLUSION

A three-stage rotary motor combining SMA wires wound on low-friction drums coupled to a common center shaft through overrunning clutches has been modelled, manufactured and tested. The multi-stage concept allows the motor to be driven electrically in series (to improve the velocity), in parallel (to improve the output torque) or in series-parallel (to improve both velocity and torque) with no changes to the mechanical hardware. A previously developed analytical model for the wire-on-drum system is adapted to describe the behaviour of the single module and is found to fit well with the measured performance in terms of applied torque and net stroke. Thanks to the unidirectional coupling offered by the overrunning clutches, the motor can run indefinitely with no limits on the magnitude of the shaft rotation. The three-stage prototype tested presents specific strokes, specific output torque and, above all, specific output work per cycle which place the device in the upper end of performance reported for SMA actuators and motors. Preliminary endurance tests on the motor indicate a fatigue life of the wires ranging from 1,500 to 7,500 cycles under stresses of about 260 MPa. Though these values are lower than reported for straight wires under similar stress levels, the performance of the device can be optimized by proper selection of the ratio between wire diameter and drum diameter.

REFERENCES

[1] Jacot, A.D., Julien, G.J., and Clingman, D.J., 2000, *"Shape memory rotary actuator"*, US Patent US6065934 A.

[2] Keefe, A.C., and Carman, G.P., 2000, "Thermomechanical characterization of shape memory alloy torque tube actuators", *Smart Materials and Structures*, **9**(5), pp. 665-672.

[3] Mehrabi, R., Kadkhodaei, M., Taheri Andani, M., and Elahinia M., 2014, "Microplane modeling of shape memory alloy tubes under tension, torsion, and proportional tension–torsion loading", *J. Intelligent Material Systems and Structures*, DOI: 10.1177/1045389X14522532.

[4] Toki Corporation, *"Biometal SmartServo RC-1"*, http://www.toki.co.jp/biometal (access date: December 9 2014).

[5] Miga Motor Company, *"NanoMuscle NM70R-6P - Rotary Memory Metal Actuator"*, http://www.migamotors.com/index.php?main_page=product_info&c   Path=1&products_id=29 (access date: December 9 2014).

[6] Jansen, S., Breidert, J., and Welp E.G., 2004, "Positioning actuator based on shape memory wires", *ACTUATOR 2004*, 9th International Conference on New Actuators, pp. 94-97.

[7] Spinella, I., Scirè Mammano, G., and Dragoni, E., 2009, "Conceptual Design and Simulation of a Compact Shape Memory Actuator for Rotary Motion", *J. of Materials Engineering and Performance*, **18**(5-6), pp. 638-648.

[8] Lan, C-C., Wang, J-H., and Fan, C-H., 2009, "Optimal design of rotary manipulators using shape memory alloy wire actuated flexures", *Sensors and Actuators A: Physical*, **153**(2), pp. 258-266.

[9] Yoshida, E., 2002, *"Continuous rotary actuator using shape memory alloy"*, US Patent US6484848 B2.

[10] Kim, W., Utter, B., Luntz, J., and Brei, D., 2013, "Model-based Memory Alloy Wire Ratchet Actuator Design", *ASME Conference SMASIS 2013*, Snowbird, UTAH, Sept. 16-18.

[11] Park, B.H., Shantz, M., and Prinz, F., 2001, "Scalable rotary actuators with embedded shape memory alloy", *Proceedings on SPIE*, **4327**, pp. 79–87.

[12] Pöhlau, F., and Meier, H., 2004, "Extremely compact high-torque drive with shape memory actuators and strain wave gear Wave Drive®", *ACTUATOR 2004*, 9th International Conference on New Actuators, pp.98-102

[13] Sharma, S.V., Nayak, M.M., and Dinesh, N.S., 2008, "Modelling, design and characterization of shape memory alloy-based poly-phase motor", *Sensors and Actuators A: Physical*, **147**(2), pp.583–592.

[14] Zhang, X.Y., and Yan, X.J., 2012, "Continuous Rotary Motor Actuated by Multiple Segments of Shape Memory Alloy Wires", *J. of Materials Engineering and Performance*, **21**(12), pp. 2643-2649.

[15] Hwang, D., and Higuchi, T., 2014, "A cycloidal wobble motor driven by shape memory alloy wires", *Smart Materials and Structures*, **23**(5), 055023.

[16] Hwang, D., and Higuchi, T., 2014, "A Rotary Actuator Using Shape Memory Alloy (SMA) Wires", *IEEE/ASME Transactions on Mechatronics*, **19**(5), 1625-1635.

[17] Song, G., 2007, "Design and control of a NiTi wire actuated rotary servo", *Smart Materials and Structures*, **16**(5), pp. 1796–1801.

[18] Scirè Mammano, G., and Dragoni, E., 2011, "Modeling of wire-on-drum shape memory actuators for linear and rotary motion*", J. of Intelligent Material Systems and Structures*, **22**(11), pp. 1129–1140.

[19] Shigley, J., Mischke, C., and Brown T., 2004, Standard Handbook of Machine Design, McGraw-Hill Professional, New York.

[20] Scirè Mammano, G., and Dragoni, E., 2011, "Increasing stroke and output force of linear shape memory actuators by elastic compensation", *Mechatronics*, **21**(3), pp. 570–580.

[21] Berselli, G., Scirè Mammano, G., and Dragoni, E., 2014, "Design of a Dielectric Elastomer Cylindrical Actuator With Quasi-Constant Available Thrust: Modeling Procedure and Experimental Validation", *ASME J. of Mechanical Design*, **136**(12), 125001 (11 pages).

[22] Hannen, J.C., Crews, J.H., and Buckner G.D., 2012, "Indirect intelligent sliding mode control of a shape memory alloy actuated flexible beam using hysteretic recurrent neural networks", Smart Materials and Structures, 21(8), 085015 (11 pages).

[23] Scirè Mammano, G., and Dragoni, E., 2013, "Effect of heating speed and degree of transformation on the functional fatigue of NiTi shape memory wires", *6th ECCOMAS Conference on Smart Structures and Materials SMART2012*, Politecnico di Torino, 24-26 June.

[24] Scirè Mammano, G., and Dragoni, E., 2014, "Effect of Loading and Constraining Conditions On the Thermomechanical Fatigue Life of Niti Shape Memory Wires", *J. of Materials Engineering and Performance,* **23**(7), pp. 2403-2411.

[25] Scirè Mammano, G., and Dragoni, E., 2014, "Functional fatigue of Ni–Ti shape memory wires under various loading conditions", *Int. J. of Fatigue*, **69**(12), pp. 71-83.

[26] Incerti, L., Rota A., Valeri, S., Miguel, A., García, J.A., Rodríguez, R.J., and Osés, J., 2011, "Nanostructured self lubricating CrN-Ag films deposited by Arc Discharge and PVD Magnetron Sputtering", *Vacuum* , **85**(12), pp. 1108-1113.

[27] Nespoli, A., Bessegnini, S., Pittaccio, S., Villa, E., and Viscuso, S., 2010, "The high potential of shape memory alloys in developing miniature mechanical devices: A review on shape memory alloy mini-actuators", *Sensors and Actuators A: Physical*, **158**(1), pp. 149-160.

NONLINEAR OSCILLATIONS AND ENERGY LOCALIZATION IN CARBON NANOTUBES

Angelo Oreste Andrisano
Department of Engineering "Enzo Ferrari",
University of Modena and Reggio Emilia, Italy
E-mail: angelooreste.andrisano@unimore.it

Leonid I. Manevitch
N.N. Semenov Institute of Chemical Physics,
Russian Academy of Sciences, Moscow, Russia
E-mail: lmanev@chph.ras.ru

Francesco Pellicano
Department of Engineering "Enzo Ferrari",
University of Modena and Reggio Emilia, Italy
E-mail: francesco.pellicano@unimore.it

Matteo Strozzi
Department of Engineering "Enzo Ferrari",
University of Modena and Reggio Emilia, Italy
E-mail: matteo.strozzi@unimore.it

Abstract. *In this paper, the low-frequency nonlinear oscillations and energy localizations of Single-Walled Carbon Nanotubes (SWNTs) are analysed. The SWNTs dynamics is studied within the framework of the Sanders-Koiter thin shell theory. The circumferential flexure vibration modes (CFMs) are considered. Simply supported boundary conditions are investigated. Two different approaches are compared, based on numerical and analytical models. The numerical model uses a double series expansion for the displacement fields based on the Chebyshev polynomials and harmonic functions. The Lagrange equations are considered to obtain a set of nonlinear ordinary differential equations of motion which are solved using the implicit Runge-Kutta numerical method. The analytical model considers a reduced form of the shell theory assuming small circumferential and tangential shear deformations. The Galerkin procedure is used to get the nonlinear ordinary differential equations of motion which are solved using the multiple scales analytical method. The natural frequencies obtained by considering the two approaches are compared in linear field. The effect of the aspect ratio on the analytic and numerical values of the localization threshold is investigated in nonlinear field.*

Keywords: nonlinear oscillations, energy localization, carbon nanotubes

1. INTRODUCTION

The spatially localized excitations represent one of the most interesting phenomena in the nonlinear dynamics of solids and structures [1]; in particular, the spatial confinement of the

nonlinear vibrations generated by external loads can be used to develop robust shock and vibration isolation designs for certain classes of engineering systems [2].

In the cases of discrete structures, the nonlinear energy localization can be studied in the framework of nonlinear normal modes (NNMs) or limiting phase trajectories (LPTs).

NNMs are usually employed to describe nonlinear elementary stationary processes with a weak energy exchange between coupled oscillators or oscillatory chains, where localized NNMs denote stationary energy localizations [3].

Conversely, LPTs allow to describe nonlinear elementary strongly non-stationary processes with a strong energy exchange between the different parts of finite nonlinear systems, where localized LPTs denote non-stationary energy localizations [4].

The concepts of effective particles and limiting phase trajectories have been extended also to the SWNTs, which represent finite discrete carbon structures consisting of needle-like tubes, described as helical microtubules of graphitic carbon.

Notwithstanding their small size and discrete nature, SWNTs were found to behave similarly to thin walled continuous structures presenting both membrane and bending stiffness; in particular, the analogies between the elastic thin shell model and the SWNT structure led to an extensive application of the continuous shell theories for the SWNTs structural analysis [5].

The effect of the boundary conditions on the nonlinear vibrations of circular cylindrical shells has been deeply investigated in the pertinent literature in the past years; in particular, shells with simply supported (periodic), clamped and free edges have been considered [6].

In the present paper, the low-frequency vibrations and energy localization of SWNTs are investigated on the basis of the Sanders-Koiter shell theory. The CFMs are examined. Simply supported boundary conditions are applied.

Two different approaches are compared. The numerical model uses a double mixed series expansion for the displacement fields based on the Chebyshev polynomials and the harmonic functions. The Lagrange equations are considered to obtain a set of nonlinear ordinary differential equations of motion which is solved by using the implicit Runge-Kutta numerical methods.

The analytical model considers a reduced form of the shell theory assuming small circumferential and tangential shear deformations. The Galerkin procedure is used to obtain the nonlinear ordinary differential equations of motion, which are solved by using the multiple scales analytical method.

The natural frequencies obtained by considering the analytical and numerical approaches are compared.

The effect of the aspect ratio on the analytical and numerical values of the localization threshold are investigated in nonlinear field.

2. SANDERS-KOITER SHELL THEORY

In Figure 1, a circular cylindrical shell having radius R, length L and thickness h is shown; a cylindrical coordinate system $(O; x, \theta, z)$ is considered where the origin O of the reference system is located at the centre of one end of the shell.

In Figure 1, three displacement fields are represented: longitudinal u (x, θ, t), circumferential v (x, θ, t) and radial w (x, θ, t), where (x, θ) are the longitudinal and angular coordinates, z is the radial coordinate along the thickness h and t is the time.
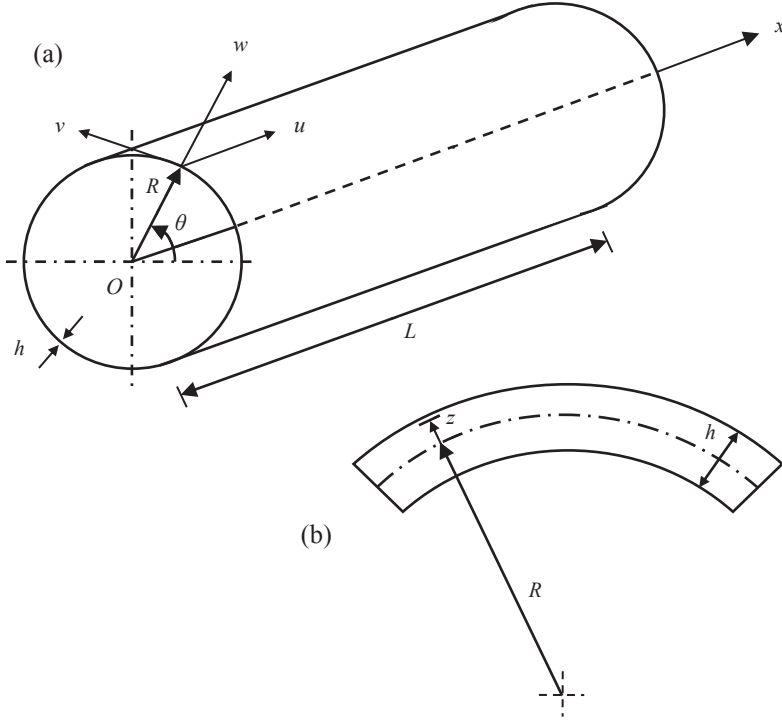
Figure 1. Geometry of the shell. (a) Complete shell; (b) cross-section of the shell surface.

Elastic Strain Energy

The nondimensional elastic strain energy of a cylindrical shell is written in the form

$$\tilde{E} = \frac{1}{2}\frac{1}{(1-\nu^2)}\left[\int_0^1\int_0^{2\pi}\left(\tilde{\varepsilon}_{x,0}^2 + \tilde{\varepsilon}_{\theta,0}^2 + 2\nu\tilde{\varepsilon}_{x,0}\tilde{\varepsilon}_{\theta,0} + \frac{(1-\nu)}{2}\tilde{\gamma}_{x\theta,0}^2\right)d\eta d\theta\right.$$
$$\left. + \frac{\beta^2}{12}\int_0^1\int_0^{2\pi}\left(\tilde{k}_x^2 + \tilde{k}_\theta^2 + 2\nu\tilde{k}_x\tilde{k}_\theta + \frac{(1-\nu)}{2}\tilde{k}_{x\theta}^2\right)d\eta d\theta\right] \tag{1}$$

where ($\tilde{\varepsilon}_{x,0}$, $\tilde{\varepsilon}_{\theta,0}$, $\tilde{\gamma}_{x\theta,0}$) are the nondimensional middle surface strains, ($\tilde{k}_x$, $\tilde{k}_\theta$, $\tilde{k}_{x\theta}$) are the nondimensional middle surface changes in curvature and torsion and $\beta = h/R$.

Kinetic Energy

The nondimensional kinetic energy of a cylindrical shell is given by

$$\tilde{T} = \frac{1}{2}\gamma\int_0^1\int_0^{2\pi}(\tilde{u}'^2 + \tilde{v}'^2 + \tilde{w}'^2)d\eta d\theta \tag{2}$$

where ($\tilde{u}', \tilde{v}', \tilde{w}'$) denote the nondimensional velocity fields and $\gamma = \rho R^2 \omega_0^2 / E$.

Numerical Solution of the Sanders-Koiter Shell Theory

In order to carry out the numerical analysis of the CNT dynamics, a two-steps procedure is applied: i) the three displacement fields are expanded by using a double mixed series, then the Rayleigh-Ritz method is applied in order to obtain an approximation of the linear eigenfunctions; ii) the displacement fields are re-expanded by using the linear approximated eigenfunctions and the Lagrange equations are considered to obtain a set of nonlinear ordinary differential equations of motion.

Linear Vibration Analysis. A modal vibration can be written in the form

$$\tilde{u}(\eta, \theta, \tau) = \tilde{U}(\eta, \theta)\tilde{f}(\tau) \qquad \tilde{v}(\eta, \theta, \tau) = \tilde{V}(\eta, \theta)\tilde{f}(\tau) \qquad \tilde{w}(\eta, \theta, \tau) = \tilde{W}(\eta, \theta)\tilde{f}(\tau) \qquad (3)$$

where $\tilde{U}(\eta, \theta)$, $\tilde{V}(\eta, \theta)$, $\tilde{W}(\eta, \theta)$ represent the mode shape and $\tilde{f}(\tau)$ describes the time law.

The mode shape $(\tilde{U}, \tilde{V}, \tilde{W})$ are expanded by means of the Chebyshev polynomials $T_m^*(\eta)$ in the longitudinal direction and the harmonic functions $(\cos n\theta, \sin n\theta)$ along the circumferential direction

$$\tilde{U}(\eta, \theta) = \sum_{m=0}^{M_u} \sum_{n=0}^{N} \tilde{U}_{m,n} T_m^*(\eta) \cos n\theta$$

$$\tilde{V}(\eta, \theta) = \sum_{m=0}^{M_v} \sum_{n=0}^{N} \tilde{V}_{m,n} T_m^*(\eta) \sin n\theta \qquad (4)$$

$$\tilde{W}(\eta, \theta) = \sum_{m=0}^{M_w} \sum_{n=0}^{N} \tilde{W}_{m,n} T_m^*(\eta) \cos n\theta$$

where $(\tilde{U}_{m,n}, \tilde{V}_{m,n}, \tilde{W}_{m,n})$ are the generalized coordinates.

Boundary Conditions. Simply supported boundary conditions are given by

$$\tilde{w} = 0 \qquad\qquad \tilde{v} = 0 \qquad\qquad \tilde{M}_x = 0 \qquad\qquad \tilde{N}_x = 0 \qquad \eta = 0,1 \qquad (5)$$

where the nondimensional force $\tilde{N}_x$ and moment $\tilde{M}_x$ are given by

$$\tilde{N}_x = \tilde{\varepsilon}_{x,0} + \nu \tilde{\varepsilon}_{\theta,0} \qquad\qquad\qquad \tilde{M}_x = \tilde{k}_x + \nu \tilde{k}_\theta \qquad (6)$$

The previous conditions (5,6) applied to expansions (4) imply the following equations

$$\sum_{m=0}^{M_w} \tilde{W}_{m,n} T_m^*(\eta) = 0 \qquad n \in [0, N] \qquad \theta \in [0, 2\pi] \qquad \eta = 0,1$$

$$\sum_{m=0}^{M_v} \tilde{V}_{m,n} T_m^*(\eta) = 0 \qquad n \in [0, N] \qquad \theta \in [0, 2\pi] \qquad \eta = 0,1$$

$$\sum_{m=0}^{M_w} \tilde{W}_{m,n} T_{m,\eta\eta}^*(\eta) = 0 \qquad n \in [0, N] \qquad \theta \in [0, 2\pi] \qquad \eta = 0,1 \tag{7}$$

$$\sum_{m=0}^{M_u} \tilde{U}_{m,n} T_{m,\eta}^*(\eta) = 0 \qquad n \in [0, N] \qquad \theta \in [0, 2\pi] \qquad \eta = 0,1$$

The linear system given by the equations (7) can be solved analytically in terms of the linearly dependent coefficients $(\tilde{U}_{1,n},\ \tilde{U}_{2,n},\ \tilde{V}_{0,n},\ \tilde{V}_{1,n},\ \tilde{W}_{0,n},\ \tilde{W}_{1,n},\ \tilde{W}_{2,n},\ \tilde{W}_{3,n})$.

Rayleigh-Ritz Procedure. The maximum number of variables needed for describing a general vibration mode with n nodal diameters is given by $(N_p = M_u + M_v + M_w + 3 - p)$, with $(M_u = M_v = M_w)$ as maximum degree of the Chebyshev polynomials and p as number of equations for the boundary conditions to be respected.

A specific convergence analysis was carried out to select the degree of the Chebyshev polynomials: degree 11 was found suitably accurate, $(M_u = M_v = M_w = 11)$.

For a multi-mode analysis including different values of nodal diameters n, the number of degrees of freedom is computed by the relation $(N_{max} = N_p \times (N + 1))$, where N represents the maximum value of the nodal diameters n to be considered.

After imposing the stationarity to the Rayleigh quotient, one obtains the eigenvalue problem

$$(-\omega^2 \tilde{M} + \tilde{K})\tilde{q} = \tilde{0} \tag{8}$$

which gives approximate natural frequencies (eigenvalues) and modes (eigenvectors).

The vector function

$$\tilde{Q}^{(j)}(\eta, \theta) = \begin{bmatrix} \tilde{U}^{(j)}(\eta, \theta) \\ \tilde{V}^{(j)}(\eta, \theta) \\ \tilde{W}^{(j)}(\eta, \theta) \end{bmatrix} \tag{9}$$

is the approximation of the j-th eigenfunction vector of the original problem.

Nonlinear Vibration Analysis. In the nonlinear analysis, the displacement fields $\tilde{u}(\eta, \theta, \tau)$, $\tilde{v}(\eta, \theta, \tau)$, $\tilde{w}(\eta, \theta, \tau)$ are expanded by using the previous linear mode shapes $\tilde{U}^{(j,n)}(\eta, \theta)$, $\tilde{V}^{(j,n)}(\eta, \theta)$, $\tilde{W}^{(j,n)}(\eta, \theta)$ in the form

$$\tilde{u}(\eta, \theta, \tau) = \sum_{j=1}^{N_u} \sum_{n=1}^{N} \tilde{U}^{(j,n)}(\eta, \theta) \tilde{f}_{u,j,n}(\tau)$$

$$\tilde{v}(\eta,\theta,\tau) = \sum_{j=1}^{N_v} \sum_{n=1}^{N} \tilde{V}^{(j,n)}(\eta,\theta) \tilde{f}_{v,j,n}(\tau) \tag{10}$$

$$\tilde{w}(\eta,\theta,\tau) = \sum_{j=1}^{N_w} \sum_{n=1}^{N} \tilde{W}^{(j,n)}(\eta,\theta) \tilde{f}_{w,j,n}(\tau)$$

where the modal coordinates $(\tilde{f}_{u,j,n}(\tau), \tilde{f}_{v,j,n}(\tau), \tilde{f}_{w,j,n}(\tau))$ are unknown functions.

Lagrange Equations. The nondimensional Lagrange equations of motion in the case of free vibrations can be expressed as

$$\frac{d}{d\tau}\left(\frac{\partial \tilde{T}}{\partial \tilde{q}_i'}\right) + \frac{\partial \tilde{E}}{\partial \tilde{q}_i} = 0 \qquad\qquad i \in [1, N_{max}] \tag{11}$$

where N_{max} depends on the modes used in (10) and $(\tilde{q}_i, \tilde{q}_i')$ are nondimensional lagrangian coordinates.

By using the Lagrange equations (11), a set of nonlinear ordinary differential equations of motion is obtained, which is finally solved by implicit Runge-Kutta numerical methods.

3. REDUCED SANDERS-KOITER SHELL THEORY

For the CFMs ($n = 2$), the nonlinear expansions of the nondimensional displacement fields are

$$\tilde{u}(\eta,\theta,\tau) = \tilde{U}_0(\eta,\tau) + \tilde{U}(\eta,\tau)\cos(2\theta)$$
$$\tilde{v}(\eta,\theta,\tau) = \tilde{V}(\eta,\tau)\sin(2\theta) \tag{12}$$
$$\tilde{w}(\eta,\theta,\tau) = \tilde{W}_0(\eta,\tau) + \tilde{W}(\eta,\tau)\cos(2\theta)$$

where $\tilde{U}_0$ and $\tilde{W}_0$ are the axisymmetric component of longitudinal and radial displacements.

By neglecting the nondimensional middle surface circumferential normal strain

$$\tilde{\varepsilon}_{\theta,0} = \frac{\partial \tilde{v}}{\partial \theta} + \tilde{w} = 0 \tag{13}$$

and the nondimensional middle surface tangential shear strain

$$\tilde{\gamma}_{x\theta,0} = \frac{\partial \tilde{u}}{\partial \theta} - \alpha \frac{\partial \tilde{v}}{\partial \eta} = 0 \tag{14}$$

the nondimensional longitudinal and circumferential displacement fields can be written as functions of the nondimensional radial displacement field.

The nonlinear equation of motion for the nondimensional radial displacement field is written as

$$\frac{\partial^2 \tilde{W}}{\partial \tau^2} + \frac{36\beta^2}{5}\tilde{W} - \frac{\alpha^2 \beta^2 (3+\nu)}{10}\frac{\partial^2 \tilde{W}}{\partial \eta^2} + \frac{\alpha^2}{20}\frac{\partial^4 \tilde{W}}{\partial \eta^2 \partial \tau^2} +$$

$$\frac{\alpha^4 (3+4\beta^2)}{60}\frac{\partial^4 \tilde{W}}{\partial \eta^4} + \frac{81}{40}\left[\tilde{W}\left(\frac{\partial \tilde{W}}{\partial \tau}\right)^2 + \tilde{W}^2 \frac{\partial^2 \tilde{W}}{\partial \tau^2}\right] - \frac{9\alpha^2}{40}\times$$

$$\left[\frac{\partial^2 \tilde{W}}{\partial \tau^2}\left(\frac{\partial \tilde{W}}{\partial \eta}\right)^2 + 2\frac{\partial \tilde{W}}{\partial \tau}\frac{\partial \tilde{W}}{\partial \eta}\frac{\partial^2 \tilde{W}}{\partial \eta \partial \tau} - \tilde{W}\left(\frac{\partial^2 \tilde{W}}{\partial \eta \partial \tau}\right)^2 + \left(\frac{\partial \tilde{W}}{\partial \tau}\right)^2 \frac{\partial^2 \tilde{W}}{\partial \eta^2} +\right.$$

$$\left. W\frac{\partial^2 \tilde{W}}{\partial \tau^2}\frac{\partial^2 \tilde{W}}{\partial \eta^2} + 4\alpha^2\left(\frac{\partial \tilde{W}}{\partial \eta}\right)^2 \frac{\partial^2 \tilde{W}}{\partial \eta^2}\right] - \frac{\alpha^4}{40}\left[\left(\frac{\partial^2 \tilde{W}}{\partial \eta \partial \tau}\right)^2 \frac{\partial^2 \tilde{W}}{\partial \eta^2} +\right. \tag{15}$$

$$2\frac{\partial \tilde{W}}{\partial \eta}\frac{\partial^3 \tilde{W}}{\partial \eta \partial \tau^2}\frac{\partial^2 \tilde{W}}{\partial \eta^2} - 2\alpha^2\left(\frac{\partial^2 \tilde{W}}{\partial \eta^2}\right)^3 + 2\frac{\partial \tilde{W}}{\partial \eta}\frac{\partial^2 \tilde{W}}{\partial \eta \partial \tau}\frac{\partial^3 \tilde{W}}{\partial \eta^2 \partial \tau} +$$

$$\left(\frac{\partial \tilde{W}}{\partial \eta}\right)^2 \frac{\partial^4 \tilde{W}}{\partial \eta^2 \partial \tau^2} - 8\alpha^2 \frac{\partial \tilde{W}}{\partial \eta}\frac{\partial^2 \tilde{W}}{\partial \eta^2}\frac{\partial^3 \tilde{W}}{\partial \eta^3} - \alpha^2\left(\frac{\partial \tilde{W}}{\partial \eta}\right)^2 \frac{\partial^4 \tilde{W}}{\partial \eta^4}\right\} = 0$$

This governing partial differential equation allows to calculate the natural frequencies in linear field as well as to estimate the effect of the nonlinearity at different boundary conditions.

Boundary Conditions

The linearization of equation (15) leads to the following expression

$$\frac{\partial^2 \tilde{W}}{\partial \tau^2} + \frac{36}{5}\beta^2 \tilde{W} - \frac{(3+\nu)}{10}\alpha^2 \beta^2 \frac{\partial^2 \tilde{W}}{\partial \eta^2} + \frac{1}{20}\alpha^2 \frac{\partial^4 \tilde{W}}{\partial \eta^2 \partial \tau^2} + \frac{1}{60}\alpha^4 (3+4\beta^2)\frac{\partial^4 \tilde{W}}{\partial \eta^4} = 0 \tag{16}$$

Assuming the radial displacement $\tilde{W}(\eta, \tau) = \overline{W}(\eta)\cos(\omega\tau)$, equation (16) becomes

$$\overline{W}(\eta) = c_1 \cos(\mu\eta + \delta_1) + c_2 \exp(-\gamma\eta + \delta_2) + c_3 \exp(\gamma\eta + \delta_3) \tag{17}$$

This equation contains both a harmonic-type solution and an aperiodic exponential-type solution in η; the equation should be completed with the suitable boundary conditions.

Simply Supported Edges. Simply supported boundary conditions can be expressed in the terms of the radial displacement $\overline{W}$ as

$$\overline{W}(\eta) = 0 \qquad\qquad \frac{\partial^2 \overline{W}(\eta)}{\partial \eta^2} = 0 \qquad\qquad \eta = (0,1) \tag{18}$$

Substituting these expressions into equation of motion (17), we get two transcendent equations with respect to parameters μ and γ; these equations are then solved analytically by applying the asymptotic expansion and the multiple scales method, in order to obtain an approximated analytical solution describing the dynamics of low-frequency nonlinear normal modes.

4. NUMERICAL RESULTS

In the first part of this section, the natural frequencies of the simply supported SWNTs obtained considering the analytical and numerical methods are compared; then, the analytical and numerical values of the localization thresholds are compared in nonlinear field for different aspect ratios.

Natural Frequency Spectra

In Figure 2, comparisons between analytical and numerical natural frequencies of SWNT in Ref. [5] with simply supported edges and aspect ratio $L/R = 20$ are reported for CFMs.

From these comparisons, it can be seen that the differences between the analytical and numerical methods are significant only for high values of the longitudinal wave-number (high frequencies), since in these cases the effect of the circumferential and tangential shear deformations is not negligible and therefore the hypotheses of the reduced Sanders-Koiter shell theory cannot be applied.

On the other hand, when the value of the longitudinal wave-number is small (low frequencies), the differences between the two approaches can be neglected.

Therefore, the analytical and numerical approaches show a good correspondence for the low-frequency CFMs in linear field.
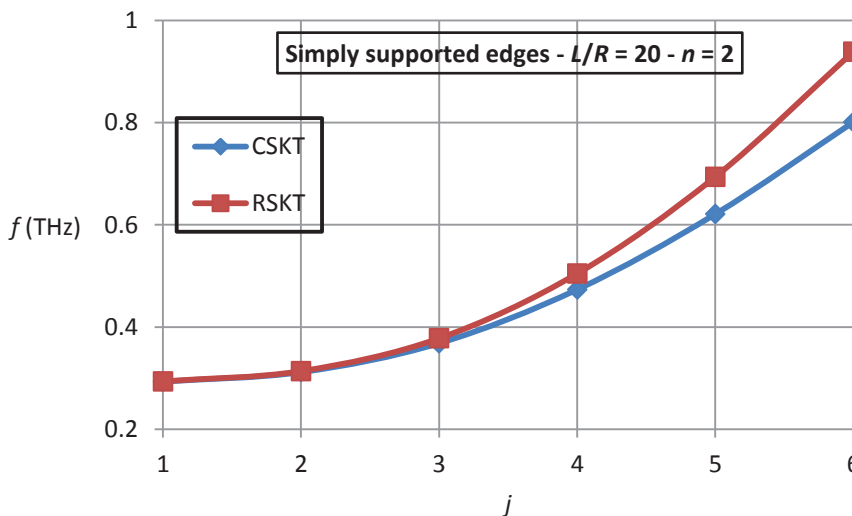

Figure 2. Natural frequencies of the SWNT with simply supported edges of Ref. [5]. Aspect ratio $L/R = 20$. CFMs. "-♦-", complete Sanders-Koiter shell theory (CSKT); "-■-", reduced Sanders-Koiter shell theory (RSKT).

Energy Localization Thresholds

In this part, the analytical and numerical values of the localization thresholds are compared.

These comparisons are carried out in the interval of the aspect ratios $\lambda = 20 \div 110$, where a resonant interaction between the two lowest modes of the frequency spectrum takes place.

In the considered case of simply supported boundary conditions, see Figure 3, a very good correspondence between the results of the analytical and numerical methods can be noted for the interval of the aspect ratios $\lambda = 20 \div 80$, since these boundary conditions are the simplest to be modelled.

Moreover, a fast increase of the value of the localization threshold in the lower region of aspect ratios $\lambda \leq 40$ and an early achievement of the horizontal asymptote $\lambda = 50$ is seen.

Finally, the results of analytical and numerical methods coincide at an aspect ratio $\lambda \geq 80$, since the boundary conditions effect can be neglected far from the edges.

5. CONCLUSIONS

In this paper, the low-frequency oscillations and energy localizations of simply supported SWNTs are analysed in the framework of the Sanders-Koiter elastic thin shell theory. The circumferential flexure modes are studied. Numerical and analytical models are compared.

The natural frequencies obtained by considering the previous methods are different for high longitudinal wave-numbers involving not negligible circumferential and tangential shear deformation effects. Conversely, the two methods show a good correspondence for low longitudinal wave-numbers.

The analytical and numerical values of the localization thresholds coincide at high aspect ratios, since the boundary effects can be neglected far from the edges. Moreover, a very good correspondence between the methods in the intermediate interval, a fast increase of the localization threshold in the lower region and an early achievement of the horizontal asymptote can be seen.
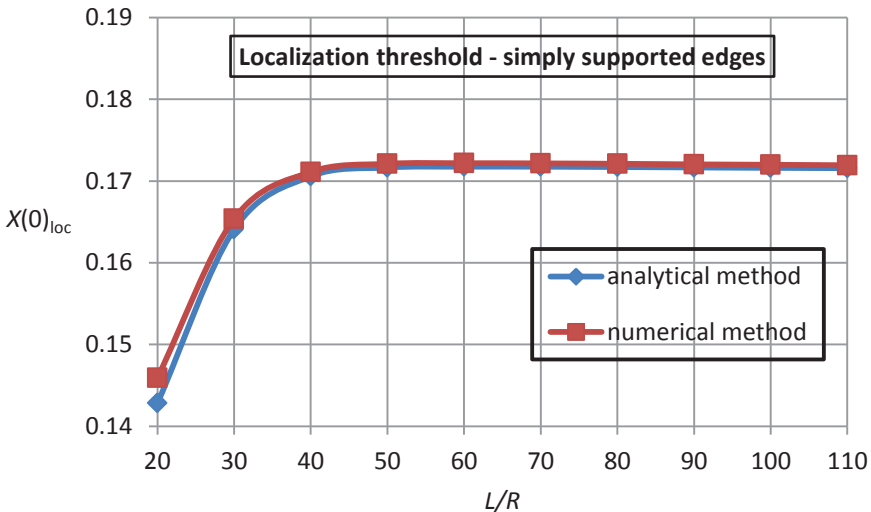

Figure 3. Effect of the aspect ratio on the amplitude of the localization thresholds for the SWNT with simply supported edges of Ref. [5]. "-♦-", analytical results (RSKT); "-■-", numerical results (CSKT).

REFERENCES

[1] Manevitch LI, Gendelman OV, 2011. Tractable Models of Solid Mechanics. Formulation, Analysis and Interpretation.

[2] Balandin DV, Bolotnik NN, and Pilkey WD, 2001. *Optimal Protection From Impact, Shock, and Vibration*.

[3] Jiang D, Pierre C, and Shaw SW, 2005. "Nonlinear normal modes for vibratory systems under harmonic excitation", *Journal of Sound and Vibration*, **288**, pp. 791-812.

[4] Manevitch LI, Smirnov VV, 2010. "Limiting phase trajectories and the origin of energy localization in nonlinear oscillatory chains", *Physical Review E*, **82**, pp. 1-9.

[5] Strozzi M, Manevitch LI, Pellicano F, Smirnov VV, and Shepelev DS, 2014. "Low-frequency linear vibrations of Single-Walled Carbon Nanotubes: analytical and numerical models", *Journal of Sound and Vibration*, **333**, pp. 2936-2957.

[6] Strozzi M, Pellicano F, 2013. "Nonlinear vibrations of functionally graded cylindrical shells", *Thin-Walled Structures*, **67**, pp. 63-77.

DESIGN OF A NOVEL MAGNETORHEOLOGICAL DAMPER WITH INTERNAL PRESSURE CONTROL

Nicola Golinelli
Dipartimento di Scienze e Metodi dell'Ingegneria,
University of Modena and Reggio Emilia, Italy
E-mail: nicola.golinelli@unimore.it

Andrea Spaggiari
Dipartimento di Scienze e Metodi dell'Ingegneria,
University of Modena and Reggio Emilia, Italy
E-mail: andrea.spaggiari@unimore.it

Abstract - *In this work we designed and manufactured a novel magnetorheological (MR) fluid damper with internal pressure control. Previous authors' works showed that the yield stress τ_B of MR fluids depends both on the magnetic field intensity and on the working pressure. Since the increase of the magnetic field intensity is limited by considerations like power consumption and magnetic saturation, an active pressure control leads to a simple and efficient enhancement of the performances of these systems. There are three main design topics covered in this paper about the MR damper design. First, the design of the magnetic circuit; second the design of the hydraulic system and third the development of an innovative pressure control apparatus. The design approach adopted is mainly analytical and provides the equations needed for system design, taking into account the desired force and stroke as well as the maximum external dimensions.*

Keywords *- Magnetorheological damper, design and manufacturing, squeeze-strengthen effect.*

1 INTRODUCTION

Nowadays, there are several industrial applications in which magnetorheological fluids (MRFs) are used [1, 2, 3]. In particular, this paper focuses on the optimal design methodology for magnetorheological dampers (MRDs). The purpose of traditional dampers, or so-called shock absorbers, is to dissipate energy. MRDs compared to traditional dampers, exploit the change in the rheological behavior of MR fluids in order to achieve variable damping properties. The changing of the properties of MR fluids occurs when a magnetic field is applied. The magnetic field is typically generated by an axial coil, for which connecting leads are usually brought out through the hollow piston rod [4]. The main classification for MRDs concerns the methods by which the insertion volume of the rod is accommodated. This is a major design problem because the oil itself is nowhere near compressible enough to accept the internal volume reduction of 10% or more associated with the full stroke insertion. The aim of this work consists in exploiting the effect of pressure on MRFs to generate further controllable damping force, so accommodating the change in volume is very important. Clearly,
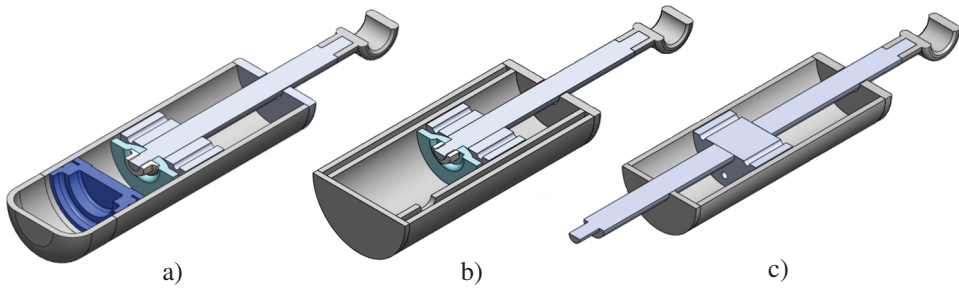
Figure 1. Telescopic architectures. a) Single-tube, b) double-tube and c) through-rod.

a static pressure can be applied only when nearly incompressible material are used in the system, so no air or gases are allowed in the design. Several studies have been carried out in order to comprehend the influence of pressure on the properties of MRFs. In [5], a novel compressible MR fluid has been synthesized with additives that provide compressibility to the fluid. MR fluids are influenced by the presence of internal pressure [6, 7, 8, 9, 10, 11]. In combined squeeze-shear mode, with a magnetic field of 300 mT, passing from 0 to 30 bar the yield shear stress to doubles its value. In flow mode instead, with a magnetic field intensity of 800 mT, the yield stress τ_B increments its value by nearly ten times. There are three basic MRDs architectures [4], as is shown in Figure 1: single-tube, double-tube and through-rod. The single-tube architecture (Figure 1a) is based on a single-rod cylinder structure, in which the piston head divides the damper into extension and compression chamber. During piston movement, MR fluid passes through the control valve which is obtained into the piston head. A floating piston separates the MRF from the accumulator filled with compressed gas. The accumulator is used to compensate the volume change due to the piston rod moving inward the cylinder. To eliminate the floating piston, emulsified oil may be used, distributing the expansion and rod-accommodation volume throughout the main oil volume. The gas separates, but quickly re-emulsifies on action. The valves must be rated to allow for the passage of emulsion rather than liquid oil. Mineral damper oil has long chain hydrocarbon molecules which do not pack efficiently together. This allows a higher compressibility than a liquid such as water because the long molecular chains can distort. In the double-tube type of telescopic (Figure 1b), a pair of concentric cylinder is used. The external one contains some gas to accommodate the rod displacement volume. The through-rod telescopic (Figure 1c) avoids the displacement volume issue by having a passing-through rod which causes no volume variation. However this has several disadvantages; there are external seals at both ends subject to high pressures that causes additional friction, the protruding free end may be inconvenient or dangerous, and there is still no provision for thermal expansion of the oil. However it is a simple solution which is used for example in some seismic application. Even though this architecture has proved impractical for suspension damping, it is sometimes used for damping of the steering.

2 MATERIALS AND METHODS

Since the active control of the pressure is needed, no flexible diaphragms or compressible gases are allowed. This is because flexible parts would absorb the change in pressure. Hence,
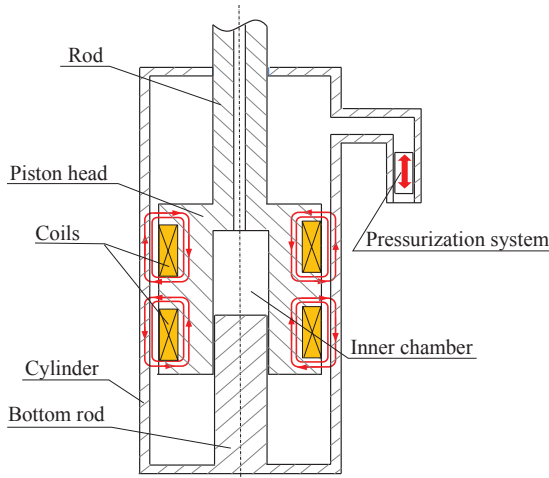
Figure 2. Conceptual scheme of the MR damper.

Table 1. main dimensions.

Cylinder length, (mm)	192
Cylinder diameter, (mm)	50
Rod diameter (mm)	20

Table 2. Technical specifications.

Maximum Force (N)	2000
Maximum Velocity (mm/s)	150
Stroke (mm)	50
Maximum input current (A)	2
Maximum body diameter (mm)	50
Maximum pressure (bar)	40

it is necessary an architecture without volume compensation. Figure 2 shows the conceptual scheme of the damper presented in this paper. We used a bottom-rod fixed to the end plug and coupled with the piston head. The bottom-rod has the same diameter of the upper-rod so that there is no volume variation. During piston movement, the bottom-rod is moving inward the chamber obtained into the piston head. The chamber is also directly connected to the canal through the upper-rod in order to bring out the coil's wire. Thereby, overpressure or depression within the chamber will not occur. It is worth noting that two coils were adopted. In this way, the longer axial length of the piston head is exploited to maximize the concatenated magnetic flux. The main dimensions of the damper are shown in Table 1. The design of the MR damper consisted in two main parts: the hydraulic-mechanical design [12] and the magnetic circuit design. The specifications of the damper we developed are listed in Table 2. In order to keep the manufacturing of the damper as simple as possible, a commercial hydraulic cylinder and the associated cylinder head were chosen [13]. Hence, knowing the outer diameter of the cylinder (50 mm) and the wall thickness (5 mm), even the inner diameter of the cylinder was also fixed (40 mm) (Figures 3(d),3(c)). The axial length of the hydraulic cylinder is 192 mm. The commercial cylinder head is arranged for a piston rod diameter of 20 mm (Figure 3(a)) and it has its own system of seals (Figure 3(b)). The mini-

Figure 3. Commercial components. Cylinder head for a 20 mm diameter rod (a) and its sealing system (b). Hydraulic cylinder (c) and welded boss for pressurization system (d).

mum axial length of the piston head was also fixed and had to be at least $L = 90$ mm. That is because we decided to compensate for the piston volume using the piston head, so it has to host a compensating bottom rod (50 mm), as presented in Figure 2.

Optimal design of magnetorheological devices requires the knowledge and the characterization of the properties of the materials involved. Firstly, the knowledge of the yield shear stress of the fluid as function of the magnetic field is necessary. The yield stress $\tau_B(H_{mrf})$ of MRF 140-CG [14] is given by the experimentally-derived equation from [15], [16] and depends on the magnetic field intensity and the particle volume fraction ϕ:

$$\tau(H) = 271700 C \phi^{1,5239} \tanh(6,33 \times 10^{-6} H) \tag{1}$$

ϕ is 0.4 and C is a coefficient dependent on the carrier fluid of the MR fluid ($C = 1$ for hydrocarbons). The magnetic B-H relationship of a MR fluid can be defined as [17]:

$$B = 1,91 \phi^{1,133}[1 - e^{(-10,97\mu_0 H_{mrf})}] + \mu_0 H_{mrf} \tag{2}$$

Therefore, a MR fluid's relative permeability can be defined as:

$$\mu_r = \frac{dB}{dH_{mrf}} = 1,91 \phi^{1,133}(10,97\mu_0 e^{-10,97\mu_0 H_{mrf}}) + \mu_0 \tag{3}$$

where, B is in Tesla, H_{mrf} is in A/m, and $\mu_0 = 1,25 \times 10^{-6}$ H/m is the permeability of free space. Figure 4 shows the graphs of the B-H relationship of the MRF 140-CG and
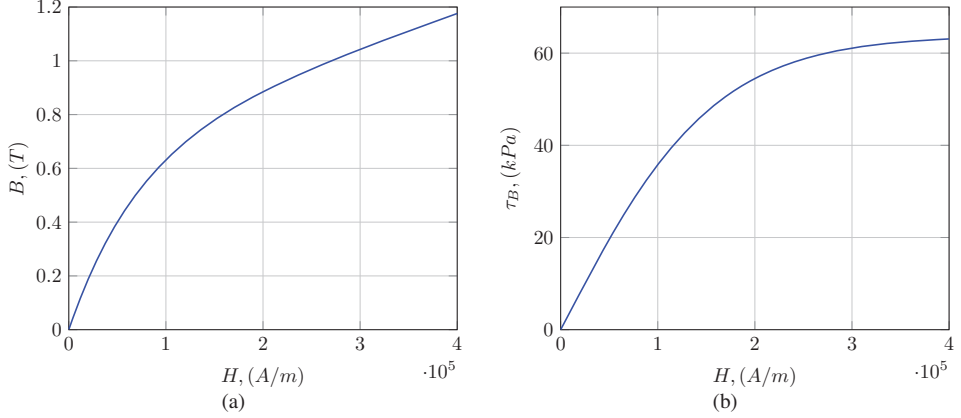
Figure 4. (a) B-H relationship and (b) yield shear stress τ_B of MRF 140-CG as a function of the magnetic field intensity.

the values of yield stress τ_B as a function of the magnetic field intensity H_{mrf}. In order to reach the best performances, the material which composes the magnetic circuit should have high magnetic permeability and high magnetic saturation. A material with such properties is the AISI 1010, which is a low-carbon steel (C% < 0.10). This material though, is hardly available because of is being used for niche applications. Hence the AISI 430 was used. AISI 430 is a ferritic stainless steel with a high relative magnetic permeability, of about 600.

2 Analytical design of MR damper

Figure 5 shows the forces involved for a magnetorheological damper [18, 19]. Considering the parallel-plate Bingham model the forces can be decomposed into three contributes (6)[20]. First, the controllable force F_τ (Equation 4) directly correlated to the magnetic field applied through the yield stress τ_B.

$$F_\tau = c\frac{\tau_B L_P A_A}{h} sign(V_D) \tag{4}$$

where L_P is the axial activation length of the piston head, A_A is the annular piston's area, h is the fluid gap and c is a coefficient that depends on the volumetric flow rate, the viscosity and the yield stress. Second, F_η, Eq. 5, represents the viscous forces and depends on the length of the orifice, the fluid's viscosity and flow rate.

$$F_\eta = k\frac{12\eta Q L A_A}{wh^3} \tag{5}$$

where Q is the flow rate, L is the total axial length of the piston head, w is the mean circumference of the damper's annular flow path and k is a constant depending on the volumetric flow rate and the velocity. Third, F_f that stands for the friction forces like those related to the seals system. Moreover we should also account for the force derived from the effect of pressure F_P. Hence, the total force will be obtained by adding up all these contributions:

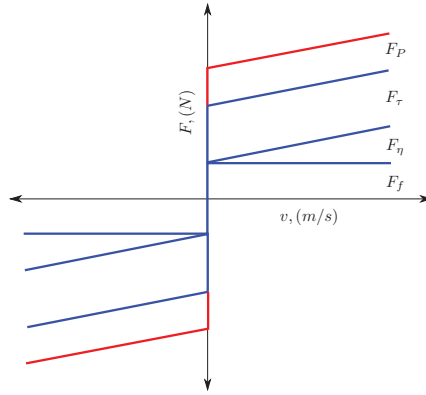$$F_{tot} = F_\tau + F_\eta + F_f \tag{6}$$

Figure 5. Force decomposition of MRD.

The Dynamic Range is a fundamental parameter which provides an estimates of the influence of the control variable on the system behaviour. D can be calculated as the controllable forces divided by the uncontrollable forces (Equation 7).

$$D = \frac{F_c}{F_{unc}} = \frac{F_\tau + F_\eta + F_f}{F_\eta + F_f} \tag{7}$$

2 Design of the magnetic circuit

The aim in the design of a magnetic circuit is to determine the necessary amp-turn (NI) able to develop the required magnetic field and therefore the required damping forces. An optimal design requires to reach the desired magnetic field induction in the fluid gap while minimize the energy lost in steel flux conduit and region of non-working area. The entire circuit should have low reluctance, so soft iron or high permeability steel should be used. At high flux density, the iron may saturate, and be a limiting factor, so the cross-section of the iron must be adequate all around the magnetic circuit. The total flux in the circuit is the same at all sections around the circuit, so the critical point of the iron is the part with the lower cross-sectional area. The number of coils may vary to meet system requirements. Figure 6(a) shows the most common configuration in which the flux lines flow around a single coil. The last two configurations in Figure 6 have multiple coils and similar characteristics, except for the polarity of the magnetic field. In configuration Figure 6(b), the magnetic flux lines have all one only direction from the center of the solenoid. In configuration Figure 6(c), there is a trade-off between the different coils, which also affects the circuit length. The main advantage of this solution is a decrease of the overall inductance of the circuit that allows, compared to other, less response time of the same device.

The typical design process for a magnetic circuit can be summarize as follow [13]:

- Determine the magnetic induction B_{mrf} in the MR fluid to give the desired yield stress τ_B.

- Using the B-H relationship of the fluid, determine the magnetic field intensity H_{mrf}.
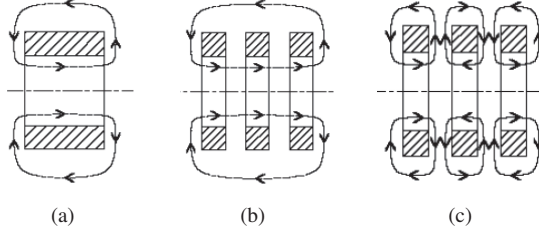
Figure 6. Coil configurations. Single coil (a), coherent multiple coils (b), incoherent multiple coils (c).

- The magnetic induction flux is given by $\Phi = B_{mrf} A_{mrf}$, where A_{mrf} is the effective area of activation of the fluid. Since the magnetic induction flux remains constant through all the circuit length, the magnetic induction in the steel B_{steel} is given by:

$$B_{steel} = \frac{\Phi}{A_{steel}} = \frac{B_{mrf} A_{mrf}}{A_{steel}} \tag{8}$$

- Determine the magnetic field induction B_{steel} using its B-H relationship.

- By using Kirchoff's Law of magnetic circuits, the required number of amp-turns (NI) is:

$$NI = \sum H_i L_i = H_{mrf} h + H_{steel} L \tag{9}$$

where h is the fluid gap and L the single length of each links which compose the circuit.

3 Magnetic finite element method analysis

After the analytical design of the magnetic circuit a magnetic finite element analysis was performed. This operation is a useful method to compare the calculated values with the simulated ones. Furthermore, these simulations allow one to verify that the magnetic saturation will not occur in every section of the magnetic circuit. The software FEMM $v4.2$ [21] was adopted to perform all the simulations. Figure 7(a) represents the discretized axisymmetric model of the magnetic circuit which comprehend part of the piston head, the flange and the cylinder's wall. The material chosen came from the FEMM material library. AISI 430 was used for the piston head and the flange. Since the real material of the cylinder which is FE 510 is not included in the library, the closest material in terms of magnetic properties is the AISI 1020. For the MR fluids, a new material was set up whit the magnetic properties described by Equation 2. Figure 7(b) shows the path and the values of the magnetic field density resulted whit a working current of 1 A. As it can be seen the values of B are lower than 1.2 T. At the beginning of the design, considering the force required and a current of 1 A, a yield stress $\tau_B = 20kPa$ is needed. That implies a magnetic field of $B_{MRF} = 300$ mT along the activation area. Figure 7(e) depicts the values of B through the red line in the activation gap (Figure 7(c)). The simulated values are lower than those obtain from the analytical calculation probably because AISI 430 was considered even for the cylinder.
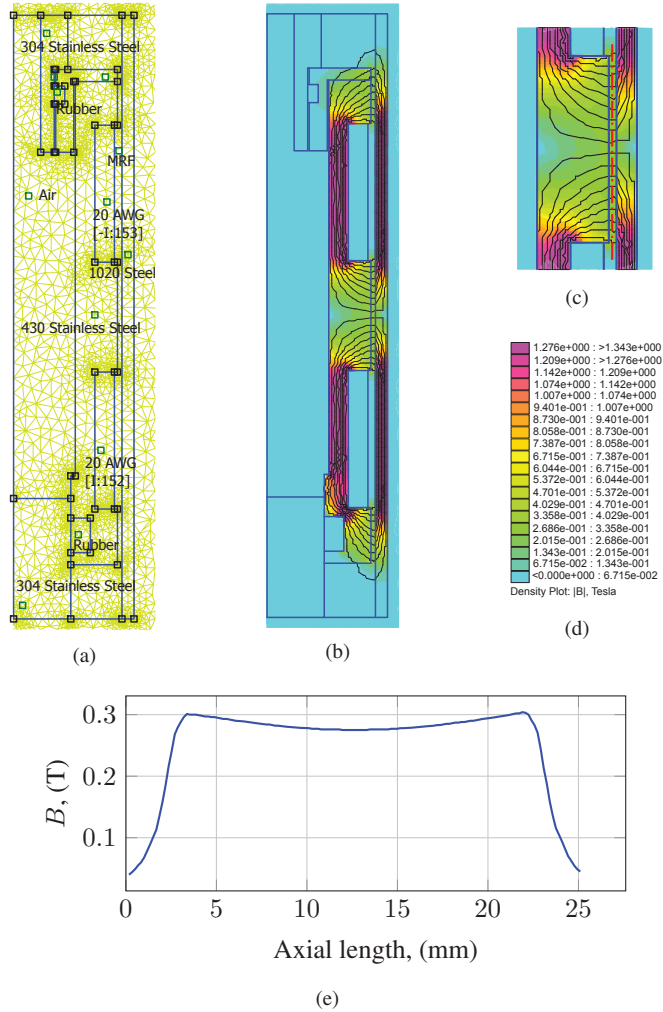
Figure 7. 2D FEMM model of the piston head (a), magnetic field values (b) and graph of the magnetic field across the central activation gap along the red line (c)(d).

4 PRESSURIZATION SYSTEM

The aim of the pressurization system is the active regulation of the fluid pressure. This task has to be done in a totally controllable manner without the aid of volumetric pumps, which are incompatible with MR fluids because of the too high viscosity. Moreover, in hydraulic centralized circuits that use volumetric pumps the pressure regulation is quite expensive in terms of energy required because both the circuit and the control unit have to be constantly working in order to maintain the desired pressure. Contrarily, the new system presented does not need a continuous supply of electrical power. The designed pressurization system is schematically shown in Figure 8. The system is composed of a stepper motor that converts the motion from rotary to translatory by a screw and nut mechanism. This system controls
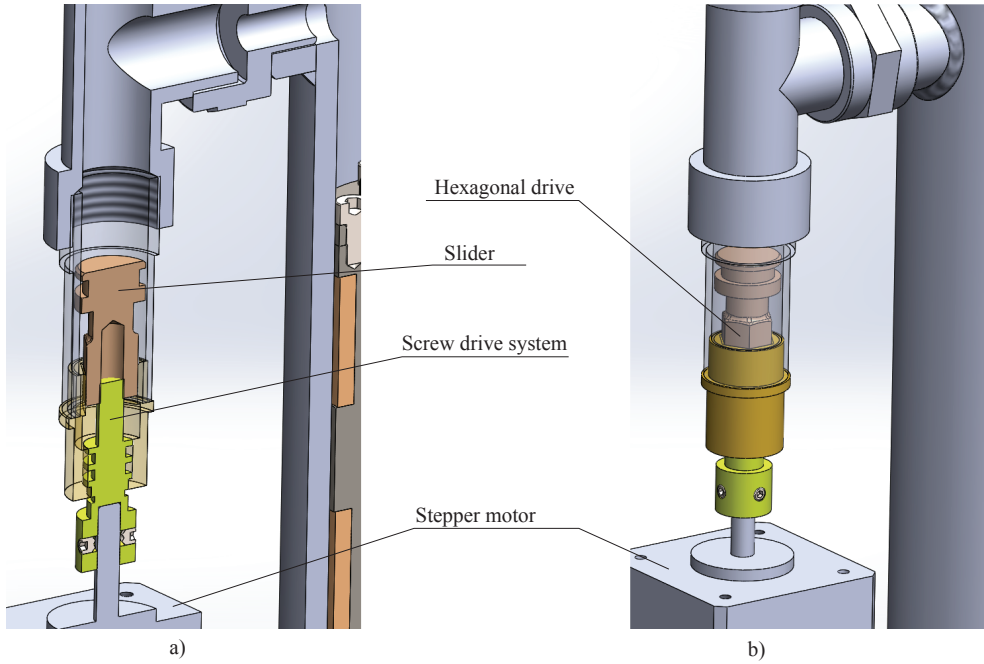
Figure 8. Pressurization system. Low pressure configuration (a) and high pressure configuration (b).

a slider that insists on the volume of MR fluid. Lowering the volume of fluid causes an increase of the internal pressure. Such system would be energetically convenient compared with other linear actuators currently present on market, for example coil valves. Indeed, due to the friction forces between the threads there is no retrograde motion. Hence, the desired static pressure level can be maintained with no power consumption. The MR fluid used is a silicone-based fluid that is quite compressible (bulk modulus β of about 1000 MPa) so a pressure control not excessively abrupt is allowed. Considering the low compressibility of the fluid, varying the value of pressure requires slider's strokes of few millimeters. The stroke of the slider is calculated analytically knowing the bulk modulus β, the total volume of the fluid V and the desired pressure variation. The equations involved are:

$$\beta = -\frac{\Delta P}{\Delta V}V \tag{10}$$

$$\Delta V = -\frac{V}{\beta}\Delta P \tag{11}$$

$$\Delta x = \frac{V}{A_{cu}\beta}\Delta P \tag{12}$$

in which A_{cu} is the area of the slider. Stepper motors are the most suitable for this application. By knowing the number of steps and the screw pitch an accurate control of the slider's stroke Δx is possible without position sensor.

5   RESULTS AND DISCUSSION

Figure 9 shows the section of the 3D model of the damper. To allow the assembly, the piston head is composed of two parts: the main body of the piston head and the flange. The flange connects the piston head to the upper-rod using four screws M 4x6. Particular attention was paid for the sealing system. A dynamic rod seal was used between the bottom part of the piston head and the bottom rod. Moreover, two static seal (O-Ring) were adopted between the flange and the inner chamber of the piston head. As it can be seen in Figure 10, the coil wires pass through the drilled screw, the flange and the rod.

The end-plug and the bottom-rod were glued to the cylinder using an acrylic adhesive (LOCTITE 638). The MR fluid was poured through the welded boss into the cylinder. To eliminate the air into the damper, the system was placed in a vacuum chamber. Then, two ball joint ends were screwed to the rod and the end plug (Figure 11).
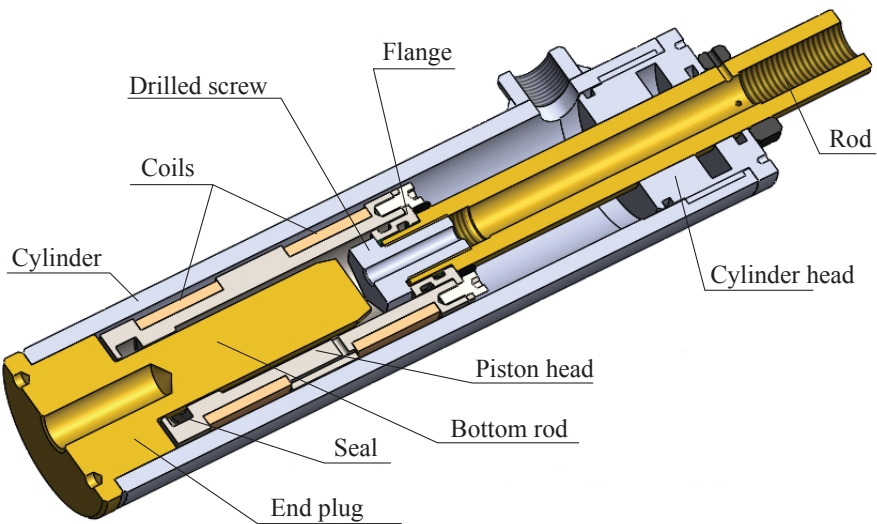

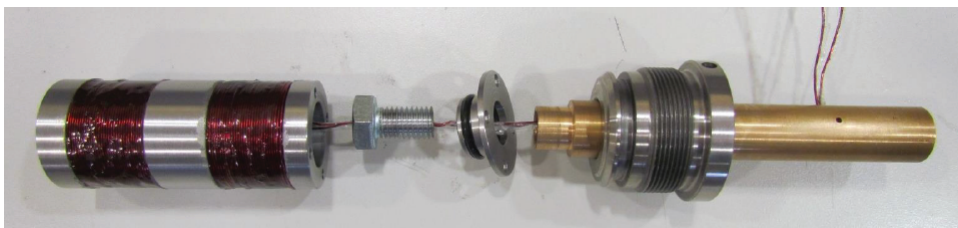**Figure 9.** Cross-sectional view of the prototype of the damper.

Figure 10. Exploded view. (From the right) Piston head, drilled screw, flange, rod and cylinder head.

Figure 11. Final assembled prototype.

6   CONCLUSION

This work shows a design method for a magnetorheological damper with pressure control. By means of analytical equations the magnetic circuit and the hydraulic circuit have been designed. The new MR damper has an innovative architecture able to drive the internal pressure level. A bottom-rod has been adopted which has the same diameter of the upper rod. The main consequence is that the internal volume of the damper remains constant during the operation and an accumulator is no more needed. In order to increase the feasibility of the prototype, commercial components were used: a hydraulic cylinder, its cylinder head and two ball joint ends. Instead, the piston rod, the piston head and the bottom rod were designed and manufactured. Finally, all components were assembled paying particular attention to the concentricity between the cylinder, the piston head and the bottom rod. A conceptual design of pressurization system has also been presented. Such system consists of a screw drive mechanism that controls the stroke of a slider. Moving the slider leads to control the internal volume of the damper and consequently changes the internal pressure. To our best knowledge the prototype presented is the first of its kind ever realized. Several tests will be carried out to test the behavior of this device. The results might bring up new considerations that could lead to an optimization of the properties of the damper and to its commercialization.

REFERENCES

[1] S. Kaluvan, S-B Choi, 2014. "Design of current sensor using a magnetorheological fluid in shear mode". *Smart Materials and Structures*, 23(12):127003.

[2] M. S. Alkan, H. Gurocak, and B. Gonenc, 2013. "Linear magnetorheological brake with serpentine flux path as a high force and low off-state friction actuator for haptics". *Journal of Intelligent Material Systems and Structures*, 24(14):1699-1713.

[3] P. Yadmellat and M.R. Kermani, 2014. "Adaptive Modeling of a Magnetorheological Clutch". *IEEE/ASME Transactions on Mechatronics*, 19(5):1716-1723.

[4] X. Zhu, X. Jing, and L. Cheng, 2012. "Magnetorheological fluid dampers: A review on structure design and analysis". *Journal of Intelligent Material Systems and Structures*, 23(8):839-873.

[5] A. Fuchs, A. Rashid, Y. Liu, B. Kavlicoglu, H. Sahin, and F. Gordaninejad, 2010. "Compressible magnetorheological fluids". *Journal of Applied Polymer Science*, 115(6):3348-3356.

[6] A. Spaggiari and E. Dragoni, 2011. "Effect of Internal Pressure on Flow Properties of Magnetorheological Fluids", *In ASME 2011 Conference on Smart Materials, Adaptive Structures and Intelligent Systems, Volume 1, pages 7-15.*

[7] A. Spaggiari and E. Dragoni, 2012. "Effect of pressure on the physical properties of magnetorheological fluids", *Fracture and Structural Integrity*, (23):Pages 75-86.

[8] A. Spaggiari and E. Dragoni, 2013. "Combined squeeze-shear properties of magnetorheological fluids: Effect of pressure", *Journal of Intelligent Material Systems and Structures*, 25(9):1041-1053.

[9] A. C. Becnel and N. M. Wereley, 2013. "Demonstration of Combined Shear and Squeeze Strengthening Modes in a Searle-Type Magnetorheometer", *Volume 1: Development and Characterization of Multifunctional Materials; Modeling, Simulation and Control of Adaptive Systems; Integrated System Design and Implementation*, page V001T03A036.

[10] X. Tang, X. Zhang, R. Tao, and Y. Rong, 2000. "Structure-enhanced yield stress of magnetorheological fluids", *Journal of Applied Physics*, 87(5):2634.

[11] C. Guo, X. Gong, S. Xuan, L. Qin, and Q. Yan., 2013. "Compression behaviors of magnetorheological fluids under nonuniform magnetic field", *Rheologica Acta*, 52(2):165-176.

[12] Q-H, N. Choi and Seung-Bok, 2012. "Optimal Design Methodology of Magnetorheological Fluid Based Mechanisms", *InTech*.

[13] H. Gavin, J. Hoagg, and M. Dobossy, 2001. "Optimal design of MRF dampers", *U.S. - Japan Workshop on Smart Structures for Improved Seismic Performance in Urban Regions*, number August, pages 225-236.

[14] LORD Corporation. MRF-140CG Magnetorheological fluid, 2001. Technical Datasheet: http://www.lordfulfillment.com/upload/DS7012.pdf, (accessed 20 Feb 2015).

[15] J.D. Carlson, 2008. "Magnetorheological fluids", *Smart Materials*, CRC Press, New York.

[16] J-H. Lee, C. Han, D. Ahn, J. K. Lee, S-H. Park, and S. Park, 2013. "Design and performance evaluation of a rotary magnetorheological damper for unmanned vehicle suspension systems", *The Scientific World Journal*, 2013:894016.

[17] N. M. Wereley, 2013. "Magnetorheology: Advances and Applications", *Royal Society of Chemistry*.

[18] K-I. Jang, B-K. Min, and J. Seok, 2011. "A behavior model of a magnetorheological fluid in direct shear mode", *Journal of Magnetism and Magnetic Materials*, 323(10):1324-1329.

[19] G. Yang, 2001. "Large-scale magnetorheological fluid damper for vibration mitigation: modeling, testing and control", PhD thesis, University of Notre Dame.

[20] G. Yang, B.F. Spencer, J.D. Carlson, and M.K. Sain, 2002. "Large-scale MR fluid dampers: modeling and dynamic performance considerations", *Engineering Structures*, 24(3):309-323.

[21] D. Meeker. FEMM 4.2 - Finite Element Method Magnetics, www.femm.info/wiki/HomePage, (accessed 19 Jen 2015).

CHATTER STABILITY ANALYSIS OF HIGH SPEED MACHINING BY MEANS OF SPECTRAL DECOMPOSITION MODELING

Antonio Carminelli
Department of Mechanical and Aeronautical Engineering,
University of Bologna, Italy
E-mail: antonio.carminelli@ unibo.it

Giuseppe Catania
Department of Mechanical and Aeronautical Engineering,
University of Bologna, Italy
E-mail: giuseppe.catania@unibo.it

Abstract. *A technique to study the stability of high speed milling machining process and the chatter vibration is proposed. The equation of motion of a one degree of freedom (dof) model of the milling machine-tool system is considered. The system is described by means of a linear, ordinary, time dependent parameter, Periodic Delay Differential Equation (PDDE). A spectral decomposition is applied to the solution variable, and a generalized harmonic balance technique is then applied, so that a linear, ordinary, constant parameter, PDDE is obtained. Solution instability, associated to the occurrence of chatter vibration during milling, is evaluated by solving a non standard eigenvalue problem. A numerical example is presented in order to test the proposed approach. Both the well known Semi-Discretization (SD) method and the time solution obtained by means of direct integration of the original equation are used as a reference to validate the proposed technique.*
Strengths and limits of the proposed approach are critically discussed and compared with the SD method.

Keywords: chatter, milling, PDDE, spectral decomposition

1. INTRODUCTION

High speed milling machining is required when high levels of productivity are to be dealt with, but critical working conditions may easily arise. In many applications the appearance of chatter vibrations may become a limiting factor. Chatter vibration is a self-excited high amplitude oscillation of the tool originating from a loss of stability of the milling operation. The prevision and control of the chatter occurrence may avoid rapid tool wear and break and unacceptable workpiece condition due to poor surface finish. Moreover, the life of the cutting tools and machine components can be longer if chatter vibrations are minimized. Therefore, a method to effectively and efficiently predict the system stability is needed in order to choose the optimal cutting parameters, such as the spindle speed and the depth of cut.

A well known and accepted cutting model for milling operations was introduced by Altintas [1] and experimentally validated in [2]. The interrupted nature of the cutting force, since each tooth engages and leaves the workpiece, is taken into account by means of

periodic coefficients, considering a constant spindle speed. A delay term is introduced in order to model the regenerative effect of the cutting force. The resulting model is a set of PDDEs for which a closed form solution for studying the stability conditions is unknown [3]. Several numerical methods to study the stability of PDDEs were proposed [3-7,12]. Among them the SD method is well known and tested. It is based on the Floquet theory [8] that, originally developed for studying the stability of periodic differential equations, was extended to PDDEs [9-10]. In the SD method the stability properties of DDEs are mapped by approximating the monodromy operator of the system by means of a transition matrix so that the related infinite-dimensional eigenvalue problem is transformed into an approximate finite dimensional one. In practical application, models with a large number of dofs are employed and the dimension of the eigenvalue problem can become very large [11], so that the SD algorithm could not be suited for real time diagnostic application.

A method to study the stability of a high speed milling machining process is presented in this paper. The proposed method is based on a spectral decomposition technique [13] and the stability of the model is studied by solving a non standard eigenvalue problem. A numerical example is shown in order to test the proposed approach and a comparison with the SD method is carried out.

2. SINGLE DOF MILLING SYSTEM

The equation of motion of the 1-dof milling model is considered [1]:

$$\ddot{x}(t) = -2\zeta\omega_n \dot{x}(t) - \omega_n^2 x(t) - \frac{w}{m} h(t) \left[x(t) - x(t-\tau) \right] - \frac{w f}{m} h(t) \tag{1}$$

where:

$$h(t) = \sum_{j=1}^{N} \sin\varphi_j \left[K_t \cos\varphi_j + K_n \sin\varphi_j \right] g(\varphi_j) \tag{2}$$

$$\varphi_j(t) = \Omega t + j \frac{2\pi}{N} \tag{3}$$

$$g(\varphi_j(t)) = \begin{cases} 1 & if\ \varphi_{IN} \leq \varphi_j(t) \leq \varphi_{EX} \\ 0 & otherwise \end{cases} \tag{4}$$

The parameter nomenclature is reported in Tab.1. The φ_{IN} and φ_{EX} angle in case of down-milling cutting are:

$$\varphi_{ST} = \arccos\left(2\frac{a}{D} - 1 \right) \tag{5}$$

$$\varphi_{EX} = \pi$$

Eq.(1) can be expressed in $\mathbf{z} = \{x \quad \dot{x}\}^T$ state-space as:

$$\dot{\mathbf{z}}(t) = \mathbf{A}(t)\,\mathbf{z}(t) + \mathbf{B}(t)\,\mathbf{z}^\tau\ ; \qquad where\ f^\tau = f(t-\tau) \tag{6}$$

Tab.1 Description of the adopted symbols

Symbol	Definition
N	number of cutters
ω_n	natural frequency
$\overline{m}$	modal mass
ζ	modal damping
τ	time delay
K_t	tangential cutting force coefficient
K_n	normal cutting force coefficient
a/D	radial depth of cut ratio
f	feed rate
w	axial depth of cut
Ω	spindle speed
ω	fundamental frequency

3. THE SEMI-DISCRETIZATION METHOD

The time interval τ is sampled with m uniform lenght $\Delta t = \tau/m$ intervals $[t_i, t_{i+1}[$, $i=0, 1,\dots,m-1$, where $\Delta t = t_{i+1} - t_i$. On the i-th interval the equation is approximated with:

$$\dot{\mathbf{z}} = \mathbf{A}_i \mathbf{z} + \mathbf{B}_i \mathbf{z}_i^\tau \tag{7}$$

where [5]:

$$\mathbf{A}_i = \frac{1}{\Delta t} \int_{t_i}^{t_{i+1}} \mathbf{A}(t)\, dt \tag{8}$$

$$\mathbf{B}_i = \frac{1}{\Delta t} \int_{t_i}^{t_{i+1}} \mathbf{B}(t)\, dt \tag{9}$$

$$\mathbf{z}_i^\tau = \frac{\mathbf{z}_{i-m} + \mathbf{z}_{i-m+1}}{2} \tag{10}$$

$$\mathbf{z}_i = \mathbf{z}(t_i) \tag{11}$$

The following approximate solution is used on each interval:

$$\mathbf{z}(t) = e^{\mathbf{A}_i(t-t_i)}\left(\mathbf{z}_i + \mathbf{A}_i^{-1}\mathbf{B}_i\mathbf{z}_i^\tau\right) - \mathbf{A}_i^{-1}\mathbf{B}_i\mathbf{z}_i^\tau \tag{12}$$

Evaluating the solution for $t=t_{i+1}$ yields:

$$\mathbf{z}_{i+1} = \mathbf{E}_i \mathbf{z}_i + \frac{1}{2}\mathbf{H}_i \mathbf{z}_{i-m+1} + \frac{1}{2}\mathbf{H}_i \mathbf{z}_{i-m} \tag{13}$$

where:

$$\mathbf{E}_i = e^{\mathbf{A}_i \Delta t} \tag{14}$$

and

$$\mathbf{H}_i = \left(e^{\mathbf{A}_i \Delta t} - \mathbf{I}\right)\mathbf{A}_i^{-1}\mathbf{B}_i \tag{15}$$

By defining:

$$\mathbf{d}_i = \left\{ \begin{array}{c} \mathbf{z}_i \\ \vdots \\ \mathbf{z}_{i-m} \end{array} \right\} \tag{16}$$

(where $\mathbf{d}_i$ is a $\bar{N} = \bar{n}(m+1)$ dimensional vector, with $\bar{n}$ being the dimension of the $\mathbf{z}_i$ vector) a discrete map can be defined from time t_i to t_{i+1}

$$\mathbf{d}_{i+1} = \mathbf{\Phi}_i \mathbf{d}_i \tag{17}$$

where:

$$\mathbf{\Phi}_i = \begin{bmatrix} \mathbf{E}_i & \mathbf{0} & \mathbf{0} & \cdots & \frac{1}{2}\mathbf{H}_i & \frac{1}{2}\mathbf{H}_i \\ \mathbf{I} & \mathbf{0} & \mathbf{0} & \cdots & \mathbf{0} & \mathbf{0} \\ \mathbf{0} & \mathbf{I} & \mathbf{0} & \cdots & \cdots & \mathbf{0} \\ \vdots & \cdots & \ddots & \cdots & \vdots & \vdots \\ \mathbf{0} & \cdots & \mathbf{0} & \mathbf{I} & \mathbf{0} & \mathbf{0} \\ \mathbf{0} & \cdots & \cdots & \mathbf{0} & \mathbf{I} & \mathbf{0} \end{bmatrix} \tag{18}$$

$$\mathbf{d}_m = \mathbf{\Phi}_{m-1}\mathbf{\Phi}_{m-2}\cdots\mathbf{\Phi}_0 \cdot \mathbf{d}_0 = \mathbf{\Phi} \cdot \mathbf{d}_0 \tag{19}$$

where $\mathbf{\Phi}$ is an approximation of the transition matrix Ψ, relating $\mathbf{d}_0$ and $\mathbf{d}_m$.

In order to analyze the system stability properties, the eigenvalue problem:

$$\left(\mathbf{\Phi} - \lambda\mathbf{I}\right)\mathbf{v} = \mathbf{0} \tag{20}$$

has to be solved. The system in unstable if at least one of the eigenvalues of the $\mathbf{\Phi}$ matrix has norm greater than one.

4. SPECTRAL DECOMPOSITION METHOD

Eq.(1) is a linear delay differential equation with time-varying periodic coefficients. Solution $x(t)$ is approximated by means of Eq.(21), with L time-varying coefficients d_k and orthogonal functions p_k:

$$x(t) = \sum_{k=1}^{L} d_k(t) p_k(t) \tag{21}$$

$$x^\tau(t) = \sum_{k=1}^{L} d_k^\tau(t) p_k(t-\tau) \tag{22}$$

$$d_k^\tau(t) = d_k(t-\tau) \tag{23}$$

Eq.(1) is then multiplied by $p_k(t) \cdot C_k$ and integrated on [0,T],

$$C_k \int_0^T \ddot{x}(t) p_k(t) dt = C_k \int_0^T F\left(\dot{x}(t), x(t), x(t-\tau), t\right) p_k(t) dt \tag{24}$$

With the hypothesis that $d_k(t)$ varies slowly on [0,T] the following approximate result is obtained:

$$\ddot{\mathbf{d}} = \mathbf{R} \begin{bmatrix} \mathbf{d} \\ \dot{\mathbf{d}} \end{bmatrix} + \mathbf{S}\, \mathbf{d}^\tau + \mathbf{Q} \tag{25}$$

where:

$$\mathbf{d} = \begin{bmatrix} d_1 \\ \vdots \\ d_L \end{bmatrix} \;;\qquad \mathbf{d}^\tau = \begin{bmatrix} d_1^\tau \\ \vdots \\ d_L^\tau \end{bmatrix} \tag{26}$$

and the coefficients in the $\mathbf{R}$, $\mathbf{S}$ and $\mathbf{Q}$ matrices are time-stationary.
The following system of equations can be obtained as well:

$$\dot{\mathbf{z}} = \mathbf{U}\mathbf{z} + \mathbf{V}\mathbf{z}^\tau + \begin{bmatrix} \mathbf{0} \\ \mathbf{Q} \end{bmatrix} \tag{27}$$

where:

$$\dot{\mathbf{z}} = \begin{bmatrix} \dot{\mathbf{d}} \\ \ddot{\mathbf{d}} \end{bmatrix} \qquad \mathbf{z} = \begin{bmatrix} \mathbf{d} \\ \dot{\mathbf{d}} \end{bmatrix} \qquad \mathbf{z}^\tau = \begin{bmatrix} \mathbf{d}^\tau \\ \dot{\mathbf{d}}^\tau \end{bmatrix} \tag{28}$$

Stability

The homogeneous side of Eq.(27) is considered for stability evaluation:

$$\dot{\mathbf{z}}(t) = \mathbf{U}\mathbf{z}(t) + \mathbf{V}\mathbf{z}^{\tau} \tag{29}$$

After Laplace transforming, null initial conditions:

$$s\mathbf{Z} = \mathbf{U}\mathbf{Z} + \mathbf{V}\mathbf{Z}e^{-s\tau} \tag{30}$$

the following eigenproblem can be obtained:

$$\left[s\mathbf{I} - \left(\mathbf{U} + \mathbf{V}e^{-s\tau} \right) \right]\mathbf{Z} = \mathbf{0} \tag{31}$$

The eigenproblem is solved by means of an iterative technique, where at the first step the following standard eigenproblem is solved:

$$\left[s_0\mathbf{I} - \left(\mathbf{U} + \mathbf{V} \right) \right]\mathbf{Z}_0 = \mathbf{0} \tag{32}$$

where s_0 is the smallest eigenvalue in norm and $\mathbf{Z}_0$ its associated eigenvector.

The following matrix is defined at the *k-th* step ($k=1,\dots$):

$$\mathbf{C}_k = \left(s_{k-1}\mathbf{I} - \mathbf{U} - \mathbf{V}e^{-\tau s_{k-1}} \right)^{-T} \tag{33}$$

and the approximation at the *k-th* step of eigenvector is:

$$\mathbf{Z}_k = \frac{C_k\mathbf{Z}_{k-1}}{\left\| C_k\mathbf{Z}_{k-1} \right\|} \tag{34}$$

and of the eigenvalue:

$$s_k = \frac{\mathbf{Z}_k^H C_k \mathbf{Z}_k}{\left\| \mathbf{Z}_k^H \mathbf{Z}_k \right\|} \tag{35}$$

The iteration is stopped when:

$$\left\| s_k - s_{k-1} \right\| < \varepsilon \tag{36}$$

where ε is a user defined error tolerance.

A shifting technique [14] is used in order to obtain an eigenvalue near a starting point. The technique showed to be robust, converging in a few iterations in the application test reported in this paper.

Application to the 1-dof milling model

A spectral decomposition with 2n+1 time-varying coefficients and the function set $p = \left\{ 1, \cos(\omega t), \sin(\omega t), \cos(2\omega t), \sin(2\omega t), \cdots, \cos(n\omega t), \sin(n\omega t) \right\}$ is considered:

$$x(t) = a_0(t) + \sum_{k=1}^{n} \left[b_k(t)\cos(k\omega t) + c_k(t)\sin(k\omega t) \right] \tag{37}$$

$$x^{\tau}(t) = a_0^{\tau}(t) + \sum_{k=1}^{n} \left[b_k^{\tau}(t) \cos(k\omega(t-\tau)) + c_k^{\tau}(t) \sin(k\omega(t-\tau)) \right] \quad (38)$$

$$
\begin{aligned}
a_0^{\tau}(t) &= a_0(t-\tau) \\
b_k^{\tau}(t) &= b_k(t-\tau) \\
c_k^{\tau}(t) &= c_k(t-\tau)
\end{aligned}
\quad (39)
$$

Eqs.(38-39) are used in Eq.(1): 2n+1 equations can be obtained as explained at the beginning of Section 4. The first equation can be obtained after integration of Eq.(1) on [0,T] multiplied per 1/T:

$$\frac{1}{T}\int_0^T \ddot{x}(t)\,dt = \frac{1}{T}\int_0^T \left\{ -2\zeta\omega_n \dot{x}(t) - \omega_n^2 x(t) - \frac{w}{m} A(t)\left[x(t) - x(t-\tau) \right] - \frac{wf}{m} A(t) \right\} dt \, . \quad (40)$$

and from Eqs.(37-40):

$$\ddot{a}_0 = -2\zeta\omega_n \dot{a}_0 - \left(\omega_n^2 + \frac{wA_I}{mT} \right) a_0 - \frac{w}{mT}\left(\mathbf{B}^T\mathbf{b} + \mathbf{C}^T\mathbf{c} + \mathbf{B}^{\tau T}\mathbf{b}^{\tau} + \mathbf{C}^{\tau T}\mathbf{c}^{\tau} \right) + \frac{wA_I}{mT}\left(a_0^{\tau} - f \right) \quad (41)$$

where:

$$\mathbf{b} = \begin{bmatrix} b_1 \\ \vdots \\ b_k \\ \vdots \\ b_n \end{bmatrix} \qquad \mathbf{c} = \begin{bmatrix} c_1 \\ \vdots \\ c_k \\ \vdots \\ c_n \end{bmatrix} \qquad \mathbf{b}^{\tau} = \begin{bmatrix} b_1^{\tau} \\ \vdots \\ b_k^{\tau} \\ \vdots \\ b_n^{\tau} \end{bmatrix} \qquad \mathbf{c}^{\tau} = \begin{bmatrix} c_1^{\tau} \\ \vdots \\ c_k^{\tau} \\ \vdots \\ c_n^{\tau} \end{bmatrix} \quad (42)$$

$$\mathbf{B} = \begin{bmatrix} B_1 \\ \vdots \\ B_k \\ \vdots \\ B_n \end{bmatrix} \qquad \mathbf{B}^{\tau} = \begin{bmatrix} B_1^{\tau} \\ \vdots \\ B_k^{\tau} \\ \vdots \\ B_n^{\tau} \end{bmatrix} \qquad \mathbf{C} = \begin{bmatrix} C_1 \\ \vdots \\ C_k \\ \vdots \\ C_n \end{bmatrix} \qquad \mathbf{C}^{\tau} = \begin{bmatrix} C_1^{\tau} \\ \vdots \\ C_k^{\tau} \\ \vdots \\ C_n^{\tau} \end{bmatrix} \quad (43)$$

$$A_I = \int_0^T A(t)\,dt$$

$$B_k = \int_0^T A(t)\cos(k\omega t)\,dt$$

$$B_k^\tau = \int_0^T A(t)\cos(k\omega(t-\tau))\,dt \qquad (44)$$

$$C_k = \int_0^T A(t)\sin(k\omega t)\,dt$$

$$C_k^\tau = \int_0^T A(t)\sin(k\omega(t-\tau))\,dt$$

The following n equations are obtained by applying the harmonic balance technique, i.e. by [0,T] integrating Eq.(1) multiplied by $\dfrac{2}{T}\cos(\overline{k}\,\omega t)$:

$$\frac{2}{T}\int_0^T \ddot{x}(t)\cos(\overline{k}\,\omega t)\,dt =$$
$$= \frac{2}{T}\int_0^T \left\{ -2\zeta\omega_n \dot{x}(t) - \omega_n^2 x(t) - \frac{w}{m}A(t)\big[x(t) - x(t-\tau) + f\big] \right\}\cos(\overline{k}\,\omega t)\,dt \qquad (45)$$

After substitution of Eq.(38-39) in Eq.(46):

$$\ddot{b}_{\overline{k}} = -2\overline{k}\,\omega\dot{c}_k + \left(\overline{k}^2\omega^2 - \omega_n^2\right)b_{\overline{k}} - 2\zeta\omega_n\left(\dot{b}_{\overline{k}} + \overline{k}\,\omega\dot{c}_k\right) +$$
$$- \frac{2w}{Tm}\left[B^{\overline{k}}a_0 + \mathbf{M}_{\overline{k}}\mathbf{b} + \mathbf{N}_{\overline{k}}\mathbf{c} - B^{\overline{k}}a_0^\tau - \mathbf{M}_{\overline{k}}^\tau\mathbf{b}^\tau - \mathbf{N}_{\overline{k}}^\tau\mathbf{c}^\tau + B^{\overline{k}}f \right] \qquad (46)$$

where:

$$\mathbf{M}_{\overline{k}} = \begin{bmatrix} M_{\overline{k}}^1 & \cdots & M_{\overline{k}}^k & \cdots & M_{\overline{k}}^n \end{bmatrix}$$
$$\mathbf{M}_{\overline{k}}^\tau = \begin{bmatrix} M^{\tau 1}_{\overline{k}} & \cdots & M^{\tau k}_{\overline{k}} & \cdots & M^{\tau n}_{\overline{k}} \end{bmatrix} \qquad (47)$$

$$\mathbf{N}_{\overline{k}} = \begin{bmatrix} N_{\overline{k}}^1 & \cdots & N_{\overline{k}}^k & \cdots & N_{\overline{k}}^n \end{bmatrix}$$
$$\mathbf{N}_{\overline{k}}^\tau = \begin{bmatrix} N^{\tau 1}_{\overline{k}} & \cdots & N^{\tau k}_{\overline{k}} & \cdots & N^{\tau n}_{\overline{k}} \end{bmatrix} \qquad (48)$$

$$M_{\overline{k}}^k = \int_0^T A(t)\cos(k\omega t)\cos(\overline{k}\,\omega t)\,dt$$

$$M^{\tau k}_{\overline{k}} = \int_0^T A(t)\cos(k\omega(t-\tau))\cos(\overline{k}\,\omega t)\,dt \qquad (49)$$

$$N_{\bar{k}}^{k} = \int_0^T A(t)\sin(k\omega t)\cos(\bar{k}\omega t)dt$$

$$N^{\tau k}_{\bar{k}} = \int_0^T A(t)\sin(k\omega(t-\tau))\cos(\bar{k}\omega t)dt \tag{50}$$

The last n equations are obtained by [0,T] integrating Eq.(1) multiplied by $\frac{2}{T}\sin(\bar{k}\omega t)$:

$$\frac{2}{T}\int_0^T \ddot{x}(t)\sin(\bar{k}\omega t)dt =$$

$$= \frac{2}{T}\int_0^T \left\{ -2\zeta\omega_n\dot{x}(t) - \omega_n^2 x(t) - \frac{w}{m}A(t)[x(t) - x(t-\tau) - f] \right\}\sin(\bar{k}\omega t)dt \tag{51}$$

After substitution of Eq.(38-39) in Eq.(52):

$$\ddot{c}_{\bar{k}} = 2\bar{k}\omega\dot{b}_{\bar{k}} + (\bar{k}^2\omega^2 - \omega_n^2)c_k - 2\zeta\omega_n(\dot{c}_{\bar{k}} - \bar{k}\omega b_{\bar{k}}) +$$

$$- \frac{2w}{Tm}\left[C^{\bar{k}}a_0 + \mathbf{P}_{\bar{k}}\mathbf{b} + \mathbf{Q}_{\bar{k}}\mathbf{c} - C^{\bar{k}}a_0^{\tau} - \mathbf{P}^{\tau}_{\bar{k}}\mathbf{b}^{\tau} - \mathbf{Q}^{\tau}_{\bar{k}}\mathbf{c}^{\tau} + C^{\bar{k}}f \right] \tag{52}$$

where:

$$\mathbf{P}_{\bar{k}} = \begin{bmatrix} \mathbf{P}^1_{\bar{k}} & \cdots & \mathbf{P}^k_{\bar{k}} & \cdots & \mathbf{P}^n_{\bar{k}} \end{bmatrix}$$

$$\mathbf{P}^{\tau}_{\bar{k}} = \begin{bmatrix} \mathbf{P}^{\tau 1}_{\bar{k}} & \cdots & \mathbf{P}^{\tau k}_{\bar{k}} & \cdots & \mathbf{P}^{\tau n}_{\bar{k}} \end{bmatrix} \tag{53}$$

$$\mathbf{Q}_{\bar{k}} = \begin{bmatrix} Q^1_{\bar{k}} & \cdots & Q^k_{\bar{k}} & \cdots & Q^n_{\bar{k}} \end{bmatrix}$$

$$\mathbf{Q}^{\tau}_{\bar{k}} = \begin{bmatrix} Q^{\tau 1}_{\bar{k}} & \cdots & Q^{\tau k}_{\bar{k}} & \cdots & Q^{\tau n}_{\bar{k}} \end{bmatrix} \tag{54}$$

$$P^k_{\bar{k}} = \int_0^T A(t)\cos(k\omega t)\sin(\bar{k}\omega t)dt$$

$$P^{\tau k}_{\bar{k}} = \int_0^T A(t)\cos(k\omega(t-\tau))\sin(\bar{k}\omega t)dt \tag{55}$$

$$Q^k_{\bar{k}} = \int_0^T A(t)\sin(k\omega t)\sin(\bar{k}\omega t)dt$$

$$Q^{\tau k}_{\bar{k}} = \int_0^T A(t)\sin(k\omega(t-\tau))\sin(\bar{k}\omega t)dt \tag{56}$$

Eq.(57) thus results:

$$\begin{Bmatrix} \ddot{a}_0 \\ \ddot{b} \\ \ddot{c} \end{Bmatrix} = R_1 \begin{Bmatrix} \dot{a}_0 \\ \dot{b} \\ \dot{c} \end{Bmatrix} + R_0 \begin{Bmatrix} a_0 \\ b \\ c \end{Bmatrix} + S \begin{Bmatrix} a_0^\tau \\ b^\tau \\ c^\tau \end{Bmatrix} + Q . \tag{57}$$

5. NUMERICAL EXAMPLE

The 1-dof milling model introduced in the previous sections is adopted in order to test the method. The parameter values adopted in the numerical example are listed in Tab.2. The SD method is used to obtain a stability diagram and, keeping constant the spindle speed Ω=6000 rpm, four test configurations (A,B,C,D) were selected (Fig.1) and analyzed, by varying the axial depth of cut w:

A): $w = 1$ mm   B): $w = 1.5$ mm
C:) $w = 2$ mm   D): $w = 3$ mm

Tab.2

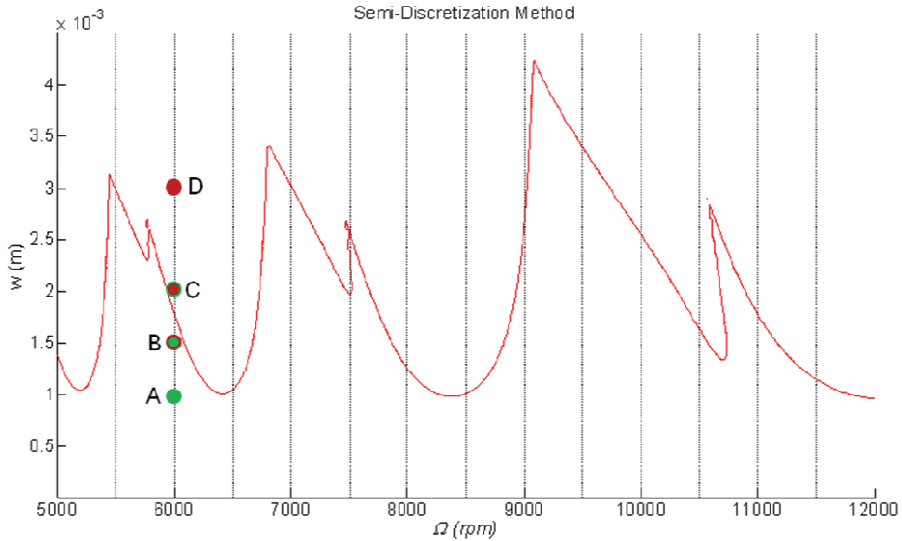| Symbol	Value
N	2
ω_n	922 Hz
$\overline{m}$	0.03993 kg
ζ	0.011
τ	$1/(N\,\Omega\,)$
K_t	$6 \cdot 10^8$ N/m^2
K_n	$2 \cdot 10^8$ N/m^2
a/D	0.1

Fig.1. Stability diagram obtained by means of the SD method.

The following parameters are used for the spectral decomposition:

$$T = 0.1 \text{ s}$$
$$\omega = 10 \text{ Hz}$$
$$n = 10$$

For each configuration, the time solution obtained by means of the spectral decomposition is compared with that obtained by means of direct integration of the Eq.(1) in Figs.2,4,6,8. Moreover Figs. 3,5,7,9 show the time-varying amplitude $Z_0 = |a_0|$ and the higher frequency amplitude $Z_k = \sqrt{b_k^2 + c_k^2}$, $k=1,...,n$. Configuration A ($w=1$ mm) is a stable configuration. Configurations B ($w=1.5$ mm) , C ($w=2$ mm) are close to the stability limit. Configuration D ($w=3$ mm) is an unstable configuration.
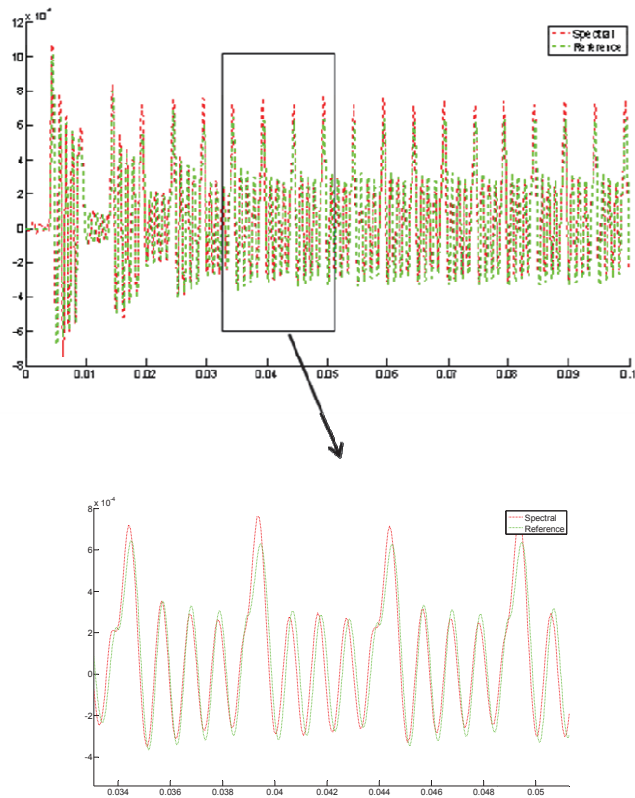

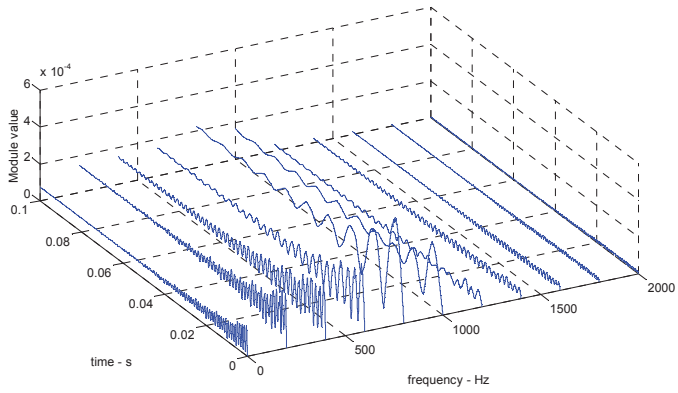
Fig.2. Time response comparison for configuration A.

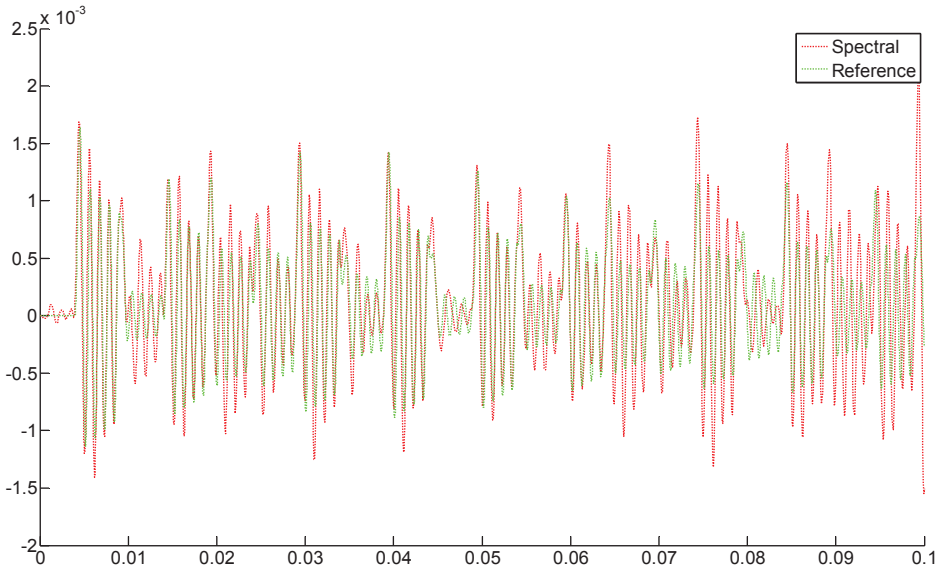Fig. 3. Time-varying amplitudes Z_k for configuration A.

Fig. 4. Time response comparison for configuration B.

Tab. 3 reports the real part of the smaller eigenvalue found by means of the proposed method.
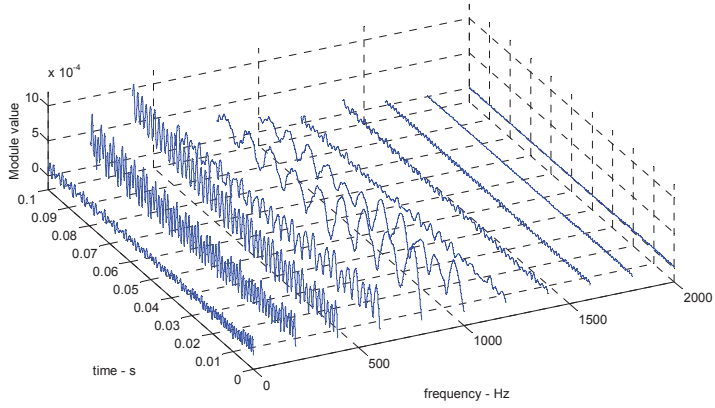
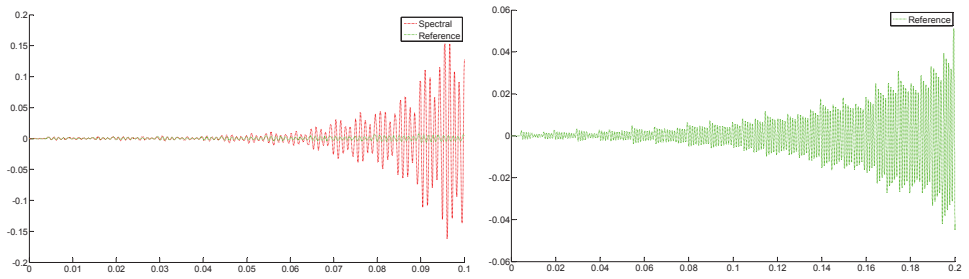Fig.5. Time-varying amplitudes Z_k for configuration B.

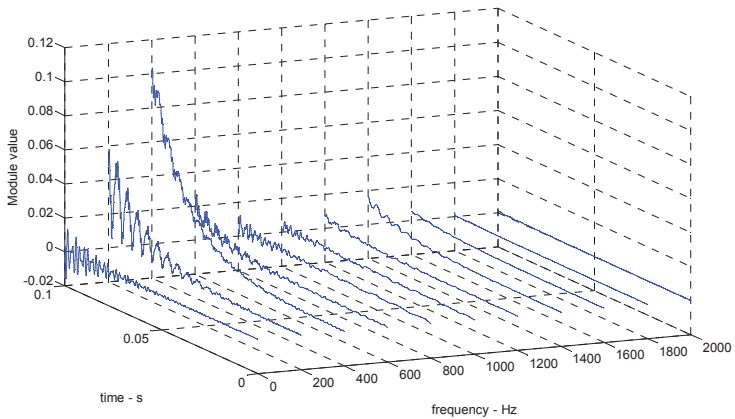Fig.6. Time response comparison for configuration C.

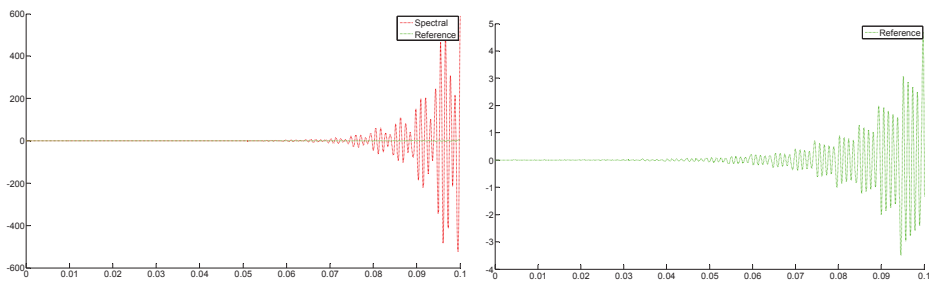Fig.7. Time-varying amplitudes Z_k for configuration C.

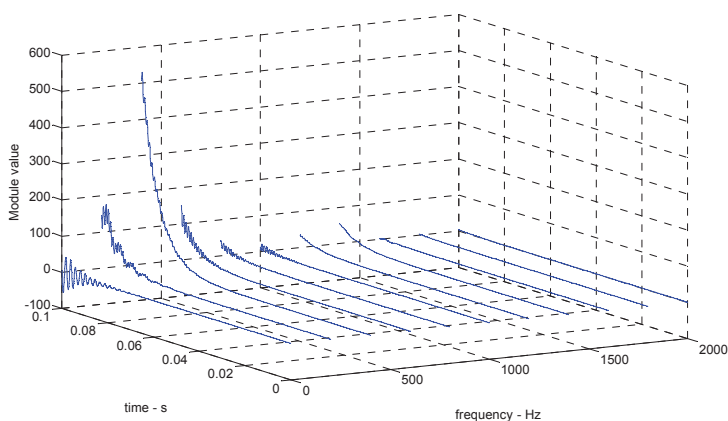Fig.8. Time response comparison for configuration D.

Fig.9. Time-varying amplitudes Z_k for configuration D.

Tab. 3

Condition	A	B	C	D
Real part of the smaller eigenvalue	-0.02	-0.05	0.02	0.06

6. CONCLUSIONS

A novel method to study the stability of high speed milling machining processes is presented in this paper. The proposed method is based on the spectral decomposition and the generalized harmonic balance technique. The stability of the model is studied by solving a non standard eigenvalue problem. The approximated model proposed showed that the stability characteristics of the original system is preserved. With respect to the well known SD technique, a lower computational cost is expected by using this proposed approach, since the solution of an eigenproblem of lower dimension is required, so that extension to n-dofs model problem can be more easily dealt with.

Future work will address the generalization of the method and its applications to a complete *n* dofs machine-spindle-tool model. Moreover the implementation of a sensitivity analysis for a real-time control procedure will be also considered.

Acknowledgements

REFERENCES

[1]   Altintas, Y., 2000. *Manufacturing Automation*, Cambridge University Press,.

[2]   Gradisek, J., et al.,2005. Mechanistic identification of specific force coefficients for a general end mill, *International Journal of Machine Tools and Manufacture,* **45**.

[3]   Insperger, T. and Stèpán, G., 2002. Semi-Discretization method for delayed systems, *International Journal for Numerical Methods in Engineering*, **55**; pp. 503-518

[4]   Mann, B.P. , Bayly, P.V., Davies, M.A. and Halley, J.E., 2003. Stability of interrupted cutting by temporal finite element analysis, *Journal of Manufacturing Science and Engineering*, **125**.

[5]   Insperger, T. and Stèpán, G., 2004. Updated semi-discretization method for periodic delay-differential equations with discrete delay, *International Journal for Numerical Methods in Engineering*, **61**, pp. 117-141.

[6]   Insperger, T., Stèpán, G. and Turi, J., 2008. On the higher-order semi-discretizations for periodic delayed systems, *Journal of Sound and Vibration*, **313**, pp. 334–341.

[7]   Faassen, R.P.H., van de Wouw, N., Oosterling, J.A.J. and Nijmeijer, H., 2003. Prediction of regenerative chatter by modelling and analysis of high-speed milling, *International Journal of Machine Tools & Manufacture*, **43**, pp.1437–1446.

[8]   Floquet, M., 1883. Equations differentielles lineaires a coefficients periodiques, *Annales Scientifiques de l'Ecole Normale Superieure*, **12**, pp.47-89.

[9]   Hale, J.K., 1977. *Theory of Functional Differential Equations*, Springer-Verlag, New York.

[10]   Farkas, M., 1994. *Periodic Motions*, Springer-Verlag, Berlin, New York.

[11]   Catania, G. and Mancinelli, N., 2011. Theoretical-experimental modeling of milling machines for the prediction of chatter vibration, *International Journal of Machine Tools & Manufacture*, **51**, pp. 339–348.

[12]   Engelborghs, K., 2000. *Numerical bifurcation analysis of delay differential equations*, Ph.D. Thesis, Katholieke Universiteit Leuven.

[13]   Luo, A.C.J., 2013. Analytical solutions for periodic motions to chaos in nonlinear systems with/without time-delay, *International Journal of Dynamics and Control*, **1**:4, pp.330-359.

[14]   Acton, F.S., 1990. *Numerical methods that works*, The Mathematical Association of America.

IMPROVEMENT OF THE DYNAMIC BEHAVIOUR OF A TEST BED DRIVELINE BY NUMERICAL AND EXPERIMENTAL INVESTIGATIONS

Marco Cocconcelli
Department of Science and Engineering Methods,
University of Modena and Reggio Emilia, Italy
E-mail: marco.cocconcelli@unimore.it

Marco Troncossi
Department of Engineering for Industry,
University of Bologna, Italy
E-mail: marco.troncossi@unibo.it

Alessandro Agazzi
Department of Engineering,
University of Ferrara, Italy
E-mail: alessandro.agazzi@unife.it

Emiliano Mucchi
Department of Engineering,
University of Ferrara, Italy
E-mail: emiliano.mucchi@unife.it

Riccardo Rubini
Department of Science and Engineering Methods,
University of Modena and Reggio Emilia, Italy
E-mail: riccardo.rubini@unimore.it

Alessandro Rivola
Department of Engineering for Industry,
University of Bologna, Italy
E-mail: alessandro.rivola@unibo.it

Giorgio Dalpiaz
Department of Engineering,
University of Ferrara, Italy
E-mail: giorgio.dalpiaz@unife.it

Abstract. *This work regards the dynamic analysis of the coupling elements in IC engine test rigs from a numerical and experimental standpoint. Two mathematical models of an IC test rig have been developed: a torsional lumped-parameter (LP) model (developed in Matlab-Simulink) for the estimation of the torsional dynamic behavior and a 3D finite element (FE) model for the estimation of the natural frequencies of the coupling elements. The numerical models take into account the stiffness and damping of the flexible elements as well as the*

test rig inertia properties. A large experimental campaign has been carried out in order to validate the models. In particular, torsional vibration measurements have been achieved by a coder-based technique using high-quality optical sensors and equidistantly spaced markers (zebra tape) on the rotating components (high flexible couplings). Eventually, the validated models have been used in order to evaluate the effect of design modifications of the coupling elements in terms of natural frequencies (torsional and bending) and torsional vibration amplitude.

1. INTRODUCTION

This work addresses the dynamic analysis of the coupling elements in internal combustion (IC) engine test rigs from a numerical and experimental standpoint. In the current set up, the output shaft of the engine is connected to an electromechanical brake through a transmission shaft, which hosts an elastic coupling with rubber elements (high flexible couplings). Recently, the rising performance of engines has led to an abrupt increase of the dynamic loads affecting the driveline and in particular the elastic couplings. In this scenario, early failures of the rubber elements of the coupling have occurred.

The methodology used in order to solve the problem accounts both numerical and experimental activities. Firstly, an experimental campaign has been carried out with the aim of quantifying and characterizing the dynamic behavior of the driveline. In particular, torsional vibration measurements have been performed by a coder-based technique using high-quality optical sensors and equidistantly spaced markers (zebra tape) on the rotating components. The optical sensors were mounted before and after the coupling rubber elements, at the engine-side and brake-side, respectively.

Secondly, a 3D finite element (FE) model of the driveline has been developed in order to estimate the natural frequencies and mode shapes of the system being investigated and to evaluate which modes can negatively affect the dynamic behavior of the driveline in operational conditions. The numerical model takes into account the entire driveline with particular attention to the stiffness and inertia properties of the flexible coupling. The FE model has been experimentally validated by using data acquired during the experimental campaign mentioned above. It will be deeply discussed later on in the paper that the early failure of the elastic coupling is due to resonance phenomenon of the driveline excited at particular operational conditions. Thus, the assessed numerical model has been used in order to foresee the effect of design modifications of the coupling elements. The goal was to move the natural frequencies of the driveline outside the range of excitation of the engine harmonics.

Eventually, a lumped parameter (LP) model of the entire test rig (engine, driveline, brake) has been developed in order to estimate the torsional vibration of the system in operational conditions for the different design modifications suggested in the FE analysis. In the torsional model, developed in Matlab-Simulink environment, a precise evaluation of the variable inertia properties and torque of the engine as well as the dynamic behavior of the driveline has been included. The torsional LP model has been experimentally assessed by comparison with the experimental measurements described above. Furthermore, the torsional model enables the evaluation of the power losses in the flexible coupling in operating conditions.
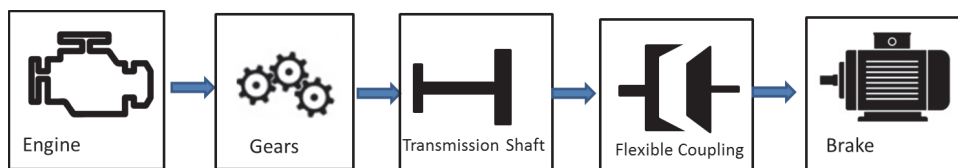
Figure 1. Schematic of the system under study.

A schematic of the test rig being studied is depicted in Fig. 1. The test rig consists of a few main components. The crankshaft of the engine drives a transmission shaft by means of the gear with a fix gear ratio. The transmission shaft is connected to the electromagnetic brake by a flexible coupling. The flexible coupling is composed of two rubber elements working in series and clumped to three metallic parts.

2. EXPERIMENTAL ANALYSIS

A brief overview of the experimental campaign is hereafter presented as well as the main results. Torsional vibration measurements have been carried out by using two optical sensors, type Optel Thevon 152 G7 GP RV4; one equipped with probe Optel Thevon MULTI TBYO 6M HM6X100 SURG and one with probe Optel Thevon MULTI SLIT YO 6M HM6X80 SURG. The zebra tape has been mounted in the two end-sections of the flexible coupling, at the brake-side and engine-side. An adequate number of lines of the zebra tape has been used in order to guarantee suitable resolution in the torsional measurement. Moreover, the tacho signal from a phonic wheel (with 8 teeth) fixed to the engine crankshaft has been acquired. The system was tested at different operational conditions, namely stationary regimes and run ups, and for different working conditions (in terms of velocity and throttle). The measured data were analyzed in the Time, Frequency, and Time-Frequency domains. Figure 2a reports the relative instantaneous angular speed (IAS) between the two end-sections of the flexible coupling during a run up of 44 s and Fig. 2b the relative Short Time Fourier Transform (STFT). The figures clearly highlight the phenomenon that determines an early failure of the coupling. In particular, in the time range between 18 and 30 seconds, the amplitude of the IAS strongly increases (Fig. 2a). The STFT clearly shows that this increase is due to a resonance of the system at about 180 Hz. The complete experimental characterization of the test rig can be found in other papers of the authors.

3. FINITE ELEMENT ANALYSIS

Model Development

An FE model (Fig. 3) has been developed in order to estimate the natural frequencies and mode shapes of the driveline. The FE model accounts the transmission shaft and the flexible coupling, which is composed of three flanges; the outer flanges allow the connections with the transmission shaft (engine-side) and with the brake, while the middle flange joins the rubber elements to the outer flanges. The engine and the brake have been included in the FE model as lumped mass elements and relative inertia (points 1 and 4 in Fig. 3): their stiffness characteristics have been neglecting. Particular attention has been devoted to the modeling of the transmission shaft and the rubber elements of the flexible coupling, since they have been identified as the most flexible components of the test rig.
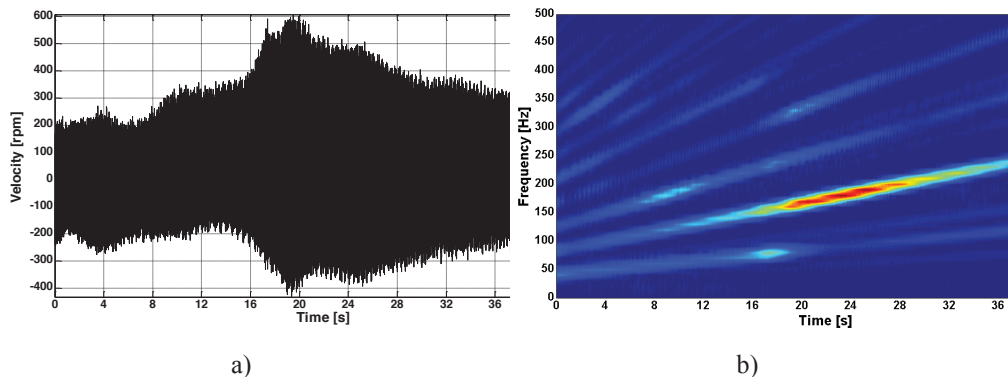
137

Figure 2. Relative instantaneous angular speed between the two end-sections of the flexible coupling during a run up (a) and relative STFT (b) for the 45Sh rubber element configuration.

The flanges of the flexible coupling have been considered as lumped mass and relative inertia (points 2,3,4 in Fig. 3). Rigid links have been used in order to connect the lumped masses (the flanges, engine and brake) to the 3D meshes of the transmission shaft and rubber elements;

Table 1 collects the features of the 3D mesh. Constrains have been added (points A and B in Fig. 3) in order to represent the real boundary conditions. At the engine-side the three orthogonal displacements have been clamped while at the brake-side only the rotational coordinate θ_z has been included.
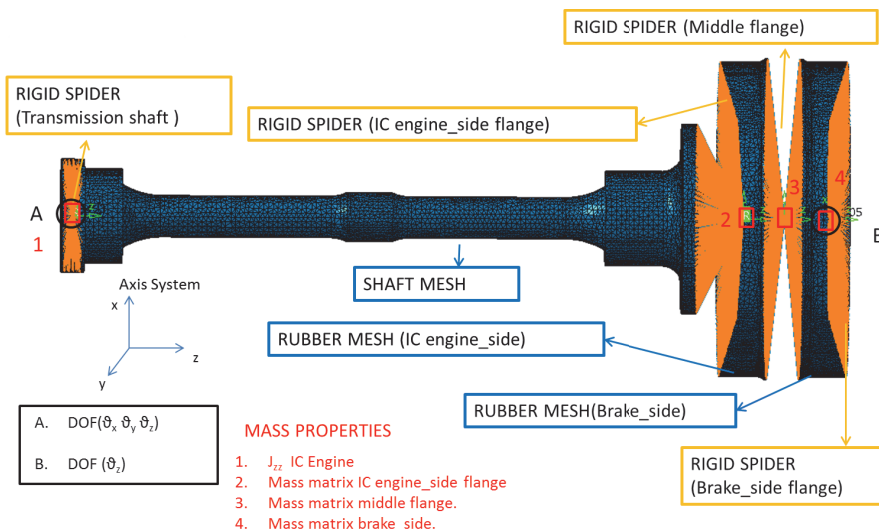

Figure 3. FE model

Figure 4. Experimental set up for estimation of rigid body inertia properties

A specific procedure has been carried out in order to evaluate the input parameters to include in the FE model. The coupling manufacturer provided the global torsional stiffness of the coupling, but the 3D FE model requires the Young's modulus of the rubber elements. Therefore, an iterative procedure based on a static FE model of the coupling has been performed in order to estimate the correct Young's modulus. A unitary torque has been applied to the FE model of the coupling and by a static analysis (MSC.Nastran SOL 101) the rotational displacement and thus the torsional stiffness have been calculated. Several simulations have been performed by changing the Young's Modulus in order to reach the torsional stiffness value provided by the manufacturer. After a few iterations, the correct Young's modulus was determined. The calculation has been repeated three times in order to find the Young's modulus for three different stiffness categories (i.e. 45Sh, 60Sh, 70Sh), as collected in Tab. 2.

The 3D-FE model requires the complete inertia tensor of the coupling flanges, while only the moment of inertia around the rotational axis was provided. In order to estimate the missing parameters, an experimental technique based on frequency response functions (FRFs) measurements (Fig. 4) has been performed for the indirect measurement of the rigid body inertia properties; such a methodology is based on the well-known Inertia Restrain Method, a technique suitable for a wide range of applications (mechanical, medical, etc [1-2]) because often the mass distribution of components or assemblies is not known. This method requires that in the FRFs, the mass line between the highest rigid body mode and the lowest flexible body mode is rather flat.

Table 2 collects the elastic properties of the rubber element estimated by the FE static analysis, the inertia properties estimated by the experimental procedure and the moment of inertia of the flanges around the rotational axis provided by the manufacturer.

Table 1. 3D meshes features

	Element type	Number of nodes	Number of elements
Transmission shaft	TETRA 4	23850	106553
Rubber element	TETRA 4	18844	80412

Model Validation

The results obtained through a numerical modal analysis (Sol 103 in MSC.Nastran) regarding 45 and 70 Shore rubber configurations have been compared with measurements (Section 2) The experimental STFT with those two rubber configurations clearly show a few resonance regions in the frequency range 0-500 Hz that are collected in Tab. 3a and Tab. 4a. Tab. 3b and Tab. 4b collect the natural frequencies estimated by the FE analysis. Regarding the 45 Shore rubber configuration, four numerical modes are very close to the resonance regions detected by the STFT. The first matching concerns the first torsional mode of the driveline, where the elements in the zone between the engine-side and the middle flange move out of phase with respect to the brake (15Hz vs 14.5Hz). The second matching regards the second torsional mode, which is characterized by a high amplitude displacement of the middle flange (70-70Hz vs 74.3Hz). Finally the last two experimental frequencies (160-190 Hz and 340Hz) correspond respectively to the 5th (184.2 Hz) and the 8th (348.3 Hz) numerical modes. In particular the 5th numerical mode is a double mode (two roots at same frequency due to symmetry) and involved the rotation of the middle flange around axes Y and X. This is the mode mainly excited in operational conditions. The remaining modes detected in the FE analysis are not present in the experimental map, since they are not exited by the engine harmonics in operational conditions due to their particular shape. Similar considerations can be done for the 70 Sh rubber configuration (Tab. 4). The comparison between the experimental and the numerical results shows that the mode that determine the highest peaks in the experimental maps regards the third local mode of the coupling. Thus, attention should be paid in order to move this mode far away from the excitation harmonics.

4. DYNAMIC BEHAVIOR IMPROVEMENT

Experimental results have clearly shown that within the frequency band of interest (i.e. 90-300Hz, where the main excitation harmonics due to the engine lie) resonances occur.

Table 2. Input data for FE analysis. cat→from catalogue of manufacturer; exp→from experiments.

Rubber Properties	Value
Rubber Density (45-60-75 Shore)	1000 kg/m^3
Poisson's ratio	0.49
Young's modulus rubber 45 Shore (60 °C)	1.32E+06 N/m^2
Young's modulus rubber 60 Shore (60 °C)	3.11E+06 N/m^2
Young's modulus rubber 70 Shore (60 °C)	4.72E+06 N/m^2
Coupling Inertial Properties	
Mass [kg]	5.68 kg (cat)
Jxx [kgm^2]	0.01337 kgm^2 (exp)
Jyy [kgm^2]	0.01337 kgm^2 (exp)
Jzz [kgm^2]	0.01961 kgm^2 (cat)

Table 3. 45 Shore configuration. a) List of experimental resonances, b) List of simulation natural frequencies.

a)	Experimental frequencies 45 Shore	b)	Simulation results 45 Shore
Mode 1	15 Hz	Mode 1	14.5 Hz (First torsional mode)
		Mode 2	35.2 Hz (First local mode of coupling)
Mode 2	70 – 80 Hz	Mode 3	74.3 Hz (Second torsional mode)
Mode 3		Mode 4	98.4 Hz (Second local mode of coupling)
	160 – 190 Hz	Mode 5	184.2 Hz (Third local mode of coupling)
		Mode 6	220 Hz (Third torsional mode)
		Mode 7	253 Hz (Axial mode middle flange)
Mode 4	340 Hz	Mode 8	348.3 Hz (First bending mode output shaft)

Table 4. 70 Shore configuration. a) List of experimental resonances, b) List of simulation natural frequencies.

a)	Experimental frequencies 70 Shore	b)	Simulation results 70 Shore
Mode 1	30 – 40 Hz	Mode 1	25.5 Hz (First torsional mode)
		Mode 2	65.1 Hz (First local mode of coupling)
Mode 2	120 – 150 Hz	Mode 3	128.5 Hz (Second torsional mode)
		Mode 4	185.8 Hz (Second local mode of coupling)
		Mode 5	301 Hz (Third torsional mode)
		Mode 6	302.1 Hz (Third local mode of coupling)
		Mode 7	417.8 Hz (Axial mode middle flange)
		Mode 8	425.5 Hz (First bending mode output shaft)

Moreover, FE simulations have defined the corresponding mode shapes of such resonances. This section presents three design modifications (MOD 1, MOD 2, and MOD 3) that try to move the resonances outside the band of interest. The shifting in frequency of the resonances outside the operational bandwidth or the reduction of the number of excited modes, are the tasks for the improvement of system dynamic behavior. However, a number of design constrains should be respected as geometrical dimensions and final weight. The used methodology is as follows. The resonances close to the lower threshold of the bandwidth have been shifted below in frequency, by adding mass or reducing stiffness in specific zones, depending on the mode shape involved. The resonances close to the upper threshold have been move above in frequency by reducing mass or increasing stiffness of connection shaft and rubber elements.

Design Modification 1 – MOD 1

The first design modification (MOD 1) takes into account regards the 45Sh rubber element configuration, with increased weight of the middle flange in order to reduce the frequency of the third mode (at 89.2Hz) of the coupling; furthermore the steel connection shaft has been replaced by a stiffer titanium shaft keeping the third torsional mode outside the operational bandwidth.

Table 5. Simulation results of modified drivelines.

a)	Simulation results 45 Shore MOD 1
Mode 1	12.3 Hz (First torsional mode)
Mode 2	30.4 Hz (First local mode of coupling)
Mode 3	40 Hz (Second torsional mode)
Mode 4	69.2 Hz (Second local mode of coupling)
Mode 5	89.2 Hz (Third local mode of the coupling)
Mode 6	130.6 Hz (Axial of middle flange)
Mode 7	361 Hz (Third torsional mode)
Mode 8	493.2 Hz (First bending of output shaft)

b)	Simulation results 70 Shore MOD 2
Mode 1	22.6 Hz (First torsional mode)
Mode 2	67.1 Hz (First local mode of coupling)
Mode 3	121.6 Hz (Second torsional mode)
Mode 4	168.5 Hz (Second local mode of coupling)
Mode 5	304.3 Hz (Third local mode of coupling)
Mode 6	365.5 Hz (Axial of middle flange)
Mode 7	402.2 Hz (Third torsional mode)

c)	Simulation results 60 Shore MOD 3
Mode 1	18.7 Hz (First torsional mode)
Mode 2	57.3 Hz (First local mode of coupling)
Mode 3	124.7 Hz (Second torsional mode)
Mode 4	163.4 Hz (Second local mode of coupling)
Mode 5	310.9 Hz (Third local mode of coupling)
Mode 6	365.7 Hz (Axial of middle flange)
Mode 7	388 Hz (Third torsional mode)

Eventually, a flywheel has been introduced on the engine shaft in order to guarantee the second torsional frequency at low frequency. The comparison between Tab. 3and Tab. 5a shown that targets have been reached successfully but MOD 1 leads to a rather heavy design, which could arise issues at high-speed conditions. Therefore modifications for 70Sh configuration have been studied. Note that Mode 6 remains in the frequency range of excitation after the modification, but due to its particular shape it is not excited in operational conditions.

Design Modification 2 – MOD 2

The second design modification (MOD 2) concerns the 70Sh rubber element configuration, where the middle flange has been lightened, a flywheel on the engine shaft and a stiffer connection shaft have been placed. Table 5b collects the resulting natural frequencies. Natural frequencies still remain in the frequency range of interest, but it will be illustrated later on in Section 5, by means of the LP model, the benefits of this modification.

Design Modification 3 – MOD 3

The last design modification (MOD 3) concerns the 60 Sh rubber element configuration. The standard middle flange has been lightened by milling some parts and by replacement of steel screws with titanium ones. The transmission shaft has been included in titanium and a flywheel has been mounted on the engine shaft. Tab. 5c collects the natural frequencies. The third local mode of the coupling is above the 300Hz threshold, while the second torsional mode is still inside the operational bandwidth but the 60Sh rubber has the highest relative damping value, thus the vibration amplitude at this resonance should be reduced with respect to 70Sh. The goodness of these improvements can be appreciated also in the next section.

5. ELASTODYNAMIC ANALYSIS

Model Development

As argued in Section 3, the main dynamics effects of the coupling elements are due to the local mode of the coupling. In order to avoid these criticalities a number of design changes has been proposed in the previous section. Unfortunately the design changes are not free from possible cons in the torsional dynamics of the system. A detailed elastodynamic model is necessary to simulate the working behavior of the coupling, proving the effectiveness of suggested design corrections. Since in the frequency range of interest, after the design modifications, only torsional modes occurs (as well as a not-excited axial mode), a torsional LP model can capture the real dynamic behavior of the test rig. For these reasons the elastodynamic model of the driveline has been focused on the torsional dynamics only through a lumped parameter torsional model.

The macro physical elements of the driveline are the IC engine, the coupling, the brake and the shafts linking them to each other. Since the focus of the model is on the coupling elements, it is further divided into three main parts: the two halves facing the IC motor and the brake respectively, and the middle flange which is connected to the halves by means of rubber elements. These macro elements of the driveline are indeed the same that have been used in the FE model.

A preliminary analysis of the linking shafts inertia and stiffness suggests substituting them with a pure torsional spring of the same stiffness, while part of the inertia has been

divided between the two linked elements. The analysis is focused on the oscillations around steady working conditions only, thus the brake system will not be taken into account, i.e.. the half of the coupling facing the brake, the brake itself and the linking shaft will be considered as a fixed frame (ground). As a consequence the complexity of the mechanical system is reduced to a three degrees of freedom (DOFs) model: the torsional displacement of the IC engine (θ_1), the coupling half facing the motor (θ_2), and the middle flange of the coupling (θ_3). Figure 5 shows a schematic drawing of the 3 DOFs physical model, where J_1 is the inertia of the IC engine, J_2 of the coupling half and J_3 of the middle flange. Connections *a, b, c* refer to the transmission shaft, and the two rubber parts of the coupling, respectively. External torques acting on the single inertia are named as T_i. Note that rotational coordinates θ_1 and θ_2 correspond to the two measured locations: engine crankshaft and end-section of the coupling at the engine-side.

Inertia. Inertia J_2 and J_3 are easy to compute since they coincide with the inertia of the single mechanical parts with respect to their center of gravity, namely the half coupling and the middle flange. These values could be assumed from the FE analysis.

The computation of inertia J_1 is not trivial. It is the sum of different contributions of the internal components in the IC motor, some of them rotating with different angular speed. In order to reduce the complexity of the model, all main components – in terms of inertia – have been transported to the output axis of the motor, i.e. the one directly connected to the transmission shaft linked to the coupling. The main parts of the motors considered within inertia J_1 are:

- The alternator
- The crankshaft
- The gearboxes
- The timing system
- The clutch

Damping And Stiffness Elements. Each linking element *a, b, c* (see Fig. 5) is modeled as a spring and a viscous damper element in parallel. The resulting viscoelastic torque (T_{ve}) can be expressed as:

$$T_{ve} = k \cdot \Delta\theta + c \cdot \Delta\dot{\theta} \tag{1}$$

where *k* and *c* are the stiffness and viscous coefficient respectively, while $\Delta\theta$ and $\Delta\dot{\theta}$ are the relative rotation and relative speed of the linking element ends.
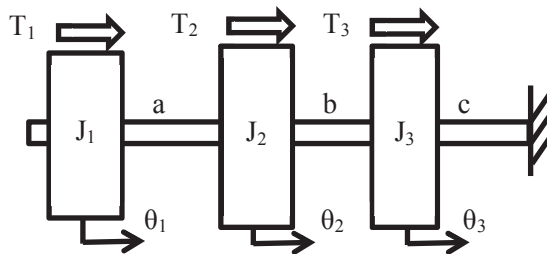

Figure 5. Schematic drawing of the physical model

Table 6. Nomenclature of the external torque parameters

Symbol	Description	Symbol	Description
P_i	Pressure in i-th cylinder	m_b	mass of the piston rod (p.r.)
d	bore of the piston	l	length of the p.r.
r	length of the crank	J_b	Inertia of the p.r.
m_p	mass of the piston	l_a	Distance COG and head of p.r.
COG	center of gravity	l_b	Distance COG and foot of p.r.

Indeed the characteristics of the transmission shaft (link *a*) are quite different from the rubber elements of the two coupling halves (links *b, c*). While the viscous damper model is correct for the steel material (in the elastic domain), for the rubber material an equivalent viscous coefficient is computed starting from an hysteretic damping model [3]. The resulting viscous coefficient is:

$$c = \frac{k \cdot \gamma}{2\pi \cdot \omega} \tag{2}$$

where γ is the relative damping value of the rubber and ω is the angular speed of the hysteretic loop. In this model ω is speed of the IC motor cycle.

External Torques. The only non-zero external torque is T_1, acting on inertia J_1 ($T_2 = T_3 = 0$). T_1 is the result of the combustion cycles of the motor in each cylinder. The torque contribution of each cylinder comes from the expansion phase in the IC cycle and the inertia momentum of each part of the crank-slide mechanism.

With reference to the nomenclature in Tab. 6 the contribution of the motor's four cylinders to the external torque gives the Eqn. (3).

$$T_1 = \sum_{i=1}^{4} \left[P_i \cdot \pi \cdot \left(\frac{d}{2}\right)^2 \cdot r_{vi} - \left(m_p + m_A - \frac{J_0}{l^2}\right) \cdot \left(\dot{\phi}_i^2 \cdot r_{ai} + \ddot{\phi}_i \cdot r_{vi}\right) \cdot r_{vi} \right] \tag{3}$$

where:

$$\begin{cases} m_A = m_b \cdot \dfrac{l_B}{l} \\[2mm] J_0 = J_b - m_b \cdot l_A \cdot l_B \\[2mm] r_{vi} = r \cdot \left(\sin\phi_i + \dfrac{1}{2} \cdot \dfrac{r}{l} \cdot \sin 2\phi_i\right) \\[2mm] r_{ai} = r \cdot \left(\cos\phi_i + \dfrac{r}{l} \cdot \cos 2\phi_i\right) \end{cases} \tag{4}$$

A detailed description of the formula in Eqn. (3) and (4) can be found in several books about the theory of machines and mechanisms, e.g [4]. Note that the quantities in Eqn. (3) and (4) without subscript index are supposed to be the same for all the cylinders, while the others differ one to each other through the combustion phase (φ_i) of each cylinder with respect to a reference (e.g. the angular displacement θ_1^* of the inertia J_1):

$$\phi_i = \theta_1^* + \varphi_i \qquad i = 1, \dots, 4 \tag{5}$$

145

The superscript asterisk remembers to the reader that the angular displacement in Eqn. (5) should be the absolute displacement, not just the oscillation of inertia J_1 around the equilibrium configuration.

Equations Of Motion. The equations of (torsional) motion of the three DOFs system are computed in matrix form:

$$
\begin{bmatrix} J_1 & 0 & 0 \\ 0 & J_2 & 0 \\ 0 & 0 & J_3 \end{bmatrix} \cdot \begin{bmatrix} \ddot{\theta}_1 \\ \ddot{\theta}_2 \\ \ddot{\theta}_3 \end{bmatrix} + \begin{bmatrix} c_1 & -c_1 & 0 \\ -c_1 & c_1+c_2 & -c_2 \\ 0 & -c_2 & c_2+c_3 \end{bmatrix} \cdot \begin{bmatrix} \dot{\theta}_1 \\ \dot{\theta}_2 \\ \dot{\theta}_3 \end{bmatrix} + \begin{bmatrix} k_1 & -k_1 & 0 \\ -k_1 & k_1+k_2 & -k_2 \\ 0 & -k_2 & k_2+k_3 \end{bmatrix} \cdot \begin{bmatrix} \theta_1 \\ \theta_2 \\ \theta_3 \end{bmatrix} = \begin{bmatrix} T_1 \\ 0 \\ 0 \end{bmatrix}
$$

(6)

where c_2 and c_3 come from Eqn. (2), and T_1 from Eqn. (3). The resulting Simulink model of the test rig is shown in Fig. 6.

Model Validation

The validation of the elastodynamic model is based on the experimental analysis described in Section 2. It should be noted that experimental data collected in the 45Sh rubber element configuration cannot be used for the validation of such a model. In fact those data are mainly affected by the local mode of the coupling, which cannot be predicted by the pure-torsional model described above.
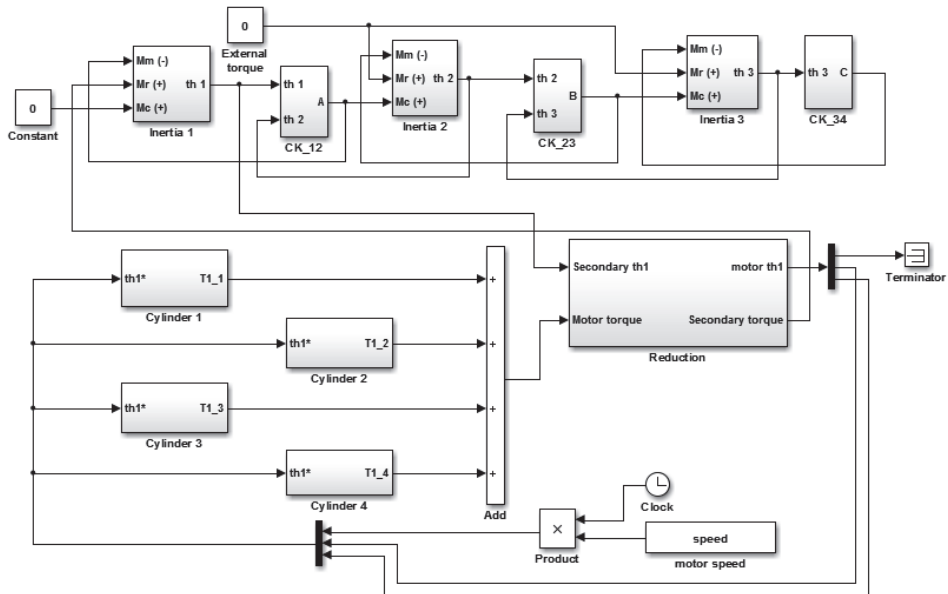

Figure 6. Simulink model of the test rig

a)	Experimental resonances	b)	FE results	c)	LP results
Mode 1	30 – 40 Hz	Mode 1	25.5 Hz (1st tor.)	Mode 1	22.38 Hz
		Mode 2	65.1 Hz (1st coupl)		
Mode 2	120 – 150 Hz	Mode 3	128.5 Hz (2nd tor.)	Mode 2	124.57 Hz
		Mode 4	185.8 Hz (2nd coupl)		
		Mode 5	301 Hz (3rd tor.)	Mode 3	291.18 Hz
		Mode 6	302.1 Hz (3rd coupl.)		
		Mode 7	417.8 Hz (Axial mid)		
		Mode 8	425.5 Hz (1st bend shaft)		

The model validation is performed on data acquired in the 70 Sh rubber element configuration. As mentioned in Section 3, the coupling is available with three different types of elastic rubber elements: 45, 60 and 70 Shore of rubber hardness.

The output parameter for both experimental data and simulation results is the ratio between half the peak-to-peak and the mean value of the body oscillations, expressed as percentage. Results in correspondence of the rotational coordinates at different speed of the motor are shown in Tab. 8.

Table 8. Comparison between simulation results and experimental data

Simulation	Speed 1	Speed 2	Speed 3	Speed 4	Speed 5	Speed 6
θ_1	4.5	3.5	2.9	2.5	2.1	1.3
θ_2	4.9	2	2.2	2.7	3.0	3.4
θ_3	10.3	3.3	2.0	1.7	1.4	4.0

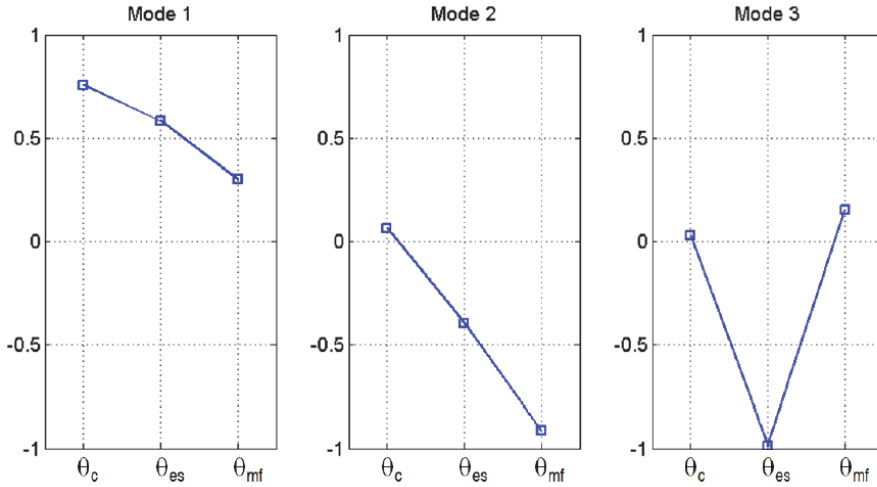| Experiment	Speed 1	Speed 2	Speed 3	Speed 4	Speed 5	Speed 6
θ_1	5.4	4.3	3.5	2.9	2.5	2.1
θ_2	7.9	4.0	2.9	2.4	1.8	3.2

Figure 7. Normalized mode shapes of the driveline

Due to non-disclosure agreements the speed values are not present, the speed linearly increases from Speed 1 to Speed 6. θ_1, θ_2, θ_3 are three rotational coordinates. In particular θ_1 regards the oscillation of the IC motor, θ_2 the half coupling and P_3 the middle flange of the coupling. Unfortunately location θ_3 was not measured in the experimental analysis then it is shown for simulation results only for completeness.

Simulation results are in good accordance with the experimental data, both clearly identify a higher oscillation at Speed 1 which decreases as the speed increases from 1 to 5, and then it increases again until Speed 6. The increased oscillations at Speed 1 and 6 are confirmed also by location θ_3. The advantage of the elastodynamic model is that the causes of the increased oscillation could be easily investigated through the simulation. In particular the analysis of the resonance frequencies of the system shows that mode shape 2 is particularly burdensome for coordinate θ_3 (see Fig. 7). The corresponding natural frequency is quite close to the 1x of rotational speed 1, thus justifying both simulation results and experimental analysis. Moreover the same natural frequency is still close to the 0.5x of the rotational speed 6.

Simulation Results And Discussion

With reference to section 4 the elastodynamic model of the driveline has been used to simulate the dynamic behavior of the system after three different design changes. The same designation of the modifications discussed in section 4 is used. Results are given as the ratio between half the peak-to-peak and the mean value of the bodies oscillations, expressed as percentage – the same output parameter used in section 0.

Table 9. Simulation results of MOD 1

MOD 1	Speed 1	Speed 2	Speed 3	Speed 4	Speed 5	Speed 6
θ_1	2.4	2.1	1.8	1.3	0.9	0.7
θ_2	3.4	4.2	1.9	1.6	3.2	1.4
θ_3	0.30	0.19	0.13	0.07	0.04	0.03

Table 10. Simulation results of MOD 2

MOD 2	Speed 1	Speed 2	Speed 3	Speed 4	Speed 5	Speed 6
θ_1	2.4	2.1	1.8	1.3	1.0	0.7
θ_2	2.8	2.7	2.2	1.4	1.8	1.1
θ_3	3.24	1.55	1.14	1.04	2.09	0.35

The first design modification (MOD 1) regards 45Sh rubber elements, with increased weight of the middle flange, titanium transmission shaft and a flywheel on the engine shaft. Results are shown in Tab. 9.

The second design modification (MOD 2) concerns 70Sh rubber elements, lightened middle flange, flywheel on the engine shaft and titanium transmission shaft. Results are shown in Tab. 10.

The third design modification (MOD 3) differs from MOD 1 and MOD 2. Lighted middle flange, titanium screws, titanium connection shaft and a flywheel on the engine shaft. Results are shown in Tab. 11.

A further indicator used is the power loss. According to standard DIN 740 the relative damping is the ratio between the damping power of one vibration cycle and elastic deformation energy. The elastic deformation energy depends on the main frequency in the oscillation spectrum of the coupling and can be easily computed, while the relative damping is usually given in the manufacturer's catalog (it is the γ parameter in equation 2). The damping power of one vibration cycle for different hardness of the rubber and different speeds is collected in Tab. 12.

Modification 1 keeps torsional vibrations at low level, with a stable and limited oscillation around the reference speed. Consequently the power loss has low values compared to the other modifications. As a drawback the FE analysis shows that all the resonance frequencies are shifted to lower values, e.g. six resonances lay in the band (0-300 Hz). Even if they are outside the frequency band of interest (90 – 300 Hz), it is not excluded that the test rig will be used at lower speed regimes in the future, with the consequent need of further design modifications to avoid resonance problems again. Moreover the MOD 1 requires a sensible increase of the coupling's mass and then a further structural load on the supports of the test rig.

Modification 2 and 3 go in the opposite direction of MOD 1. They shift the resonance frequencies at higher values out of the selected frequency bandwidth. Torsional vibrations are still acceptable; the speed oscillation is less than 5% with respect to regime.

In MOD2 the FE model shows that the local mode frequency is outside the limit of 300 Hz but still close (304 Hz), while MOD 3 takes a little bit higher safety factor (311 Hz).

Table 11. Simulation results of MOD 3

MOD 3	Speed 1	Speed 2	Speed 3	Speed 4	Speed 5	Speed 6
θ_1	2.4	2.0	1.7	1.3	1.0	0.7
θ_2	2.7	4.4	2.0	1.5	4.0	1.2
θ_3	2.82	1.43	1.16	1.19	1.51	0.32

Table 12. The damping power of one vibration cycle for each design modification

[W]	Speed 1	Speed 2	Speed 3	Speed 4	Speed 5	Speed 6
MOD 1	1.03	1.23	0.72	0.99	0.98	0.87
MOD 2	31.87	13.18	4.80	4.14	2.90	1.88
MOD 3	19.14	9.76	3.83	3.54	2.66	1.89

Comparing the damping power in Tab. 12, MOD 2 shows an increased value at Speed 1 and 2 – probably due to a close resonance – which is reduced in MOD 3. These considerations lead to choose MOD 3 as the optimal design improvement.

6. CONCLUSIONS

This paper deals with the dynamic analysis of coupling elements in IC engine test rig. The test rig consists of a few main components: the engine, gears, a transmission shaft, a flexible coupling and a break. The crankshaft of the engine drives a shaft by means of the gear with a fix gear ratio. The transmission shaft is connected to the electromagnetic brake by an elastic coupling. The coupling is composed of two rubber elements working in series and clumped to three metallic parts: two halves facing the engine and the break, and a middle flange, which works as a torsional vibrations damper. Despite the peculiarity of the case study described, this paper aims to prove the complexity of a complete dynamic analysis of a mechanical system. In particular full understanding of the dynamic behavior requires more than one modeling besides an experimental activity. The first step of a dynamic analysis starts from an FE model of the system. The FE model allows the comprehension of the resonances of the system, i.e. a torsional resonances rather than a flexural or axial resonance. The experimental activity clearly shows which resonance is burdensome for the characteristic working conditions of the system, and it guides the choice of proper design modifications in order to remove critical working conditions. It must be stressed that design modifications focus on – let's call – primary dynamics effects, e.g. the flexural vibration resonance that causes an abrupt break of the system. Unfortunately the design modifications could have secondary dynamic effects, e.g. some impacts on the torsional vibrations that have not been considered yet. As a consequence the second step is the development of a lumped parameter model focused on these secondary dynamic effects, which assure the effectiveness of the design modifications in all the working conditions of the test rig. In this paper the proposed methodology is applied to the dynamic analysis of a flexible coupling. Experimental activity has shown the presence of a resonance close to the working condition of the coupling, which leads to a quickly breaking of the rubber elements of the joint. The FE model enables the characterization of the shape of the mode that determines such a resonance and the suggestion of three different design modifications to avoid the resonance in working conditions. The LP model allowed choosing the design modification less burdensome in terms of torsional vibration of the driveline.

The presented methodology could be a very useful tool in prototype design and optimization, as well as to identify the origin of unwanted dynamic effects in test rig. Although these quantitative results concern a particular test rig, the used methodology and the drawn conclusions have a general meaning from the qualitative point of view: they can be applied to a large variety of mechanical systems and applications and give useful

guidelines in order to foresee the influence of operational conditions and design modifications on vibration generation.

Acknowledgements

REFERENCES

[1] Mucchi, E., Bottoni, G., and Di Gregorio, R., 2009. "Indirect Measurement of the Inertia Properties of a Knee Prosthesis through a Simple Frequency-Domain Technique", *Journal of Medical Devices*, **3**, December, 044501-5.

[2] Mucchi, E., Fiorati, S., Di Gregorio, R., and Dalpiaz, G., 2011, "Determining the rigid-body inertia properties of cumbersome systems: comparison of techniques in time and frequency domain", *Experimental techniques*, May/June.

[3] Rao, S.S.,2003, *Mechanical Vibrations*, Prentice Hall, New York.

[4] Uicker, J., Pennock, G., Shigley, J., 2010, *Theory of Machines and Mechanisms*, Oxford University Press, New York.

ANALISI VIBRAZIONALE NUMERICA E SPERIMENTALE DI UN TRABATTO PER PASTA ALIMENTARE

Marco Buzzoni
Dipartimento di Ingegneria di Ferrara,
Università degli Studi di Ferrara, Italia
E-mail: marco.buzzoni1@unife.it

Emiliano Mucchi
Dipartimento di Ingegneria di Ferrara,
Università degli Studi di Ferrara, Italia
E-mail: emiliano.mucchi@unife.it

Giorgio Dalpiaz
Dipartimento di Ingegneria di Ferrara,
Università degli Studi di Ferrara, Italia
E-mail: giorgio.dalpiaz@unife.it

Abstract. *Questo lavoro riguarda l'analisi dinamica di un trabatto per pasta alimentare dal punto di vista sperimentale e numerico allo scopo di limitare il livello delle vibrazioni del sistema. Il trabatto è un essiccatore a tre piani paralleli, detti cassetti, vincolati al telaio mediante balestre inclinate. Le balestre sono deformate da un sistema biella-eccentrico e generano il moto sussultorio necessario alla movimentazione del prodotto. E' stata condotta una indagine sperimentale che ha riguardato l'analisi modale di alcuni componenti chiave del sistema e la misura di vibrazioni in condizioni operative. I risultati conseguiti sono stati usati per identificare le cause del comportamento dinamico non accettabile del sistema proponendo delle modifiche migliorative verificate sperimentalmente. E' stato infine sviluppato un semplice modello cinematico ad un grado di libertà di un cassetto per verificare l'influenza della variazione della velocità di rotazione sulla legge di moto imposta ai cassetti.*

Keywords: *Vibratory feeder, Operational vibration measurements, Modal analysis, Kinematic analysis*

1. INTRODUZIONE

La crescita delle dimensioni e della velocità di lavoro dei macchinari al fine di soddisfare gli elevati volumi di produzione richiesti dal mercato, ha portato le aziende a porre una maggiore attenzione alla limitazione delle vibrazioni per evitare inconvenienti quali, ad esempio, guasti e rumorosità.

In questo articolo, si affronterà un problema di elevati livelli di vibrazione riscontrati in un essiccatore per pasta alimentare, chiamato trabatto A, progettato a partire da un modello di taglia inferiore, chiamato trabatto B. Il sistema in questione ha un funzionamento molto

simile a un alimentatore a vibrazioni con la differenza che, in genere, la frequenza di funzionamento è piuttosto lontana dalla frequenza di risonanza del sistema.

In letteratura sono presenti numerosi lavori che trattano lo studio dinamico di questi sistemi sotto diversi punti di vista. Alcuni di questi riguardano uno studio teorico e/o sperimentale [1-2], altri invece concernono lo sviluppo e la validazione sperimentale di un modello per la stima delle frequenze naturali [3]. In questa memoria si tratterà la problematica da una prospettiva differente. Questo lavoro si articola principalmente in due parti: la prima parte riguarda una campagna di misure sperimentali allo scopo di identificare le cause del problema vibratorio del trabatto A e i parametri di funzionamento del trabatto B preso come riferimento, nella seconda parte si presenta un modello cinematico del trabatto al fine di chiarire e approfondire i fenomeni che causano il malfunzionamento del trabatto A.

2. SISTEMA MECCANICO

Il trabatto A (Figura 1) è composto da 3 piani paralleli porta pasta: quello superiore e quello inferiore sono solidali tra loro e il loro insieme è denominato "cassetto dispari" mentre il piano in mezzeria è denominato "cassetto pari". Ogni cassetto è vincolato al telaio con 12 balestre inclinate, di materiale composito, aventi la funzione sia di sorreggere i cassetti sia di vincolo cinematico grazie alla loro elasticità. Ciascun cassetto è inoltre collegato all'albero principale da una biella e un eccentrico per ciascun lato. Gli eccentrici, calettati sull'albero principale, sono sfasati di 180° in modo da far muovere i cassetti in controfase. L'albero principale è movimentato da un motore asincrono trifase attraverso una trasmissione a cinghie.

Negli alimentatori a vibrazione il trasporto del prodotto avviene, in genere, sfruttando l'inclinazione del piano o per gravità. In questo sistema meccanico invece, il moto sussultorio dei cassetti è ottenuto grazie alla spinta alternativa delle bielle che a loro volta deformano le balestre. Le balestre si deformano prevalentemente a flessione imponendo ai cassetti una traiettoria ad arco di cerchio nel piano yz.

La modalità di trasporto del prodotto è la seguente: la pasta entra nel piano superiore del cassetto dispari dal lato posteriore del trabatto (opposta al lato motore), si sposta dal lato posteriore a quello anteriore, giunge al cassetto pari spostandosi successivamente dal lato
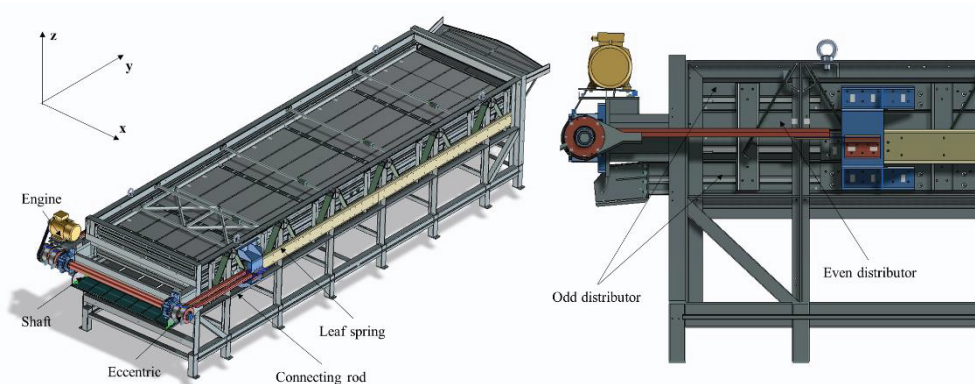

Figura 1. Modello CAD del trabatto A (x è la direzione trasversale, y la direzione longitudinale, z è la direzione verticale).

anteriore a quello posteriore, infine va nel piano inferiore del cassetto dispari fuoriuscendo dal lato anteriore.

3. CAMPAGNA SPERIMENTALE

La campagna di misure sperimentali è costituita da: misura delle accelerazioni in condizioni operative, misura delle oscillazioni torsionali, analisi modale sperimentale. Le prove sperimentali riguardano entrambi i trabatti A e B e hanno lo scopo di:

- valutare quale sia l'origine dell'elevato problema di vibrazioni sul trabatto A;
- individuare i parametri rappresentativi della dinamica del sistema in modo da avere uno strumento di confronto oggettivo tra le diverse taglie e condizioni operative;
- identificare i valori di soglia di buon funzionamento del sistema a partire dal trabatto B assunto come riferimento.

Nei seguenti sotto paragrafi verrà descritto il set up e i risultati principali di ogni misura.

Misure vibrazionali operative traslazionali

Le misure vibrazionali operative sono state condotte per entrambi i trabatti sia a velocità costante sia con rampa di velocità ascendente. Il setup di misura è costituito da tre accelerometri triassiali piezoelettrici posizionati in diversi punti significativi del sistema: uno sulla staffa di collegamento tra la biella e il cassetto pari (Figura 2b), uno sulla staffa di collegamento tra la biella e il cassetto dispari e uno sul cuscinetto di banco sinistro dell'albero principale (Figura 2a). I segnali accelerometrici nel tempo sono stati acquisiti con una frequenza di campionamento di 512 Hz. La durata delle acquisizioni a velocità costante è pari a 40 s mentre le rampe di velocità sono state ottenute accelerando da 180 rpm a 400 rpm. I dati ottenuti con le rampe di velocità sono stati elaborati e visualizzati mediante grafici velocità-frequenza-accelerazione. Il segnale di accelerazione a velocità costante è stato invece elaborato calcolandone lo spettro e il valore RMS risultante valutato tra la direzione longitudinale e quella verticale.
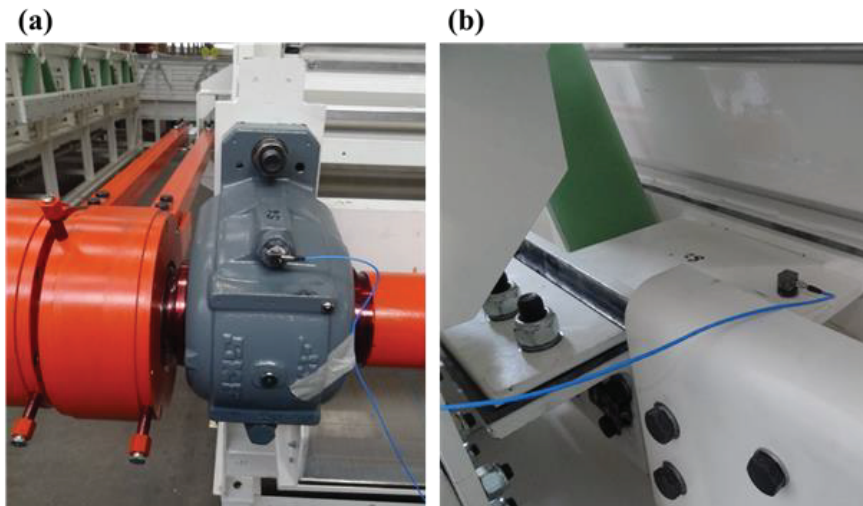

Figura 2. Posizione di alcuni accelerometri: (a) sensore sul cuscinetto di banco e (b) sensore sul cassetto pari.
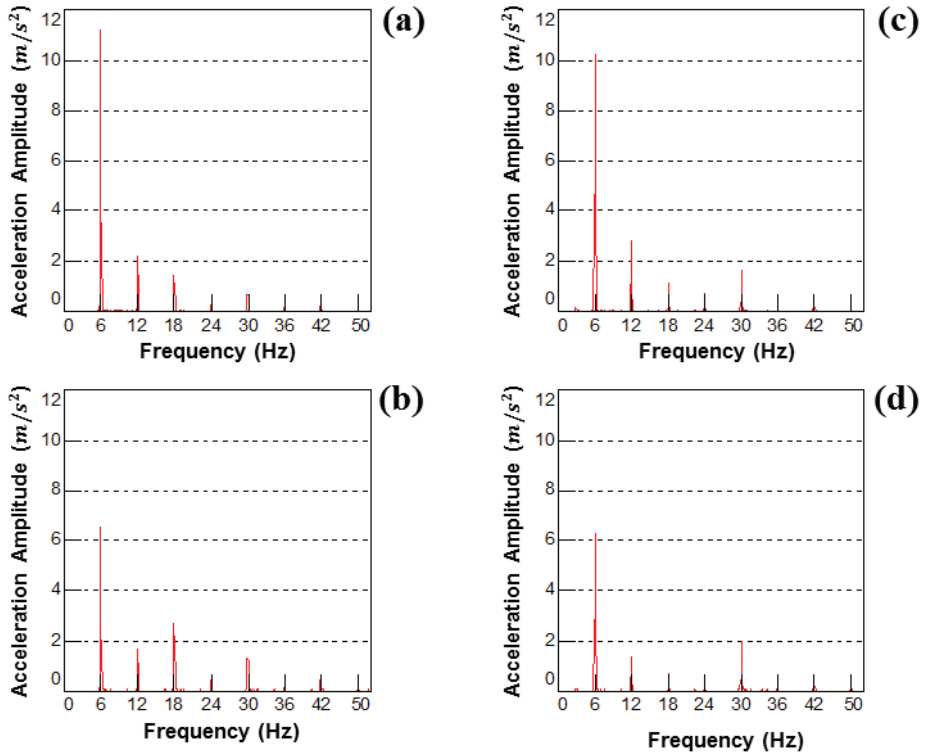
Figura 3. Ampiezza dello spettro delle accelerazioni misurate sui cassetti del trabatto A: (a) cassetto dispari in direzione longitudinale, (b) cassetto dispari in direzione verticale, (c) cassetto pari in direzione longitudinale, (d) cassetto pari in direzione verticale.

Dall'analisi preliminare delle ampiezze delle accelerazioni si può dedurre che la direzione trasversale del sistema ha ampiezze trascurabili. Lo spettro delle accelerazioni misurate sui cassetti del trabatto A (Fig. 3) mostra, come prevedibile, che la componente prevalente è quella in corrispondenza della prima armonica (1X) della frequenza di rotazione dell'albero (6 Hz); tuttavia si individuano anche delle armoniche successive non trascurabili alla 2X, 3X, 4X e 5X sia in direzione verticale che in direzione orizzontale. Gli spettri delle accelerazioni misurate sul telaio del trabatto A (Fig. 4a e 4b) indicano che le masse dei cassetti sono correttamente bilanciate, poiché la componente alla 1X si riduce a un valore trascurabile, ma i picchi relativi alle armoniche successive restano pressoché invariati. Le stesse considerazioni possono essere tratte per il trabatto B (Fig. 4c e 4d).

I grafici rpm-frequenza ottenuti con rampe di velocità (Fig. 5 e Fig. 6) evidenziano che:
- la condizione di lavoro più penalizzante per il trabatto A è a 360 rpm;
- potrebbero essere presenti dei fenomeni di risonanza a circa 13 Hz, 18 Hz, 19 Hz, 26 Hz, 30 Hz e 32 Hz.

I valori della risultante RMS delle prove a velocità costante (Tab. 1) mostrano, come già visto negli spettri, che nelle condizioni nominali di lavoro (360 rpm) il trabatto A ha un livello vibratorio superiore al trabatto B. Inoltre nel trabatto A si osserva che alla velocità di 360 rpm il valore RMS è più che doppio rispetto a 330 rpm.
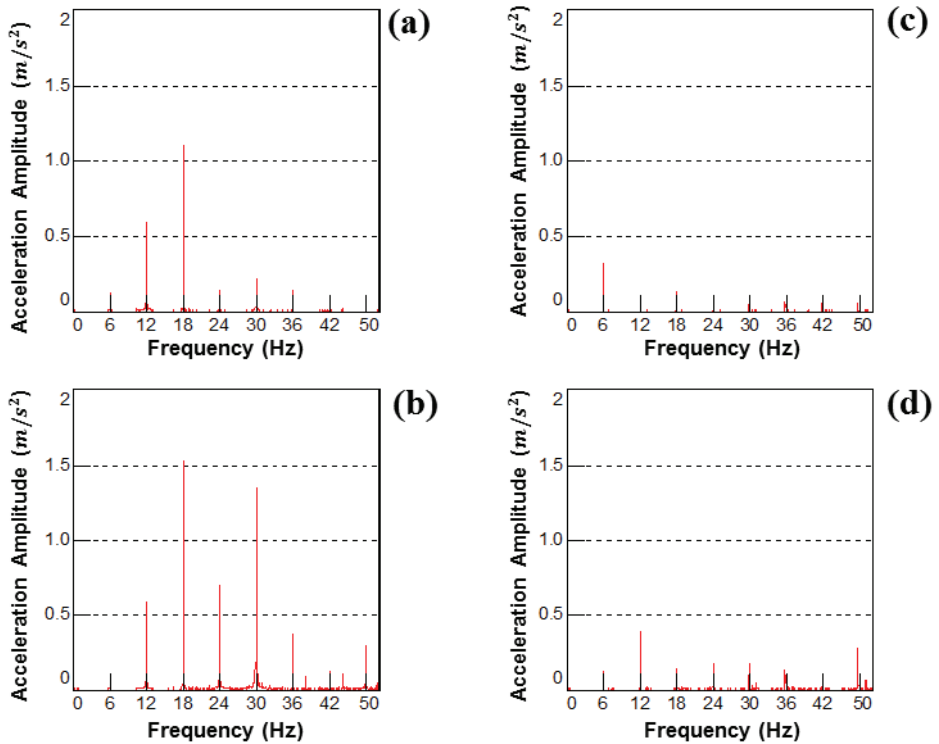
Figura 4. Spettri delle accelerazioni misurati sul telaio: (a) trabatto A in direzione longitudinale, (b) trabatto A in direzione verticale, (c) trabatto B in direzione longitudinale, (d) trabatto B in direzione verticale.
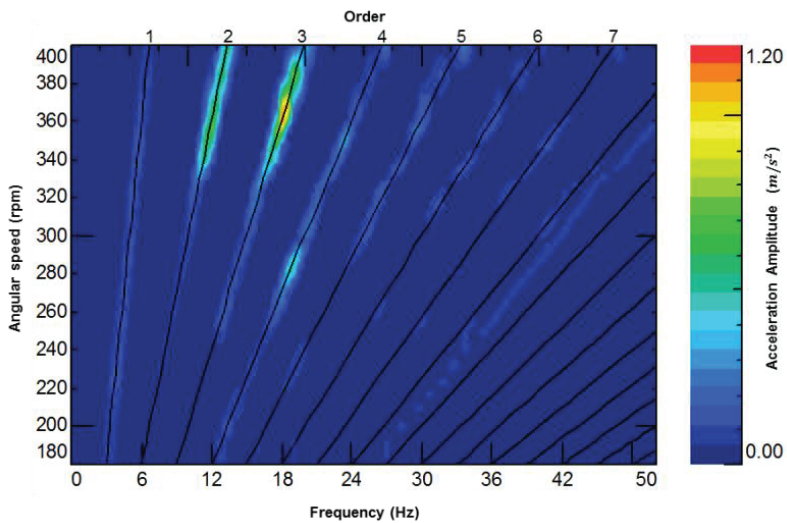

Figura 5. Grafico dell'ampiezza delle accelerazioni misurate sul telaio del trabatto A in direzione longitudinale durante una rampa di velocità.
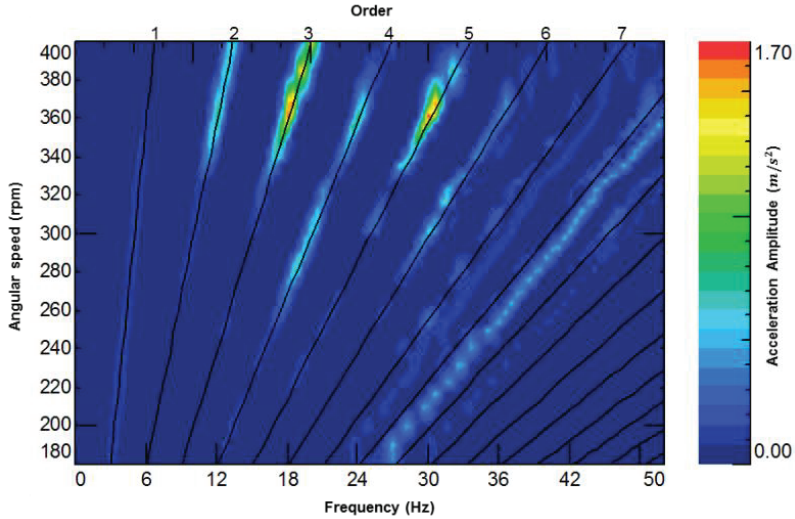
Figura 6. Grafico dell'ampiezza delle accelerazioni misurate sul telaio del trabatto A in direzione verticale durante una rampa di velocità.

Tabella 1. Valori RMS complessivi misurati sul telaio del trabatto A e B.

Velocità di rotazione dell'albero principale (*rpm*)	RMS Risultante Trabatto A (*m/s²*)	RMS Risultante Trabatto B (*m/s²*)
300	0.9	-
330	1	-
360 (velocità di lavoro)	2.6	1.2
400	2.8	-

Misure dell'oscillazione dell'torsionale

La misura dell'oscillazione torsionale è stata condotta in entrambi i sistemi in studio nei seguenti regimi di rotazione nominale: 145 rpm, 250 rpm e 360 rpm. Il set up di misura illustrato nella Fig. 7 è costituito da: una sonda ottica (Optel Thevon 152 G7 GP RV4) fissata su di un supporto magnetico solidale al telaio e uno zebra tape applicato all'albero principale. Questo test ha permesso di valutare la velocità istantanea dell'albero e le variazioni di velocità angolare dell'albero in funzione del tempo.

Per valutare in che modo varia la velocità angolare (Fig. 8), i segnali acquisiti nel tempo sono stati processati calcolandone lo spettro. I risultati di queste prove mostrano che il trabatto A presenta una variazione di velocità superiore al trabatto B a tutti i regimi di velocità testati. Inoltre si osserva che, all'aumentare della velocità dell'albero, la componente 1X aumenta e si ha una significativa amplificazione dalla componente 2X

Analisi modale

L'analisi modale è stata condotta sui piani porta pasta superiore e inferiore del cassetto dispari
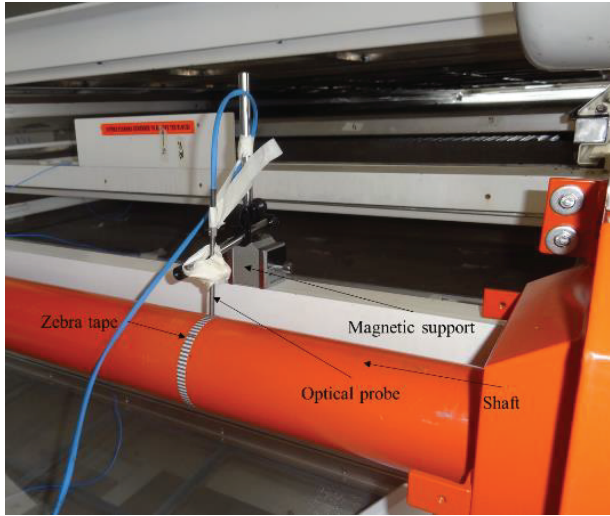
Figura 7. Set up di misura dell'oscillazione torsionale del trabatto B.
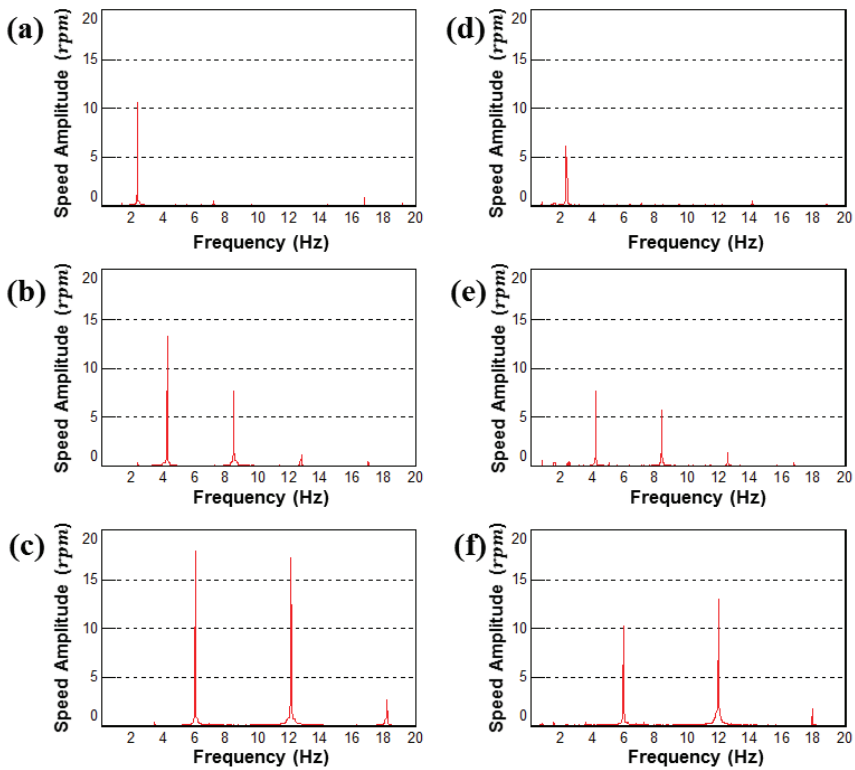

Figura 8. Spettro dell'ampiezza della velocità di rotazione dell'albero: (a) Trabatto A a 145 rpm, (b) Trabatto A a 250 rpm, (c) Trabatto A a 360 rpm, (d) Trabatto B a 145 rpm, (e) trabatto B a 250 rpm, (f) Trabatto B a 360 rpm.

e sul piano porta pasta del cassetto pari. L'obiettivo del test è valutare se l'elevato livello di vibrazioni misurato sul trabatto A alla velocità di lavoro è imputabile a fenomeni di risonanza. Il test è stato condotto mediante martello strumentato (PCB 086D20) e accelerometro (PCB 356B21) con una frequenza di campionamento di 256 Hz e una risoluzione in frequenza di 0.25 Hz. Allo scopo di ridurre il fenomeno del leakage è stata applicata una finestra esponenziale per i segnali accelerometrici mentre una force window è stata applicata per i segnali di forza. I punti di misura considerati non hanno coperto l'intera struttura a causa sia delle elevate dimensioni sia della difficoltà di accesso a molte parti del sistema. Si è valutata inoltre la coerenza di ogni singola martellata in tempo reale per garantire la qualità dell'eccitazione.

Ai fini di questo studio, sono state stimate le sole frequenze naturali (Tab. 2, Tab. 3 e Tab. 4) con il metodo PolyMAX [4] nella banda di frequenze comprese tra 0 a 40 Hz. L'analisi ha evidenziato la presenza di frequenze naturali prossime alle frequenze eccitate in condizioni di lavoro. Ad esempio, le frequenze naturali a circa 20 Hz e 28 Hz sono visibili in modo chiaro in Fig. 5 e Fig. 6.

Tabella 2. Frequenze naturali del piano porta pasta inferiore del cassetto dispari del trabatto A.

Modo	Frequenza naturale (Hz)
1	12.9
2	19.7
3	25.6
4	26.8
5	27.9
6	28.0
7	31.6

Tabella 3. Frequenze naturali del piano porta pasta superiore del cassetto dispari del trabatto A.

Modo	Frequenza naturale (Hz)
1	20.5
2	24.7
3	27.5
4	30.0
5	34.2

Tabella 4. Frequenze naturali del piano porta pasta del cassetto pari del trabatto A.

Modo	Frequenza naturale (Hz)
1	13.2
2	22.1

Discussione dei risultati e degli effetti delle modifiche progettuali

Dai dati sperimentali è possibile osservare che:
- il valore della risultante RMS delle accelerazioni misurate sul cuscinetto di banco è assunto come parametro rappresentativo del livello vibratorio del sistema. Il confronto tra il trabatto A e B ha oggettivato che il sistema A ha un livello vibratorio superiore al sistema B;
- i risultati ottenuti sul telaio del trabatto A dalle rampe di velocità evidenziano che è presente una significativa amplificazione delle armoniche proprio al regime di velocità di lavoro (360 rpm), mentre a regimi di velocità minori sono di molto inferiori;
- i risultati dell'analisi modale condotta sui cassetti del trabatto A dimostra che l'elevato livello di vibrazioni a 360 rpm è causato da fenomeni di risonanza;
- la misura delle oscillazioni torsionali dell'albero principale dei due sistemi in studio ha evidenziato che la velocità sul trabatto A ha oscillazioni superiori al trabatto B, in particolare al regime di lavoro previsto.

I risultati sperimentali ottenuti suggeriscono, da un lato, di evitare il regime di velocità operativo di 360 rpm e, dall'altro, di ridurre il grado di irregolarità del sistema. Innanzitutto può essere conveniente diminuire la velocità di lavoro del sistema in modo da non eccitare attraverso la legge di moto imposta le frequenze naturali dei cassetti. Per ovviare al problema dell'aumento dei tempi di trasporto del prodotto dovuti alla diminuzione di velocità la dimensione degli eccentrici dovrà essere aumentata. La significativa variazione di velocità dell'albero del trabatto A può essere invece limitata aumentando sia la potenza del motore asincrono trifase (in modo da controllare la coppia erogata più efficacemente) sia adottando un volano. In virtù di queste considerazioni sono state apportate le seguenti modifiche al trabatto A:
- riduzione del regime di velocità di lavoro da 360 rpm a 330 rpm;
- aumento della dimensione degli eccentrici da 7.5 mm a 9 mm;
- adozione di un motore più potente (si è passato da 4 kW a 7.5 kW);
- aumento del momento d'inerzia della puleggia calettata sull'albero principale.

Sperimentalmente si sono verificati gli effetti delle modifiche apportate al sistema in condizioni operative con le stesse metodologie esposte nella prima parte di questo paragrafo. Dalla Tab. 5 si osserva che, grazie alle modifiche apportate, il valore RMS dell'accelerazione misurata sul trabatto A si attesta a un valore inferiore a quello preso come riferimento relativo al trabatto B.

4. ANALISI CINEMATICA

Modello cinematico

Nel seguente sotto paragrafo si descriverà un modello cinematico a un grado di libertà usato per valutare la legge di moto descritta da un cassetto del trabatto. Il modello rappresentato in Fig. 9 rappresenta il sistema in condizioni di riposo, ossia nella condizione in cui la balestra non è deformata, ed è costituito da: una biella infinitamente rigida ($\overline{PQ}$) di lunghezza L_2, un eccentrico infinitamente rigido ($\overline{CQ}$) di dimensione L_3 e una balestra flessibile ($\overline{PT}$) di lunghezza L_1. Il cassetto è considerato come un elemento puntuale posto in P. L'angolo ϕ, che rappresenta la coordinata libera, è l'angolo spazzato dall'eccentrico rispetto all'asse x, l'angolo $\beta(\phi)$ è l'angolo spazzato da $\overline{PQ}$ rispetto all'asse x, ψ è l'angolo compreso tra $\overline{PQ}$ e x in condizioni di riposo.

Tabella 5. Confronto della risultante RMS delle accelerazioni misurate sul telaio.

	Risultante RMS (m/s^2)
Trabatto A (prima delle modifiche)	2.6
Trabatto A (dopo le modifiche)	1.0
Trabatto B	1.2

Nel seguito si ricaverà la posizione nel piano del punto P rappresentativo del cassetto in funzione dell'angolo di rotazione dell'eccentrico ϕ. La posizione del punto P (Eq. (3) e (4)) nel piano xy è derivabile dall'identità tra l'Eqn. (1) e (2):

$$\bar{Q} = \bar{P} + (\overline{Q - P}) \tag{1}$$

$$\bar{Q} = \bar{C} + (\overline{Q - C}) \tag{2}$$

$$x_P(\phi) = x_C + L_3 \cdot \cos\phi - L_2 \cdot \cos\big(\beta(\phi)\big) \tag{3}$$

$$y_P(\phi) = y_C + L_3 \cdot \sin\phi - L_2 \cdot \sin\big(\beta(\phi)\big) \tag{4}$$

Nelle Eqn. (3) e (4) l'angolo β dipende dall'angolo di manovella ϕ e, per esplicitare la sua dipendenza, si ricorrerà all'equazione dell'equilibrio dei momenti delle azioni elastiche nel punto P rispetto al polo Q.

Nel modello cinematico la balestra è rappresentata come una trave a incastro avente una rigidezza complessiva equivalente a 12 balestre in parallelo. La matrice di rigidezza della balestra nel punto P è data dall'Eqn. (5) ed è ricavabile moltiplicando la matrice di rigidezza
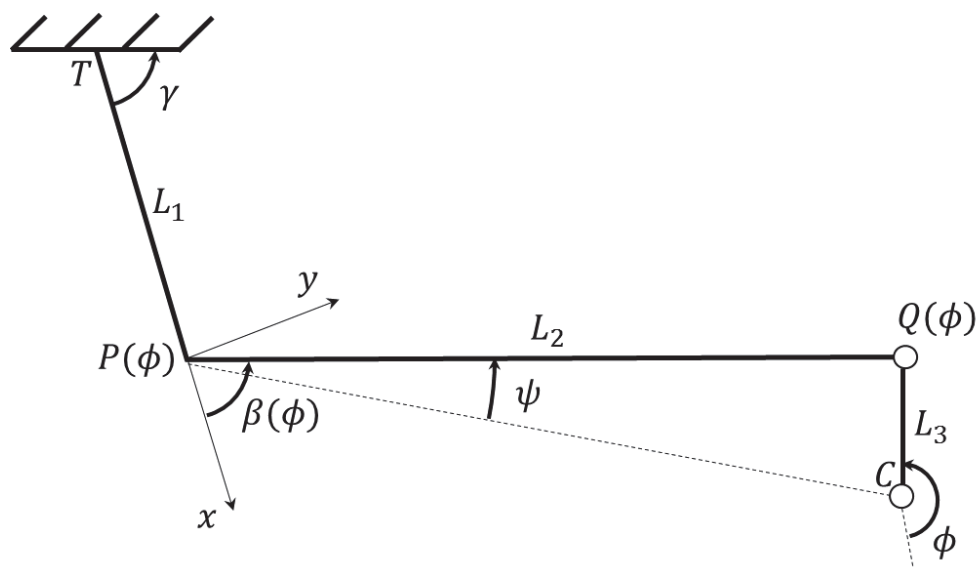
Figura 9. Modello cinematico di un cassetto del trabatto.

dell'estremo libero di una trave a sbalzo, nota in letteratura [5], per il numero di balestre sul singolo cassetto. Sia n il numero di balestre su un singolo cassetto e sia θ l'angolo di rotazione dell'estremo della balestra non vincolato al telaio, la matrice di rigidezza della balestra $\overline{PT}$ sull'estremo P è:

$$[K] = n \cdot \begin{bmatrix} k_{xx} & 0 & 0 \\ 0 & k_{yy} & k_{y\theta} \\ 0 & k_{y\theta} & k_{\theta\theta} \end{bmatrix} \tag{5}$$

La matrice $[K]$ è nota poiché dipende solamente dalle caratteristiche dal materiale della balestra e dalla geometria. Si può pertanto scrivere il legame tra le forze elastiche in P e lo spostamento nel punto P sapendo che $\theta(\phi) = \gamma - \beta(\phi)$:

$$\begin{Bmatrix} F_x \\ F_y \\ M \end{Bmatrix} = [K] \begin{Bmatrix} x_P \\ y_P \\ \gamma - \beta \end{Bmatrix} \tag{6}$$

Il momento delle forze elastiche in P rispetto a Q si ottiene dalla seguente relazione:

$$(\bar{P} - \bar{Q}) \times \bar{F} = \begin{vmatrix} \bar{\imath} & \bar{\jmath} & \bar{k} \\ x_P - x_Q & y_P - y_Q & 0 \\ F_x & F_y & 0 \end{vmatrix} \tag{7}$$

Sostituendo l'Eqn (7) all'interno dell'equazione di equilibrio dei momenti in P si ottiene

$$M + \left[F_y \cdot (x_P - x_Q) - F_x \cdot (y_P - y_Q) \right] = 0 \tag{8}$$

Dall'Eqn. (8) si ottiene, sostituendo al suo interno l'Eqn. (3), (4) e (6), l'espressione dell'angolo β in funzione dell'angolo ϕ. Una volta esplicitato $\beta(\phi)$ si può sostituirlo nell'Eqn. (3) e (4) per ricavare la posizione di P nel piano in funzione di ϕ.

Risultati

Le caratteristiche geometriche e dei materiali del trabatto A sono completamente note, pertanto si procede alla risoluzione dell'Eqn. (3) e (4) nell'ipotesi di velocità costante pari a 360 rpm. Si ottiene così lo spostamento del cassetto in funzione del tempo attraverso la relazione:

$$\phi = \omega \cdot t \tag{9}$$

Si analizzeranno qualitativamente i risultati ottenuti nella direzione ortogonale rispetto all'asse della balestra in quanto lo spostamento dovuto alla flessione è maggiore rispetto all'elongazione assiale. Dalla Fig. 10, ottenuta calcolando lo spettro dell'accelerazione in direzione y del punto P valutata derivando numericamente l'Eqn. (4), si osserva che l'accelerazione di P è con ottima approssimazione sinusoidale. Da questo risultato si evince che la legge di moto, nel caso di velocità di rotazione costante, produrrebbe solamente
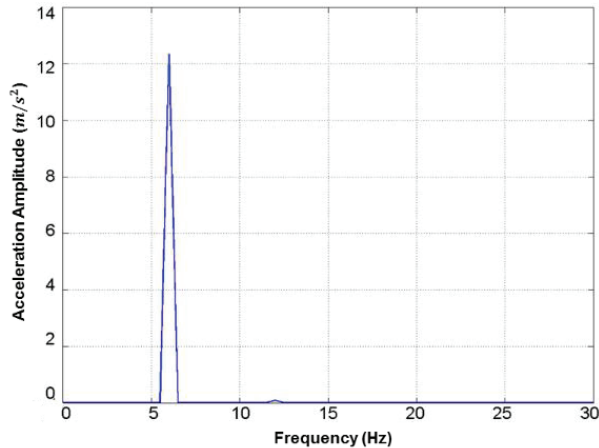
Figura 10. Spettro dell'ampiezza delle accelerazioni valutate lungo la direzione y del modello numerico con velocità costante.

un'eccitazione alla 1X; i dati sperimentali, tuttavia, mostrano la presenza di armoniche successive.

Si vuole, a questo punto, valutare dal punto di vista qualitativo l'effetto che avrebbe una velocità di rotazione variabile sulla legge di moto di un cassetto. La misura della velocità istantanea illustrata nella Fig. 8c, infatti, mostra che la velocità di rotazione del sistema non è costante come si è ipotizzato nel modello e ha componenti alla frequenza 1X e 2X.

Sfruttando i dati sperimentali, ottenuti dall'analisi dell'oscillazione torsionale dell'albero principale del trabatto A, si è scritta analiticamente una velocità di rotazione da inserire nel modello avente caratteristiche prossime a quella misurata:

$$\Omega = \Omega_0 + A \cdot \sin(\Omega_0 \cdot t) + B \cdot \sin(2 \cdot \Omega_0 \cdot t) \qquad (10)$$

dove Ω_0 è velocità di rotazione nominale di lavoro (360 rpm), A è la semi ampiezza della componente alla 1X della velocità di rotazione misurata sperimentalmente sul trabatto A e B è la semi ampiezza della componente alla 1X della velocità di rotazione misurata sperimentalmente sul trabatto A. La Fig. 11 mostra che la variazione di velocità angolare influenza in modo significativo la legge di moto. La 1X resta predominante ma si evidenziano ora una serie di armoniche successive alle frequenze 2X, 3X e 4X che risultavano assenti o trascurabili nel caso a velocità costante (Fig. 10).

5. CONCLUSIONI

In questo articolo si è presentata una campagna di misure sperimentali di un trabatto avente un elevato livello di vibrazioni e di un modello cinematico ad un grado di libertà per valutare la legge di moto descritta da un cassetto del trabatto.

Le misure sperimentali hanno efficacemente identificato le cause dell'elevato livello di vibrazioni del trabatto A, in particolare:
- eccitazione di frequenze naturali del sistema;
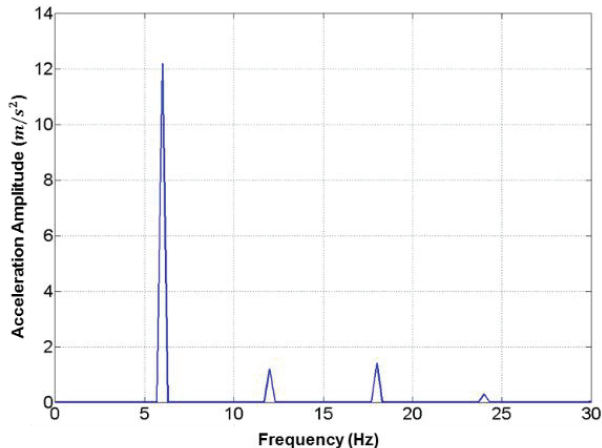- elevato grado di irregolarità dell'albero degli eccentrici.

Figura 11. Spettro dell'ampiezza delle accelerazioni valutate lungo la direzione y del modello numerico con velocità variabile.

Le modifiche apportate sulla base dei risultati sperimentali hanno permesso di ridurre le vibrazioni del sistema in modo soddisfacente.

Lo sviluppo di un modello cinematico a un grado di libertà ha mostrato la relazione che lega la legge di moto dei cassetti con la velocità dell'albero degli eccentrici. In particolare si è osservato che, con una velocità di rotazione variabile, le accelerazioni del cassetto sono differenti rispetto al caso in cui la velocità è assunta costante. Questa può essere una possibile spiegazione di come l'elevato grado di irregolarità del sistema generi una serie di armoniche successive nella legge di moto imposta ai cassetti. Queste armoniche successive a certi regimi di velocità vanno a eccitare le frequenze di risonanza causando un comportamento dinamico complessivo del trabatto non accettabile. Questo fenomeno spiegherebbe quindi il motivo per cui la riduzione del grado di irregolarità comporta una diminuzione significativa delle vibrazioni sul telaio del trabatto A.

Ringraziamenti

RIFERIMENTI

[1] Silversides, R., Dai, J.S., Seneviratne, L., 2005. "Force analysis of a vibratory bowl feeder for automatic assembly", *Journal of Mechanical Design*, 127, pp. 637–645.

[2] Maul, G.P., Maul, M.B., 1997. "A system model and simulation of the vibratory bowl feeder", *Journal of Manufacturing Systems*, 16(5) pp. 309–314.

[3] Mucchi, E., Di Gregorio, R., Dalpiaz, G., 2013. "Elastodynamic analysis of vibratory bowl feeders: Modeling and experimental validation", *Mechanism and Machine Theory*, 60, 60-72.

[4] In book, Heylen, W., Lammens, S., Sas, P., 2003. *Modal Analysis Theory and Testing*, Katholieke Univeriteit Leuven, Leuven.

[5] In book, Ghersi, A., Coraggio, R., 1990. *Analisi matriciale di strutture intelaiate*, CUEN, Napoli.

ANALISI DINAMICA NUMERICO-SPERIMENTALE DI UNA MOTOSEGA

Andrea Tosini
Dipartimento di Ingegneria (EnDIF),
Università degli Studi di Ferrara, Italia
E-mail: andrea.tosini@unife.it

Emiliano Mucchi
Dipartimento di Ingegneria (EnDIF),
Università degli Studi di Ferrara, Italia
E-mail: emiliano.mucchi@unife.it

Giorgio Dalpiaz
Dipartimento di Ingegneria (EnDIF),
Università degli Studi di Ferrara, Italia
E-mail: giorgio.dalpiaz@unife.it

Abstract*. Nell'ambito dell'analisi della durata a fatica di componenti meccanici la valutazione del danneggiamento mediante simulazioni numeriche si sta affiancando sempre più ai tradizionali approcci basati sulla costruzione di prototipi. Nel presente lavoro viene illustrata una metodologia di implementazione di un modello numerico che fa uso di simulazioni multibody e analisi agli elementi finiti per simulare il comportamento dinamico di una motosega. Il presente modello potrà essere utilizzato per minimizzare il danneggiamento a fatica del basamento della motosega e migliorarne le performance dinamiche. In particolare verranno affrontate le problematiche connesse alla realizzazione di un modello del propulsore aderente alla realtà sperimentale e la validazione del modello ad elementi finiti del basamento.*

Keywords*: analisi dinamica, multibody, modellazione a corpi flessibili.*

1. INTRODUZIONE

Oggigiorno nelle industrie, al fine di diminuire i costi di produzione, si è accentuata l'esigenza di progettare prodotti in tempi sempre più brevi, riducendo al minimo l'uso di prototipi. A seguito di questa tendenza, la valutazione del danneggiamento a fatica mediante tecniche numeriche si sta affiancando sempre più ai tradizionali approcci basati sull'utilizzo di prove sperimentali in laboratorio.

L'utilizzo di CAD moderni combinati con solutori agli elementi finiti e simulatori multibody permette di valutare velocemente l'efficacia di nuove soluzioni progettuali, senza ricorrere a fasi intermedie di prototipazione. La prova di laboratorio viene relegata solo a uno stadio finale dello sviluppo, quando le simulazioni hanno dato esito positivo sull'affidabilità del componente oggetto di studio [1].

In questo contesto si inserisce il presente lavoro, che descrive la realizzazione di un modello multibody di una motosega il cui chassis, realizzato in materiale polimerico, sarà in

futuro oggetto di modifiche strutturali per migliorarne la resistenza a fatica, nell'ottica di un restyling del prodotto. Verranno discusse le problematiche dell'implementazione di un modello che accoppia analisi multibody e analisi agli elementi finiti e verrà illustrato come le soluzioni adottate hanno permesso di implementare un modello numerico validato sperimentalmente dal punto di vista del comportamento dinamico dello chassis.

2. MODELLO MULTIBODY

Tipicamente le motoseghe sono dotate di uno chassis (nel seguito chiamato anche basamento) che ha la funzione di supporto per il motore e la barra di taglio, oltre a tutti gli altri accessori necessari al funzionamento della macchina. Nella motosega oggetto di studio il basamento è realizzato in poliammide rinforzata con fibra di vetro.

La macchina modellata (Fig.1) è equipaggiata con un motore due tempi di 52cc, in grado di erogare 2.3kW a 9000rpm. Nel modello, il motore è costituito esclusivamente da corpi rigidi ed è accoppiato a un modello a elementi finiti del basamento: le forze che si generano nel manovellismo si propagano al basamento flessibile, rendendo possibile studiare l'evoluzione di tensioni e deformazioni in funzione dell'angolo di manovella e del regime di rotazione. Il modello è stato realizzato in ambiente LMS Virtual.Lab Motion.

Modellazione del manovellismo

Il manovellismo è stato schematizzato raggruppando in un unico corpo rigido le masse dotate di moto alterno: il pistone completo di fasce elastiche, lo spinotto e la gabbia a rulli del piede di biella. Un secondo corpo rigido contiene tutte le masse dotate di moto rotatorio, ovvero l'albero motore e il cuscinetto della testa di biella. Biella, volano e frizione centrifuga completa di campana costituiscono ulteriori tre corpi rigidi del sistema. Infine, un ulteriore corpo è costituito dall'assemblaggio di cilindro e carter pompa: il suo compito è quello di trasmettere al basamento le forze provenienti dal manovellismo, inoltre costituisce una considerevole massa che grava sullo chassis e di cui è necessario tenere conto per poter modellare in modo attendibile il comportamento dinamico dell'intero assemblato.
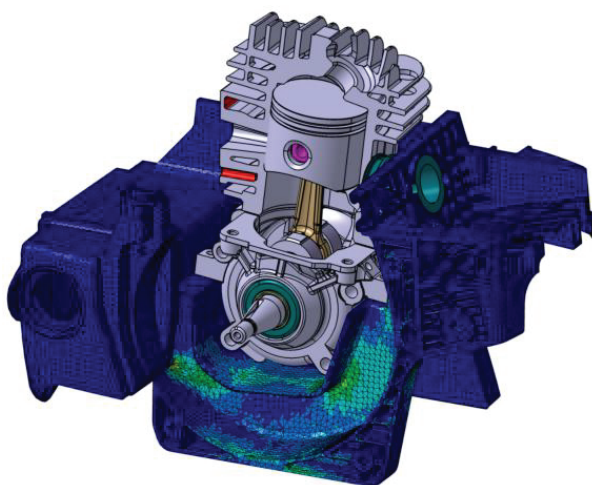

Figura 1. Modello multibody a corpi flessibili della motosega

La modellazione delle coppie cinematiche che connettono i vari membri ha richiesto un'attenta analisi per evitare che l'eventuale presenza di gradi di libertà ridondanti nel meccanismo generassero un meccanismo la cui legge di moto non corrisponde alla realtà. A tal fine sono state utilizzati due revolute joint per connettere la biella all'albero e al pistone e un planar joint per modellare l'accoppiamento pistone-cilindro. L'assemblaggio del volano e della frizione con l'albero motore è stato realizzato attraverso bracket joints.

Menzione particolare meritano i cuscinetti di banco: essendo cuscinetti a sfere rendono iperstatico l'albero e una loro schematizzazione attraverso revolute joint renderebbe sovravincolato il modello, costringendo il solutore multibody a disattivare in automatico uno dei due. Così facendo però le forze provenienti dal manovellismo si scaricherebbero su un solo supporto del blocco motore rendendo la distribuzione delle forze sul basamento diversa dal comportamento reale. Per aggirare il problema si è scelto di adottare dei bushing elements, e modellare le coppie cinematiche in corrispondenza dei cuscinetti con elementi dotati di una propria cedevolezza, in grado di applicare forze elastiche e smorzamenti viscosi fra albero e blocco motore.

Le forze elastiche applicate da ogni bushing dipendono dalla rigidezza dei corrispondenti cuscinetti. Avendo a diposizione le caratteristiche geometriche dei cuscinetti è stato possibile stimare la loro rigidezza radiale attraverso una simulazione agli elementi finiti. Applicando un carico noto alla ralla interna di ogni cuscinetto di banco in direzione radiale e misurandone lo schiacciamento è possibile stimare la rigidezza dal rapporto forza/schiacciamento. Vista la semplicità costruttiva del propulsore, ci si è limitati a ricercare un valore medio di rigidezza per ogni cuscinetto. In particolare per ognuno di essi si sono considerate due posizioni estreme:

      i)   sfera perpendicolare al carico (Fig.2a)
      ii)   vuoto perpendicolare al carico (Fig.2b).

Dal rapporto forza/schiacciamento dell'anello interno sono stati ricavati due valori diversi di rigidezza, la cui media è stata usata come valore di rigidezza radiale all'interno della simulazione.

Le forzanti in ingresso al modello sono la forza generata dalla combustione e una coppia resistente applicata all'albero motore. La forza agente sul cielo del pistone è nota da campagne sperimentali del costruttore che ha misurato la pressione in camera di combustione e nella camera di manovella in funzione dell'angolo di rotazione (Fig.3).

Trattandosi di un motore due tempi, che quindi aspira e comprime parzialmente la miscela aria-carburante nel carter, è necessario conoscere anche la pressione che si sviluppa nella camera di manovella e tenerne conto quando si calcola la risultante delle forze sul pistone: la forza risultante si ottiene a partire dalla somma vettoriale delle forze generate dalle pressioni sopra e sotto il cielo del pistone. Nel modello sviluppato, è stato possibile ricavare tale forza in funzione dell'angolo di manovella e del regime di rotazione del motore da 7000rpm a 9000rpm.

Modellazione delle dissipazioni per attrito e per pompaggio

In condizioni di funzionamento reali il motore è sottoposto ad azioni frenanti quali la forza di attrito fra i vari membri e le perdite per pompaggio, ma il modello fino ad ora descritto ancora non contempla nessuna di queste dissipazioni.

Per fare in modo che il comportamento del modello sia comparabile al comportamento del motore reale è necessario introdurre queste dissipazioni di energia. Tuttavia, benché diversi lavori presenti in letteratura riguardo modelli multibody di motori a combustione interna affrontino l'argomento [2-3], l'interesse è stato rivolto soprattutto a motori quattro tempi per
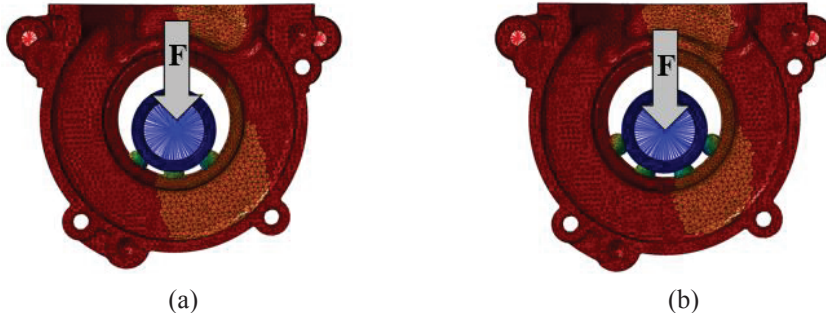
(a)   (b)

Figura 2. Stima della rigidezza dei cuscinetti di banco: (a) sfera perpendicolare al carico, (b) vuoto perpendicolare al carico
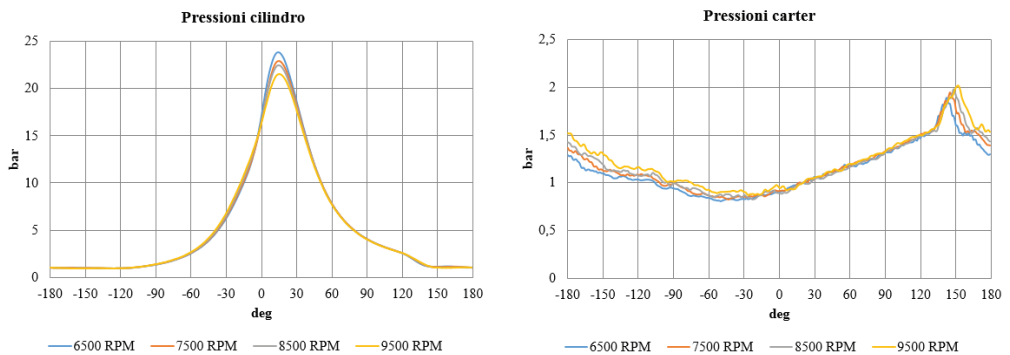

Figura 3. Pressioni misurate in camera di combustione e nel carter (la posizione a 0° corrisponde al punto morto superiore)

autotrazione o due tempi diesel per applicazioni navali [4]. La maggioranza dei lavori poi, è concentrata alla modellazione tribologica delle coppie cinematiche, in particolare nell'accoppiamento pistone-cilindro visto che è la zona in cui si concentrano la maggioranza delle perdite per attrito[5-7].

Nel presente lavoro invece, si è preferita seguire una metodologia semplificata, scegliendo di inglobare tutte le dissipazioni in una coppia concentrata a un'estremità dell'albero motore. È doveroso sottolineare che questo modo di procedere funziona bene solo quando il meccanismo viene modellato interamente con corpi rigidi, non fornisce però risultati affidabili quando si introduce la flessibilità di un componente del manovellismo.

Scegliendo opportunamente la coppia resistente si può regolare la velocità di rotazione del motore simulato al regime desiderato fra 7000 e 9000rpm, e l'andamento della velocità angolare della manovella è confrontabile con ottima approssimazione con quella sperimentale.

Diverse strategie possono essere seguite per impostare la coppia resistente: la più semplice, quella di imporre un opportuno valore costante nel tempo, permette di simulare il motore in regime costante attorno la velocità media ma generalmente, con questa strategia, si osserva che le oscillazioni della velocità angolare attorno al valore medio sono diverse da

quelle misurate al banco prova. Poiché il nostro interesse era quello di sviluppare un modello in cui le variazioni di velocità angolare attorno alla velocità media fossero confrontabili con quelle del motore reale, si è scelto di modellare l'andamento della coppia resistente in funzione dell'angolo di manovella, ottenendo le distribuzioni di Fig.4.

Si può risalire agevolmente alla formulazione della coppia resistente da un bilancio delle coppie applicate alla manovella [8]. Definito θ l'angolo percorso dall'albero motore dal punto morto superiore, r il raggio di manovella e l la lunghezza della biella, il coefficiente di velocità del manovellismo è definito come:

$$rK(\theta) = r\left(\sin\theta + \frac{1}{2}\frac{r}{l}\sin 2\theta\right) \tag{1}$$

La coppia generata dalla combustione dei gas è immediatamente ricavabile dalla pressione misurata sperimentalmente $P_{gas}(\theta)$ e dalla superficie del cielo del pistone A_{pist}:

$$T_{gas} = rK(\theta)P_{gas}(\theta)A_{pist} \tag{2}$$

La biella può essere sostituita da un sistema di due masse dinamicamente equivalente concentrate nella testa e nel piede. Indicando con m_{alt} la somma di tutte le masse dotate di moto alterno, la coppia ridotta all'albero causata dalla loro inerzia è calcolabile come:
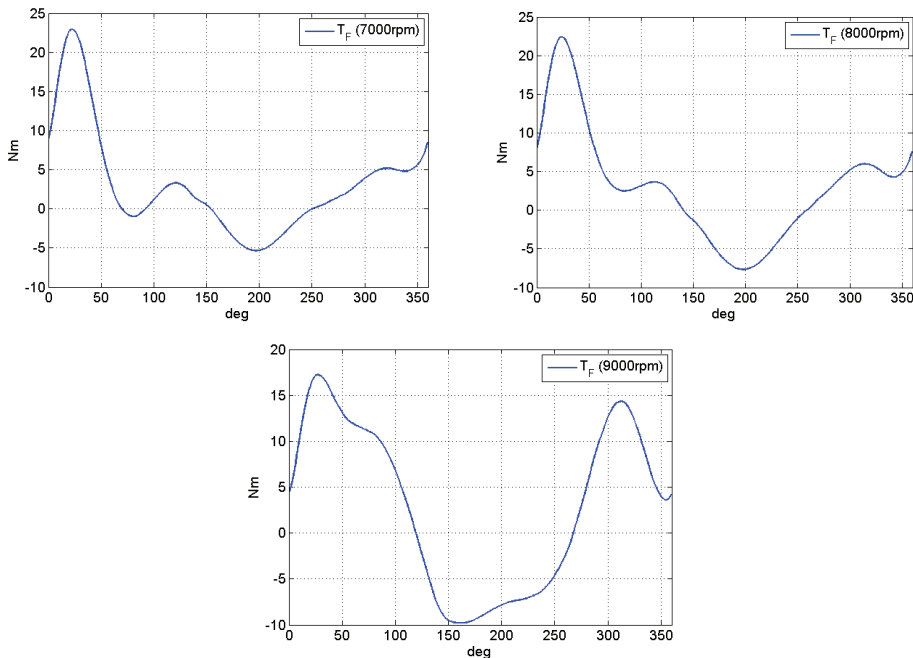
Figura 4. Coppia resistente in funzione dell'angolo di manovella per ogni regime preso in considerazione

$$T_{INalt} = rK\left[m_{alt}r\left(K\dot{\omega} + \omega^2 \frac{dK}{d\theta} \right) \right] \tag{3}$$

Chiamato I il momento di inerzia delle masse rotanti, la coppia generata dalla loro inerzia è esprimibile come:

$$T_{INrot} = I\dot{\omega} \tag{4}$$

Le ultime coppie che intervengono nel bilancio sono la coppia frenante applicata dal banco freno T_{brake} e la coppia ridotta all'albero causata da tutti gli attriti interni del motore $T_{friction}(\theta)$.

La coppia resistente che agisce sul motore è data dalla risultante della coppia applicata dal freno e quella causata dagli attriti. Chiamando la risultante $T_F(\theta)$, attraverso un bilancio di tutte le coppie in gioco si riesce a di risalire alla sua formulazione in funzione dell'angolo di manovella:

$$T_F(\theta) = T_{friction}(\theta) + T_{brake} = T_{gas}(\theta) - T_{INalt}(\theta) - T_{INrot}(\theta) \tag{5}$$

L'andamento di ognuna delle coppie che interviene nel bilancio è riportato in Fig.5, prendendo in considerazione il regime di 7000 giri/min.

Introduzione della flessibilità del basamento nel modello multibody

L'analisi della flessibilità nel basamento è stata realizzata attraverso l'analisi di Craig-Bampton. Il basamento plastico è stato dapprima discretizzato con elementi tetraedrici lineari per poter eseguire l'analisi ad elementi finiti (FE). L'accoppiamento del modello agli elementi finiti con il modello a corpi rigidi del motore è stato eseguito inserendo elementi rigidi (Nastran RBE2, evidenziati in Fig.6a) nelle zone in cui il blocco si avvita al basamento, inoltre altre interfacce sono state inserite nelle zone di ancoraggio delle molle fra il basamento e il manico che viene impugnato dall'operatore.
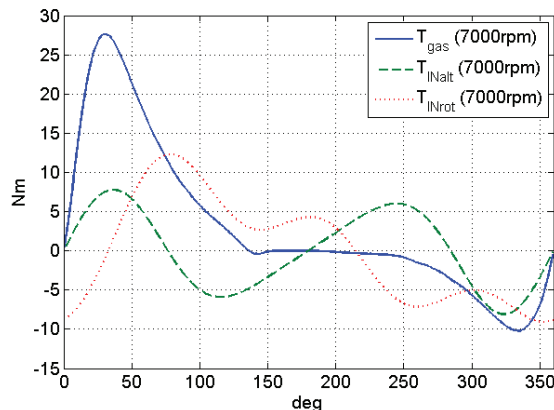

Figura 5. Distribuzioni delle coppie che intervengono nel calcolo della coppia frenante del modello
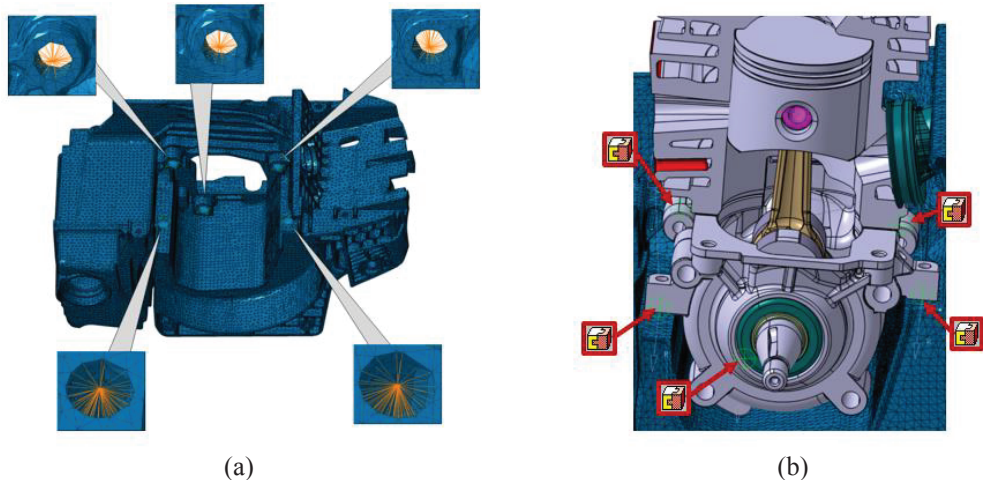
Figura 6. Zone di interfaccia fra il basamento flessibile e il modello a corpi rigidi del motore. (a) elementi Nastran RBE2, (b) bracket joints

Nei software multibody è possibile creare interfacce fra corpi diversi attraverso la definizione di vincoli cinematici che collegano i vari corpi. I vincoli scelti per la modellazione sono bracket joint per le zone di ancoraggio con il blocco motore, in quanto sono adatti per modellare il collegamento rigido che le viti creano con il basamento (Fig.6b).

Le molle che connettono basamento e manico invece sono state modellate con elementi bushing e quindi non necessitano di ulteriori vincoli cinematici.

Gli elementi bushing che modellano le molle necessitano della definizione della rigidezza in tutte e tre le direzioni spaziali ma, usualmente, per molle elicoidali è nota solo la rigidezza a trazione della molla. Il limite è stato superato impostando un'analisi agli elementi finiti simile a quella descritta per i cuscinetti di banco anche per le molle, imponendo a una estremità un carico di taglio e misurando lo spostamento della spira caricata. Ripetendo il procedimento per tutte e tre le direzioni spaziali si sono potute stimare con attendibilità i valori di rigidezza da inserire nei bushing elements corrispondenti.

Inoltre, dal momento che l'elemento bushing di Virtual.Lab supporta anche la definizione di smorzamenti viscosi, si è introdotto anche un coefficiente di smorzamento per ogni molla, valutato in modo iterativo fino alla convergenza con i risultati dei rilievi accelerometrici sperimentali ricavati al banco prova.

3. VALIDAZIONE SPERIMENTALE DEL MODELLO

Il modello multibody descritto è stato oggetto di validazione sperimentale sia per quanto riguarda la modellazione del motore, sia per l'analisi FE del basamento flessibile.

Validazione della velocità angolare

La velocità angolare misurata all'uscita dell'albero motore del modello fino qui descritto è stata confrontata con quella misurata sperimentalmente al banco prova impiegando un encoder magnetico a 360 impulsi/giro.

Il confronto è stato fatto operando una media sincrona sul segnale acquisito dall'encoder per minimizzare la componente random della misurazione. L'applicazione di un filtro passabasso fino alla terza armonica ha permesso di regolarizzare la distribuzione della velocità angolare eliminando componenti spurie causate da vibrazioni torsionali a alta frequenza.

I grafici seguenti (Fig.7-9) riportano il confronto nel dominio degli angoli e nel dominio degli ordini fra l'andamento della velocità angolare prevista dal modello multibody e quella rilevata sperimentalmente a diversi regimi. Le differenze fra le curve sono imputabili all'intervento del controllo attivo operato dal banco freno per mantenere costante la velocità angolare: nel modello sviluppato invece l'azione del freno è stata modellata come una coppia frenante costante nel tempo. In generale è comunque possibile affermare che i risultati numerici hanno un buon riscontro rispetto a quelli sperimentali.
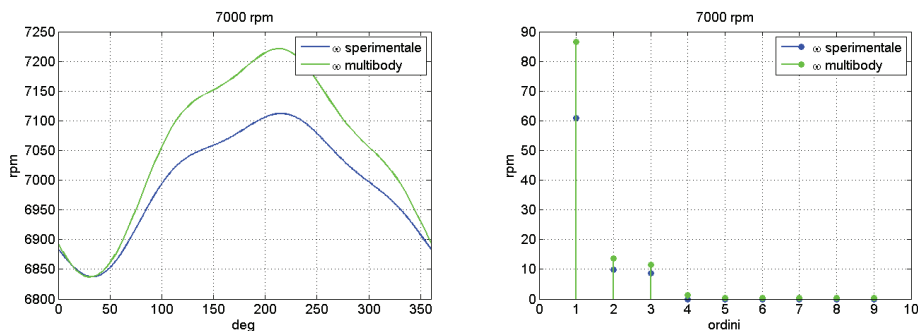
Figura 7. Confronto fra la velocità angolare sperimentale e quella prevista dal modello. Regime di 7000rpm
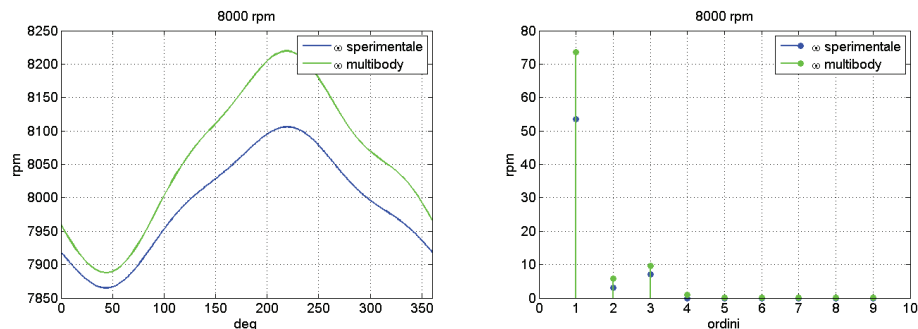
Figura 8. Confronto fra la velocità angolare sperimentale e quella prevista dal modello. Regime di 8000rpm
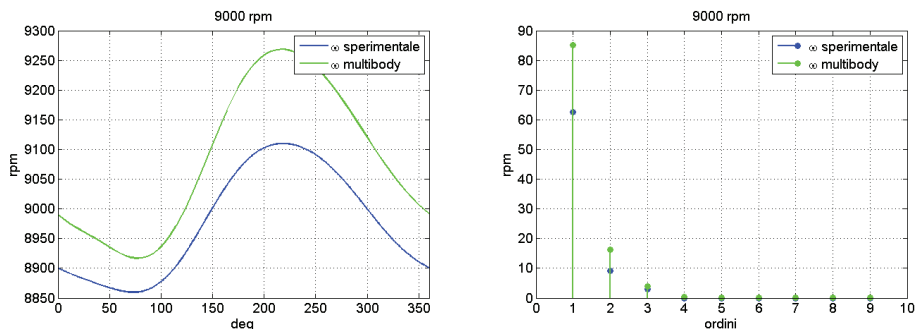
Figura 9. Confronto fra la velocità angolare sperimentale e quella prevista dal modello. Regime di 9000rpm

Correlazione numerico-sperimentale del modello flessibile del basamento

Poiché l'analisi di Craig-Bampton adottata dal codice multibody si basa sulla determinazione delle matrici modali del modello FE, si è ritenuto opportuno validare le deformate modali del basamento attraverso l'analisi modale sperimentale.

Il controllo è stato fatto sulle frequenze naturali stimate dal modello agli elementi finiti e sulle forma modale corrispondente a ogni frequenza naturale. Si è ritenuto sufficiente considerare solo le prime 3 frequenze naturali perché, da test accelerometrici effettuati sul basamento della macchina in condizioni di funzionamento, sono risultate essere le frequenze maggiormente eccitate dal motore. L'analisi è stata effettuata sul solo basamento (Fig.10a), senza la presenza del motore e di altri accessori della motosega, mantenendolo in condizioni libere e utilizzando un martello strumentato (PCB 086D05) e un accelerometro triassiale (PCB 356B21).

Il Modal Assurance Criterion (MAC) è stato utilizzato per correlare le deformate modali sperimentali con le deformate del modello agli elementi finiti corrispondente e, come si vede dalla matrice in Fig.10b, i valori ottenuti sulla diagonale sono prossimi a 1, indice che le prime tre deformate modali previste dal modello numerico sono molto simili a quelle reali.
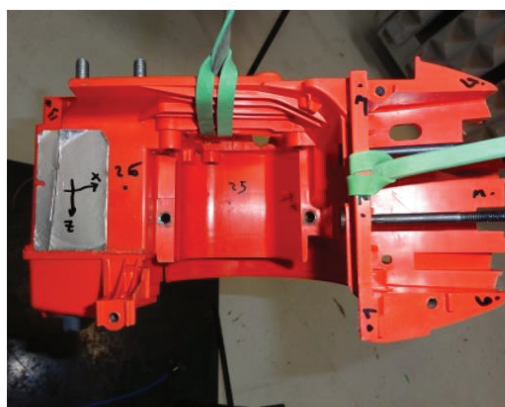
(a)   (b)

Figura 10. (a) basamento sospeso in condizioni libere, (b) matrice del MAC

L'analisi modale sperimentale inoltre, ha permesso anche di risalire agli smorzamenti modali del basamento: i valori ottenuti, inseriti nella analisi di Craig-Bampton, sono necessari per ottenere tensioni e deformazioni accurate dello chassis.

Misure accelerometriche sul basamento

Una campagna sperimentale è stata condotta anche sulle accelerazioni sperimentate dal basamento durante il funzionamento mantenendo un'accelerazione costante del motore da 6000 a 10000 giri/min.

Scopo delle misure era di quantificare il livello di filtraggio operato dalle molle che sostengono il manico dell'utilizzatore e risalire allo smorzamento della sospensione per poterlo implementare nel codice multibody.

La macchina è stata preparata al banco freno e equipaggiata con accelerometri monoassiali e triassiali (dello stesso tipo utilizzato per l'analisi modale sperimentale) in diversi punti del basamento e dell'impugnatura del manico (Fig.11).

Due accelerometri triassiali sono stati posizionati sul basamento e sul manico in prossimità del serbatoio olio, nella zona anteriore della macchina, misurando l'efficacia di filtraggio della molla a cui si aggancia il manico in quel punto. Due accelerometri monoassiali invece sono stati posizionati a monte e a valle della molla di sostegno nella zona laterale della motosega, permettendo così di avere una panoramica delle accelerazioni a cui è sottoposto lo chassis.

I valori RMS di accelerazione acquisiti in prove a regime costante sono stati utili per calibrare rigidezza e smorzamento degli elementi bushing che schematizzano le molle di sostegno del manico nel modello multibody.

Conclusioni

Nel presente lavoro è stata presentata una metodologia di modellazione multibody di una motosega con motore a combustione interna il cui chassis è stato modellato come un elemento flessibile di cui si vuole studiare l'evoluzione nel tempo di deformazioni e tensioni.

Il modello presentava delle criticità di implementazione e una larga parte del lavoro è stata dedicata alla descrizione di una metodologia semplificata per modellare gli attriti interni del motore attraverso una coppia concentrata sulla manovella che tiene conto di tutte le resistenze presenti nel motore (frenatura del banco di prova, attrito fra pistone e cilindro, dissipazioni di energia per pompaggio, ecc…)
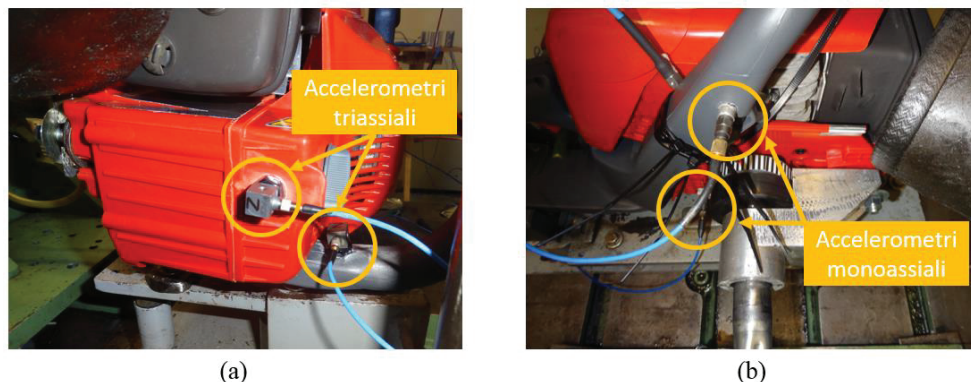

(a)   (b)

Figura 11. Posizioni degli accelerometri sul basamento

La validazione sperimentale del modello ha interessato più aspetti: è stata condotta una verifica della distribuzione di velocità angolare dell'albero motore in funzione dell'angolo di manovella prevista dal modello con quella misurata con un encoder magnetico, sono state condotte misure di accelerazione del basamento e comparazioni delle deformate modali previste dal modello numerico con quelle sperimentali.

Le previsioni del modello si sono sempre attestate in linea con le misurazioni sperimentali, con margini di errori contenuti.

Il modello risulta essere affidabile per successive analisi di tensioni e deformazioni e per prevedere eventuali modifiche da apportare alla geometria nell'ottica di ottimizzare la durata a fatica del basamento.

REFERENCES

[1] Ambrogi, F., Braccesi, C., and Cianetti, F., 2001. "Analisi di affidabilità di un componente meccanico". *XXX Convegno Nazionale AIAS.*

[2] Drapal, L., Novotny, P., Pistek, V., and Beran, M., 2012. "Cranktrain dynamics simulation". *Journal of Automobile Engineering,* **7**(4), December, pp. 26–34.

[3] Perera, M., Theodossiades, S., and Rahnejat, H., 2010. "Elasto-multi-body dynamics of internal combustion engines with tribological conjunctions". *Proc. IMechE part K: Multi-body Dynamics,* **224**, March, pp. 261–277.

[4] Jiménez Espadafor, F.J., et al., 2014. "Measurement and analysis of instantaneous torque and angular velocity variations of a low speed two stroke diesel engine". *Mech. Syst. Signal Process.,* **49**(1-2), December, pp. 135–153.

[5] Sutaria, B.M., Bhatt, D.V., and Mistry, K.N., 2009. "Simulation and modelling of friction force and oil film thickness in piston ring-cylinder liner assembly of an I.C. engine". *Proceedings of the World Congress on Engineering,* **2**, July.

[6] In book, Heywood, J.B., 1988. *Internal Combustion Engine Fundamentals*, McGraw Hill, Chap. 13, pp. 729–734.

[7] Ma, Z., Henein, N.A., and Bryzik, W., 2006. "A model for wear and friction in cylinder liners and piston rings". *Tribology Transactions*, **49**(3), pp. 315-327.

[8] Rezeka, S.F., and Henein, N.A., 1984. "A new approach to evaluate instantaneous friction and its components in internal combustion engines". *SAE Technical Paper*.

SOLUTION OF AN INVERSE PROBLEM IN THE HIGH CYCLE FATIGUE THEORY

Alessandro Freddi
Professor Emeritus
Department of Industrial Engineering,
University of Bologna, Italy
E-mail: alessandro.freddi@unibo.it
af468@cam.ac.uk

Abstract. *A simulation model of the fatigue strength and the stress concentration at critical points is discussed. This is an inverse problem that is presented for slender as well as for massive structures.*

SYMBOLS

R_m = Ultimate Stress in Tension.

R_s = Yielding Stress in Tension for 0.2%.

R_{bs} = Yielding Stress in Bending.

τ_s = Yielding Shear Stress in Torsion.

$\sigma_{zdW}{}^1$ = Fatigue Amplitude Limit for Alternate Load (R=-1) in Push/Pull Test.

σ_{zdo} = Upper Fatigue Limit for ($R = 0$) in Push/Pull Test.

σ_{bW} = Fatigue Amplitude Limit for Alternate Load ($R = -1$) in Bending Tests

  (with Moment in one plane or with rotating Moment).

σ_{bo} = Upper Fatigue Limit for ($R = 0$) in Bending Tests

  (with Moment in one plane).

σ_m = Mean value

τ_W = Fatigue Amplitude Limit with Torsional Alternating Moment ($R = -1$).

τ_o = Upper Fatigue Limit for ($R = 0$) in Torsion Test.

χ'_{load} =Relative Stress Gradient

K_t =Stress Concentration Factor

σ_D =fatigue Endurance Limit

σ_{Dk} =Component Fatigue Endurance Limit

$(d\sigma/dx)_{load}$ =Stress Gradient due to load

$\sigma_{res.}$ =Residual Stress

σ_{tot} =Total Stress due to Load plus Residual Stress

Suffixes

a = Amplitude

zd = Tension/compression stress

b = Bending stress

W = Fully reversed stress $(R = -1)$

o = Stress at origin $(R = 0)$

s = Yielding

1. MODELS FOR NOTCH EFFECT DESCRIPTION

For slender structures with geometrical discontinuities (e.g. a cylindrical body with circumferential groove) subject to cyclic loading with $(R = -1)$, the Notch Fatigue Factor K_f (in German literature β_k) is defined for each basic loading state (push/pull, bending, torsion) as:

$$K_f = \beta_k = \frac{\sigma_{aD}}{\sigma_{aDk}} \qquad (1)$$

where σ_{aD} is the *nominal* endurance fatigue limit of a *smooth specimen* with the diameter of the notch root, and: σ_{aDk} is the *nominal* endurance fatigue limit of the *notched* specimen.

The semi-logarithmic diagram in Fig.1 is an example [1], for push/pull tested specimens.
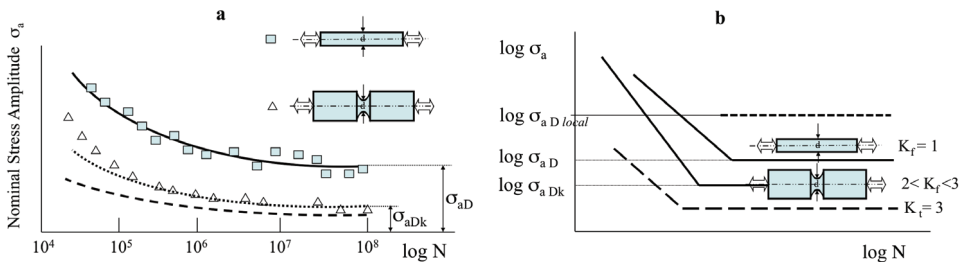
Figure 1. a) Semi-logarithmic and b) double-logarithmic fatigue curves for notched specimens, obtained from the fatigue curve for smooth specimens reduced by the stress concentration factor K_t and by the fatigue factor K_f
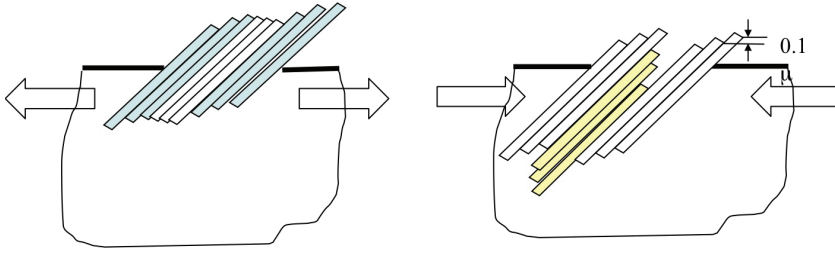
Figure 2. Generation of extrusions and intrusions for a cyclic load at the surface of a body

It might be argued that notched specimens have fatigue limits of smooth specimens reduced by the factor K_t. The dotted curve at the bottom of the diagram a) shows that this estimation does not agree with the experimental results (triangular marks) of the actual notched specimens.

The most realistic estimation (especially beyond $5 \cdot 10^4$ cycles, i.e. in actual high cycle fatigue condition) of the endurance fatigue limit for notched specimens, is obtained from the fatigue curve of the corresponding smooth specimens, with a reduction K_f, being, in this example $2 < K_f < K_t$ with $K_t = 3$. The experimental measurements for fatigue at a low number of cycles do not agree with this prevision, as it is possible to observe in the same Figure a). The fatigue factor (defined for the loading condition $R = -1$) interprets the reduction of the fatigue life in a notched specimen compared to a smooth specimen. This conclusion depends on material properties, as well as on the concentration factor K_t and on the kind of load (tension/compression, bending, torsion). In order to clarify the difference between K_f and K_t, it is necessary to look at the physics of the material at the root of the notch.

The crack nucleation can be explained by the dislocations theory. This explains the displacements of the atomic planes placed in the most favorable directions of shear stresses at 45 degrees with respect to the maximum normal stress (that is tangent to the surface) when high fatigue loading is present. This slip movement generates not reversible extrusions and intrusions from which small plastic valleys and peaks and, progressively, micro-cracks arise after a sufficient number of cycles.

The formation of the plastic slip is confined to a small but finite volume of material, Fig. 2. This volume is circumscribed by a curve at $\tau_{max} = const.$ i.e. the threshold value for a critical shear stress at the root of the notch, Fig.3 and can thus be visualized by the isochromatic curves, given by the Photoelasticity stress analysis method, see e.g. Fig. 7 b). The presence of the micro-cracks clarifies the reason for a lower value of K_f in comparison with K_t and justify a hypothesis on the fatigue notch factor: fatigue damage is due not only to a single stress value but to the whole state of stress in a small volume, close to the maximum value. It is thus reasonable to consider the effective critical stress not as the maximum elastic value but as the mean value on a finite small volume: $\sigma_{eff} = K_f \cdot \sigma_{nom}$

A second definition of K_f, can thus be obtained as, Fig.3:

$$K_f = \frac{\sigma_{eff}}{\sigma_{nom}} < K_t = \frac{\sigma_{max}}{\sigma_{nom}} \qquad (2)$$

The reduction of K_f is not to be interpreted as due to an extensive plasticity, that is not compatible with the fatigue phenomenon at a high number of cycles. The phenomenon remains essentially elastic, hypothesizing only a local effect of micro-plasticity.
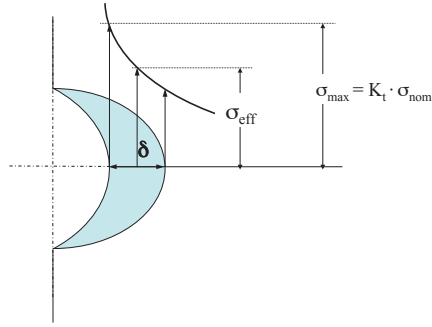
Figure 3. Shape of the maximum shear stress at the root of a notch

2. SUPPORT FACTOR

In order to overcome the limits of the Saint Venant theory based on slender (1D rod-shaped) or thin (2D shell-shaped) components, a theory was developed for extending the integrity assessment to 3D block-shaped bodies. It is not unusual for some parts in mechanical structures to be massive or, more often, for some details in slender constructions to have three-dimensional states of stress. In these cases neither the elementary theory hypothesis is respected, nor a reference cross-section can be defined.

In these cases we introduce the concept of *Support Factor* at the most stressed points where a potential fatigue crack can nucleate, sometimes called critical points or *reference points* in [2].

This hypothesis assumes that the fatigue strength is not a material property but a component property (at its reference points), so that the assessment of fatigue strength for a component is done comparing the state of stress with the fatigue limits at those points. The theory defines the strength, through the concept of the stress gradient, a local value that takes into account the support effect of the points close to the reference ones, i.e. of the effect of the confining material volume.

This is not the only theory that tries to evaluate the support of internal fibers. A proposal, [3] based on an idea of *Lazzarin* and *Tovo* [4], argues that the local fatigue strength is sensitive to the integral of the stress contiguous to the most stressed points. This integral can be extended on a critical volume, on a critical area or on a critical length, depending on the geometry of the discontinuity.

A problem is due to the practical determination of these volumes, areas or length sizes. These parameters are determined via the value of ΔK_{th}, a Fracture Mechanics parameter. In this way a unified theory between fatigue and Fracture Mechanics is achieved, [5]. In spite of this attractive perspective, the Fracture Mechanics parameter is not easy to determine, especially in the case of surface treatments and possible states of residual stresses in thin surface layers.

Support Factor in Slender Bodies

Starting from slender bodies for which the stress concentration factor as well as the fatigue factor can be defined, it is possible to write in a different way the previous Eq.1, here re-

peated:[2]:

$$\sigma_{aDk} = \frac{\sigma_{aD}}{K_f}$$

Multiplying both members for K_t, having called n the ratio:

$$n = \frac{K_t}{K_f} \qquad (3)$$

we obtain the following Equation:

$$\sigma_{aDk} \cdot K_t = \sigma_{aD} \cdot n \qquad (4)$$

or:

$$n = \frac{\sigma_{aDk} \cdot K_t}{\sigma_{aD}} \qquad (5)$$

Even if a relationship between n and η exists, the n factor, called *Support Factor*, expresses a more general concept than η, because it keeps its validity also for not slender bodies.[3] Before demonstrating this statement, it is appropriate to remember two points:

- The stress concentration for each type of loads that can act on a structure (tension/compression, shear, bending and torsion) is defined referring it to the nominal area of specimen cross-section, *cleansed* by the discontinuity.

- the Notch Fatigue Factor K_f, for each kind of loads is defined as:

$$K_f = \beta_k = \frac{\sigma_{aD}}{\sigma_{aDk}} \qquad (8)$$

where: σ_{aD} is the endurance fatigue limit (max. value for $R = -1$) of a smooth specimen with the diameter at the notch root and: σ_{aDk} is the endurance fatigue limit (max. value for $R = -1$) of the notched specimen. It is important to remark that both factors are conventionally defined, all the values of σ_a being *nominal values* and, similarly conventional, the endurance limit of a smooth specimen for a tension/compression fatigue case could be assumed, for each type of internal stress.

Support Factor for 3D-bodies

Eq. 5 can be read as follows (see Fig. 1):

$$n = \frac{\sigma_{aD\ local}}{\sigma_{aD\ smooth}} \qquad (9)$$

---

[2]The author decided to adopt, for mathematical symbols, indexes and formulas, the notation used in the German Fatigue Handbooks (as [2]), see Symbols Section. It offers unambiguity in distinguishing among symbols, in spite of a high number of suffixes. The apparent difficulty of the choice avoids the doubts that arise in interpreting the meaning of a great number of variables.

[3]This factor is related to the more common *Notch Sensitivity Factor*:

$$\eta = \frac{K_f - 1}{K_t - 1} \qquad (6)$$

by the relationship:

$$n = \frac{K_t}{\eta(K_t - 1) + 1} \qquad (7)$$

where:

$$\sigma_{aD\ local} = \sigma_{aDk} \cdot K_t \tag{10}$$

i.e. the n factor can be defined as:

The ratio between the (endurance) local limit at a reference point of the body (peak, not nominal, strength value) and the (endurance) limit of a smooth specimen of the same material having uniform stress distribution, assumed as reference.

The term:

$$\sigma_{aDk} \cdot K_t \tag{11}$$

has the meaning of a *Local Endurance Fatigue Limit* because it represents the material fatigue resistance at a given point. The maximum stress at that point must be compared to this value.

With this extension, the theory of the Support Factor is able to model three-dimensional bodies, remaining compatible with the simplified theory for slender bodies.

Factors K_f, K_t and consequently n have an alternative meaning if they refer to material or to applied stresses.

- Referring to material: the n factor represents the **support** given to the fatigue resistance by the material close to it, due to the beneficial effect of local limited plasticity that redistributes the strain on the nearest points. [4] This is the reason for the name *Support Factor*.

- Referring to the applied stress: n represents the reduction of the actual stress with respect to the static one. In this meaning, the factor assumes the alternative name of *Dynamic Stress Reduction Factor*.

- No support is offered to local strength in two cases:

  1. For absence of material plasticity.
  2. For uniform stress distribution.

.

Modeling Non-uniform Stress States by Means of the Relative Stress Gradient

The parameter that distinguishes a non-uniform stress distribution in a geometrical discontinuity from the uniform stress distribution in a reference specimen is the stress gradient, normalized with respect to the maximum stress at the reference point. This is the *Relative Stress Gradient* RSG, defined as:

$$\chi' = \frac{1}{\sigma} \frac{d\sigma}{dx} \tag{12}$$

Fig. 4 explains the meaning of this parameter, keeping the maximum stress constant. When the stress gradient is high, Fig. a), the χ' is high and the volume affected by local shear deformation is small: the support effect is high, because the nearest fibers collaborate and give support to the most loaded ones. Fig. b) shows the other extreme case of low stress gradient, i.e. the low value for χ'. The volume affected by maximum stress is larger and

---

[4]Satisfying the equilibrium of stresses over the section leads to a partial transfer of the load from the most loaded to the less loaded fibers, that is not possible when stresses are uniformly distributed in the cross-section.

support effect is minimum with a reasonable probability of micro-crack nucleation.

Moving from the beams theory to three dimensional bodies, instead of:

$$K_f = f(K_t, mat.)$$

the following relation has to be considered:

$$n = g(\chi', mat.) = \frac{\sigma_{aDk\ \chi'\neq 0}}{\sigma_{aD\ \chi'=0}} \qquad (13)$$

where χ' takes the place of K_t.

Relative Stress Gradient in Slender Beams For simple shapes the χ' can be calculated by numerical methods or, at least approximately, by the theory of elasticity. Equivalence theories like the Von Mises theory can handle the simplest cases of multi-axial states of stress.

According to the definition of Eq.12, the following expressions should be applied in the cases of tension/compression and bending stresses:

$$X' = \frac{1}{\sigma_{max}} \cdot \frac{d\sigma}{dx} = 0 \qquad\qquad X' = \frac{1}{\sigma_{max}} \cdot \frac{d\sigma}{dx} = \frac{2}{d}$$

Approximate theoretical expressions of Relative Stress Gradient for common discontinuities in slender beams are shown in the Table of Fig. 5.

Relative Stress Gradient for Three Dimensional Bodies Numerical and experimental methods are the proper tools for determining χ' at reference points of complex structures, in which three principal stress values are originated in terms of amplitudes and mean values, $\sigma_{1a}, \sigma_{2a}, \sigma_{3a}$ and $\sigma_{1m}, \sigma_{2m}, \sigma_{3m}$. Generally, reference points are located at the surface, and χ' is evaluated along the perpendicular direction for the stress components lying on the surface.

An experimental determination of the Relative Stress Gradient for plane and three-dimensional
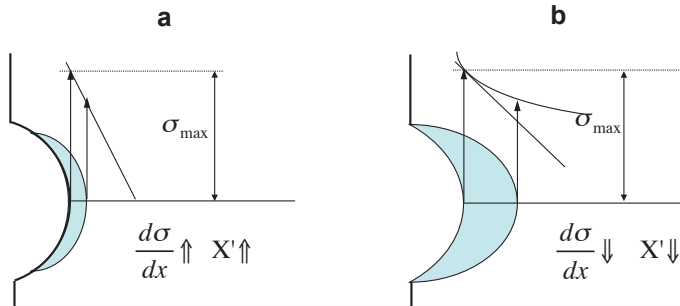

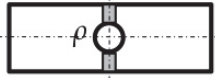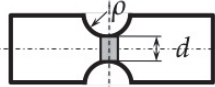**Figure 4.** For a fixed value of σ_{max} the Relative Stress Gradient χ' determines the dimensions of the most stressed material zone
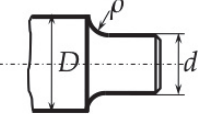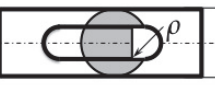
	Assiale	A flessione	A torsione
	$\chi' = \dfrac{2}{\rho}$	-	-
	$\chi' = \dfrac{2}{\rho}$	$\chi' = \dfrac{2}{\rho}+\dfrac{2}{d}$	-
	$\chi' = \dfrac{2}{\rho}$	$\chi' = \dfrac{2}{\rho}+\dfrac{2}{d}$	$\chi' = \dfrac{2}{d}+\dfrac{1}{\rho}$
	$\chi' = \dfrac{2}{\rho}$	$\chi' = \dfrac{2}{D+d}+\dfrac{2}{\rho}$	$\chi' = \dfrac{2}{D+d}+\dfrac{1}{\rho}$
	-	-	$\chi' = \dfrac{2}{\rho}$

Figure 5. Approximate theoretical expressions of RSG for common discontinuities in structural elements

cases may be obtained by a photoelastic analysis by a method due to Kuske, [6].

The Relative Stress Gradient can be written as:

$$\chi' = \frac{1}{\sigma_1}\frac{d\sigma_1}{ds_2} \tag{14}$$

where σ_1 is the principal stress along the isostatic s_1, assuming a positive stress value, Fig.6. The stress σ_1 is tangent to the boundary in a vertical direction and s_1 is the isostatic of the first family. Since $\sigma_2 = 0$, Eq.14 gives:

$$\chi' = \frac{1}{\sigma_1 - \sigma_2}\frac{d(\sigma_1 - \sigma_2)}{ds_2} + \frac{1}{\sigma_1 - \sigma_2}\frac{d\sigma_2}{ds_2}$$

Remembering the equilibrium Equations due to *Maxwell*:

$$\frac{d\sigma_2}{ds_2} + \frac{\sigma_1 - \sigma_2}{\rho_1} = 0$$

we have:

$$\chi' = \frac{1}{\sigma_1 - \sigma_2}\frac{d(\sigma_1 - \sigma_2)}{ds_2} - \frac{1}{\rho_1} \tag{15}$$

where ρ_1 is the curvature radius at the root of the notch.

The χ' is derived directly as inverse of the intercept $\overline{AB}$ of the straight line on the s_2 axis, minus the inverse of ρ_1:

$$\frac{\sigma_1 - \sigma_2}{\overline{AB}} = \frac{d(\sigma_1 - \sigma_2)}{ds_2} \qquad \frac{1}{\overline{AB}} = \frac{1}{\sigma_1 - \sigma_2}\frac{d(\sigma_1 - \sigma_2)}{ds_2} \tag{16}$$
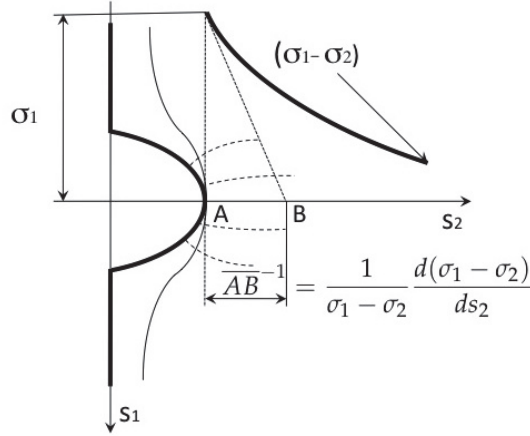
Figure 6. Direct measurement of χ' from photoelastic isochromatic fringes

then:

$$\chi' = \frac{1}{\overline{AB}} - \frac{1}{\rho_1} \tag{17}$$

E.g. we can apply now the method to a circular hole in a thin plate of finite width H, loaded in one direction, with reference to Fig. 7.

Theoretically, but for a large plate ($2a/H \to 0$), it is possible to calculate the Relative Stress Gradient χ' in two ways: either through the single term of Eq. 14 or through the two terms of Eq. 15. In the first case χ' is obtained as a limit of the ratio $\frac{1}{\sigma_1}/d(\sigma_y - \sigma_x)ds_2$ for x tending to a, [5] while in the second case χ' is obtained in two parts: as a limit for x tending to a of Eq. 16 minus the inverse of the stress trajectory radius at that point.

Fig. 7 a) shows plots of both Equations that achieve their limit values for x tending to a, respectively equal to 0.1296 for the first case, and 0.1852 for the term $1/AB$ in the second case. Consequently, the theoretical value of the term $1/\rho_1$ of Eq. 15 must be 0.0556 or $\rho_1 = 18\,mm$ that is the hole radius AC. From the image of Fig. 7 b), χ' is determined by Eq. 17.

In the present example, in the model real scale, the value of $\overline{AB}$ is $18/2.65 = 6.792$ and $1/AB = 0.147$. This experimental value is lower of the $0.1852 - 0.147/0.1852 * 100 = 21\%$ than the theoretical one, obtained for a large plate.

The correspondent experimental value of χ', according to Eq. 17, is:

$$0.147 - 1/18 = 0.0914\ mm^{-1}$$

valid for $2a/H = 0.295$ vs. a theoretical value of 0.1296. The discrepancy between the theoretical value of χ' for a large plate and the experimental value for the plate utilized in the experiment is $(0.1296 - 0.0914)/0.1296 = 29.4\%$.

An approximate solution is shown in the table of Fig. 5. The χ' for a hole in a plane strip is given by the formula $2/\rho$ that in the present example gives $2/18 = 0.111$.

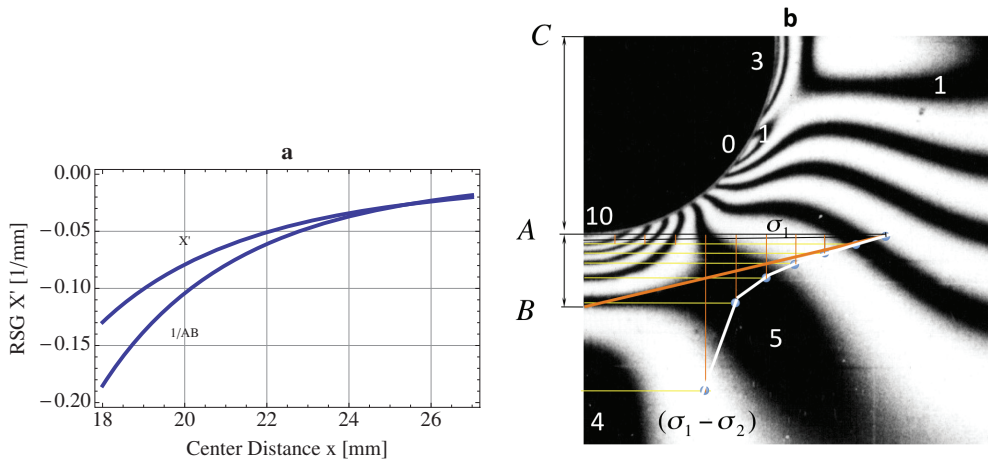[5] σ_x is zero for $x = a$

Figure 7. a) Plot of the term of Eq. 14 and of the first term of Eq. 15 and b) the direct measurement of the χ' from photoelastic isochromatic fringes

Table 1. Comparison of fatigue limits for alternate bending and alternate push-pull load for different materials

N.	$\dfrac{\sigma_{bW}}{\sigma_{zdW}}$	Materials
1	1.09	Structural Steels
2	1.07	Hardening and Relieving
3	1.03	Case Hardening Steels
4	1.48	Grey Cast Iron
5	1.33	Light Metals

3. DEPENDENCE OF FATIGUE STRENGTH ON THE SUPPORT FACTOR

Fatigue resistance at a reference point is different for uniform and non-uniform stress distribution because of the different support effect offered by the surrounding material. This property is well known: bending fatigue limits, with a χ' greater than zero are always bigger than the corresponding ones for push/pull load, Tab. 1, from [7].

1. Construction Steels
2. Hardened Steels
3. Case hardened Steels
4. Gray Cast Iron
5. Light Metal

A drawback of predicting models based on χ' estimation is that, if the stress distribution is very steep, it could be critical to estimate the gradient values. It would require the adoption of a finite-element model with very high mesh refinement with relatively long computational
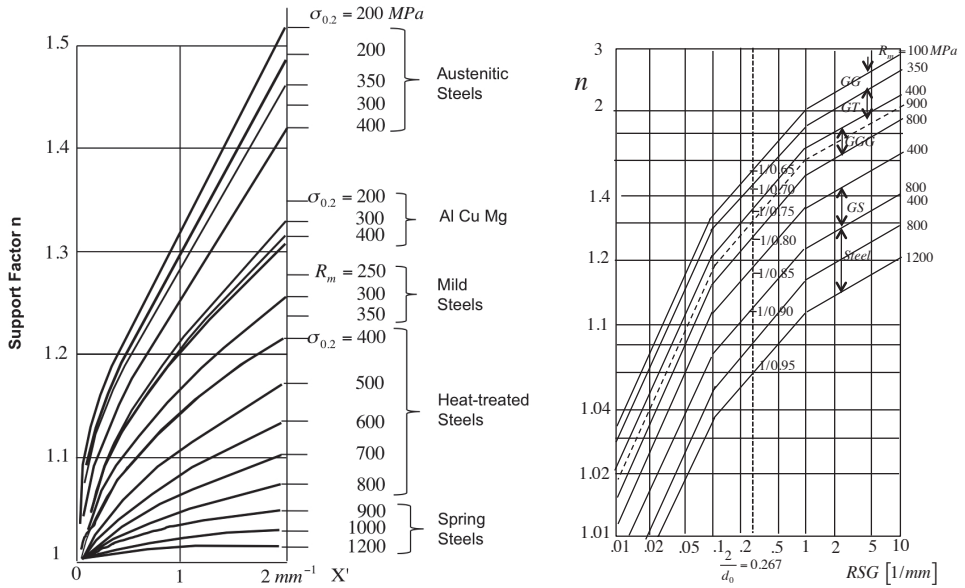
Figure 8. Examples of curves of Support Factor (or dynamic stress reduction factor) for normal stress versus Relative Stress Gradient for various metals in normal coordinates on the left (after Siebel and Stieler) and in logarithmic coordinates from [2] on the right

times, or an alternative very accurate high cost experimental analysis. Nevertheless, it must be observed that the Support Factor does not increase indefinitely as the gradient increases: the risk of an overestimation of the Support Factor is reduced for high values of χ'.

Size Effect Another advantage of the Relative Stress Gradient χ', whose dimension is the inverse of a length, is that it automatically takes into account the size effect: as the body dimensions increase, stress gradients and, consequently, Support Factors decrease and larger volumes of material support higher stress levels. The most loaded fibers do not take advantage of local stress redistribution and the likelihood of presence of micro-structural defects also increases; both effects are responsible for a fatigue strength reduction.

Model of the Support Factor as a Function of the Relative Stress Gradient

The simulations were proposed by the researchers that first developed extensive experimental tests on this factor, [8, 9], summarized in Fig. 8 a) together with the correspondent curves in log-log coordinates, [2] in b).

Siebel-FKM Model The original model due to Siebel and Stieler [10, 8, 9, 7] is a function of two parameters, χ' ([1/mm]) and S_g. The last one is the size of a critical volume in a perpendicular direction to the surface where the shear deformations are located and has the same order of magnitude as the grains diameter.

The Support Factor n is to be computed from the Relative Stress Gradient and from S_g

189

after Equations:

$$n = 1 + \sqrt{S_g \cdot \chi'} \tag{18}$$

where S_g is equal to:

$$S_g = -0.0375 \cdot \ln R_m + 0.27 \tag{19}$$

(R_m in MPa)

The model suggested by FKM guidelines [2] distinguishes three fields of the Support Factor, for different Relative Stress Gradient ranges:

For $\chi' \leq 0.1 \ mm^{-1}$:

$$n = 1 + \chi' \cdot 10^{-\left(a_G - 0.5 + \frac{R_m}{b_G}\right)} \tag{20}$$

For $0.1 \ mm^{-1} < \chi' \leq 1 \ mm^{-1}$:

$$n = 1 + \sqrt{\chi'} \cdot 10^{-\left(a_G + \frac{R_m}{b_G}\right)} \tag{21}$$

For $1 \ mm^{-1} < \chi' \leq 100 \ mm^{-1}$:

$$n = 1 + \sqrt[4]{\chi'} \cdot 10^{-\left(a_G + \frac{R_m}{b_G}\right)} \tag{22}$$

Constants in the formula must be chosen as material functions, according to the Table 2.

GS = Cast Steel

GG = Grey Cast Iron

GGG = Spheroidal Gray Cast Iron

GT = Hardened Cast Iron

χ' in $1/mm$ and R_m in MPa.

- These formulas are valid at the reference points for a stress gradient normal to the surface, for normal stresses only. The numerical values $1/0.65 \div 1/0.95$ in the diagram give the difference of the fatigue limit for reversed stress in tension-compression and in bending, for specimen of diameter $d_0 = 7.5 \ mm$ (and χ' equal to 0.267).

- In the case of slender bodies the diagrams and the relative Equations give the Support Factor that in this case is $n = K_t / K_f$. These factors are valid only for tension/compression.

Table 2. a_G and B_G as a function of the kind of material

$Mat.$	Stainless Steels	Other Steel	GS	GGG	GT	GG
a_G	0.40	0.50	0.25	0.05	-0.05	-0.05
b_G	2400	2700	2000	3200	3200	3200

- The same diagram is valid for a 3D-shaped body, where n is the ratio between the *local fatigue strength* for ($\chi' \neq 0$) and the *fatigue strength in a reference specimen* of the same material, in uniaxial loading condition ($\chi' = 0$), and also for massive details with 3D stresses if existing in slender bodies.

- The local values of component fatigue limit (for totally reversed stress) are obtained from the material fatigue limits, multiplying by the Support Factors.

Eq. 21 is shown in Fig. 8 on the right in double-logarithmic diagrams: (χ' in $1/mm$ and R_m in MPa).

For $\chi' \leq 0.1 \ mm^{-1}$:

$$\log(n-1) = \log \chi' - \left(a_G - 0.5 + \frac{R_m}{b_G} \right) \tag{23}$$

For $0.1 \ mm^{-1} < \chi' \leq 1 \ mm^{-1}$:

$$\log(n-1) = 1/2 \cdot \log \chi' - \left(a_G + \frac{R_m}{b_G} \right) \tag{24}$$

For $1 \ mm^{-1} < \chi' \leq 100 \ mm^{-1}$:

$$\log(n-1) = 1/4 \cdot \log \chi' - \left(a_G + \frac{R_m}{b_G} \right) \tag{25}$$

From this point of view:

- The approach defines the concept of *component fatigue limits*; the fatigue limit is no longer a characteristic of a material but a property of a structural component that can have one or more reference points at which the fatigue life must be assessed.

- In 3D-components the calculation of the local stress state is supposed to be done by finite-elements methods or obtained by an experimental analysis, in order to evaluate principal stresses $\sigma_1 \ \sigma_2 \ \sigma_3$ at each reference point, in terms of amplitudes and means values.

- If the all stresses vary proportionally to the load and consequently their amplitude and mean values, the directions of principal stresses remain unchanged and the principal stresses can be treated with the equivalence stresses.

- In the case of non-proportional stresses, it is necessary to distinguish the case of proportional amplitudes but non-proportional mean values from the more general case of total non-proportionality. In the first case, since the amplitudes are the dominant parameters of fatigue life, the problem can be re-conducted to the case of proportional stresses. In the second case, approximate methods can be developed, but a direct experimental assessment is always recommended, [2].

- At the reference point, that is generally located on the external surface of the component, if 1 and 2 are the principal stress directions on the surface and 3 is the direction
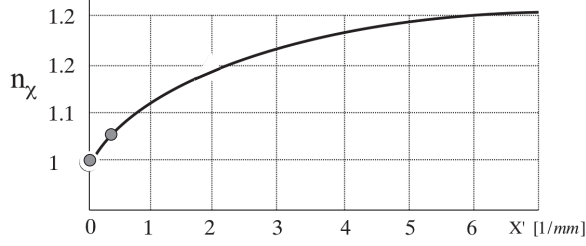
Figure 9. Curve of Support Factor versus Relative Stress Gradient derived from two reference tests of Push-Pull ($\chi' = 0$) and fully reversed bending Moment ($\chi' = 0.267 \quad 1/mm$)

normal to the surface, only gradients along 3 are taken into account for the calculation of the endurance fatigue limits $\sigma_{a1} \, \sigma_{a2}$. The diagram of Fig. 8 or the relative mathematical models, give the values of Support Factors for σ_{a1} and σ_{a2}, respectively $n_{\sigma_{a1}}$ and $n_{\sigma_{a2}}$.

E.g., according to [2], the *fatigue limits* of 3D components, in directions 1, 2 and 3 are:

$$\begin{cases} \sigma_{a1,WDK} = n_{\sigma_{a1}} \cdot \sigma_{a1 \, zd \, DW} \\ \sigma_{a2,WDK} = n_{\sigma_{a2}} \cdot \sigma_{a2 \, zd \, DW} \\ \sigma_{a3,WDK} = \sigma_{a3 \, zd \, DW} \end{cases} \tag{26}$$

where index a means amplitude, the index W totally reverse stress and K *Component*, for which $\chi' \neq 0$.

***Eichlseder* Model** Unlike the [2] model, the simulation for the Support Factor in [11] is based on the knowledge of fatigue response of the same material under two reference fatigue tests, for χ' equal to zero (tension/compression of smooth specimen) and for $\chi' = 2/d_0$, (bending test). The $n_\chi = f(\chi')$ model [11] (recalled also in [12, 13, 14, 15, 16, 17]) is the following:

$$n_\chi = \frac{\sigma_{aWDK}}{\sigma_{zd \, WD \, \chi'=0}} = 1 + \left(\frac{\sigma_{b \, WD}}{\sigma_{zd \, WD}} - 1 \right) \cdot \left(\frac{\chi'}{2/d} \right)^{K_D} \tag{27}$$

where:

- $\sigma_{aWD \, \chi' \neq 0} = \sigma_{aWDK} = $ local amplitude fatigue (endurance) limit at a reference point in the case of $\sigma_m = 0$.

- $\sigma_{zd \, WD \, \chi'=0} = $ fatigue (endurance) limit for the amplitude in a tension/compression test with R=-1 (χ'=0).

- $\sigma_{b \, WD} = $ fatigue (endurance) limit for the amplitude in a bending test with R=-1, (χ'= $2/d$)

- $\chi' = 2/d$ for the specimen in bending.

- $K_D = $ Material coefficient for taking into account the non-linear behavior of the function, Fig. 9.
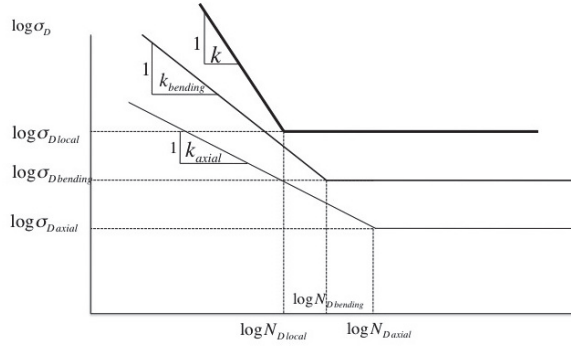
Figure 10. Local fatigue Curves at different χ' values, modified by [18] from [11]

In double logarithmic variables Eq. 27 becomes a linear Equation:

$$\log\left(n_\chi - 1\right) = \log\left(\frac{\sigma_{bWD}}{\sigma_{zdWD}} - 1\right) + K_D \cdot (\log \chi' - \log 2d) \tag{28}$$

Slope Modeling of the Local Fatigue Curve From an idea of [11], modified in [18], a model has been proposed for simulating the S/N local curve. The local k value is inferred by elementary values of Push/Pull and Bending tests slopes, with an analogy to Eq.27. If k_{zdW} is the slope of the fatigue curve obtained by a Push/Pull test, and k_{bW} is the slope of the fatigue curve obtained by a Rotating Bending test, the local value of k can be hypothesized as, Fig. 10:

$$\frac{k_{locale}}{k_{zdW}} = 1 + \left(\frac{k_{bW}}{k_{zdW}} - 1\right) \cdot \left(\frac{\chi'}{2/d}\right)^m$$

The value of m, for Low Alloy Steels is equal to 0.05, [18].

4. MODELING SUPPORT EFFECT THROUGH ROTATING-BENDING TESTS: CHARACTERIZATION OF A TITANIUM ALLOY

The difficulty to apply the FKM model for characterizing a material is represented by the high number of specimens necessary to describe the Support Factor for the whole field of the Relative Stress Gradient, together with the impractical use of two different testing machines.

As regards the simpler Eichlseder's method, an additional observation is that the interpolation is performed between two χ' values that are close to one another, (χ' is equal to 0 in tension/compression and 2 divided by the sample diameter in bending, which, considering most widely used diameters of about $6 \div 8\,mm$, gives a range of χ' from 0.33 to $0.25\,1/mm$). These values can be very different from χ' values corresponding to most notch geometries. Moreover, establishing a unified theory mixing axial tests and bending tests, performed on specimens of different shapes and dimensions with different testing machines (push/pull and bending tests), is a weak point of the procedure. A method is suggested utilizing only rotating bending tests for modeling the Support Factor of new materials, [19].

The case study refers to the fatigue characterization of a material (Ti- 6Al-4V alloy), widely used in aerospace industries for its high specific strength, excellent fatigue properties
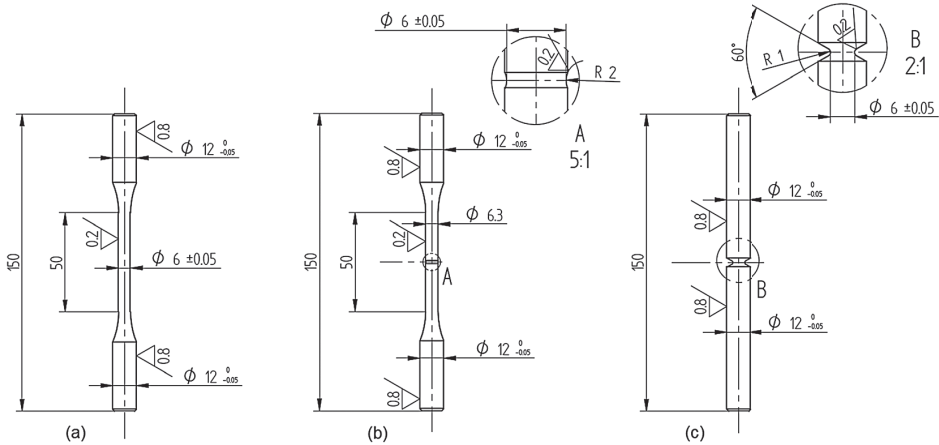
Figure 11. Specimens geometry: smooth (a), shallow notched (b) and sharply notched (c)

and corrosion resistance, but not classified in fatigue handbooks. The Ti-6Al-4V grade 5 has an ultimate strength of $950\,MPa$ and a yield strength of $880\,MPa$. Its composition is shown in Tab. 3. Ti-6Al-4V specimens, with notches of different severity, were selected to demonstrate the assumptions, Fig. 11.

The three kinds of specimens have a common reference diameter at the notch roots of $6\,mm$. The notched specimens were chosen with known values of K_t and χ', [20, 7].

For $K_t = 1.3$ the Relative Stress Gradient is $\chi' = 1.40\,mm^{-1}$ (shallow notched specimen) and for $K_t = 1.9$ is $\chi' = 1.90\,mm^{-1}$ (sharply notched specimen). For smooth specimens χ' is $0.33\,mm^{-1}$. The Dixon staircase method, [21] with $8 \div 10$ specimens for each specimen type and a stress step of $26\,MPa$ is adopted, corresponding to about 5% of the expected fatigue limit, according to the literature suggestions. Fig. 12 shows the results of the fatigue tests performed for three values of the Relative Stress Gradient. Tab. 4 shows the local values of the fatigue limit obtained multiplying the (nominal) fatigue limit σ_{bDk} of notched specimens by the Stress Concentration Factor K_t.

Predictive Model Based on Four Points

In order to add a fourth point, i.e. the reference point for $\chi' = 0$ to this interpolation made on three points (all obtained for $\chi' \neq 0$), the following strategy is suggested:

- A fourth case is introduced of a *virtual* bending moment applied to a smooth specimen with χ' equal to 0. This case is equivalent to the tension/compression case with uniform stress distribution on the cross-section, Fig. 13.
  The corresponding uniform stress value that is *equivalent* to the bending stress distri-

Table 3. Chemical composition of the Ti–Al–4V alloy

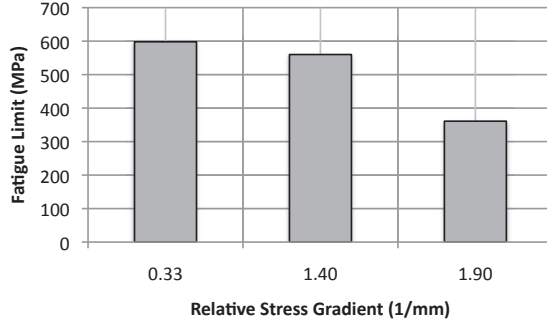| Element	Ti	Al	V	Fe	O	C	N	H
Content (%)	Balance	5.50-6.75	3.50-4.50	≤0.40	≤0.20	≤0.080	≤0.030	≤0.015

194

Figure 12. Nominal fatigue limits for smooth, shallow and sharply notched samples (= 598, 560 and 361 MPa)

bution on the same circular section is calculated. This is the new reference point for $\chi' = 0$. For the equivalence between the two distributions it is necessary to equalize the *static moments* with respect to the neutral axis of a triangular distribution and of a constant stress distribution, Fig. 13.

For a rectangular distribution the static moment with respect to the diameter is

$$M = \int_A \sigma_{rect} y dA \tag{29}$$

For a triangular distribution:

$$M = \int_A \frac{\sigma_{triang}}{R} y \cdot y dA \tag{30}$$

where: $dA = r \, dr \, d\theta$ and $y = r \sin \theta$.
Substituting this term and equalizing the two Eq. 29 and 29 we have:

$$\int_0^\pi \int_0^R \sigma_{rect} r \sin \theta r \, dr \, d\theta = \int_0^\pi \int_0^R \frac{\sigma_{triang}}{R} \cdot r^2 \cdot \sin^2 \theta \, r \, dr \, d\theta$$

. From this equality:

$$\sigma_{rect} \cdot \frac{R^3}{3} \cdot 2 = \frac{\sigma_{triang}}{R} \cdot \frac{R^4}{4} \cdot \frac{\pi}{2}$$

from which:

$$\sigma_{rect} = \frac{3}{16} \pi \cdot \sigma_{triang} = \frac{\sigma_{triang}}{c}$$

Table 4. K_f, K_t and n for three values of χ'

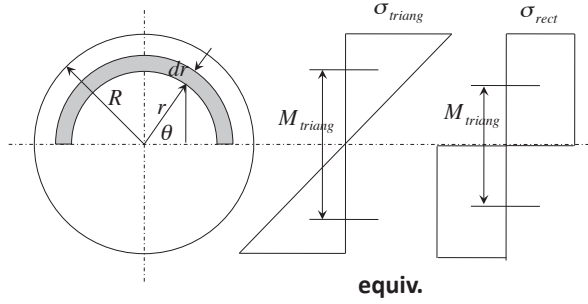| σ_{bDk}	σ_D	$K_f(\sigma_D/\sigma_{bDk})$	K_t	$n(K_t/K_f)$	χ'	$\sigma_{loc} = n \cdot \sigma_D$
598	598	1.000	1.0	1.000	0.33	598
560	598	1.068	1.3	1.217	1.40	728
361	598	1.657	1.9	1.147	1.90	686

Figure 13. Equivalence between a bending triangular stress distribution and a bending uniform stress distribution on the same circular cross-section of the smooth specimen $(c = 16/(3 * \Pi) = 16/(3 * 3.14) = 1.698$

with the constant c equal to: $c = 16/(3\pi) = 1.698$

- The previous values of the bending stress found for the three geometries must be now referred to this new stress value, the virtual case of uniform stress, equal to $598/c = 352\,MPa$ corresponding to $\chi' = 0$ and $n = 1$. Adding this new term to the values of Tab. 4 we obtain a new list of four local fatigue limits, shown in the Tab.5.

- The interpolation of these new four values gives the mathematical models of the Support Factor on the whole definition domain.

The fitting function in Fig. 14, $(n-1) = C \cdot \chi'^m$ has the constants C and m to be determined minimizing the functional of discrepancies between model and data. The minimum squares method gives the following result:

$$C = 0.886 \quad m = 0.292 \tag{31}$$

A linear fitting can be done for the logarithms of the data by the Equation:

$$\log{(n - 1)} = \log C + m \log x \tag{32}$$

A fitting offers other approximate values of the parameters:

$$C = 0.874 \quad m = 0.953 \tag{33}$$

Table 5. Support Factor $n = \sigma_{\chi'\neq0}/\sigma_{\chi'=0}$ as function of four values of RSG

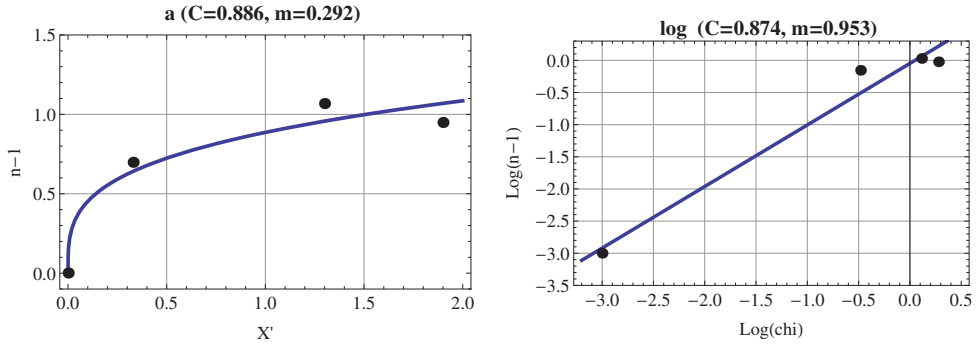| $\sigma_{\chi'\neq0}$	$K^*_{t\,new}$	n	χ'	$n - 1$
$352\ (\sigma_{\chi'=0})$	1.00	1.00	0.00	0.00
598	1.70	1.70	0.33	0.70
728	2.21	2.07	1.40	1.07
686	3.23	1.95	1.90	0.95

* $K_{t\,new} = K_{t\,old} \cdot 598/352$

Figure 14. a) Fitting to four points with a non-linear function and, on the right, a linear interpolation for the logarithms

Shot-Peening Treatment for Finding Other n Values

The interpolation can be extended to consider the shot-peening effect as a source of increment of the Relative Stress Gradient.[6]

$$\chi' = \frac{1}{(\sigma_x - \sigma_{res.})} \frac{d\sigma_x}{dx} \tag{34}$$

Fatigue tests were performed on two specimen types: respectively smooth and sharply notched. Three different treatments were experimented:

1. *Almen* intensity of 12N, with ceramic shots having a diameter of approximately 150 mm with a 200 % coverage (Z150-12N),

2. *Almen* intensity of 6A, with steel shots having a diameter of approximately 280 mm with a 200 % coverage (S110-6A),

---

[6] Residual stress distribution can be carefully estimated by diffractometric measurements. The in-depth measurements required step-by-step removal of thin material layers: this operation was performed by using an electropolishing facility to prevent considerable alteration of the pre-existent residual stress state; details in [19].

Table 6. Data for n and χ'_{tot} calculation

| Notch	shot-peen	χ'_{load}	K_t	σ_D	σ_{Dk}	$(d\sigma/dx)_{load}$	$\sigma_{res.}$	σ_{tot}	χ'_{tot} load + res.str.
no notch	no	.33	1	598	598	199	0	598	0.33
mild	no	1.40	1.30	560	756	1008	0	756	1.33
severe	no	1.90	1.90	361	635	1207	0	635	1.9
no notch	Z150-12N	0.33	1	736	736	254	-695	41	5.97
severe	Z150-12N	1.90	1.90	500	879	1671	-695	184	9.07
no notch	S110-6A	0.33	1	648	648	254	-528	120	1.80
severe	S110-6A	1.90	1.90	428	754	1433	-527	226.2	6.33
no notch	S230-12A	0.33	1	610	610	204	-532	79	2.58
severe	S230-12A	1.90	1.90	433	762	1448	-531	-531	6.28
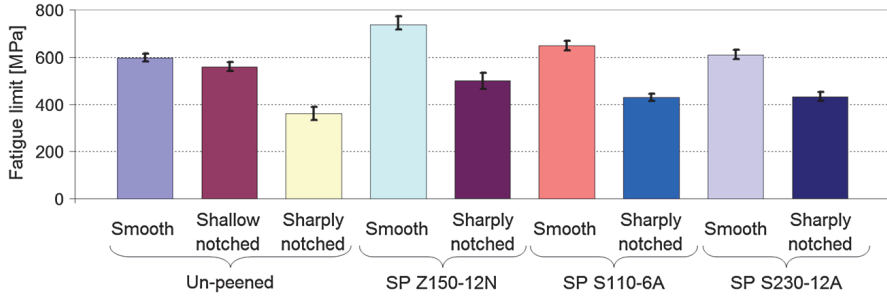
Figure 15. Nominal fatigue limits for shot-peened smooth, shallow and sharply notched samples

3. *Almen* intensity of 12A, with steel shots having a diameter of approximately 580 mm with a 200 % coverage (S230-12A).

The results of the fatigue tests are shown in Tab. 6 and in the histogram in Fig. 15.

Also in this case it is necessary to refer all the local maximum stresses to the virtual case of uniform stress value and the new Table 7 is presented with this new reference. The interpolation curves are shown in Fig. 16. It is enough to add only one point, (for a total of five points), obtained by shot-peening of a smooth specimen with $\chi' = 0.33 \, mm^{-1}$ to considerably improve the model that fits well to the all ten experimental data. The most reliable model is the following:

$$C = 0.849 \quad m = 0.239 \tag{35}$$

Criticality of Logarithmic Models In order to clarify the general criticality of a mathematical model through linearized logarithmic relationships, several minimization algorithms were used.[7], with the dubious result of obtaining different values of the factors a_G and b_G in

---

[7] FindFit of Mathematica ®by default finds a least-squares fit but possible settings are foreseen for other methods, including *ConjugateGradient, Gradient, LevenbergMarquardt, NMinimize*, and *QuasiNewton*, being the default *Mean Square Method*.

Table 7. Ten Points Data

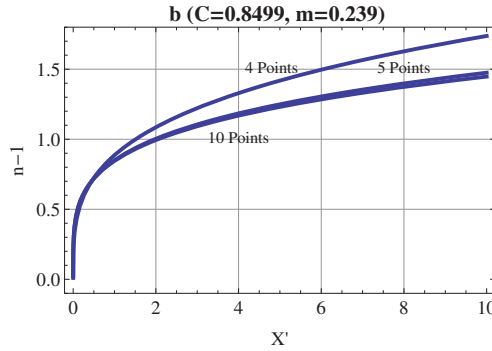| χ'	σ_{Dk}	n	n-1
0	352.3	1	0
0.333	598.0	1.698	0.698
1.400	728.0	2.067	1.067
1.900	685.9	1.947	0.947
5.976	775.2	2.201	1.201
9.075	879.5	2.497	1.497
1.803	719.4	2.042	1.042
6.334	793.7	2.253	1.253
2.581	709.8	2.015	1.015
6.283	828.3	2.352	1.352

Figure 16. Interpolating curve for $(n-1)$ as a function of χ' in five points and comparison with four and ten points
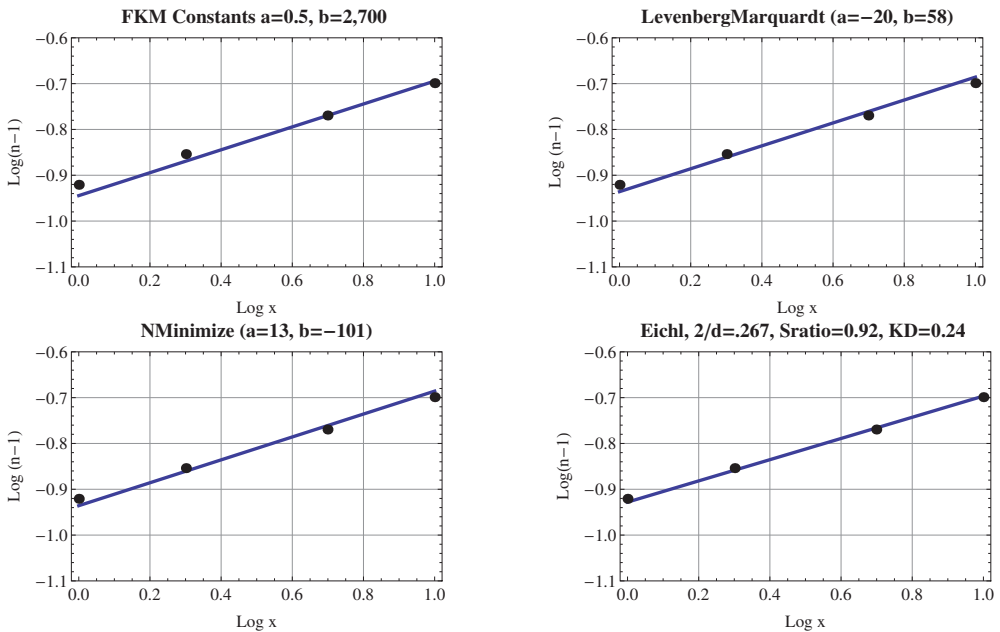

Figure 17. Comparison between fitting models, varying algorithms of the optimization method

the FKM model and also the different K_D values (with different minimization techniques), Tab. 2

5. CONCLUSIONS

The paper shows a method for obtaining a simulation model to describe the Fatigue Support Factor for a material not examined in common fatigue handbooks.

The classical well-established procedure for determining the Support Factor contemplates a mixing of axial and bending tests, performed on specimens of different shapes and

dimensions, obtained by push/pull and bending testing machines. Moreover, a fatigue campaign is demanding and heavy from an experimental point of view: every point of the diagram of Support Factor vs. Relative Stress Gradient is the result of several tests, possibly repeated.

A new method is suggested that utilizes only a rotating bending apparatus, [19] and a relatively limited number of tests. The difficulty that arises for the lack of comparison with the case of uniform stress in a reference specimen, is theoretically overcome, assuming as reference case a virtual situation of a bending stress uniformed distributed along the radius of the cross-section. In this way a general model for the Support Factor is obtained, based on four experimental fatigue tests, that is well- fitted to experimental data.

In order to extend the experimental basis of the correlation between Support Factors and stress gradients, the shot-peening technique was used with the task to induce a residual stress state that considerably increments the Relative Stress Gradient values.

In this case a different simulation model is proposed based on five fatigue data instead of four. With this adjunctive point the behavior of the Support Factor is well described also for high values of Residual Stress Factors. Concluding, if five fatigue tests can be performed on a new material, a reliable simulation model for the estimation of the fatigue strength of a structural component is found that covers the analysis of a discontinuity with low as well as with high Relative Stress Gradients.

The proposed model is simple but we believe that a simple model supported by many experimental data is better than a complex model supported by a few, being never possible, in the author's opinion, to suggest and validate a model, avoiding the weight of an heavy experimentation.

References

[1] Dowling, N. E., 2012. *Mechanical Behavior of Materials*, 4th ed., Vol. 1. Prentice Hall. ISBN-13: 978-0131395060 ISBN-10: 0131395068.

[2] Haibach, E., 2003. *FKM-Guideline: Analytical Strength Assessment of Components in Mechanical Engineering*, 5 ed. VDMA, Frankfurt, Germany.

[3] Taylor, D., 2007. *The Theory of Critical Distances - A New Perspective in Fracture Mechanics*. Elsevier Science B.V., Amsterdam, The Netherlands.

[4] Lazzarin, P., Tovo, R., and Meneghetti, G., 1997. "Fatigue crack initiation and propagation phases near notches in metals with low notch sensitivity". *Int. J. Fatigue,* **19**, pp. 647–657.

[5] Liu, C. D., Bassim, M. N., and Lawrence, S. S., 1995. "Dependence of the fatigue limit of rail steels on stress intensity factor near inclusions". *Engineering Fracture Mechanics,* **50**(2), pp. 301–307.

[6] Kuske, A., and Robertson, G., 1974. *Photoelastic Stress Analysis*, 1 ed., Vol. 1. J. Wiley and Sons, London.

[7] Niemann, G., Winter, H., and Höhn, B. R., 2001. *Maschinenelementen*, Vol. 1. Springer Verlag, Berlin.

[8] Siebel, E., and Stieler, M., 1955. "Ungleichformige spannungsverteilung bei schwingender beanspruchung". *VDI-Z,* **97**, pp. 121–126.

[9] Stieler, M., 1954. Untersuchungen Über die Dauerschwingfestigkeit metallischer Bauteile bei Raumtemeratur. Dissertation, TU Stuttgart.

[10] Siebel, E., and Bussmann, K. H., 1948. "Das kerbproblem bei schwingender beanspruchung". *Technik,* **3**, pp. 249–252.

[11] Eichlseder, W., 2002. "Fatigue analysis by local stress concept based on finite element results". *Comput. Struct.,* **80**, pp. 2109–2113.

[12] Eichlseder, W., 2005. Betriebfestigkeit. Vol.1, Montan Universitaet Leoben.

[13] Eichlseder, W., and Leitner, H., 2002. "Influence of stress gradient on s/n-curve". In Proceedings of the new Trends in Fracture and Fatigue Congress. Metz, France, 8-9 April 2002.

[14] Eichlseder, W., 2003. "Lebensdauervorhersage auf Basis von Finite Elemente Ergebnissen (Fatigue life prediction based on finite element results)". *Werkstofftech,* **34**, pp. 843–849.

[15] Leitner, H., Eichlseder, W., Gódor, I., Waggermayer, M., and Hinteregger, C., 2005. "Increased fatigue limit of gear wheels by a combination of case hardening and shot peening". In Proceedings RELMAS 2005 (6th International Conference).

[16] Gänser, H. P., Gódor, I., Leitner, H., and Eichlseder, W., 2006. "Enhanced fatigue life by mechanical surface treatments - experiment and simulation". In Proceedings 16th European Conference of Fracture.

[17] Leitner, H., Gänser, H. P., and Eichlseder, W., 2007. "Oberflächennachbehandlung durch kugelstrahlen und festwalzen-mechanismen, modellierung, methoden". *Materialprüfung,* **49**, pp. 408–413.

[18] Reggiani, B., 2007. "Simulation models in biomechanics and experimental mechanics". Ph.d. thesis, University of Bologna. Available as PDF file at URL `http://www.ingegneriaindustriale.unibo.it/it/attivita-didattica/download-tesi-di-dottorato`.

[19] Olmi, G., and Freddi, A., 2013. "A new method for modelling the support effect under rotating bending fatigue: Application to Ti-6Al-4V alloy, with and without shot peening". *Fatigue Fract. Eng. Mater. Struct.,* **36**(10), pp. 981–993.

[20] Pilkey, W. D., and Pilkey, D. F., 2008. *Peterson's Stress Concentration Factors*, 3 ed. John Wiley & Sons, Hoboken, NJ , USA.

[21] Dixon, W. J., and Massey, Jr., F. J., 1983. *Introduction to Statistical Analysis*, Vol. 1. McGraw-Hill, New York, USA.

MULTI-CYCLES DEFORMATION MODELING OF HOT FORMING TOOLS UNDER CREEP-FATIGUE REGIME

Barbara Reggiani
Department of Industrial Engineering,
University of Bologna, Italy
E-mail: barbara.reggiani4@ unibo.it

Lorenzo Donati
Department of Industrial Engineering,
University of Bologna, Italy
E-mail: l.donati@unibo.it

Luca Tomesani
Department of Industrial Engineering,
University of Bologna, Italy
E-mail: luca.tomesani@unibo.it

__Abstract__. Hot forming processes (extrusion, die casting and forging) allow the production of a wide variety of products, both in terms of worked material and achievable shapes. However, critical working conditions are involved for the tools subjected to severe thermo-mechanical loads, thus requiring an accurate design. Among the different classifications proposed in literature for hot forming die failures, one focus on separating manufacturing and in service failures. The latter category is additionally split, as proposed by the authors, in static failure, damage and deformation/deflection failures. Static failure appears after e reduced number of extruded billets as a consequence of an overload or of a poor initial die design. Damage and deflection failures are indeed induced by the synergic detrimental action of creep and fatigue phenomenon. In discriminating the relative dominant role of creep and fatigue in leading to the final die discard, the level of temperature and of the applied load as well as of the dwell-time are decisive. In extrusion, the latter is the time in which a constant load acts on the die and represents the time required to extruded each single billet function of both ram speed and billet length. Fatigue and creep can be seen as limit cases with zero and infinite dwell-time. A novel model is proposed for the prediction of the deformation undergone by hot forming tools in the creep-fatigue regime after multiple cycles. The model is presented as applied to extrusion dies and is based on a modified version of a simple creep law already implemented in all the FE codes. The model is validated against small scale dies used in physical experiments and then against industrial extrusion dies.

__Keywords__: creep, fatigue, creep-fatigue, FE modelling, hot forming, extrusion

1. INTRODUCTION

Metal hot forming processes (extrusion, die casting and forging) allow the production of a wide variety of products, both in terms of worked material and achievable shapes (Fig. 1).

However, critical working conditions are involved for the tools subjected to severe thermo-mechanical loads, thus requiring an accurate design.

By focusing on the extrusion process, dies can be considered the most critical in the tooling set for many reasons as their possible complex shape, that should lead to severe stress concentrations, or the strict dimensional tolerances that can be required for the final profiles. Other criticisms are related to the special materials used for their manufacturing that, for example, soften in service without saturation thus determining a continuous increasing of the strain accumulation [1]. Additionally, dies are of not straightforward design also due to the complex state of stress induced as consequence of the applied thermo-mechanical loads.

The demand of high quality extruded products involves the requirement of an increasing efficiency of the production systems leading to severe operational conditions for the die that is so exposed to both high temperatures and cyclic thermo-mechanical loads. Under these working conditions, die is exposed to complex damage conditions that can lead to the final mechanical failure.

Mechanical failure is intended as "*each modification of geometric dimensions, shape or proprieties of a structure, component, machine or a part of these that prevents its normal and adequate working*" [2]. Two macro categories of failure modes have been classified in literature for extrusion dies that are manufacturing and service related failures [3]. In the former group are covered all the possible defects arose during die preparation as an improper chemical composition or an erroneous heat treatment. A different set of failures is correlated to the die operational conditions (process parameters) and are classified as fatigue, wear and deflection/deformation [3]. Among these last modes, wear failure depends strongly on the surface hardening techniques applied to the die [4-7] whilst fatigue and deflection can be primarily correlated to the specific die design adopted.

Static failure can be placed as limit case of the in-service failure related both to an improper initial die design under standard operational conditions or to a proper die design subjected to an unexpected overload. In the context of the in-service related "design specific" mechanical failures, the authors propose a classification that differentiate static failures, cracked failures (or damage) and deformation/deflection failures.
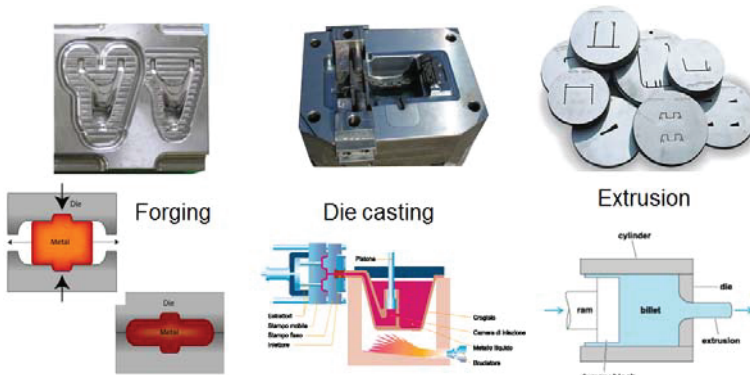

Figure 1. The metal hot forming processes and the involved tools.

Static failure appears when the entire weakest resistant section of the die (usually in the leg regions) is over the yield limit. The overcoming of the static strength can be reasonable responsible of the die failure if this appears after a reduced number of extruded billets (1 up to 5). With the increasing of both temperature and number of extruded billets, i.e. increasing also the time at which the die is exposed to high temperature, the creep and fatigue failure phenomena can appear. Die are subjected both to creep, working in a temperature range between 400°C to 580°C and under a constant load during the extrusion of each billet, and fatigue, each single billet being a loading cycle. Both mechanisms can lead to damage or deformation failures, the former appearing as material discontinuities in the form of cracks, microvoids or pores [2] the latter as an excessive level of accumulated plastic deformation resulting in an out of quote of the die design and then of the final extruded profile (Fig. 2).

While a number of experimental evidences demonstrate the effect of fatigue in generating both damage [8-10] and deformation [1,11] failures in tool steels in the working area of extrusion dies, in the same service range creep phenomenon have been proved to not produce material discontinuities but a significantly high level of deformation [12-14]. However, the issue is still open and under investigations. In a simplified temperature-number of billet diagrams, the area of major influence of the fatigue phenomenon, with respect to creep, can be placed in the region of low temperature and high number of extruded billets, while the creep phenomenon can become the dominant failure mechanisms with the raising of temperature and decreasing load frequency (Fig.3a).

If the boundary between static strength and creep/fatigue is well defined, that between fatigue and creep is not and the die deformation failure is normally consequence of the interaction of both phenomena [1, 15-18]. In the definition of this interaction, an additional influencing parameter is the dwell-time, i.e. the time of constant load maintenance required to extrude each single billet. Fatigue and creep can be seen as limit cases of zero and infinite dwell-time respectively. During each fatigue cycle, a certain quote of plastic deformation is accumulated; if a not zero dwell-time is used, at a level of temperature-load inducing the creep phenomenon, than, even at constant load, an additional amount of plastic deformation is collected (Fig. 3b).
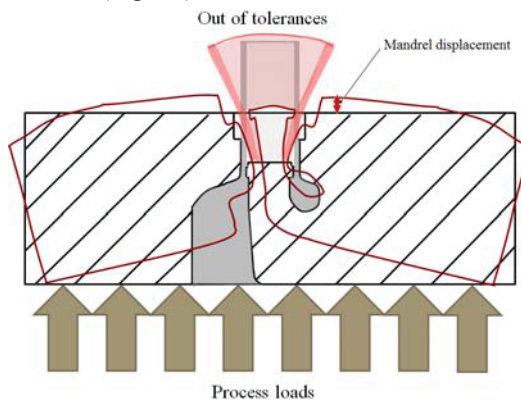

Figure 2. Schematic representation of an extrusion die (mandrel) deflection under process loads and the resulting potential out-of-tolerances of the profile.
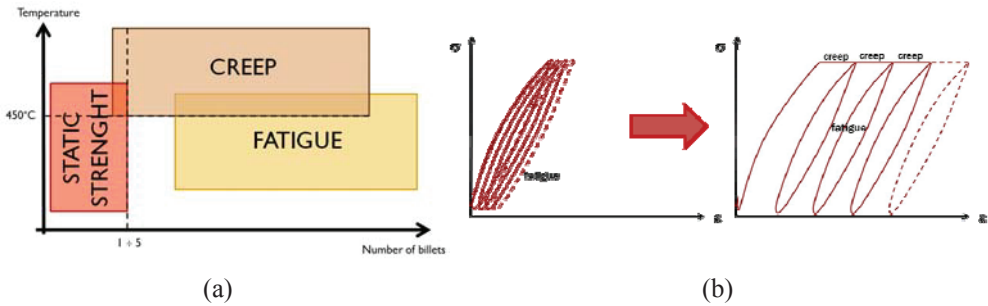
(a)   (b)

Figure 3. (a) Schematic representation of the areas of major influence of creep, fatigue and static strength in extrusion dies failure; (b) the synergic effect of creep and fatigue in the accumulation of plastic strain.

The in-service experimental assessment of the deformation exhibits by the die is not easy to accomplish due to its poor accessibility, well hidden by the additional tooling set of the press equipment (Fig. 4). In addition, an experimental monitoring of the die deflection would only provide an ex-post evaluation after that very expensive tools have been already manufactured. The possible alternative is then numerical. In literature a number of models have been already presented for such a type of assessment. The widely known is the model proposed by Chaboche [2] that allows for an accurate modeling of the behavior of each single hysteresis loops but which consists of a large number of equations and requires the determination of a large number of material's constants as function of temperature. This is probably the reason why many of the parameters determined for the different materials are not clearly reported in the scientific papers.

The aim was therefore to propose a simplified model as an alternative calculation method for modeling the deformation of hot forming tools after multiple service cycles in the creep-fatigue regime. Then, a novel analytical model was proposed for the prediction of the deformation undergone by extrusion dies in the creep-fatigue regime after multiple cycles (i.e. multiple extruded billets) based on a modified version of a simple creep law already implemented in all the FE codes and incorporating also the dwell-time effect. The model was initially verified on the results of a physical experiment reproducing the thermo-mechanical conditions of a die, also used to calibrate the model's constants. Then, it was validated against two industrial extrusion dies.
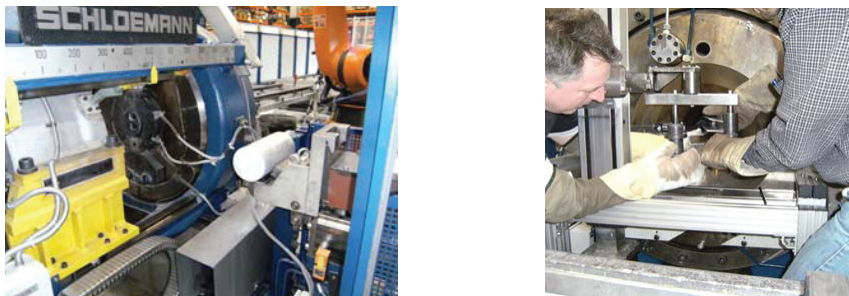

Figure 4. (left) Experimental extrusion press and (right) the front of the press as single potential access point for the an experimental die deflection monitoring

206

2. THE PROPOSED ANALYTICAL MODEL

Different formulations in literature allow to account for creep and fatigue effects on the predictions of the die life [2]. However, on one side, part of these are able to account only for a single phenomenon; for example fatigue models neglect the extrusion time and then the quote of plastic deformation due to creep while the standard use of creep models do not considers the fatigue effect due to the extrusion of multiple billets. On the other side, more comprehensive models, that could account for the interaction of creep-fatigue, are marked by time and cost consuming calibration phase and are not implemented in all the FE codes. In addition, typically, the constants of these models have to be calibrated against standard specimens thus not accounting for realistic stress distribution and surface conditions of an industrial die. Accounting for these limitations, a novel model was proposed by the authors for the prediction of the deformation undergone by extrusion dies after multiple cycles (i.e. multiple extruded billets) based on a modified version of a simple creep law already implemented in all the FE codes. The model allowed to account also for the dwell-time and then for the different extrusion time, additional parameter for a correct estimation of the final accumulated deformation.

The starting point was a physical experiment reproducing the thermo-mechanical conditions of an extrusion die performed on a Gleeble simulator by means of specimens reproducing the mandrel of a porthole die on a small scale [14]. Specimens were made of AISI H11 heat treated to 44-48 HRC typical of industrial standards. The design of experiment consisted of four levels of temperature, three levels of stress and three types of load: pure creep (load kept constant), pure fatigue (cyclic load) and creep-fatigue (cyclic load with a three minutes of dwell-time) (Fig. 5). In addition, three geometric configurations of the specimen were built with different values of curvature radii that were varied from 2 mm (R2), to 1 (R1) and 3 (R3) mm with the aim to investigate the notch effect on the results. In Fig. 5, output results in terms of peak displacement of the mandrel over the testing time are reported as example. Details are presented in [14].

It was found that creep is the mechanism that most affects the die deformation and that typical industrial conditions can be correctly described by such softening mechanism. In all the testing conditions, a comparable pattern of the mandrel displacement-time curve was found, reproducing the three stages of softening typical of the strain evolution in a standard creep test but with a marked primary phase (Fig. 6). Thus, an exponential law was chosen to predict the displacement of the mandrel over time accounting for the stress, time and temperature behaviour dependency of the material response in this region of deformation.

The chosen time hardening creep law is [19]:

$$\dot{\varepsilon} = C_1 \cdot \sigma^{C_2} \cdot T^{C_3} \tag{1}$$

By means of FE analyses, for pure creep tests performed on the small scale mandrel specimens, C_1, C_2 and C_3 were optimized, for each level of stress and temperature, on the basis of experimental data for the R2 configuration starting from values for similar alloys found in literature [20-21].
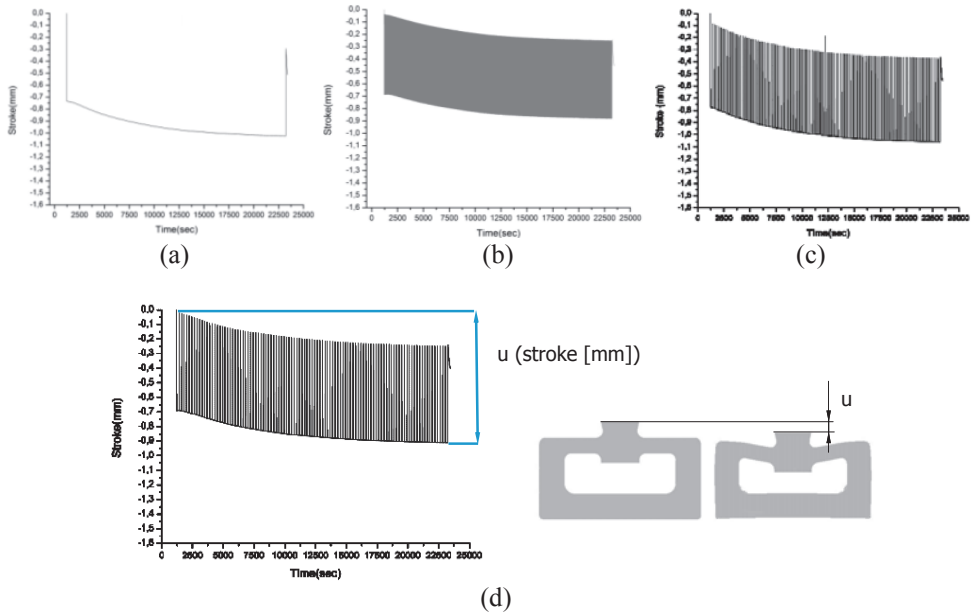
Figure 5. Results of the physical experiment on the small scale extrusion dies performed at 540°C and 600 MPa: (a) pure creep, (b) pure fatigue, (c) creep-fatigue conditions. (d) explanation of the stroke reported in the diagrams representing the small scale die lowering under load
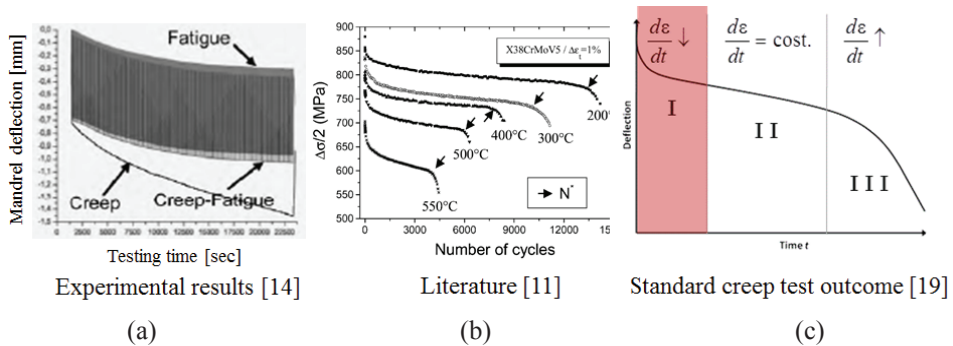

Figure 6. Comparison of the experimental mandrel lowering-time (a) with cyclic softening trends reported in literature for the same material (b) and as achievable by standard creep tests in the primary creep stage (c).

For fatigue and creep-fatigue tests, a continuous curve was extrapolated by connecting the peak values of the displacement of each cycle and applying the same approach as for the creep tests (Fig. 7). The optimized value of time hardening creep law are reported in Table 1.
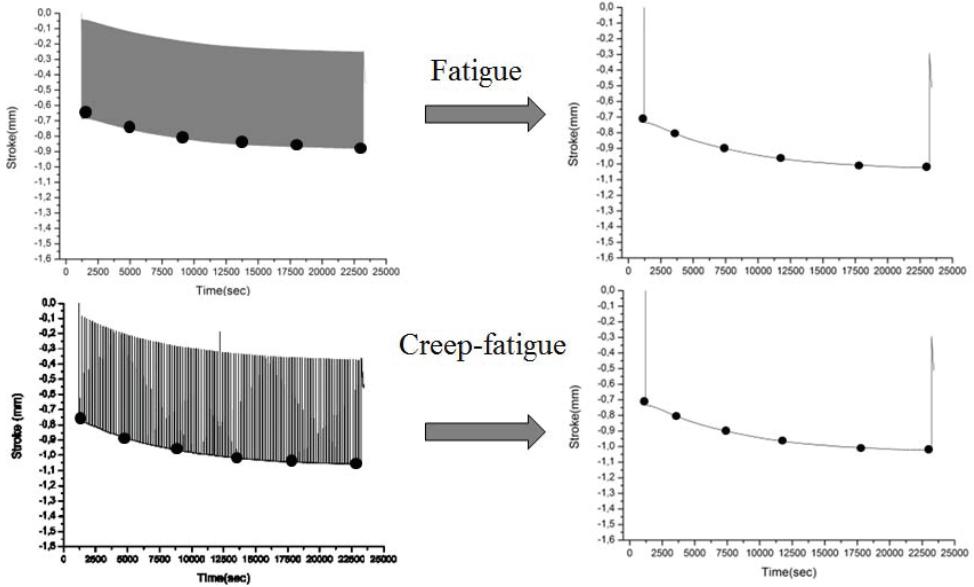
Figure 7. Extrapolation of continuous curves for the fatigue and creep-fatigue tests.

Table 1: Optimized values of the creep coeff. of Eq. 1 on the basis of experimental data.

Fatigue

C1	380 [°C]	490 [°C]	540 [°C]	580 [°C]
400 [MPa]	6,00E-14	1,33E-08	4,00E+07	3,00E-06
600 [MPa]	6,00E-14	1,33E-08	4,00E-07	
800 [MPa]	6,00E-14	1,33E-08		

C2	380 [°C]	490 [°C]	540 [°C]	580 [°C]
400 [MPa]	3,96	1,90	1,34	0,99
600 [MPa]	3,74	1,77	1,27	
800 [MPa]	3,60	1,74		

C3	380 [°C]	490 [°C]	540 [°C]	580 [°C]
400 [MPa]	-0,9325	-0,9150	-0,8700	-0,9870
600 [MPa]	-0,9325	-0,9150	-0,7900	
800 [MPa]	-0,9325	-0,8000		

Creep

C1	380 [°C]	490 [°C]	540 [°C]	580 [°C]
400 [MPa]	7,33E-14	1,44E-08	4,46E-07	4,00E-06
600 [MPa]	7,33E-14	1,44E-08	4,46E-07	
800 [MPa]	7,33E-14	1,44E-08		

C2	380 [°C]	490 [°C]	540 [°C]	580 [°C]
400 [MPa]	3,97	1,92	1,35	1,06
600 [MPa]	3,70	1,82	1,40	
800 [MPa]	3,57	1,82		

C3	380 [°C]	490 [°C]	540 [°C]	580 [°C]
400 [MPa]	-0,9325	-0,9150	-0,8700	-0,8700
600 [MPa]	-0,9325	-0,9150	-0,7900	
800 [MPa]	-0,9325	-0,8000		

Creep-fatigue

C1	380 [°C]	490 [°C]	540 [°C]	580 [°C]
400 [MPa]	6,40E-14	1,42E-08	4,20E-07	3,80E-06
600 [MPa]	6,40E-14	1,42E-08	4,20E-07	
800 [MPa]	6,40E-14	1,42E-08		

C2	380 [°C]	490 [°C]	540 [°C]	580 [°C]
400 [MPa]	3,97	1,92	1,35	1,05
600 [MPa]	3,72	1,84	1,30	
800 [MPa]	3,62	1,83		

C3	380 [°C]	490 [°C]	540 [°C]	580 [°C]
400 [MPa]	-0,9325	-0,9150	-0,8700	-0,8700
600 [MPa]	-0,9325	-0,9150	-0,7900	
800 [MPa]	-0,9325	-0,8000		

Novel regression equations were formulated in order to correlate each coefficient to the stress-temperature state and dwell-time:

$$C_1 = \left(C_{1\min} \cdot \left[\left(\frac{C_{1\max}}{C_{1\min}} - 1 \right) \cdot \left(\frac{T}{T_{\max}} \right)^{(K_1/T)} \right] \right) \cdot Q \cdot t_{dwell}^{R} \tag{2}$$

$$C_2 = \left(E \cdot \sigma^{F} \cdot T^{G} \right) \cdot N \cdot t_{dwell}^{U} \qquad \text{If } T \geq 380°C \tag{3}$$

$$C_2 = \left(V \cdot \sigma^{W} \cdot T^{Z} \right) \cdot N \cdot t_{dwell}^{U} \qquad \text{If } T < 380°C \tag{4}$$

$$C_3 = -\left(C_{3\min} \cdot \left[1 + \left(\frac{C_{3\max}}{C_{3\min}} - 1 \right) \cdot \left(\frac{T}{T_{\max}} \right)^{(K_3/T)} \right] \right) \tag{5}$$

Table 2: Regression coefficients for Eq. 1 to 5.

C_1		C_2		C_3	
K_1	16650	E	1.30E+08	K_3	3000
		F	-0.11245		
		G	-2.8021		
		V	9.95E+04		
		W	-0.172		
		Z	-1.52		

In eqns. (2) to (5), K_1, K_3, Q, R, E, F, G, N, U, V, W and Z are material constants; t_{dwell} is the time in which, during a creep-fatigue test, the imposed load is kept constant and, as previously observed, it is correlated to both the billet length and ram speed.

The coefficients C_{1max}, C_{1min} and C_{3max}, C_{3min} represent the values of the coefficients found for the maximum and minimum temperatures in the selected range of experimental investigation in case of creep-fatigue load for C_1 and C_3. Equation (4) was introduced to correct the most sensible parameter (C_2) out of the temperature experimental range. An extrapolation of the empirical formulations indeed did not account for the requirement of a rapid decreasing of creep effect for temperatures less then around 1/3 of melting temperature. It should be therefore strongly recommended the calibration of the constants in the full temperature-stress range of the die in-service conditions.

The optimized material constants in the Eq. (2) to (5) are reported in Table 2.

3. APPLICATION OF THE ANALYTICAL MODEL TO THE SMALL SCALE EXTRUSION DIES EXPERIMENTS

The procedure schematically described in Fig. 8 was applied by means of a purposely developed subroutine implemented within a structural FE code in which the temperature distribution in the specimen was derived by means of a coupled thermo-electric transient simulations [22]. The FE model of the specimen consisted of 41747 10-node tetrahedral elements (Fig. 9a). The nodal temperatures were then imported within the structural simulation environment and the mechanical elasto-plastic properties [15] assigned to each element as a function of temperature in order to obtain, for the first loading step in which the creep effect can be neglected, the stress distribution. This allowed to get an element-by-element assessment of the coefficients as a function of the specific (σ,T) state, thus resulting to be applicable and more suitable to model the deformation behaviour of an industrial die that exhibits a wide range of temperatures and stresses.

Experimental results and numerical predictions of the mandrel displacement history were compared in terms of general trend and percentage error for the creep-fatigue loading condition at different stress and temperature levels. In Tab. 3 are reported the results for each level of tested stress and temperature for the creep-fatigue loading configuration. In Fig. 10 is reported a magnification of the typical comparison output.
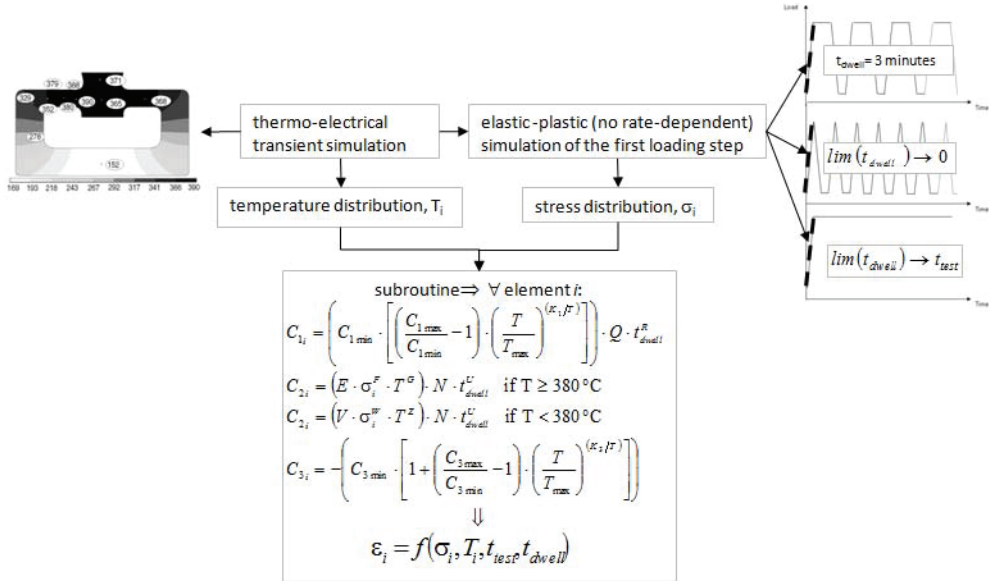
Figure 8: The procedure developed to compute the creep deformation rate according to eqns. (1)-(5) for each element of an FE model.
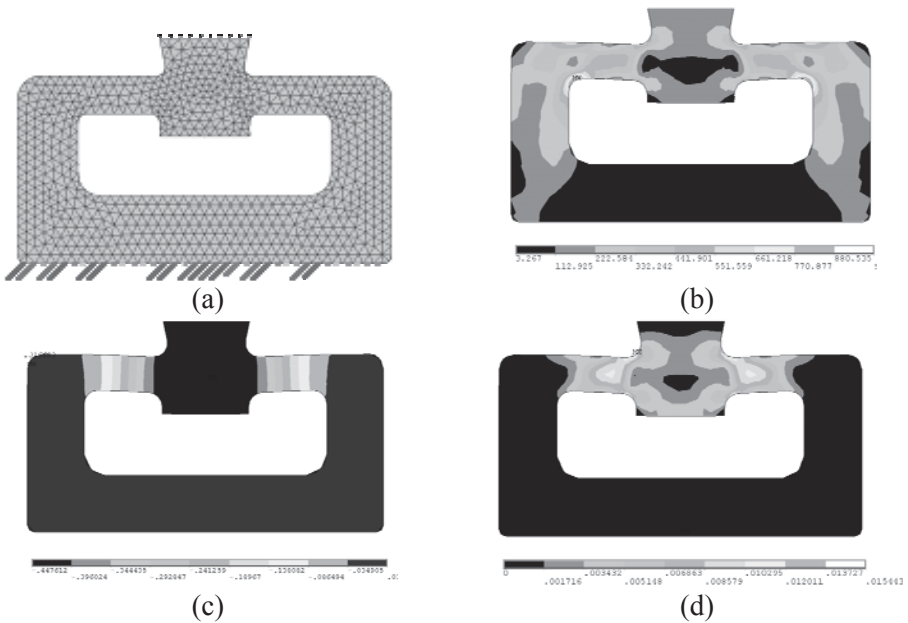

(a)

(b)

(c)

(d)

Figure 9: (a) Numerical FE model of the specimen; (b) Von Mises stress distribution, (b) peak displacement along the load direction and (c) equivalent creep strain for the testing condition of 490°C and 400 MPa.

The average percentage error over all the simulated conditions for the creep-fatigue load was 14.3%. The applied methodology fit an average behaviour since in a number of comparisons the numerical data overestimate the experimental results while in other cases the predicted displacement underestimate the experimental one. The higher discrepancy with the increasing temperature was due to the lack of a complete set of experimental data at 540 and 580°C; indeed, data corresponding to a premature failure of the specimen (i.e. 540°C-800MPa, 580°C-600MPa and 580°C-800MPa) were not accounted for to obtain the coefficients of the regression equations. These testing conditions were therefore less fitted and represented by the defined material constant of the time-hardening law that covers the primary phase corresponding to a decreasing strain rate. Analogous consideration were applied for the testing case of pure creep and pure fatigue loading conditions reaching average percentage errors of 12.7% and 32.5%. In case of pure fatigue load, an higher level of error was obtained since when dwell-time approached the zero value, the predictive model reduces its accuracy. However, the overall discrepancies can be consider adequate accounting for possible small experimental uncertainties and for numerical approximations of both the thermo-electrical and structural simulations. The achieved results are good goals considering in addition the high sensibility to even small variation of the adopted coefficients. In the Figure below are reported the model of the specimen and some output results of the FE simulation.

Table 3. Experimental vs. Numerical displacement of the mandrel for each testing condition under the creep-fatigue load.
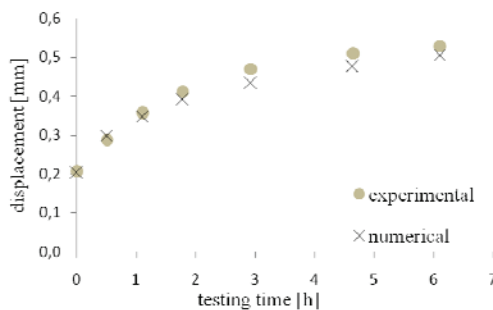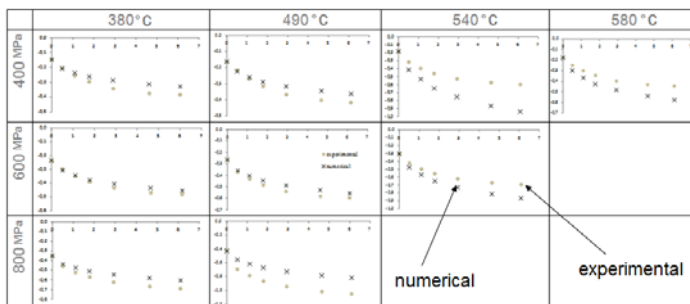
Figure 10: Example of the comparison between experimental and numerical results. Experimental dots represent the data extrapolated at the same time steps of the numerical predictions.

4. FIRST VALIDATION TEST: SMALL SCALE DIES

The developed procedure was then validated against additional experimental data not included in the calibration phase of the model constants. While the R2 configuration was used for this calibration step, the R1 and R3 geometric configurations of the specimen were tested in the creep-fatigue condition only at 540°C for the stress levels of 400 MPa and 800 MPa with the aim to investigate the notch effect on the output results (Fig. 11).

An average percentage error less than 8% was achieved for both the R1 and R3 configurations. The poor agreement for the R1 specimen at 800MPa can be explained with a premature failure of the specimen that broke after only 2 cycles thus falling into the circumstances not well fitted by the proposed model, as previously explained.

5. SECOND VALIDATION TEST: A TWO U-SHAPED HOLES EXTRUSION DIE

The developed procedure was then applied to an industrial die previously tested during a controlled experimental benchmark specifically focused on the measurement of the die deflection during the process stroke [25]. The die consisted of 2 U-shaped orifices produced by two tongues differently supported, one fully and the other partially, thus leading to different die deflection (Fig. 12).

From experimental trials, the temperature of the die and the dwell time were extracted (Fig. 13). The temperature of the die was set to 400°C (Fig. 13a) and the dwell-time to 30 seconds for a ram speed of 10 mm/s. The total simulation time was fixed to 8.1 hours, corresponding to 1000 extrusion cycles.

Process loads (pressures and temperatures) were derived by a process simulation performed by means of HyperXtrude ® [26] (Fig, 14).
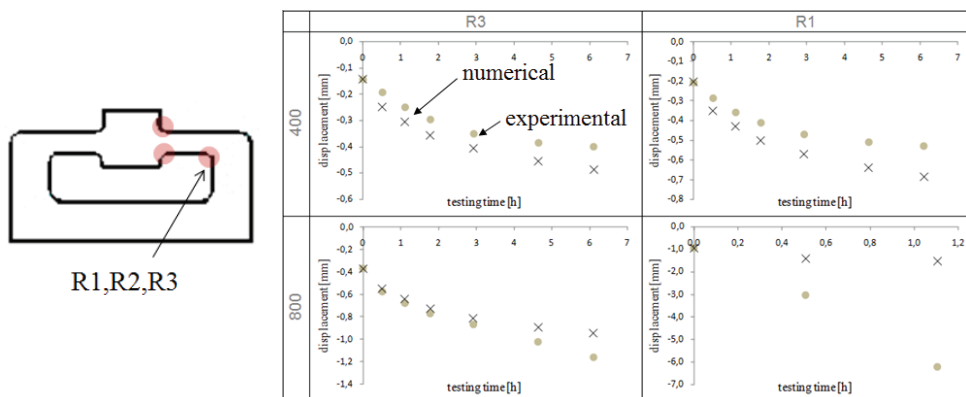
Figure 11: (right) the radii which differentiate the specimen geometric configurations R1 (1 mm) R2 (2 mm) and R3 (3 mm); (left) the output results for the R1 and R3 configurations in terms of mandrel deflection versus the testing time.
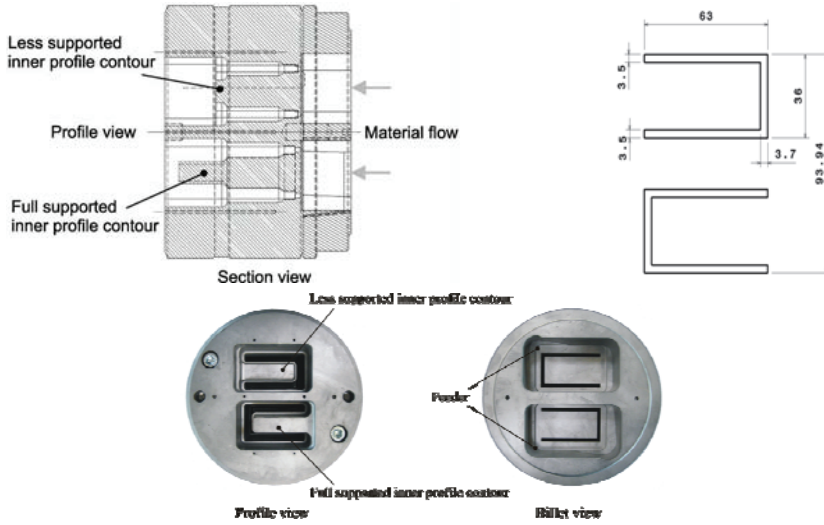
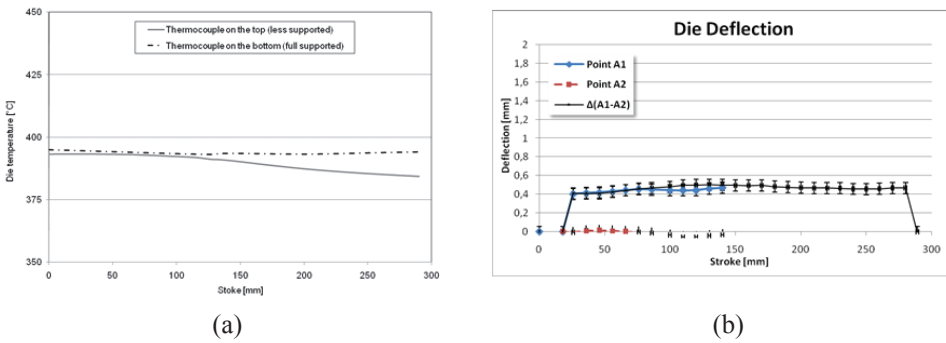**Figure 12**: Die design used in the experiment and profiles dimensions

(a)

(b)

Figure 13: Experimental die temperature and data of tongue deflection used to extract the dwell time value
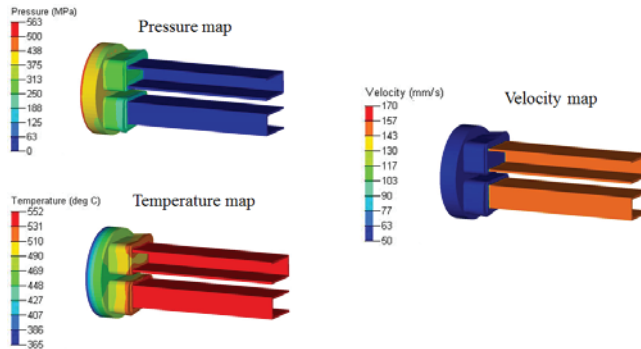

Figure14. Pressure, temperature and velocity maps as predicted by HX for the two U-shaped profiles.

An FE model of the die was then generated in a different FE code specifically dedicated to structural analyses. With respect to the process code, that incorporate a die stress module, the use of a dedicated code was proved to allow a more reliable estimation of the stress and strain distributions due to a wider choice of element types and material models. The FE model consisted of 9369 10-nodes tetrahedral elements and the pressure map was applied to the die faces.

In Fig. 15 are reported the output results of this study step. As can be seen, the difference in the prediction of the tongues deflection between a static analysis (Fig. 15a), as usually adopted for this type of computation, and that performed according to the procedure showed in Fig. 8 and Eqns. (1) to (5) (Fig. 15b) is 96%. In addition, graphs as those in Fig. 15 provide information on the maximum number of extrusion cycles that can be performed one after the other in order to avoid the overcome of a certain amount of die deflection.

(a)

(b)
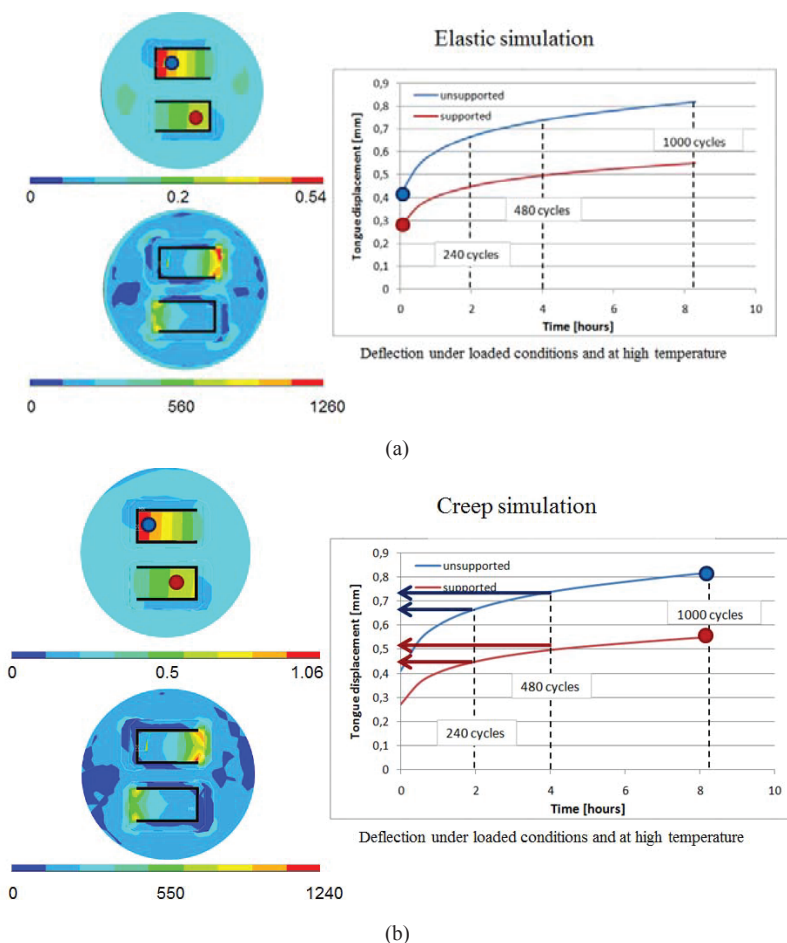
Figure 15: Die deflection along the extrusion direction as predicted with a static analysis (a) and according to the procedure of Fig. 8

6. THIRD VALIDATION TEST: PORTHOLE INDUSTRIAL EXTRUSION DIE

As last step of the work, the proposed procedure was applied to an industrial die whose data process were monitored and acquired during a controlled industrial extrusion. The analysed porthole die was used to produce a 6 mm thick round tube of 60 mm as outer diameter. In Fig 16 is reported the mandrel of the porthole die consisting of a central core mandrel, used to generate the internal shape of the profile, supported by three equal-spaced (120°) legs. Two reference pins were used to properly mount the mandrel on the die.

The die was made in H11. After 64 extrusion cycles, the experimentally measured mandrel deflection was 0.32 mm with the die dismounted by the press (permanent deflection in unloaded conditions).

In order to predict the pressure map on the die faces, a process simulation was performed by means of HX. A coupled thermo-fluid-dynamic steady-state analysis was run including the meshed billet, the porthole die and 1.8 mt of extruded profiles.

In this step of the work, the die was considered as rigid, but it was meshed in order to account for the thermal state of the tools and to get a reliable prediction of the pressure on tools. Output results of the process simulation were compared to experimental data and a good agreement was found terms of extrusion load, profiles exit velocity and die and profile temperatures, thus confirming the accuracy of the predicted process maps.

An FE model of the die was then generated in the structural code consisting of a single solid including die and mandrel thus avoiding contact generation and then significantly reducing the computational time. However, this did not alter the output results due to the rigid die-mandrel constraints as made with reference spins (Fig 16). The final model of the die consisted of 249000 10-nodes parabolic tetrahedral elements. The pressure map applied to the die faces was imported from the process simulation code (Fig17a,b). Displacement constraints were applied accounting for experimental settings: the die faces in contact with the bolster were fixed in the extrusion direction while the nodes in contact with the saddle load on the press were fixed in x and y directions (Fig. 17c).

The temperature of the die was set constant and equal to 470°C. As shown in Fig. 18a, 470°C represents an average temperature of the yielding region, i.e. the region contributing to the final total displacement that includes core mandrel and legs.

From the experimental data, an extrusion time of 300 seconds was computed, accounting for a billet length of 800 mm and a ram speed of 1.8 mm/s (Fig.18b).
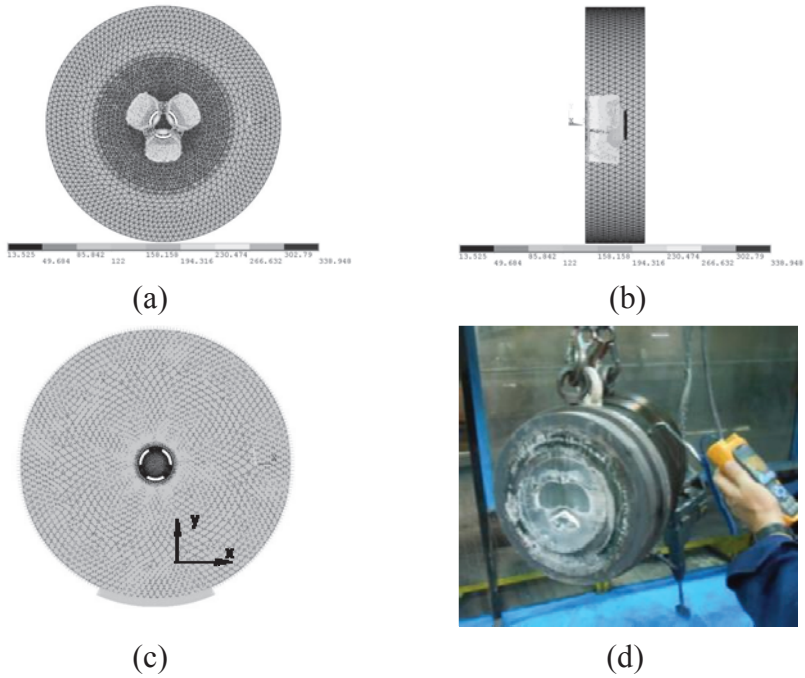

Figure16. Die design used in the experiment.

(a)

(b)

(c)

(d)

Figure 17. (a), (b) Pressure map as imported from HX; (c) Displacement constraints applied to the FE model developed in the structural code.
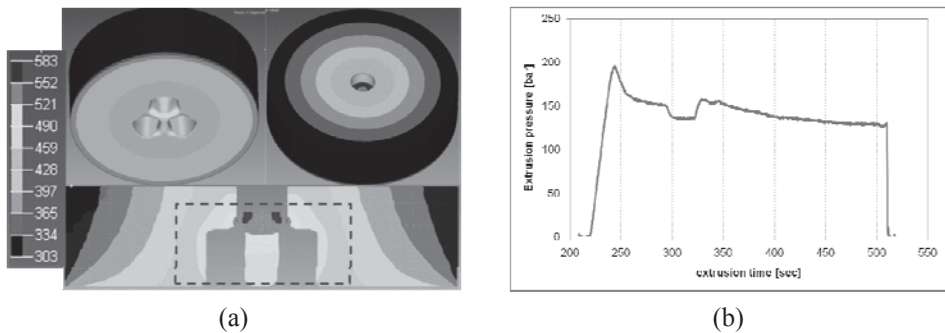

(a)

(b)

Figure 18. (a) Temperature distribution [°C] in the die as output from the process simulation (HX). Within the dashed area is the yielding region. (b)Experimental pressure-time diagram for a single extrusion.

Thus, within the developed subroutine, a dwell-time of 300 sec was imposed. The total simulation time was fixed to 16.6 hours, corresponding to around 200 extrusion cycles. As can be observed (Fig. 19b,c), the prediction of the peak mandrel deflection between the described procedure and a static analysis, after 16.6 hours of extrusion was 0.81 mm instead of 0.3 mm.
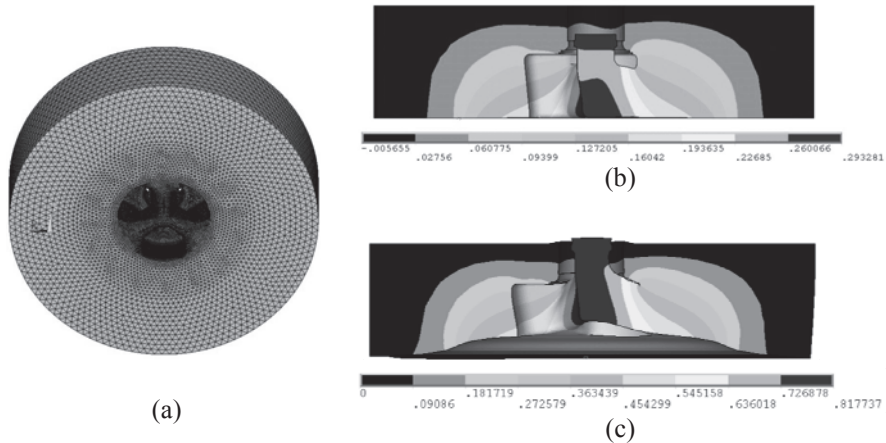
Figure 19. (a) FE model of the die as generated within the structural code. Die deflection [mm] along the extrusion direction as predicted with a static analysis (a) and according to the procedure of Fig. 8 (b).

In Fig. 20 the main output of the simulation is reported representing the mandrel displacement in unloaded configuration, thus purged by the elastic deformation, over the number of billets (total simulation time divided by the dwell time). It can be seen that after 64 extruded billet, the developed analytical model implemented in the procedure of Fig 8 was able to predict a residual mandrel deflection of 0.39 mm, well in agreement with the experimental data of 0.32 mm.

7. CONCLUSIONS

A novel procedure was presented for a reliable prediction of the level of deformation achieved by hot forming tools under the creep-fatigue regime. The procedure was presented as applied to the specific case of the extrusion dies, even if different application can be performed. The starting point of the presented method was a physical experiment in which the specimen copies the mandrel of an hollow die on a small scale. The procedure was initially tested by comparing the numerical prediction with experimental data used to calibrate the model's constants and then validated against different specimen configurations under a creep-fatigue load not included in the calibration phase. The good agreement found in each case between experimental results and numerical predictions confirmed the validity of the method. The applicability of the procedure was then verified considering an industrial die used to produce two U.shaped profiles with tongues differently supported in the extrusion direction, The main outcome of this step of the work was the significant discrepancy between the prediction of the die deflection as computed by means of a simple static analysis, as usually performed in the industrial practice, and of the proposed multi-cycles proposed procedure. This indicates that die design merely based on static numerical predications can lead to substantially different in-service performances and that more sophisticated computations are required in order to account for the behaviour evolution cycle after cycle.
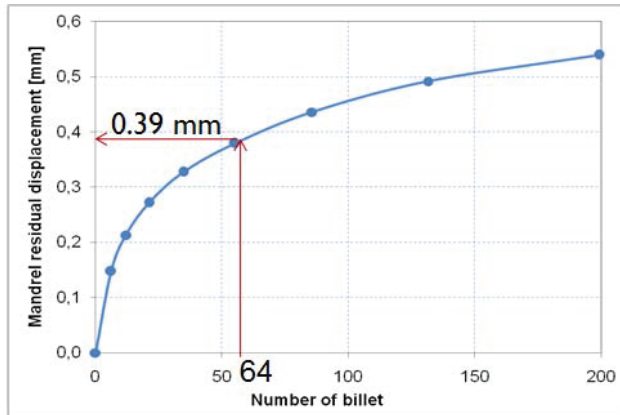
Figure 20. The numerical mandrel deflection of the three-legs porthole die in unloaded configuration

As last step of the work, the procedure was validate against an industrial extrusion porthole die that exhibited a permanent mandrel deflection of 0.32 mm, in unloaded conditions, after 64 extrusion cycles. Process loads (pressure and temperature) and boundary conditions were extracted by a transient simulation and directly by experimental data. The output of the procedure was a mandrel deflection of 0.39 mm after the same number of cycles, thus confirming the goodness of the developed analytical model.

REFERENCES

[1] V. Velay, G. Bernhart, L. Penazzi. 2006. Cyclic beahvior modelling of a tempered martensitic hot work tool steel. *Int. J. of Plasticity* **22**, pp. 459-496.

[2] J. Lemaitre, J.L. Chaboche. 1990. Mechanics of Solid Materials. Cambridge University Press, U.K. English version.

[3] A.F.M Arif, A.K. Sheikh, S.Z. Qamar, 2003. A study of die failure mechanisms in aluminium extrusion, *J. Mater. Proc. Techn.* **134**, pp. 318–328.

[4] Yucel Birol. 2012. Analysis of wear of a gas nitrided H13 tool steel die in aluminium extrusion. *Engineering Failure Analysis* **26**, pp. 203–210.

[5] T. Björk, R. Westergard, S. Hogmark, J. Bergström, P. Hedenquist. 1999. Physical vapour deposition duplex coatings for aluminium extrusion dies. *Wear* **225–229**, pp. 1123–1130.

[6] M.B. Karamis, H. Sert. 1998. The role of PVD TiN coating in wear behaviour of aluminium extrusion die. *Wear* **217**, pp. 46–55.

[7] D. Brabazon, S. Naher, P. Biggs. 2008. Glazing of tool dies for semi-solid steel forming. *Int J Mater Form,* **1**, pp. 985–988.

[8] K. Pöhlandt, 1989. Materials Testing for the Metal Forming Industry. Springer-Verlag, Berlin.

[9] C. Cosenza, L. Fratini, A. Pasta, F. Micari. 2004. Damage and fracture study of cold extrusion dies. *Eng. Frac. Mech*. **71**, pp. 1021–1033.

[10] E.-G. Yoh, Y.-I. Kim, Y.-S. Lee, H.-J. Park, K.-H. Na. 2002. Integrated analysis for die design including brittle damage evolution. *J. Mater. Process. Technol*. **130–131**, pp. 647–652.

[11] Z. Zhang, D. Delagnes, G. Bernhart. 2002. Anisothermal cyclic plasticity modelling of martensitic steels. *Int. J. of Fatigue* **24**, pp.635–648.

[12] Oudin A.. 2001- Thermo-mechanical fatigue of hot work tool steels. PhD thesis, Ecole Nationale Superieure des Mines de Paris, (non-confidential version).

[13] Delagnes D.. 1998. Isothermal fatigue behaviour and lifetime of a 5%Cr hot work tool steel around the LCF-HCF transition, PhD thesis, Ecole Nationale Superieure des Mines de Paris (in French)

[14] B. Reggiani, L. Donati, J. Zhou, L. Tomesani. 2010. The role of creep and fatigue in determining the high-temperature behaviour of AISI H11 tempered steel for aluminium extrusion dies. *J. Mater. Proc. Techn.* **210**, pp.1613-1623.

[15] Z. Ahmer, V. Velay, G. Bernhart, F. Rezai-Aria. 2008. Cyclic behaviour simulation of X38CrMoV5-47HRC (AISI H11)-tempered martensitic hot-work tool steel. *Int. J. Microstructure and Materials Properties* **3 (2/3)**, pp.326-335.

[16] R. Domagaoj, 1996. Lifetime prediction and constitutive modeling for creep-fatigue interaction. Materialkundlich-technische Reihe 13. Gebruder Borntraeger, Berlin, Stuttgart.

[17] M. Kneifl, I. Cerny, V. Bina. 2001. Damage of low-alloy high temperature steels loaded by low-cycle fatigue and creep. *Int. J. Of Pressure Vessel and Piping* **78**, pp. 921-927.

[18] C. Sommitsch, R. Sievert, T. Wlanis, C. Redl. 2008. Lifetime evaluation of two different hot work tool steels in aluminium extrusion. *Comp. Mat. Sci*. **43**, pp. 82-91.

[19] R.K. Penny and D.L. Marriott, 1971. Design for creep. Maidenhead, Berkshire, England, McGraw-Hill.

[20] H. Berns, C. Broeckmann and H.F. Hinz. 2002. Creep of high speed steels Part I- experimental investigations. In the Proc. Of the 6th International Tooling Conference Karlstad University, Sweden, 10–13 September Vol. 1, pp.325–337.

[21] H. Berns, F. Pschenitzka. 1980. Das Kriechverhaltern von Warmarbeitsstahlen mit 5%Chrom. *Zeitschrift für Werkstofftechnik*, **11,** 258-264 (german version).

[22] B. Reggiani et al., 2010. In the Proceedings of the 27th Danubia Adria Symposium, Sept. 22nd – 25th, Wrocław, Poland.

[23] B. Reggiani, L. Donati, L. Tomesani. 2010. Evaluation of different FE simulations codes in the stress analysis of extrusion die. *Int J Mater Form* **3 Suppl 1**, pp.395– 398.

[24] D'Ascenzo, M., 2009. Analisi del comportamento a caldo dell'acciaio AISI-H11 per la stima della vita utile di matrici per estrusione. Tesi di Laurea. Università degli studi di Bologna. A.a. 2008/2009 (in italian).

[25] Pietzka, N Ben Khalifa, L Donati, L Tomesani, AE Tekkaya. 2009. Extrusion Benchmark 2009 Experimental Analysis of Deflection in Extrusion Dies. *Key Eng. Mat.* **870 (424)**, 19.

[26] M. Reddy, R. Mayavaram, D. Durocher, H. Carlsson, O. Bergquist. 2004. Analysis and design optimization of aluminum extrusion dies. Proceedings of the Eigth International Aluminum Extrusion Technology Seminar (II), p. p.171.

VALIDAZIONE DEL CODICE QFORM PER L'ANALISI DEL PROCESSO DI ESTRUSIONE DI LEGHE DI ALLUMINIO

Claudia Bandini
Dipartimento di Ingegneria Industriale
Università di Bologna, Italia
E-mail: claudia.bandini4@unibo.it

Barbara Reggiani
Dipartimento di Ingegneria Industriale
Università di Bologna, Italia
E-mail: barbara.reggiani4@unibo.it

Lorenzo Donati
Dipartimento di Ingegneria Industriale
Università di Bologna, Italia
E-mail: l.donati@unibo.it

Luca Tomesani
Dipartimento di Ingegneria Industriale
Università di Bologna, Italia
E-mail: luca.tomesani@unibo.it

Sommario. *Scopo del presente lavoro è stato quello di validare un codice FEM di nuova generazione, QForm®, per giungere all'implementazione di una user-routine per la previsione dell'evoluzione microstrutturale durante processi di deformazione plastica, in particolare di estrusione. È stata quindi condotta una campagna preliminare di simulazioni al fine di validare i modelli di attrito disponibili nel codice così come le condizioni di scambio termico e i parametri che influenzano la discretizzazione della maglia e il processo. I risultati numerici sono stati confrontati con indagini sperimentali di visioplasticità riportate in letteratura [1] in termini di griglie di deformazione, andamento corsa-carico sul pistone, temperature del profilo estruso e della matrice. La determinazione del modello ottimale di attrito e dei suoi fattori caratterizzanti, reso possibile dal confronto numerico-sperimentale, ha permesso in seguito l'implementazione di una routine per la previsione dell'evoluzione microstrutturale nel codice Qform.*
.
Parole chiave: *microstruttura, attrito, estrusione, alluminio, leghe serie 6XXX, analisi FEM.*

1. INTRODUZIONE

Tra i processi di formatura plastica a caldo, l'estrusione è caratterizzato dai più alti gradienti di deformazione; in particolare, le leghe di alluminio sono tra i materiali più

ampiamente impiegati in applicazioni industriali proprio grazie alla loro elevata deformabilità.

Oggigiorno è noto che la microstruttura ha un ruolo dominante nella definizione delle caratteristiche sia meccaniche che estetiche di profili estrusi in alluminio. Il controllo della evoluzione della microstruttura del grano e quindi la possibilità di prevedere l'evolversi della lunghezza e dello spessore dei grani durante tali processi permettono di incrementare sia le proprietà del materiale (quali ad esempio resistenza meccanica, alla corrosione, a fatica, durezza), che l'efficienza dei processi di produzione [2].

In studi precedenti, sono stati proposti vari modelli teorici, in particolare Donati et al. presenta in [3] un modello di ricristallizzazione innovativo sulla base di quanto proposto da De Pari e Misiolek in [4], valido per le leghe di alluminio delle serie 6XXX e validato rispetto a dati sperimentali. Al fine di consentire anche in Qform l'accoppiamento del modello con i risultati delle simulazioni numeriche è pertanto necessaria la preventiva validazione del codice soprattutto per quanto riguarda le condizioni di attrito, scambio termico e le impostazioni di simulazione.

Come ben illustrato in [5], l'attrito è la resistenza al moto relativo che si manifesta quando due solidi sono in contatto tra loro. La forza necessaria per vincere tale resistenza, che è diretta nella direzione opposta al movimento relativo, è la forza di attrito. Tale fenomeno nel caso dell'estrusione si manifesta lungo tutta l'interfaccia tra gli utensili e la billetta, come schematizzato in Fig. (1).

Insieme alla lubrificazione e usura, l'attrito è uno degli elementi fondamentali in ambito tribologico, quindi il suo ruolo è essenziale anche nell'ottimizzazione dei processi di formatura dei metalli. In particolare, durante il processo di estrusione, le condizioni che si manifestano sulla superficie tra il materiale e gli utensili hanno una profonda influenza sulla qualità del prodotto estruso. Recentemente sono stati pubblicati diversi studi sulle condizioni di attrito che si manifestano durante il processo di estrusione; in particolare Sheppard ha verificato una condizione di perfetta adesione nell'interfaccia tra billetta e contenitore [6]; ulteriori studi sono stati fatti da Wang in.[7] sulla dipendenza del coefficiente di attrito nella zona di lavoro dalla temperatura, deformazione e stato tensionale locale mentre Ma in [8] e [9] presenta un modello in grado di descrivere la lunghezza del tratto di aderenza e slittamento nella zona di lavoro in una matrice durante l'estrusione di profilati in alluminio.

Purtroppo, nei codici FEM in commercio non è possibile considerare tutti questi parametri; come Chanda afferma in [10] e Parvizian in [11], anche oggi per modellare le condizioni tribologiche, è ancora necessario scegliere un adeguato modello impostando in modo opportuno i parametri previsti.

In particolare in QForm sono disponibili tre diversi modelli di attrito:

- Modello di Coulomb

$$\tau_C = \mu\sigma_n \qquad (1)$$

dove μ è il coefficiente di attrito $0 \leq \mu \leq \dfrac{1}{\sqrt{3}}$, σ_n è la pressione normale di contatto, τ_C è la tensione tangenziale sulla superficie di contatto del materiale.

- Modello di Siebel o modello di Tresca

$$\tau_S = mk \qquad (2)$$

dove m è il fattore di attrito il cui intervallo vede come estremi 0 (mancanza di attrito) e 1 (condizione di completa aderenza), k è la tensione di taglio e τ_S è la tensione di attrito;

inoltre, in accordo con il criterio di resistenza di Von Mises,

$$k = \tau_f = \frac{\overline{\sigma}}{\sqrt{3}} \qquad (3)$$

in cui $\overline{\sigma}$ è la tensione di flusso del materiale come indicato in [5];

-       Modello di Levanov

$$\tau_L = m \frac{\overline{\sigma}}{\sqrt{3}} \left[1 - e^{-\frac{n\sigma_n}{\overline{\sigma}}} \right] \qquad (4)$$

dove τ_L è la tensione tangenziale di attrito in un determinato punto della zona di scorrimento, $\overline{\sigma}$ è la tensione equivalente secondo il criterio di resistenza di Von Mises, σ_n è la tensione che agisce in direzione normale alla superficie (pressione), n è il coefficiente di Levanov e m, compreso tra 0 ed 1, è il coefficiente di attrito.

Levanov in [12] afferma che l'Eq. (4) corrisponde ad una legge in grado di descrivere in generale il meccanismo di attrito durante la deformazione plastica in quanto tiene conto dei seguenti fattori: dipendenza non lineare della tensione di attrito dalla pressione, l'influenza dell'incrudimento del materiale e l'aumento delle forze di attrito a seconda della natura e condizione delle superfici a contatto.

Dal grafico in Fig.(2) si evince che tale legge è una generalizzazione degli altri due modelli presentati: quando le pressioni normali di contatto sono basse (per esempio nella zona di lavoro) le forze tangenziali descritte dal modello di Levanov sono molto simili a quelle della legge di Coulomb, mentre nel caso di pressioni di contatto alte (ad esempio all'interfaccia tra superficie della billetta e quella del contenitore) l'andamento della curva tende asintoticamente a quello della legge di Siebel. Sulla base di tali considerazioni, in questa ricerca sono stati considerati e sperimentati solo i modelli di Siebel e Levanov.

Come ribadisce Liliang Wang in [13] , non è facile determinare sperimentalmente il valore dei coefficienti nelle equazioni sopra elencate, in particolare il modello di attrito di Coulomb è raramente usato nella modellazione FEM del processo di estrusione poiché tale legge viene applicata laddove si registrano bassi carichi e dove si riscontrano basse rugosità (asperità occasionali) sulle superfici a contatto ; nel caso esaminato sono invece in gioco elevate forze; per questi motivi tale modello non è stato ritenuto adatto e quindi non simulato.

Nella presente validazione, tutte le simulazioni sono state effettuate utilizzando per la prima volta un codice commerciale di nuova generazione, QForm. Si tratta di un recente ambiente di simulazione multidisciplinare per la modellazione dei processi di deformazione plastica; le principali caratteristiche tecniche e le equazioni che governano il sistema sono presentati [14]. Per determinare le corrette condizioni di attrito, scambio termico, implementazione della tensione di flusso del materiale deformato ed altri parametri riguardanti le impostazioni della maglia e di calcolo, sono state condotte simulazioni numeriche di estrusioni dirette della lega AA6060 sulla

base di prove sperimentali di visioplasticità descritte da in [1] . Fine ultimo del presente lavoro è l'implementazione di una routine capace di prevedere l'evoluzione dei grani delle leghe di alluminio 6XXX.
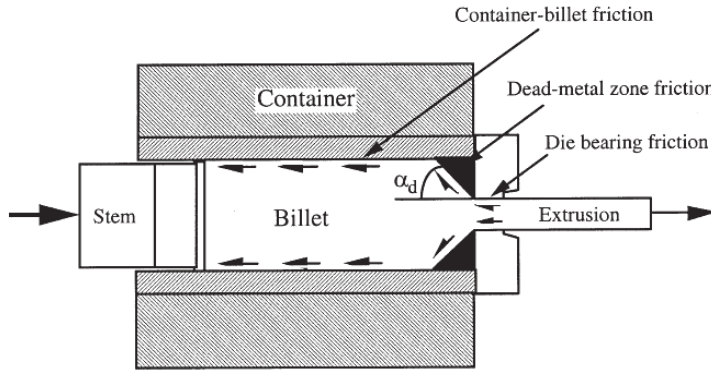
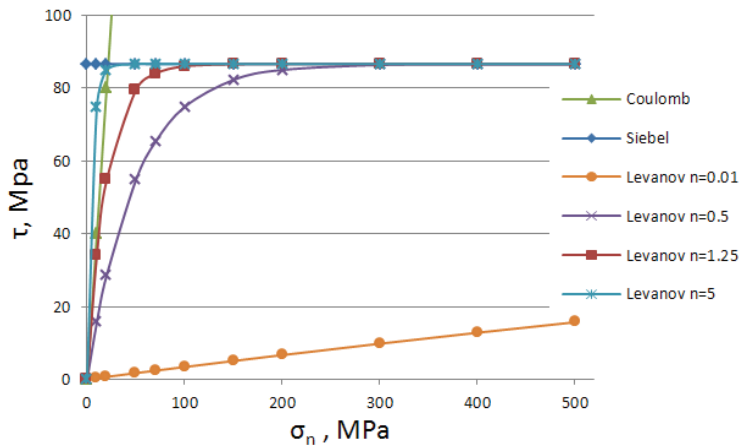**Figura 1.**Forze di attrito nell'estrusione diretta [5].

Figura 2.Grafici tensione tangenziale/pressione normale secondo i modelli di Coulomb, Siebel e Levanov.

2. PROVE SPERIMENTALI

La validazione di Qform è stata eseguita attraverso una campagna sperimentale, dettagliatamente illustrata in [1], nella quale sono stati condotti test di visioplasticità su cinque provini di lega AA 6060 (AlMgSi 0.5), in cui erano stati praticati 19 fori equidistanti di 5mm di diametro, riempiti con aste in lega AA4043 (metallo che possiede andamenti della tensione di flusso confrontabili a quelli della lega del materiale base).

Nella figura 3.a e 3.b sono messe a confronto le geometrie del provino e degli utensili utilizzati nelle prove sperimentali e nelle simulazioni. In particolare le 19 bacchette di lega AA4043 sono state modellate attraverso una griglia composta da punti posizionati all'interfaccia tra contenitore e billetta e linee equispaziate e perpendicolari all'asse dell'assemblaggio.

(a)   (b)
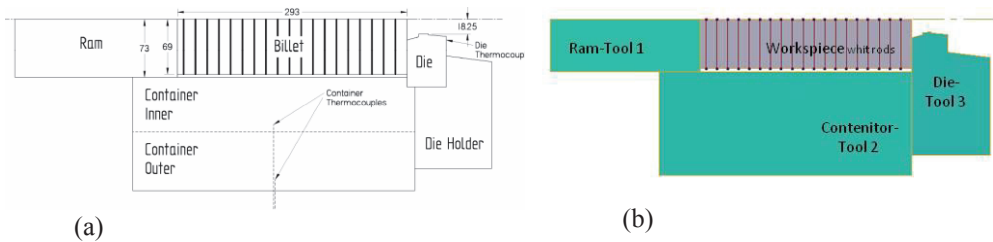
Figura 3.Geometrie degli utensili e del provino, rappresentati in simmetria assiale,
utilizzate nei test sperimentali (a) e nelle simulazioni (b)

Tabella 1. Piano e misurazioni sperimentali

		TEST 3	TEST 4	TEST 5
Piano sperimentale	Corsa pistone [mm]	150	150	175
	Velocità pistone [mm/s]	2	5	2
Grandezze misurate sperimentalmente	T matrice [°C]	350÷360	350÷380	350÷380
	ΔT profilo [°C]	20	12	20
	T contenitore [°C]	450±5	450±5	450±5
	Max carico pistone [MPa]	4,2 ±0,3	4,9±0,3	4,7±0,3
Temperature iniziali utensili	T contenitore [°C]	450	450	450
	T pistone [°C]	305	305	305
	T matrice [°C]	360	360	360

Le prove consistevano in estrusioni dirette parziali in cui sono stati variati i parametri
relativi a corsa e velocità del pistone come riassunto in Tab.(1) (qui sono presenti solo i dati
relativi alle prove scelte in seguito per le simulazioni).
I dati presi come riferimento per la validazione sono stati:
- lo scorrimento dei punti della griglia calcolato come rapporto tra la loro posizione
  finale e quella iniziale sulla interfaccia billetta- contenitore; tale andamento ha
  permesso di rilevare l'entità dell'aderenza/scivolamento del materiale deformato
  sulle pareti dell'utensile. Maggiore è l'attrito, maggiore è quindi l'aderenza.
  Nella condizione ideale di perfetta lubrificazione (quindi totale assenza di attrito)
  tutte le aste restano perfettamente perpendicolari alla superficie del contenitore, il
  coefficiente di attrito in entrambi i modelli di Siebel e di Levanov è nullo (sia nella
  formulazione teorica sia nel caso simulato)
  Diversamente varia invece il valore del fattore di attrito nello stato di completa
  adesione; questa situazione si presenta per m=1 solo nella formulazione teorica.
  Nella modellazione ottenuta con Qform infatti il coefficiente unitario rappresenta
  una condizione di attrito intermedia; per questo motivo si è reso necessario
  procedere con la validazione.
- l'andamento delle linee di flusso;
- l'andamento del carico sul pistone;
- le temperature della matrice in corrispondenza della posizione delle termocoppie;
- la temperatura del profilo estruso ad un metro dalla matrice.

3. MODELLAZIONE NUMERICA

Tutte le geometrie sono state prima disegnate su software CAD sulla base delle misure reali e successivamente importate, posizionate lungo l'asse nella direzione di estrusione e nominate in QDraft (programma di disegno 2D presente in QForm). La tensione di flusso del materiale deformato è stato inserita in forma tabellare a partire da dati ricavati da prove sperimentali di torsione sulla lega AA6060 (Fig.(4)).

In Tab.(2) sono invece riassunti tutti i rimanenti parametri di simulazione e di processo mantenuti costanti in tutte le simulazioni.

Per quanto riguarda gli utensili, le impostazioni relative a temperature ($T_{pistone}$ =305 ° C, $T_{contenitore}$ = 450 ° C, $T_{matrice}$ = 360 ° C), materiale (H11) e relativi parametri sono state mantenute costanti nell'intera campagna sperimentale e sono raccolte nella Tab. (3).

Per quanto riguarda le condizioni di scambio termico è stata preferita la modalità di flusso semplice tra billetta e contenitore a causa dell'elevata inerzia termica di quest'ultimo, dovuta alla sue notevoli dimensioni; mentre è stato impostato un flusso di calore di tipo accoppiato sulla superficie tra materiale da estrudere e i rimanenti utensili (pistone e matrice); dato che qui il flusso termico interessa l'intero volume e non solo l'area a contatto (Fig. (5)).

Tra i modelli di attrito sono stati verificati solo quelli di Siebel e Levanov, come detto in precedenza, mentre il coefficiente di trasmissione di calore tra acciaio e alluminio è stato fissato a 11000 W / (m²K) [15].

Per migliorare la qualità della discretizzazione e dei risultati, sono stati modificati alcuni parametri di simulazione, tra cui l'affinamento degli elementi della maglia nel profilo estruso in corrispondenza delle zone di lavoro, dove si registrano le deformazione più elevate, come mostrato in Fig. (6).
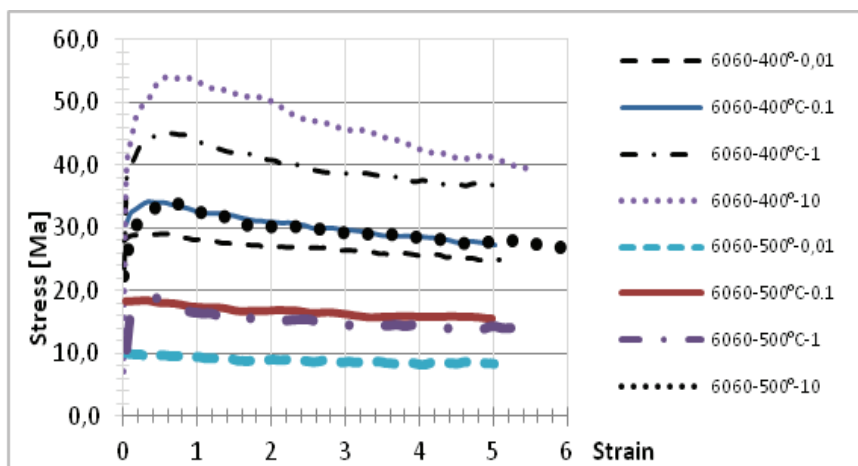

Figura 4. Tensione di flusso plastico della lega AA6060

Tabella 2. Piano e misurazioni sperimentali

Parametri di processo	Tipo di processo	Formatura con processo termico
	Tipo di problema	2D assialsimmetrico

Parametri pezzo	Densità			2700	kg/m³
	Conduttività termica			180	W/(m·K)
	Calore specifico			890	J/(kg·K)
	Temperatura di fusione			620	°C
	Modulo di Young			69000	MPa
	Modulo di Poisson			0.293	
	Coeff. Espansione term.			2.3e-5	1/°C
	Temperatura iniziale			450	°C
	Composizione chimica		min	max	
		Fe		0.7	
		Si	0.4	0.45	
		Mn		0.03	
		Mg	0.45	0.5	
		Cu		0.02	
		Cr		0.02	
		Ti		0.02	
		Zn		0.02	
		OE		0.05	
		OT		0.15	

Condizioni al contorno		Fissaggio rigido su contenitore e matrice
	Temperatura ambiente	20	°C
	Emissività	0.2	
	Coeff. scambio termico	30	W/(m²K)

Colpo	Raffreddamento in aria	60	s
	Raffred. in stampo	30	s
	Energia trasferita	100%	

Tabella 3. Piano e misurazioni sperimentali sugli utensili

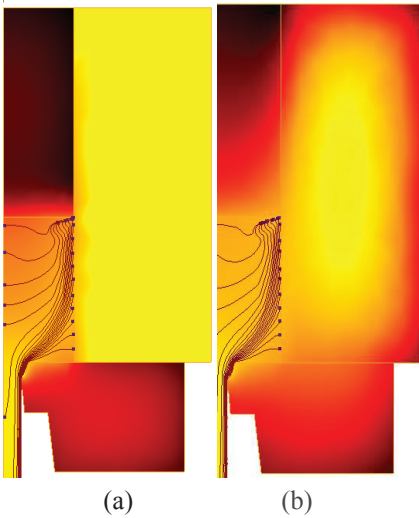| Materiale	H11 51 HRC		Modulo di Poisson		0.3	
Densità	7850	kg/m³	Tens. snervamento		1668	MPa
Conduttività termica	25	W/(m·K)	Composizione chimica		min	max
				C	0.32	0.42
Calore specifico	446	J/(kg·K)		Si	0.9	1.2
				Mn	0.25	0.55
Durezza	0.028			P		0.03
				S		0.03
Modulo di Young	210000 (T=20°C)	MPa		Cr	4.5	5.5
	160000 (T=600°C)	MPa		Mo	1.2	1.7
				V	0.3	0.5

(a)	(b)	

Figura 5. Differenze tra scambio termico accoppiato (a) e semplice (b)
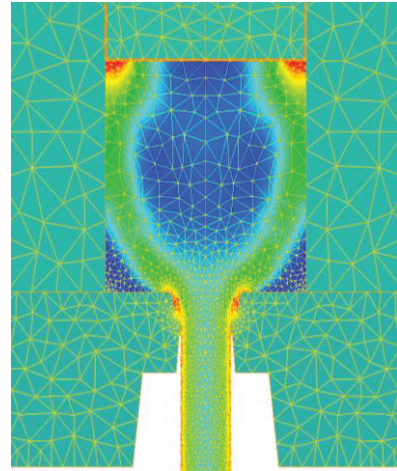
Figura 6. Discretizzazione della maglia non omogenea

In QForm è possibile impostare anche l'adeguamento automatico della grandezza di tali elementi in base alla velocità di deformazione del materiale, nonché controllare la frequenza di "remeshing" (diminuendo questo parametro l'accuratezza dei risultata aumenta a discapito dell'allungamento dei tempi di calcolo) e il numero massimo di iterazioni in ogni passo (che rappresenta i tentativi che il solutore compie per convergere alla soluzione esatta). Infine è stato verificato come l'efficienza di generazione del calore dovuta alla deformazione influisca significativamente sull'aumento di temperatura del materiale deformato e quindi sulla diminuzione del carico sul pistone; tuttavia entrambi i coefficienti di generazione del calore dovuto a deformazione e attrito sono stati mantenuti al 95% come da letteratura [16].

4. RISULTATI

È stata effettuata una sequenza di simulazioni relative al test 4 (Tab.(1)), scegliendo il modello di attrito di Levanov e modificando il coefficiente m da 0 a 5; per ciascuna di esse sono stati raccolti i risultati relativi a: andamento del carico sul pistone, temperatura della matrice e del profilo ad 1 metro, la deformazione della griglia, posizione relativa dei punti posti all'interfaccia contenitore-billetta.

In seguito alla buona concordanza tra i risultati numerici e quelli sperimentali nelle simulazioni in cui erano stati scelti valori di m=3 e m=4, sono state rilanciati i calcoli relativi al test 4 modellando l'attrito con la legge di Siebel per valori di m=3 e m=4, In seguito sono state verificate anche le condizioni relative ai test 3 e 5.

In figg.(7-8) vengono presentati i risultati delle simulazioni, in particolare sono mostrati alcuni tra i migliori confronti tra le griglie deformate, gli andamenti del carico sul pistone e i grafici in cui sono stati rilevate le condizioni di aderenza-slittamento.

Come Saha riporta in [5], la pressione di estrusione totale richiesta per un particolare rapporto di estrusione (P_T) è data da:

$$P_T = P_D + P_F + P_R \tag{5}$$

228

dove P_D è la pressione necessaria per la deformazione plastica del materiale (che dipende dal tasso e velocità di deformazione e temperatura), P_F è la pressione necessaria per vincere l'attrito sulla superficie durante il processo (che dipende dalla pressione radiale, coefficiente di attrito di tutte le superfici, lunghezza e diametro della billetta e delle zone di lavoro), P_R è la pressione necessaria per vincere il lavoro di deformazione interna (funzione del rapporto di estrusione e della tensione di flusso del pezzo). Secondo questi criteri le prove 3 e 5 hanno le stesse condizioni. Ciò viene confermato dalla similitudine tra rispettivi andamenti del carico sul pistone, mentre nella prova 4, la velocità di deformazione più elevata provoca un aumento del picco di carico (Fig.(8)).

Per quanto riguarda la distorsione delle griglie, il rapporto prossimo a 1 tra le distanze iniziali e quelle finali rappresenta una condizione di completa aderenza mentre valori inferiori corrispondono a un maggiore scorrimento; la differenza che si rileva in corrispondenza dei primi punti è invece riconducibile all'espansione del materiale che si verifica quando le billette vengono estratte dagli utensili durante i test sperimentali.

Le differenze più significative si riscontrano analizzando i due differenti approcci: il modello di Siebel sovrastima il carico massimo in tutti i casi, nonostante le tendenze del flusso siano buone; il modello di Levanov invece dà buoni risultati sia rispetto agli andamenti del carico che rispetto la deformazione delle griglie. (Fig.(7-8)).
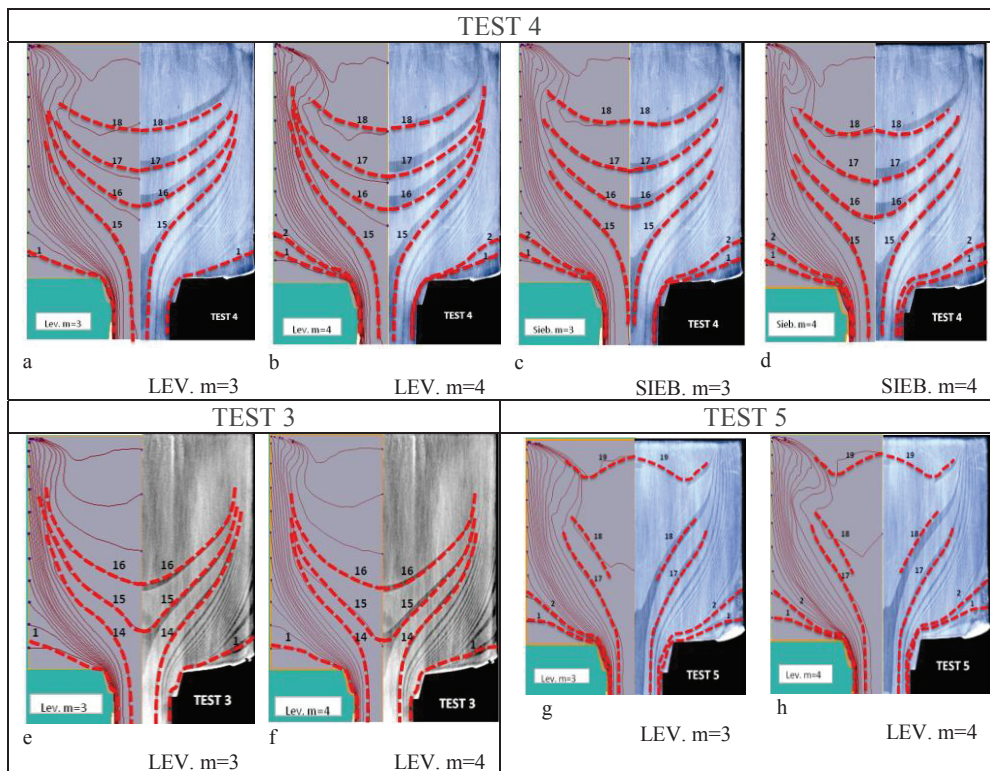

Figura 7.Confronto tra griglie deformate sperimentali e numeriche nei test 4,3,5
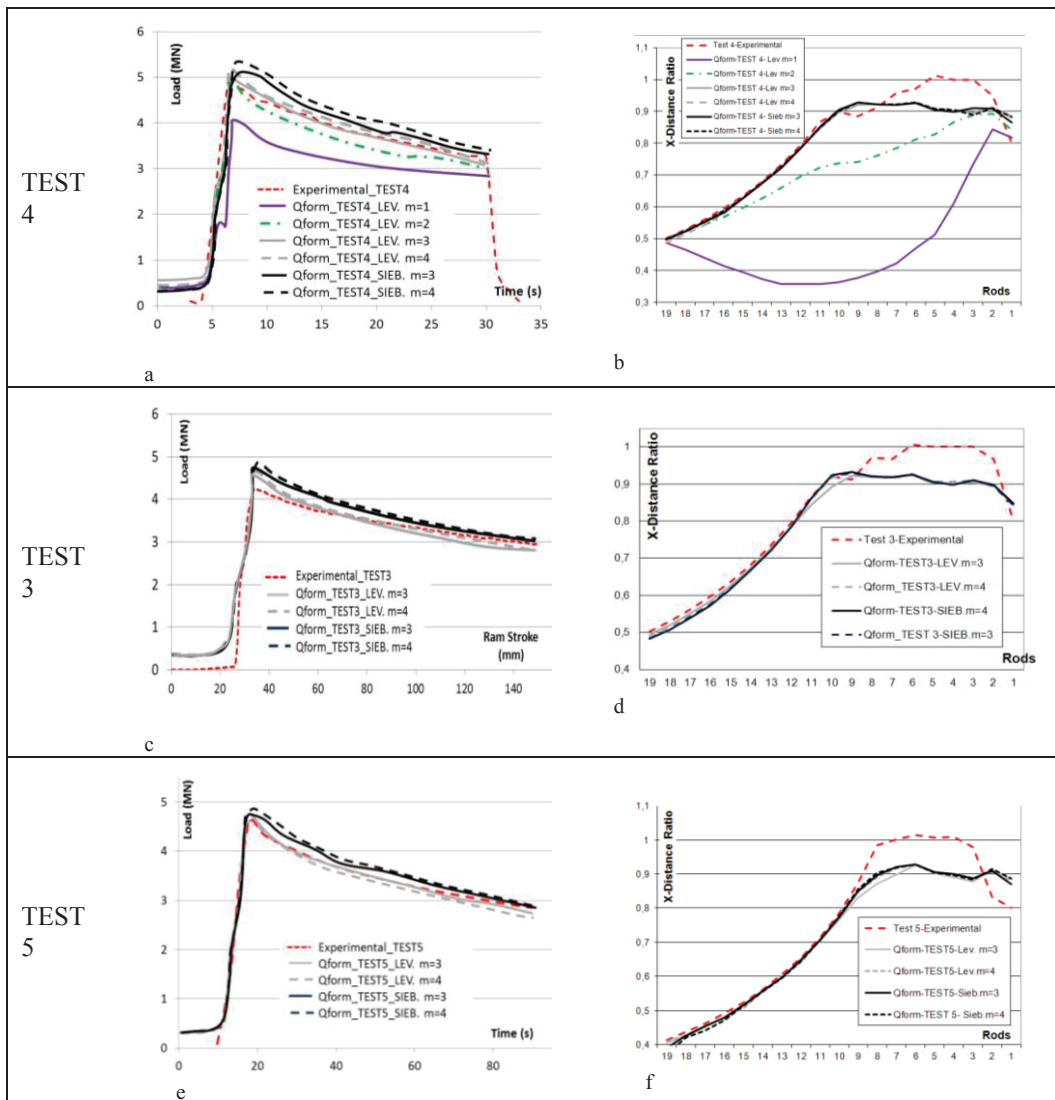
Figura 8. Confronto tra dati relative ai carichi e condizioni di scorrimento/aderenza nei test 4 (a,b), 3 (c,d), 5 (e,f)

I risultati relativi alle temperature sono in accordo con quanto affermato da Li in [15]: durante il processo in condizioni stazionarie, l'aumento della temperatura nel materiale (ΔT) è una somma di tre fattori:

$$\Delta T = \Delta T_{def} + \Delta T_{fric} + \Delta T_{loss} \qquad (6)$$

Dove ΔT_{def} è l'aumento dovuto alla deformazione, ΔT_{fric} è il contributo causato dall'attrito e ΔT_{loss} è la diminuzione di temperatura dovuto al contatto della billetta con gli utensili e l'ambiente. A causa della dipendenza diretta tra velocità di deformazione e velocità del pistone, più elevata è quest'ultima, più calore viene generato all'interno del materiale e quindi minore è il tempo a disposizione per scambiare calore con utensili e aria. Nel test 4 le temperature del profilo a 1 metro di distanza dalla zona di lavoro sono di 20 ° C superiore a quelle rilevate nei test 3 e 5. Le temperature predette numericamente sono superiori ai rispettivi valori ottenuti dalle estrusioni in pressa, le differenze sono riconducibili all' imprecisione delle misure sperimentali . Le temperature della matrice risultanti dalle simulazioni sono invece in accordo con i dati sperimentali (circa 360 ° C).

I riscontri numerici permettono di affermare che la campagna di prove condotta verifica come il modello di Levanov sia in grado di modellare le condizioni di attrito durante il processo di estrusione della serie 6XXX: tale formulazione infatti tiene conto della variazione della pressione media agente sul materiale (elevata sulla parete del contenitore e quasi nulla sulle pareti della zona di lavoro). Dai confronti effettuati si evince che m=3 è il coefficiente di attrito che consente di ottenere il miglior accordo numerico-spericmentale (con n=1,25) .

5. CONCLUSIONI

La campagna di simulazioni svolta sulla base dei dati sperimentali raccolti dai test di visioplasticità condotti sulla lega AA6060 ha permesso di individuare anche nel recente codice per la modellazione FEM dei processi di formatura, QForm, l'impostazione dei principali parametri e settaggi. In particolare sono stati individuati il modello e il valore numerico del coefficiente di attrito in grado di garantire il miglior accordo numerico-sperimentale in termini di griglia di deformazione, andamento del carico di estrusione e temperatura nel caso di lega della serie 6XXX.

Grazie a questa preliminare validazione, con il suddetto codice sarà possibile condurre un'altra serie di simulazioni per la determinazione di un modello in grado di prevedere l'evoluzione della lunghezza e spessore dei grani durante la ricristallizzazione che avviene nel processo di estrusione.

REFERENCES

[1] M. Schikorra, L. Donati, L. Tomesani, M. Kleiner, 2007. "The role of friction in the extrusion of AA6060 Aluminum alloy: process analysis and monitoring (part I)", Journal of Materials Processing Technology, Chap. 191, pp. 288–292.

[2] Håkan Hallberg, 2011. "Approaches to Modeling of Recrystallization", Metals, Chap. 1, pp. 16-48.

[3] L.Donati, A. Segatori, M. El Mehtedi, L.Tomesani, 2013 "Grain evolution analysis and experimental validation in the extrusion of 6XXX alloys by use of a lagrangian FE code", International Journal of Plasticity, Chap. 46, pp. 70–81.

[4] Luigi De Pari Jr., Wojciech Z. Misiolek, 2008 "Theoretical predictions and experimental verification of surface grain structure evolution for AA6061 during hot rolling", Acta Materialia, Chap. 56, pp. 6174–6185.

[5] Pradip K. Saha, 2000. *Aluminum Extrusion Technology*, ASM International, Chap.1, pp.12-16.

[6] T. Sheppard, 1999. "Extrusion of Aluminium Alloys", Kluwer Academic Publishers, The Netherlands.

[7] L. Wang, J. Cai, J. Zhou, J. Duszczyk, 2009. "Characteristics of the friction between aluminium and steel at elevated temperatures during ball-on-disc tests", Tribology Letters, Chap. 36, pp. 183-190.

[8] X. Ma, M.B. de Rooij, D.J. Schipper, 2012. "Friction conditions in the bearing area of an aluminium extrusion process", Wear, Chap. 278– 279, pp. 1– 8

[9] X. Ma, M.B. de Rooij, D.J. Schipper, 2010. "A load dependent friction model for fully plastic contact conditions", Wear, Chap. 269, pp. 790-796.

[10] T. Chanda, J. Zhou, L. Kowalski, J. Duszczyk, 1999. "3D FEM simulation of the thermal events during AA6061 aluminium extrusion", Scripta Materialia 41 (2) 195–202.

[11] F. Parvizian, T. Kayser, C. Hortig, B, 2009. "Svendsen, Thermomechanical modeling and simulation of aluminium alloy behavior during extrusion and cooling", Journal of Materials Processing Technology 209 876–883.

[12] A.N. Levanov, 1997. " Improvement of metal forming processes by means of useful effects of plastic fiction", Journal of Materials Processing Technology 72 314–316

[13] Liliang Wanga, Haoliang Yang, 2012. "Friction in aluminium extrusion—part 2: A review of friction models for aluminium extrusion", Tribology International 56 99–106

[14] Nikolay Biba, Sergey Stebunov, Alexey Vlasov, "Material forming simulation environment based on QFORM3D Software System".

[15] L. Li, J. Zhou, J. Duszczyk, 2004. "Prediction of temperature evolution during the extrusion of 7075 aluminium alloy at various ram speeds by means of 3D FEM simulation", Journal of Materials Processing Technology 145 360–370.

[16] N. Biba, A. Lishnij, A.Vlasov, 1998. "Simulation of coupled problem of electric upsetting", Journal of Materials Processing Technology 80–81 184–187

ADVANCES IN THE ANALYTICAL PREDICTIONS OF THE MAXIMUM EQUIVALENT STRESS IN A SHAFT-HUB PRESS-FIT

Antonio Strozzi
Department of Engineering "Enzo Ferrari"
University of Modena e Reggio Emilia, Italy
E-mail: antonio.strozzi@unimo.it

Andrea Baldini
Department of Engineering "Enzo Ferrari"
University of Modena e Reggio Emilia, Italy
E-mail: andrea.baldini@unimo.it

Matteo Giacopini
Department of Engineering "Enzo Ferrari"
University of Modena e Reggio Emilia, Italy
E-mail: matteo.giacopini@unimo.it

Enrico Bertocchi
Department of Engineering "Enzo Ferrari"
University of Modena e Reggio Emilia, Italy
E-mail: enrico.bertocchi@unimo.it

Sara Mantovani
Department of Engineering "Enzo Ferrari"
University of Modena e Reggio Emilia, Italy
E-mail: sara.mantovani@unimo.it

A b s t r a c t . Based upon a asymptotic solution obtained for the plane counterpart of the axisymmetric title problem, a simple expression is proposed for forecasting the maximum contact pressure in a shaft-hub press-fit, in which the hub bore edges are rounded.

Keywords: shaft-hub, press-fit, stress concentrations.

1. INTRODUCTION

In this paper the problem is examined of the stress concentrations in an interference-fit between a hub with rounded bore edges and a solid shaft, see Fig. (1). The interference-fit is assumed to be keyless and frictionless, and the shaft is assumed not to be subjected to bending. It is intimated that the present paper addresses a traditional stress concentration problem, and that fretting fatigue aspects are beyond the scope of this paper.

Figure 1 clarifies the meaning of the main symbols adopted. In particular, r_i denotes the shaft inner radius, r_m is the shaft outer radius, which nominally coincides with the hub inner
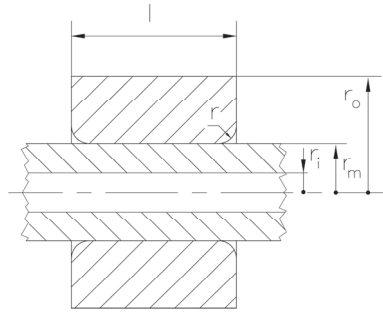
Figure 1. The shaft-hub assembly.

radius, r_o is the hub outer radius, r is the fillet radius of the hub bore edges, and l is the hub axial length. In addition, E is the Young's modulus of the shaft and the hub.

The available salient information on the stress concentrations occurring in shaft-hub interference-fits is perfunctorily summarised in the following, see [1, 2] for a solid shaft, and [3], for the extension to a hollow shaft.

To limit the outcome of very high stress concentrations, the hub bore edges are generally rounded. Moving in the shaft axis direction, the contact pressure remains almost flat in the central zone of the shaft-hub contact, where it may be confidently evaluated with the Lamé equations for thick-walled cylinders; it exhibits Hertzian-type local bumps in the lateral zones where the hub bore edges are rounded; the contact pressure becomes null at the contact extremities. The lateral bumps and the central flattish zone confer to the contact pressure distribution a camel-backed profile. The peak equivalent stress in the shaft-hub press-fit always occurs within the hub and not within the shaft, and it is located in the vicinity of the radiused edges of the hub bore. Consistent with the Hertzian nature of the pressure bumps, the maximum equivalent stress within the hub does not occur at the hub bore surface, but at a sub-superficial point.

In [2] the sign of the hub hoop stress where the hub equivalent stress is maximum was thoroughly investigated; it was found that this hoop stress is positive when the fillet radius is small, whereas it becomes negative for large fillet radii. Unfortunately, it was not possible to detect a simple parameter forecasting the sign of the hoop stress.

Although many papers are traceable that address the press-fit stress concentrations, see the literature review of [1], only a few papers report design formulae of ample validity and prompt access, *e.g.* [1- 4]. These formulae express the hub maximum equivalent stress in terms of the constant pressure originating in the central part of the shaft-hub contact, *e.g.* [1], or in terms of the central maximum equivalent stress, *e.g.* [4]. In both cases, the reported design formulae employ stress-related parameters.

Conversely, recently developed design formulae addressing the plane counterpart of the axisymmetric, press-fit problem, that is, a rectangular punch with rounded edges indenting a half plane [5, 6], suggest that it is particularly advantageous to express the maximum contact pressure, and, consequently, the stress concentration, by referring to strain related parameters. The aim of this paper is to develop design formulae for the stress concentrations in a shaft-hub press-fit, based upon strain related parameters.

2. ADVANTAGES OF STRAIN RELATED PARAMETERS

The approach employed in [1] to derive stress concentration formulae in a shaft-hub press-fit is based upon the formal description of the shaft-hub contact problem in terms of an integral equation. The effect of the edge radius of the hub bore is mainly accounted for by the normalized parameter $r_m^2/(Ir)$, where r_m is the hub inner radius, which nominally coincides with the shaft outer radius, I is the diametral interference between the shaft and the hub, and r is the hub bore fillet radius. However, in [1] it is shown that a further parameter describing the fillet radius effect must be included, namely the parameter r/r_m. The approach favoured in this paper exhibits the advantage that a single parameter, namely $(r_m/r)^{0.1507}$, see Eqn. (7) below, accounts for the fillet radius effect. In addition, in the approach of [1], the shaft-hub interference I appears twice, namely in the above parameter $r_m^2/(Ir)$, and in the definition of the central, uniform pressure p_0. In the approach favoured in this paper, the interference appears only in the definition of the central pressure p_0. In the stress-related approach, the effect of the macroscopic geometry of the shaft-hub fit, defined by the variables r_o, r_m and r_i, is described by the normalized ratios r_o/r_m and by r_m/r_i, and by the central pressure p_0, whereas in the strain-related approach the effect of the macroscopic geometry is summarized only by p_0. (The indenter length l is generally not influential; in the strain-related approach, only the microscopic variable r is not summarized by p_0.)

Additional advantages of the strain related parameters emerge by considering the example of the asymptotic design formula expressing the maximum contact pressure for the plane problem of a deformable rectangular punch with rounded edges indenting a deformable half plane, see [6] (this plane problem is particularly analogous to the title problem, in which both the shaft and the hub are deformable)

$$\frac{p_{max}}{E} \cong 0.592 \left(\frac{p_0}{E}\right)^{\frac{2}{3}} \left(\frac{w}{r}\right)^{\frac{2}{3}\times 0.226} \tag{1}$$

where p_{max} denotes the maximum contact pressure between the indenter and the half plane, p_0 is the central pressure, E is the Young's modulus, r is the fillet radius of the indenter edges, and w is the indenter length. The above formula expresses a connection between the strain-related parameters p_{max}/E and p_0/E.

It is appreciated that, starting from Eqn. (1) based upon strain-related parameters, it is possible to derive a formula based upon stress-related parameters, but at the cost of an appreciably more complex expression. In fact,

$$\frac{\dfrac{p_{max}}{E}}{\dfrac{p_0}{E}} \cong 0.592 \frac{\left(\dfrac{p_0}{E}\right)^{\frac{2}{3}}}{\dfrac{p_0}{E}} \left(\frac{w}{r}\right)^{\frac{2}{3}\times 0.226} \qquad \Rightarrow \qquad \frac{p_{max}}{p_0} \cong 0.592 \left(\frac{p_0}{E}\right)^{-\frac{1}{3}} \left(\frac{w}{r}\right)^{\frac{2}{3}\times 0.226} \tag{2}$$

By putting

$$p_0 = \frac{E\delta}{h} \tag{3}$$

where δ indicates the indenter compression, and h is the indenter height, one obtains

$$\frac{p_{max}}{p_0} \cong 0.592 \left(\frac{\delta}{h}\right)^{-\frac{1}{3}} \left(\frac{w}{r}\right)^{\frac{2}{3}\times 0.226} \tag{4}$$

It appears that Eqn. (4), expressing the stress concentrations in terms of stress-related parameters, requires that the indenter width w, the compression imposed δ, and the indenter height, h, explicitly appear in the formulae. In other words, the above example shows that the stress concentration formula expressed in terms of stress-related parameters becomes more complicated.

Because of the analogy between plane and axisymmetric problems, see the appendix of [7], the maximum contact pressure in a press-fit is expressed in this paper by a formula similar to Eqn. (1). However, it is observed in [1] that the indenter width w does not appear in the shaft-hub problem, provided that w is sufficiently large, that is, if the hub axial length is reasonably high.
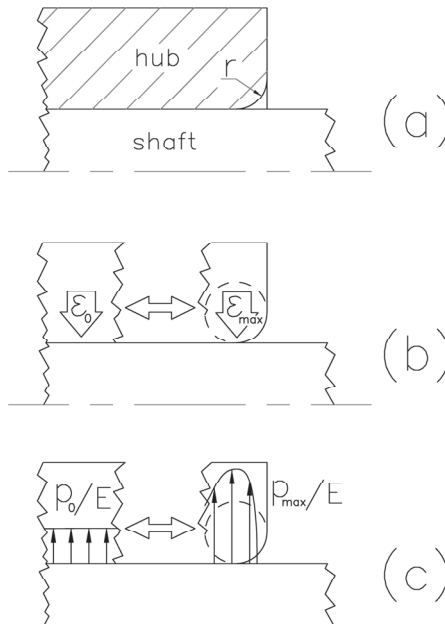

Figure 2. Usefulness of the strain-related approach.

Consequently, in Eqn. (1) w has been substituted with a reference dimension, *e.g.* the hub inner radius r_m. The formula favoured in this paper is therefore

$$\frac{p_{max}}{E} \cong C \left(\frac{p_0}{E} \right)^{\frac{2}{3}} \left(\frac{r_m}{r} \right)^{\frac{2}{3} \times 0.226} \cong C \left(\frac{p_0}{E} \right)^{\frac{2}{3}} \left(\frac{r_m}{r} \right)^{0.1507} \tag{5}$$

where in this formula the radial thickness of the hub, $r_o - r_m$, and of the shaft, $r_m - r_i$, do not appear explicitly, provided that they are sufficient to let the stresses to become uniform in the shaft axial direction, along the regions remote from the contact. Selected Finite Element (FE) numerical experiments have shown that a radial thickness for the hub and the shaft of the order of 10 times the fillet radius is sufficient to guarantee the above uniformity. In conclusion, the effect of the shaft and hub radial thickness and of the interference is expressed by the classical central solution

$$p_0 = \frac{EI}{2r_i} \frac{1}{\dfrac{r_i^2 + r_m^2}{r_m^2 - r_i^2} + \dfrac{r_m^2 + r_o^2}{r_o^2 - r_m^2}} \tag{6}$$

where r_i, r_m and r_o denote the shaft inner radius, the hub inner radius, and the hub outer radius, respectively.

One of the advantages of the formula based upon strain-related parameters is that the effect of the shaft and hub geometries and of the interference imposed is absent in Eqn. (5) expressing the maximum contact pressure in terms of strain-related parameters, apart from the presence of the normalizing parameter r_m.

Figure 2 depicts the response of the strain-related parameters in a graphical way. Figure (a) illustrates the transition zone between the central part, where the contact is flat, and the lateral part, where the hub bore fillet is rounded. Figure (b) graphically shows that a connection must hold between the central strain ε_0 and the lateral strain ε_{max}. As a result of the progressive character of this contact, the above connection is nonlinear with the imposed, central strain. This graphical representation justifies the existence of a simple relationship between the central strain expressed in terms of stress, p_0/E, and the lateral strain, p_{max}/E.

3. CALIBRATION OF THE MULTIPLYING CONSTANT

The following expression, valid for a plane contact, is proposed to describe the axisymmetric contact problem too.

$$\frac{p_{max}}{E} \cong C \left(\frac{p_0}{E} \right)^{\frac{2}{3}} \left(\frac{r_m}{r} \right)^{0.1507} \tag{7}$$

where the constant C may be calibrated versus FE forecasts.

The following ranges of the leading variables have been numerically examined, see [1]: $0.3 \leq r_m/r_o \leq 0.7$, $0.3 \leq r_i/r_m \leq 0.5$, $0.025 \leq r/r_m \leq 0.05$, $r_m/w = 0.125$. The value of the coefficient C

computed as

$$C = \dfrac{\dfrac{p_{\max}}{E}}{\left(\dfrac{p_0}{E}\right)^{\frac{2}{3}} \left(\dfrac{r_m}{r}\right)^{0.1507}} \qquad (8)$$

has been reported along the *y*-axis, whereas along the *x*-axis a representative variable of the stress concentration has been reported, namely the parameter $\Phi = Ir/r_m^2$, see [1]. Figure 3 collects 987 FE forecasts, showing that the parameter C of Eqn. (7) remains essentially constant as r_i, r_m, r_o, r, E, I fall within the above reported intervals. The most suitable value of C is 0.6. It is concluded that Eqn. (7) correctly represents the pressure peak versus the central pressure for a variety of shaft-hub press-fit geometries.

For the cases examined, the maximum error of the central pressure computed with FE and its analytical counterpart based upon the Lamè solution is 4.8 per cent, and it occurs for the highest interferences.

To fully realize the compactness of the proposed Eqn. (7), this formula should be compared to the practically equivalent, but considerably longer, Eqn. (6) of [2].
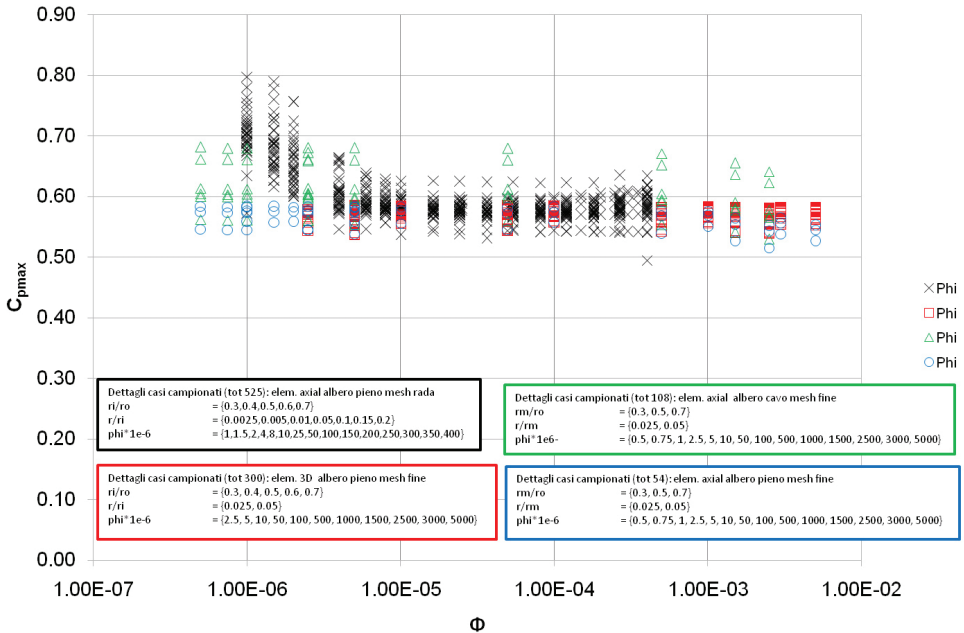

Figure 3. FE calibration of the constant *C*.

4. ACCEPTABLE AND UNACCEPTABLE SIMPLIFICATIONS

In [8] it is shown that, for a prescribed uniform pressure at the shaft-hub contact, the radial displacement in a solid shaft is generally considerably lower than its counterpart at the inner border of the hub. More precisely, for a hub outer radius twice its inner radius and for a solid shaft, the radial centrifugal displacement of the hub inner border is about ¾ of the imposed radial interference between the hub and the shaft, whereas the radial centripetal displacement of the shaft surface is ¼ of the imposed interference. Consequently, in the evaluation of the central contact pressure p_0 in terms of the interference imposed, it is often admissible to neglect the shaft radial deformation with respect to that of the hub inner border.

Conversely, when evaluating the lateral pressure peaks, it is not admissible to consider the shaft as rigid, since this simplification would not correctly model the asymptotic trend of the pressure peak when the hub bore fillet radius becomes null. In fact, if the shaft is deformable, for null fillet radius the pressure peak becomes infinite, whereas, if the shaft is rigid, the pressure remains finite, *e.g.* [6].

The above observations suggest how to choose a suitable FE mesh. In fact, the shaft mesh may be coarser than that of the hub in the zones where the contact pressure is uniform, since the shaft radial deflection is lower than that of the hub and, consequently, the error incurred with a coarse mesh must be limited. Instead, where the contact pressure exhibits high gradients, that is, in the region where the lateral pressure bumps develop, the mesh size of the shaft must be fully comparable to that of the hub.

5. ON THE CONNECTION BETWEEN THE MAXIMUM CONTACT PRESSURE AND MAXIMUM EQUIVALENT STRESS

In addition to the knowledge of the maximum contact pressure, the prediction of the hoop stress is necessary for forecasting the maximum equivalent stress. It is difficult to predict the value of the hub hoop stress where the hub equivalent stress is maximum. In [2] it is found that this hoop stress is negative when the fillet radius is small, whereas it becomes positive for large fillet radii, and a physical interpretation of this mechanical behaviour is proposed in [1]. An alternative parameter disambiguating the hoop stress sign might be the peak pressure over the central pressure. In the above works it was not possible to detect a simple, reliable parameter forecasting the sign of the hoop stress, and to define a simple relationship expressing the value of the hoop stress in terms of the maximum contact pressure.

The problems encountered in defining the above connection between the maximum contact pressure and the maximum equivalent stress betrays the three-dimensional character of this aspect.

Since the connection between the maximum pressure and the corresponding equivalent stress is a difficult matter, it was decided to confine the current analysis to the maximum contact pressure, and to defer the hoop and equivalent stress evaluation to a future paper.

6. CONCLUSIONS

Based upon an asymptotic solution obtained for the plane counterpart of the title problem, a simple expression has been proposed for forecasting the maximum contact pressure in the axisymmetric problem of a shaft-hub press-fit, in which the hub bore edges are rounded. A multiplying coefficient has been calibrated versus extensive FE forecasts. The definition of the maximum equivalent stress in terms of the central pressure is difficult, since the hoop

stress, which constitutes a component of the equivalent stress, is negative for small fillet radii, but it becomes positive for higher radii. This aspect is deferred to a future paper.

REFERENCES

[1] Strozzi, A., Baldini, A., Giacopini, M., Bertocchi, E., and Bertocchi, L., 2011. "Normalization of the stress concentrations at the rounded edges of a shaft-hub interference fit". J. Strain Analysis, 46(6), August, pp. 478–491.

[2] Strozzi, A., Baldini, A., Giacopini, M., Bertocchi, E., and Bertocchi, L., 2012. "Stress concentrations at the rounded edges of a shaft-hub interference fit". ASME 2012 Mechanical Engineering Congress, November 9 – 15, Houston, TX.

[3] Croccolo, D., De Agostinis, M., and Vincenzi, M., 2012."Normalization of the stress concentrations at the rounded edges of a shaft–hub interference fit: extension to the case of a hollow shaft". J. Strain Analysis. 47(3), February, pp. 131–139.

[4] Croccolo, D., and Vincenzi, N., 2010. "Stress concentration factors in compression-fit couplings". Proc. IMechE, Part C: J. Mechanical Engineering Science, 224(6), June, pp. 1143–1152.

[5] Sackfield A., Mugadu A., Barber J.R., and Hills D.A., 2003."The application of asymptotic solutions to characterising the process zone in almost complete frictionless contacts". Journal of the Mechanics and Physics of Solids, 51(7), pp. 1333–1346.

[6] Strozzi, A., Bertocchi, E., Baldini, A., and Giacopini, M. 2014."On the applicability of the Boussinesq influence function in modelling the frictionless elastic contact between a rectangular indenter with rounded edges and a half-plane". Proc IMechE Part C: J Mechanical Engineering Science DOI:10.1177/0954406214542641

[7] Barton, M.V., 1941. "The circular cylinder with a band of uniform pressure on a finite length of the surface". ASME J. Appl. Mech., 63(8), pp. 97–104.

[8] Strozzi, A., 1998. Costruzione di macchine, Pitagora, Bologna.

UN SEMPLICE MODELLO COESIVO CON ATTRITO PER DESCRIVERE INTERFACCE IBRIDE FORZATE E INCOLLATE

Davide Castagnetti
Department of Engineering Sciences and Methods,
University of Modena and Reggio Emilia, Italy
E-mail: davide.castagnetti@unimore.it

Eugenio Dragoni
Department of Engineering Sciences and Methods,
University of Modena and Reggio Emilia, Italy
E-mail: eugenio.dragoni@unimore.it

Abstract. *Il lavoro studia interfacce ibride forzate meccanicamente e incollate con adesivo anaerobico. Se dal punto di vista della loro resistenza statica sono state ampiamente studiate, altrettanto non è relativamente al loro comportamento fino a completo collasso. Obiettivo di questo lavoro è verificare l'applicabilità di un semplice modello costitutivo, che unisce un legame coesivo con una legge di puro attrito, per descrivere il comportamento dell'interfaccia fino a completo collasso sotto differenti livelli di pressione di contatto. Un'estesa campagna sperimentale esamina la resistenza a taglio di provini cilindrici incollati testa a testa considerando due adesivi anaerobici e quattro livelli di pressione di contatto. Le curve sperimentali confermano che l'energia di deformazione fino a completo collasso del provino è somma di un contributo coesivo e di uno di puro attrito, linearmente dipendenti dalla pressione di contatto.*

Keywords: *adesivi anaerobici, forzamento meccanico, interfacce ibride, legame costitutivo, collasso a taglio*

1. INTRODUZIONE

Il lavoro esamina sperimentalmente la resistenza a taglio, sotto differenti livelli di pressione, di interfacce ibride in cui il forzamento meccanico è supportato dall'incollaggio con adesivo anaerobico.

Obiettivo del lavoro è valutare se la risposta fino a completo collasso di queste interfacce ibride (forzate e incollate) può essere descritta mediante un semplice modello costitutivo che combina il legame coesivo con una legge di puro attrito. Gli adesivi anaerobici sono un modo semplice e molto efficace per migliorare le prestazioni di giunti per attrito, nei quali le forze di unione sono ottenute con serraggio meccanico [1]-[6]. Un metodo proposto in letteratura per calcolare la resistenza statica a taglio di giunzioni ibride forzate e incollate consiste nel sommare gli effetti della resistenza dell'adesivo e dell'attrito [7]-[9]. I risultati sperimentali mostrano, però, che nonostante la resistenza delle giunzioni

ibride aumenti con la pressione di contatto, il tasso di crescita per i giunti ibridi dipende fortemente dall'adesivo impiegato.

Figura 1 (Dragoni et al. [10]) mostra la resistenza misurata sperimentalmente in un accoppiamento cilindrico come funzione della forza di serraggio e della condizione dell'interfaccia. Quando si impiega un anaerobico forte, la resistenza complessiva del giunto è sempre maggiore di quella del giunto non incollato. Al contrario, quando si impiega un anaerobico debole, il giunto secco è più forte di quello ibrido oltre un certo livello di forza di serraggio. Secondo Dragoni et al. [10]-[12] questo comportamento è spiegabile con un semplice modello micromeccanico che ipotizza che uno strato di adesivo sia sempre presente tra le asperità superficiali degli aderendi a contatto. Secondo il modello proposto, l'alta pressione locale che agisce sullo strato di adesivo intrappolato tra le creste delle rugosità ne aumenta la resistenza a taglio rispetto a quella dell'adesivo a pressione nulla. A parità di pressione di contatto, gli adesivi più forti mostrano un incremento maggiore di quelli deboli. La validità di questo semplice modello è stato dimostrata dagli autori sia mediante un'estesa campagna di prove sperimentali [13], sia svolgendo una campagna di simulazione agli elementi finiti su scala microscopica [14-15]. In particolare, si può quindi affermare che un velo di adesivo rimane sempre presente tra le asperità delle superfici dell'interfaccia.

Dalle curve di rottura sperimentali sembra, inoltre, emergere che il comportamento dell'interfaccia ibrida fino a completo collasso possa essere descritto combinando un legame coesivo con una legge di puro attrito. In letteratura tale approccio è stato impiegato in ambiti simili. In [16], Alfano e Sacco propongono un modello coesivo con attrito per descrivere il comportamento di murature ed anche l'interazione tra fibra e matrice. In [17], lo stesso approccio viene generalizzato per studiare la propagazione di fratture in costruzioni di calcestruzzo, considerando anche l'effetto di un liquido in pressione che propaga all'interno della superficie di frattura. Nel campo delle interfacce ibride incollate con adesivi epossidici, Oinonen e Marquis propongono un approccio simile [18]-[19] che impiega il legame coesivo assieme ad un complesso modello di evoluzione del danneggiamento dell'interfaccia. Il limite principale di questo modello è nei numerosi parametri del materiale che devono essere determinati sperimentalmente.

In letteratura non si ritrovano, però, modelli costitutivi per la descrizione del comportamento fino a completo collasso di interfacce ibride che combinano il forzamento meccanico all'incollaggio con adesivo anaerobico.

Questo lavoro intende superare questa lacuna proponendo un modello costitutivo semplice che unisce un legame coesivo ad una legge di puro attrito. Due sono le fasi in cui si articola il lavoro. Nella prima fase si allestisce e si calibra il sistema di misura necessario per lo svolgimento delle prove sperimentali. Nella seconda fase si svolge un'estesa campagna sperimentale che valuta la risposta dell'interfaccia ibrida fino a completa rottura a taglio. Le variabili considerate sono due: il tipo di adesivo (un anaerobico debole ed uno forte) e la pressione nominale di contatto (su quattro livelli).

Le prove impiegano un semplice provino tubolare, mostrato in Figura 2a, analogo a quello impiegato in [13]. Il provino è composto di due aderenti che realizzano un'area anulare incollata testa a testa: in essa si sviluppa uno stato tensionale ragionevolmente uniforme sia a compressione sia a taglio, prodotto dall'applicazione sequenziale di una forza di compressione e di una coppia torcente. Le prove di rottura sono svolte applicando al provino una forza assiale iniziale, mantenuta costante durante la prova, alla quale viene sovrapposta una rotazione torsionale quasi statica. Misurando in modo continuo ed accurato
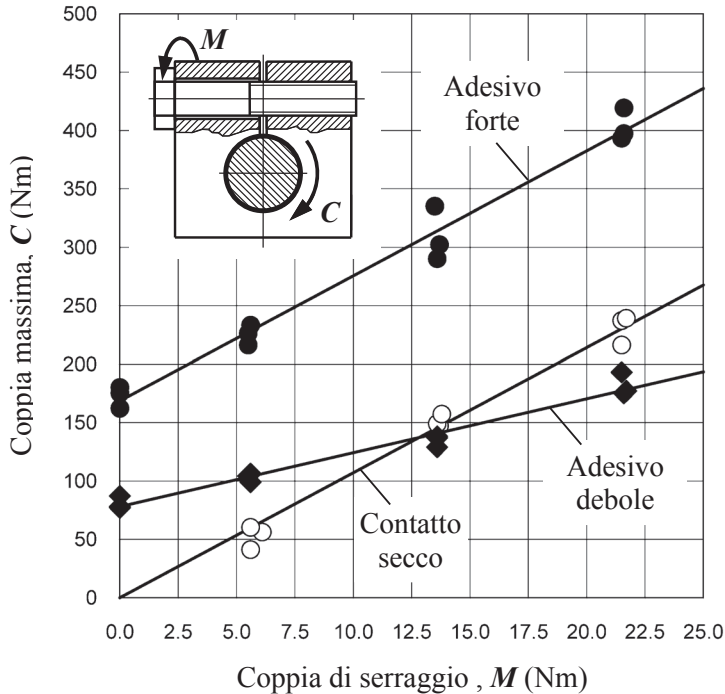
Figura 1. Andamento della coppia di rottura in funzione della coppia di serraggio per contatto secco (pallini vuoti), adesivo debole (rombi pieni) ed adesivo forte (pallini pieni).

la coppia torcente e la corrispondente rotazione fino a completo collasso della giunzione si determina l'energia di deformazione a rottura.

Il modello costitutivo proposto si basa sull'energia di deformazione fino a completo collasso dell'interfaccia ibrida scomponendola in due contributi: uno dovuto al solo attrito tra le superfici dell'interfaccia, l'altro imputabile alla frattura coesiva dello strato di adesivo interposto tra le superfici dell'interfaccia. I risultati sperimentali ottenuti mostrano, con buona ripetibilità, che entrambe queste grandezze dipendono linearmente dalla pressione nominale di contatto, con una notevole superiorità quantitativa da parte dell'adesivo anaerobico forte.

2. METODO

Figura 2a mostra il disegno dell'aderendo tubolare che va a realizzare il provino impiegato per la campagna di prove sperimentali. Gli aderendi sono eseguiti al tornio, partendo da barre rettificate ⌀22H7, in acciaio da costruzione C40 e sono impiegati in coppia con incollaggio sulla superficie anulare ⌀16x22 mm (Figura 2b). Le dimensioni dell'area d'incollaggio e, conseguentemente, dell'aderendo, sono state scelte in relazione alla forza assiale e alla coppia massime applicabili dalla macchina di prova servo idraulica MTS 858 disponibile in laboratorio. Tali dimensioni consentono di realizzare, sotto il massimo carico assiale realizzabile dalla macchina, una pressione nominale di contatto fino a 134 MPa sulla superficie d'incollaggio.
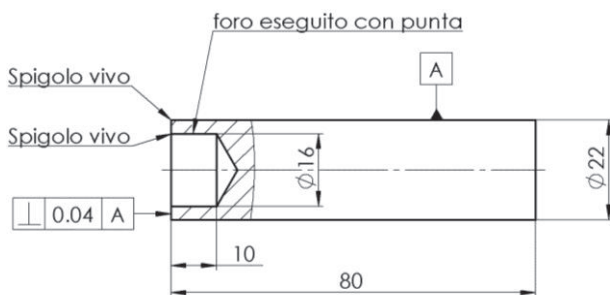
Figura 2. Schema costruttivo dell'aderendo impiegato per le prove sperimentali (a) e immagine di aderendo realizzato al tornio (b).

Considerando che il contatto avviene tra superfici rugose, per effetto dello stato tensionale localmente idrostatico che si sviluppa sulle asperità, l'acciaio degli aderendi sviluppa localmente una tensione di snervamento apparente che è tripla di quella macroscopica [20]. Di conseguenza, le pressioni di contatto tra le asperità deformate plasticamente risultano pari a circa tre volte il valore di tensione di snervamento misurato macroscopicamente. Quindi applicando una pressione media pari al valore macroscopico di snervamento del materiale, si ottiene una superficie reale di contatto che è, circa un terzo della superficie nominale di incollaggio.

Approntamento attrezzatura di prova

Per misurare in modo accurato e preciso l'angolo di rotazione del provino tubolare sia nella fase elastica sia in quella post-elastica, fino a completo collasso, si è scelto di installare un encoder rotativo direttamente sul provino in prossimità dell'interfaccia ibrida.

Figura 3 mostra uno schema del sistema messo a punto per le prove. Si è scelto un encoder rotativo ad albero cavo Hengstler RI 76TD [21] con diametro interno di 30 mm. L'encoder è di tipo incrementale da 10000 impulsi per ogni giro, alimentato in tensione continua a 5 V, con interfaccia di comunicazione RS 422 TTL e fornisce quattro canali di uscita (due principali ed i loro negati). La parte mobile dell'encoder ((7) in Figura 3) è accoppiata all'aderendo superiore (1) mediante una boccola di centraggio (8). Gli accoppiamenti tra questi tre elementi sono realizzati con gioco minimo, per minimizzare errori nella misura. Il telaio dell'encoder (6) è fissato alla staffa (5) mediante due viti di collegamento. La staffa (5) è un collare a C che viene serrata all'aderendo inferiore (2) agendo su un bullone (9). Questo sistema permette di misurare la rotazione dell'aderendo superiore (1), realizzata dall'afferraggio idraulico superiore (3), rispetto all'aderendo inferiore (2), che è mantenuto fisso dall'afferraggio idraulico inferiore (4). In particolare, la rotazione relativa è misurata in prossimità delle interfacce, escludendo quindi le cedevolezze della catena cinematica connessa alla macchina di prova.
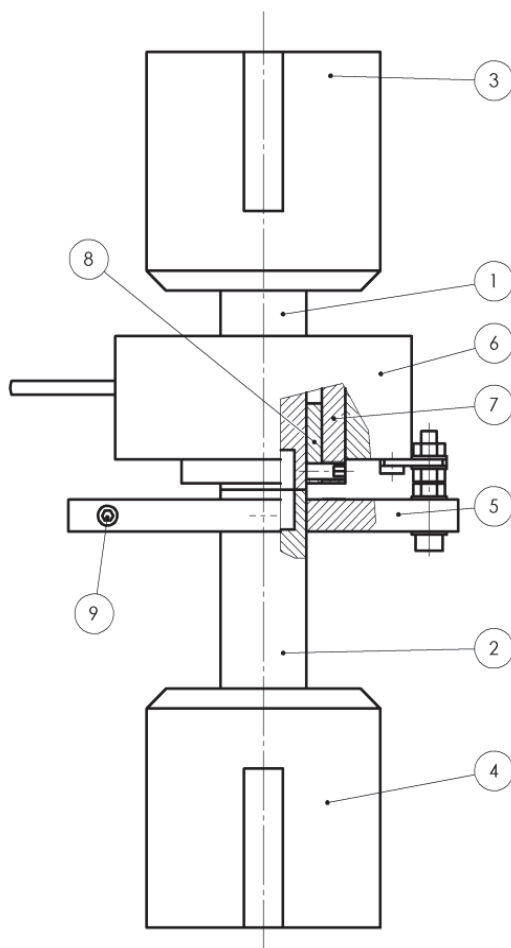
Figura 3. Schema di complessivo del provino completo di sistema di misura, montato sulla macchina di prova.

Il segnale generato dall'encoder è stato acquisito, con frequenza di 1000 Hz, mediante una scheda di acquisizione National Instruments USB 6251 [23], collegata ad un notebook. La stessa scheda di acquisizione riceve dal controllore della macchina di prova MTS il segnale di tensione, variabile nell'intervallo da -10 V a + 10V, corrispondente al momento torcente misurato dalla cella di carico. Entrambi i segnali, angolo di rotazione e momento torcente, vengono gestiti dal software Labview [23], installato sul notebook che controlla la scheda di acquisizione. In particolare, nel software si è sviluppato un algoritmo per la sincronizzazione dei segnali e la loro conversione nell'angolo di rotazione, e nel momento torcente rispettivamente. L'angolo di rotazione è proporzionale al numero di fronti d'onda di salita e di discesa di ciascun segnale. Trattandosi di due onde sfasate di 90° è possibile ottenere una risoluzione pari a 0.009°. Il momento torcente è proporzionale alla tensione elettrica. Figura 4 mostra il complesso del sistema di prova impiegato.

Campagna di prove sperimentali

Tabella 1 definisce le due variabili di prova del piano sperimentale fattoriale. Gli adesivi oggetto di prova sono un anaerobico debole (Loctite 243 [24]) ed un anaerobico forte (Loctite 638 [25]). L'interfaccia ibrida, dalla polimerizzazione dell'adesivo fino al completamento della prova di torsione a rottura, è stata soggetta a quattro livelli di pressione: 0.5 MPa (corrispondente a 90 N di carico assiale), 45 MPa (corrispondente a 8.1 kN di carico assiale), 90 MPa (corrispondente a 16.2 kN di carico assiale) e 134 MPa (corrispondente a 24 kN di carico assiale). Il valore inferiore della pressione applicata è stato scelto in modo da assicurare il contatto tra le superfici d'incollaggio. Per ciascuna configurazione si sono svolte tre repliche, esaminando in totale di 24 condizioni di prova.

I provini sono stati preparati secondo il seguente procedimento:
1. carteggiatura degli aderendi;
2. pulitura degli aderendi con solvente Loctite 7063;
3. posizionamento degli aderendi sugli afferraggi della macchina di prova;
4. posizionamento dell'assieme encoder ed adattatore sull'aderendo superiore;
5. posizionamento della staffa di fissaggio dell'encoder sull'aderendo inferiore;
6. registrazione dell'impronta di contatto sotto un carico di 1 kN e 24 kN (raggiunto caricando a 5 kN/min), impiegando un foglio di carta velina affiancato ad uno di carta carbone;
7. allontanamento degli aderendi e rimozione della carta di lettura dell'impronta;
8. deposizione dell'adesivo anaerobico;
9. avvicinamento degli aderendi fino al precarico desiderato.

Durante tutta la fase di polimerizzazione e di prova il provino è stato illuminato con due lampade alogene disposte su posizioni diametralmente opposte, al fine di innalzarne la temperatura riducendo il tempo necessario per la polimerizzazione. La temperatura è stata misurata durante differenti momenti della polimerizzazione e della prova con un termometro ad infrarossi, registrando un valore di circa 45°C per tutti i provini. Il raggiungimento di questa temperatura è stato possibile, oltre che per la presenza del sistema d'illuminazione, anche per il calore dissipato dai circuiti idraulici della macchina di prova in condizione di esercizio.

La procedura di prova si è articolata in una prima fase di precarico e polimerizzazione seguita da una seconda fase di rottura del provino. Il precarico sul provino è stato applicato ad una velocità di 5 kN/min, in modo da raggiungere la pressione desiderata prima che la polimerizzazione dell'adesivo fosse iniziata. Dal momento del raggiungimento del precarico, il provino è stato lasciato polimerizzare per 6 ore. Secondo la scheda tecnica fornita dal produttore, infatti, ad una temperatura di 45°C questo tempo è ampiamente sufficiente a garantire il raggiungimento delle piene proprietà meccaniche [9]-[10]. Al termine della polimerizzazione si è applicata una rotazione dell'aderendo superiore a velocità di 0.2°/s fino a spazzare un angolo di 90°, mantenendo costante, contemporaneamente, la forza assiale. Questo elevato angolo di rotazione si è reso necessario al fine di ottenere sempre una stabilizzazione della curva di risposta dell'interfaccia ibrida.

La procedura di prova è stata implementata sul software di controllo della macchina di prova. Ciò ha permesso di svolgere tutte le replicazioni di ciascuna condizione di prova nello stesso modo e con gli stessi tempi. Le prove sono state svolte in ordine randomizzato così da mascherare gli effetti degli errori sperimentali [11]. Prima del montaggio degli aderendi sulla macchina di prova si è svolta, su un campione pari ad un quarto del totale, la
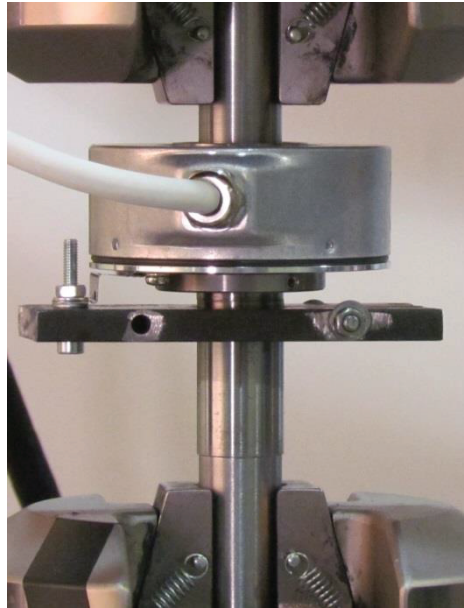
Figura 4. Immagine del provino montato sulla macchina di prova con il sistema di misura.

Tabella 1. Variabili del piano di prove sperimentali

Variabile	-		+	
Adesivo	Loctite 243		Loctite 638	
Pressione, p (MPa)	0.5	45	90	134

misurazione della rugosità della superficie d'incollaggio. La misura è stata eseguita con rugosimetro elettronico Hommelwerke.

3. RISULTATI

La rugosità media (R_a) della superficie d'incollaggio degli aderenti è risultata di circa 1.5 μm per tutti gli esemplari campionati.

Figura 5 mostra l'aspetto caratteristico dell'impronta di contatto di un provino, sotto i livelli di pressione estremi: 0.5 MPa e 134 MPa.

Figura 6 riporta le curve del momento torcente Mt applicato al provino in funzione dell'angolo di rotazione, ottenute per le quattro configurazioni sperimentali con adesivo Loctite 243, mediante il sistema di misura descritto nella Sezione precedente. Ciascun diagramma di figura contiene tre curve, corrispondenti alle tre replicazioni effettuate per ogni configurazione. Figura 7 riporta gli analoghi diagrammi per l'adesivo Loctite 638.

Figura 8 mostra le superfici di frattura di un provino incollato con adesivo Loctite 243 (Figura 8a), e con adesivo Loctite 638 (Figura 8b). Per ciascun caso è mostrato un dettaglio al microscopio della superficie di frattura (ingrandimento 100x).

Figura 9 presenta i valori della tensione tangenziale massima, τ_R, in funzione della pressione di contatto, p, all'interfaccia. La tensione tangenziale massima, τ_R, è calcolata rapportando il momento torcente di rottura, M_{tR}, al modulo di inerzia equivalente,
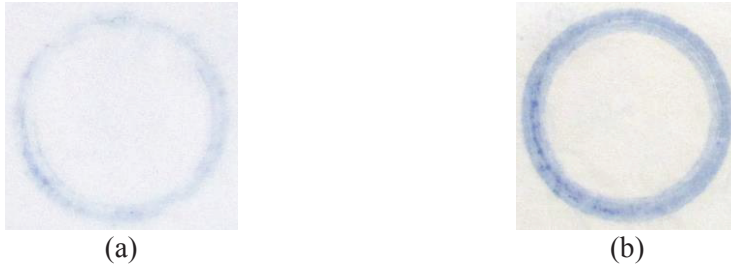
(a)　　　　　　　　　　　　　　　(b)

Figura 5. Impronta di contatto di un provino sotto una pressione 0.5 MPa (a) e 134 MPa (b).

(a)　　　　　　　　　　　　　　　(b)
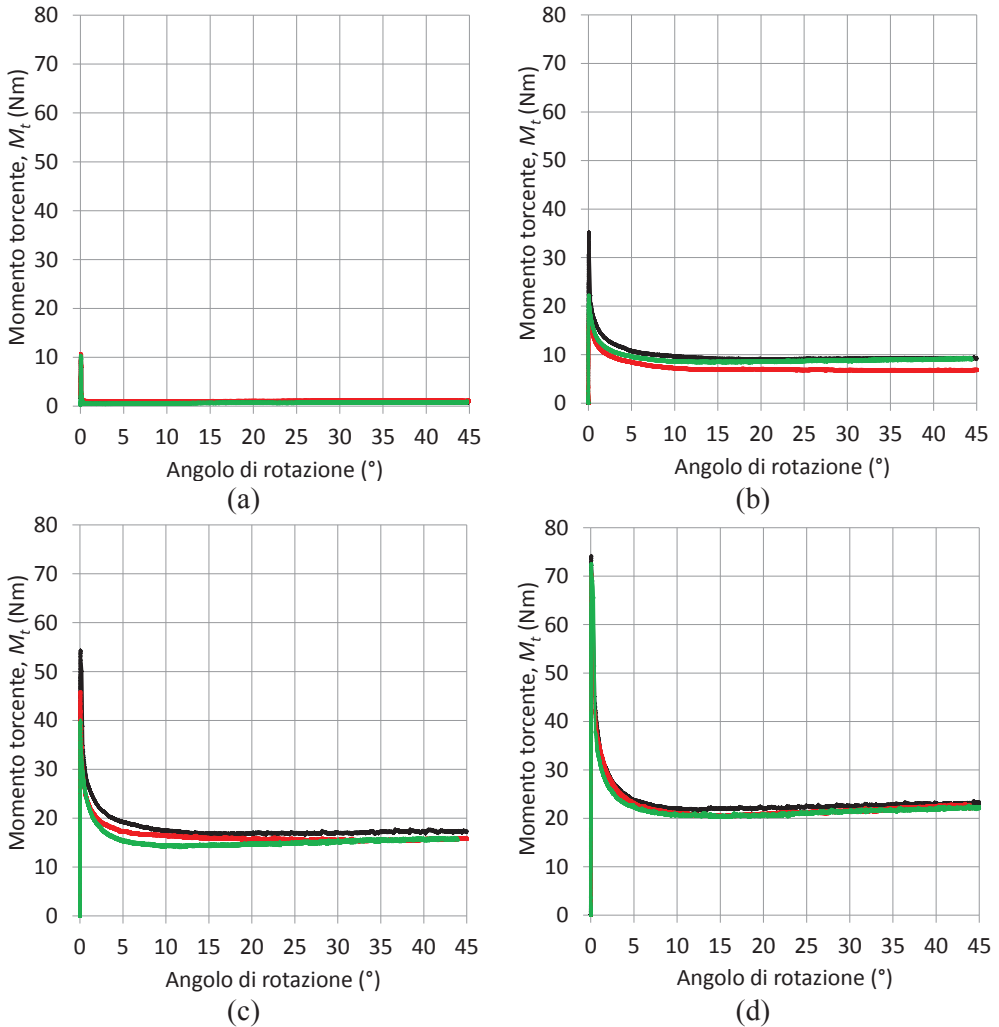
(c)　　　　　　　　　　　　　　　(d)

Figura 6. Momento torcente M_t in funzione dell'angolo di rotazione per adesivo anaerobico Loctite 243: 0.5 MPa (a), 45 MPa (b), 90 MPa (c) e 134 MPa (d).
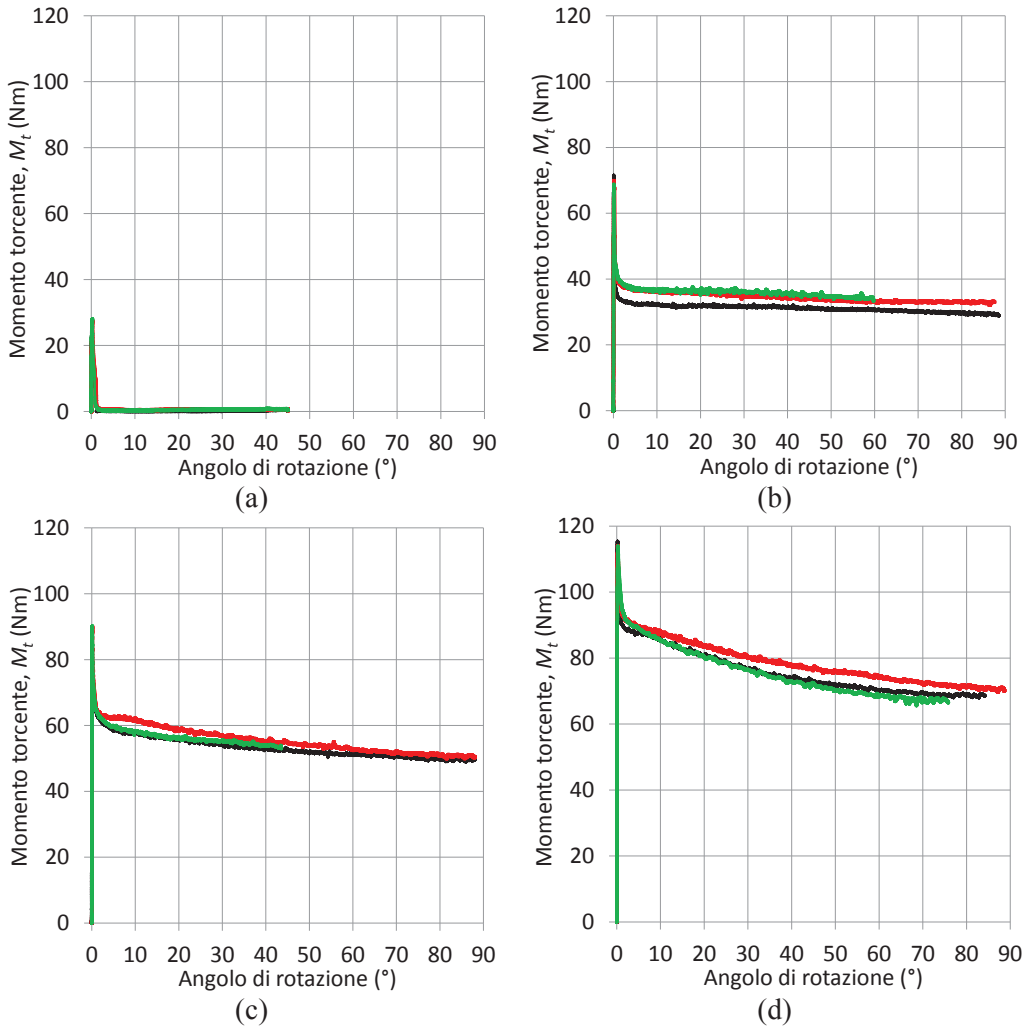
Figura 7. Momento torcente M_t in funzione dell'angolo di rotazione per adesivo anaerobico Loctite 638: 0.5 MPa (a), 45 MPa (b), 90 MPa (c) e 134 MPa (d).

secondo la formula seguente:

$$\tau_R = \frac{16 M_{tR}}{\pi \left(D^2 - d^2\right)\left(D + d\right)} \tag{1}$$

dove D rappresenta il diametro esterno del provino, d il diametro del foro. La linea continua blu rappresenta l'interpolante lineare ai punti sperimentali.

4. DISCUSSIONE

Il valore di rugosità di rugosità delle superfici di incollaggio degli aderendi che è appropriato per un incollaggio e con buona ripetibilità tra i provini. Questo, in
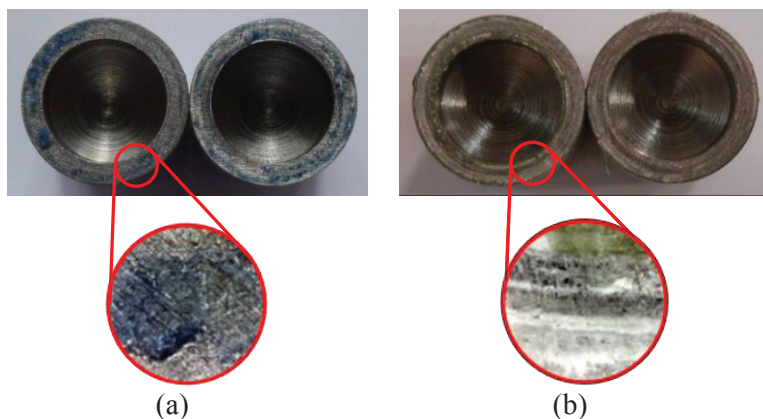
Figura 8. Superfici di frattura di provino incollato con adesivo anaerobico Loctite 243 (a) e con adesivo anaerobico Loctite 638 (d).
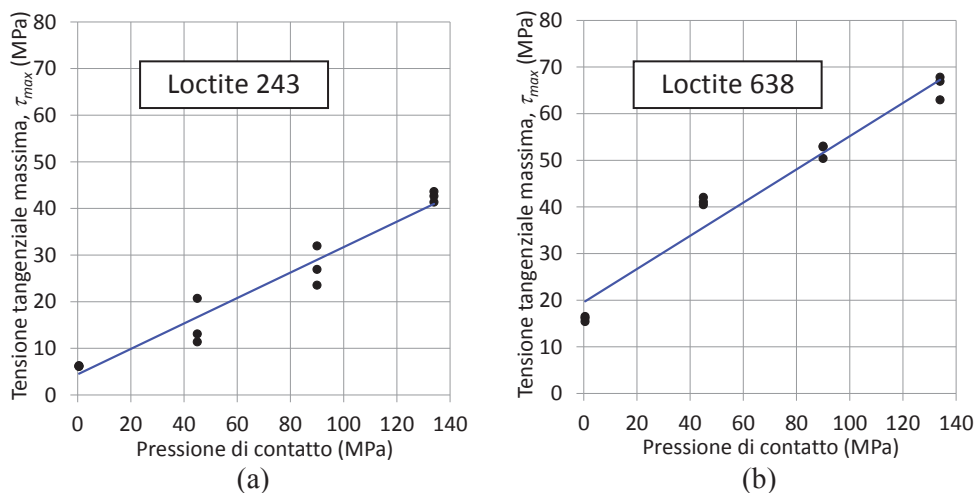

Figura 9. Tensione tangenziale massima τ_R per adesivo anaerobico Loctite 243 (a) ed adesivo anaerobico Loctite 638 (d).

combinazione con la buona concentricità dei provini ed ortogonalità delle superfici di incollaggio, ha garantito che il contatto testa a testa tra i provini fosse sempre uniforme su tutta l'area anulare (Figura 5), per ciascun valore di pressione esaminato.

Per ciascuna condizione di prova e per entrambi gli adesivi, le curve del momento torcente in funzione dell'angolo di rotazione (Figura 6 e Figura 7) evidenziano un'ottima ripetibilità della risposta, in particolare relativamente al tratto di risposta elastica lineare. Una leggera dispersione emerge nel momento torcente di rottura. Il tratto post-elastico successivo, in cui la resistenza a torsione degrada fino a stabilizzarsi su un momento torcente minimo, ha andamento molto simile tra le ripetizioni: le curve risultano quasi coincidenti anche quando il momento torcente di rottura è differente. L'incremento di

pressione di contatto produce un aumento molto evidente della resistenza a taglio del provino. E' interessante osservare che, nel tratto di risposta post-elastico, le curve si stabilizzano ad un valore di momento torcente minimo dopo un angolo che non dipende dalla pressione di contatto applicata ma che è nettamente differente per i due adesivi. Nel caso del Loctite 243 questo angolo vale circa 20°, per il Loctite 638, invece, vale circa 80°. Raggiunto questo angolo di rotazione l'adesione tra le interfacce è annullata. Inoltre, le curve dell'anaerobico Loctite 243 (Figura 6), ad eccezione del caso di pressione minima, mostrano un leggero aumento del momento torcente nella zona finale del tratto post-elastico. Questo è imputabile al raggiungimento di una condizione di scorrimento a secco in cui il velo di adesivo, inizialmente interposto tra le creste delle rugosità, è completamente consumato. Quindi, oltre tale angolo di rotazione, la resistenza a torsione è dovuta unicamente all'attrito metallo-metallo tra le facce degli aderendi.

Figura 8 permette di osservare che un velo di adesivo è effettivamente presente tra le superfici dell'interfaccia ibrida. Inoltre, il cedimento dell'interfaccia avviene secondo un modo coesivo, in quanto l'adesivo rimane su entrambe le superfici incollate.

Figura 9 evidenzia che per entrambi gli adesivi la resistenza a taglio dell'interfaccia ibrida forzata ed incollata aumenta a partire dalla resistenza a taglio propria dell'adesivo (per $p = 0$) con andamento quasi esattamente lineare all'aumentare della pressione di contatto. Nel caso dell'anaerobico forte la tensione tangenziale propria dell'adesivo è circa quattro volte più alta ed inoltre l'effetto dell'incremento di pressione è più marcato rispetto a quello debole.

5. MODELLO COESIVO CON ATTRITO

Oltre alla tensione tangenziale di massima, τ_R, sopportata dall'interfaccia (Figura 9), elaborando le curve di risposta di Figura 6 e Figura 7 è possibile ricavare altri dati utili alla formulazione di un modello costitutivo per la descrizione dell'interfaccia ibrida. In particolare, con riferimento alla curva qualitativa della tensione tangenziale in funzione dello scorrimento relativo delle superfici dell'interfaccia, riportata in Figura 10, si possono calcolare: la rigidezza k del tratto elastico delle curve; l'incremento di tensione tangenziale, $\Delta\tau$, il coefficiente d'attrito μ dell'interfaccia dopo il completo collasso coesivo; l'energia di frattura coesiva, G_c, spesa per portare a completo collasso l'adesivo presente nell'interfaccia ibrida; l'energia di deformazione dovuta all'attrito tra le superfici dell'interfaccia ibrida G_f.

Figura 11 descrive l'andamento della rigidezza k del tratto elastico di risposta delle curve di collasso al variare della pressione di contatto, per adesivo Loctite 243 (Figura 11a) e per adesivo Loctite 638 (Figura 11b). Questo parametro è calcolato come rapporto tra l'incremento della tensione tangenziale elastica e l'incremento dello scorrimento relativo tra le superfici incollate, prendendo a riferimento l'intero ramo di salita. Per ciascun livello di pressione di contatto sono riportate le tre replicazioni sperimentali svolte. La linea continua individua la migliore interpolante dell'insieme dei punti sperimentali.

Figura 12 mostra l'incremento di tensione tangenziale, τ_R, per ciascun livello di pressione di contatto, nel caso di adesivo Loctite 243 (Figura 12a) e di adesivo Loctite 638 (Figura 12b). Questo parametro è definito come differenza tra la tensione tangenziale massima raggiunta dall'interfaccia, τ_R, e la tensione tangenziale minima, τ_{min}, della fase post elastica. Anche in questo caso si riportano tutte le replicazioni svolte e la linea interpolante dell'insieme di punti sperimentali.
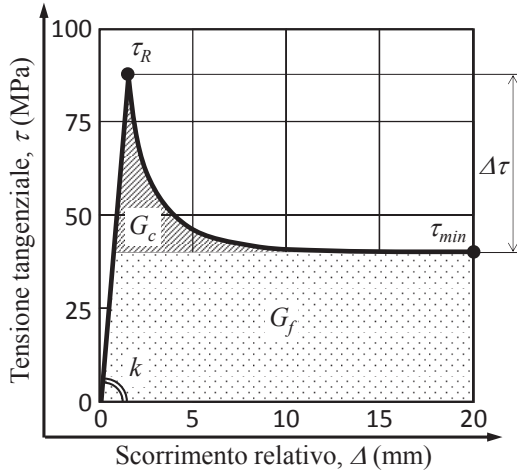
Figura 10. Andamento qualitativo di una curva tensione tangenziale - scorrimento relativo delle superfici dell'interfaccia ibrida, con in evidenza i parametri caratteristici.
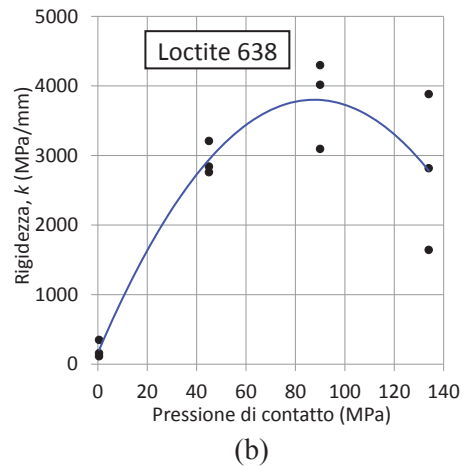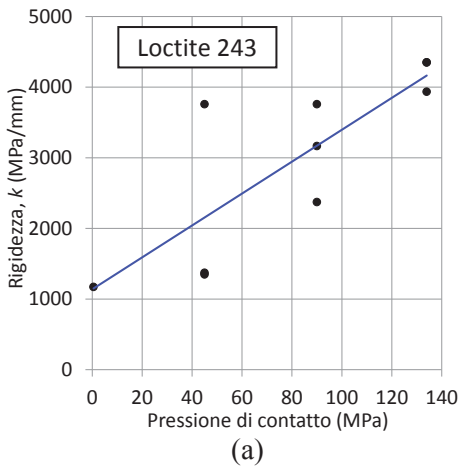

Figura 11. Rigidezza del tratto di risposta elastica per adesivo anaerobico Loctite 243 (a) ed adesivo anaerobico Loctite 638 (d).

Analogamente, per entrambi gli adesivi, Figura 13 descrive il coefficiente di attrito μ che caratterizza l'interfaccia ibrida nella fase post-elastica, al raggiungimento del completo collasso. Questo parametro è calcolato come rapporto tra la tensione tangenziale minima, τ_{min}, della fase post-elastica e la pressione nominale di contatto applicata all'interfaccia ibrida.

Infine, è possibile calcolare l'energia spesa per portare a collasso l'interfaccia ibrida forzata e incollata, distinguendo tra energia di frattura coesiva, G_c, corrispondente all'area tratteggiata in Figura 10, ed energia di deformazione per attrito, G_f, corrispondente all'area trapezoidale con campitura a punti in Figura 10. Entrambi questi parametri sono stati
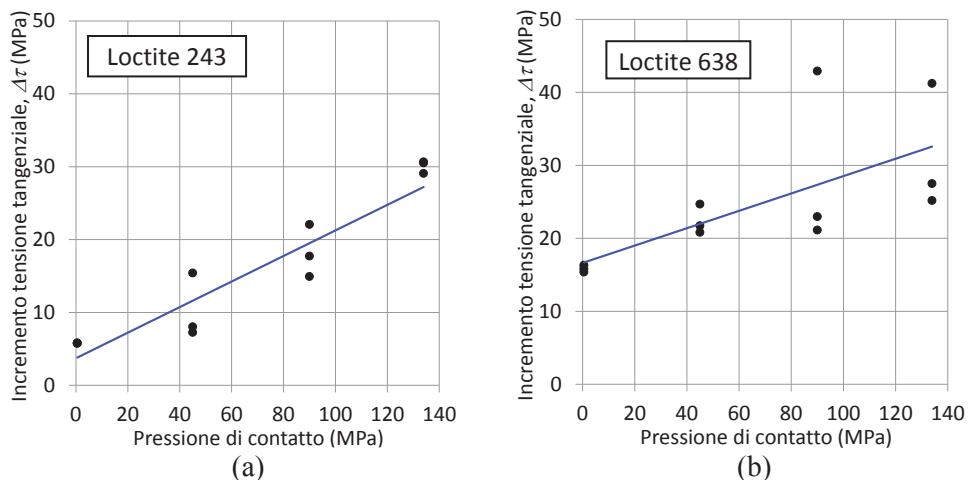
Figura 12. Incremento della tensione tangenziale $\Delta\tau$ per adesivo anaerobico Loctite 243 (a) ed adesivo anaerobico Loctite 638 (d).

calcolati mediante integrazione numerica secondo il metodo dei trapezi. Figura 14 e Figura 15 mostrano rispettivamente i valori di energia di frattura coesiva, G_c, ed energia di deformazione per attrito, G_f. Ciascun punto del diagramma descrive il valor medio, accompagnato da una barra che in positivo ed in negativo indica la deviazione standard sulle tre ripetizioni svolte per ciascuna configurazione di prova.

Nel complesso questi diagrammi mostrano che:

- la risposte misurate hanno tutte andamento lineare con la pressione nominale di contatto, ad eccezione della rigidezza dell'anaerobico forte che segue un andamento quadratico;

- su tutte le risposte, l'anaerobico forte mostra prestazioni più elevate, ad eccezione della rigidezza in cui avviene un brusco calo all'aumentare della pressione di contatto;

- la dispersione delle risposte dell'anaerobico forte è maggiore di quella dell'anaerobico debole

- relativamente all'incremento della tensione tangenziale, $\Delta\tau$, l'anaerobico forte mostra una risposta nettamente migliore a pressione bassa, ma circa uguale a quello debole a pressione elevata.

- nel caso dell'anaerobico debole, il coefficiente d'attrito, μ, per pressione di contatto minima è affetto da incertezze di misura e pertanto non viene considerato ai fini dell'interpolante.

- per l'anaerobico debole, il coefficiente d'attrito, μ, è circa costante con la pressione di contatto; al contrario, per l'anaerobico forte, il coefficiente d'attrito, μ, cala leggermente all'aumentare della pressione di contatto.

- notevolmente differenti tra i due adesivi sono l'energia di frattura coesiva, G_c, e l'energia di deformazione per attrito, G_f, aventi in entrambi i casi andamento esattamente lineare, crescente con la pressione di contatto.

- l'energia di frattura coesiva, G_c, dell'adesivo anaerobico forte è circa 5 volte maggiore di quella dell'anaerobico debole, su tutti i livelli di pressione di contato;

- l'energia di deformazione per attrito, G_f, dell'anaerobico forte è più di 10 volte
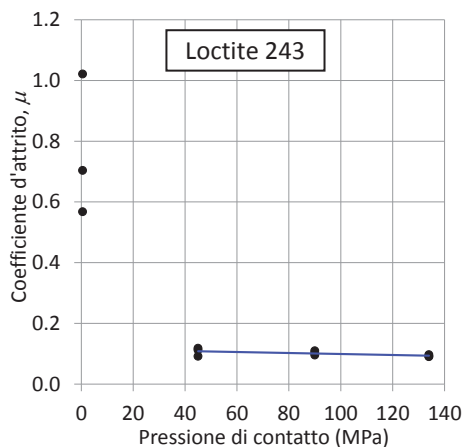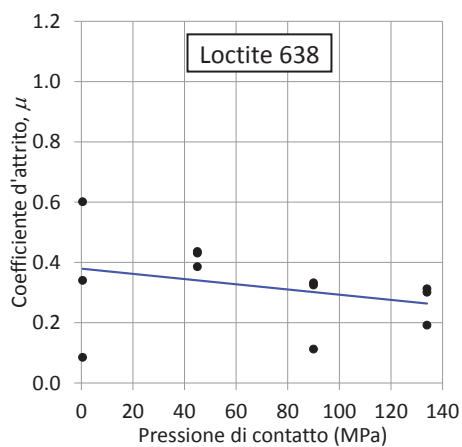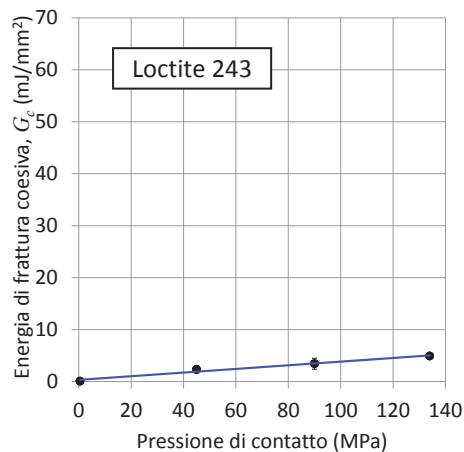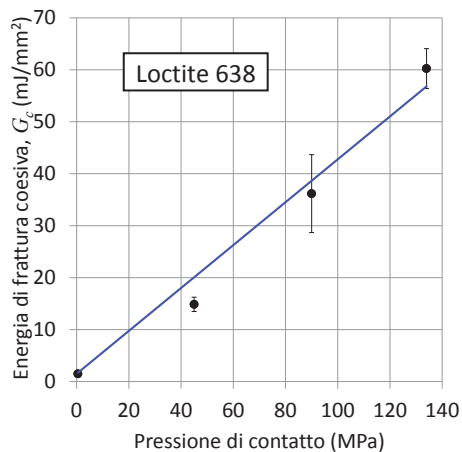
Figura 13. Coefficiente d'attrito μ per adesivo anaerobico Loctite 243 (a) ed adesivo anaerobico Loctite 638 (d).

Figura 14. Energia di frattura coesiva, G_c, per adesivo anaerobico Loctite 243 (a) ed adesivo anaerobico Loctite 638 (d).

superiore di quella dell'anaerobico debole, su tutti i livelli di pressione di contato;

- confrontando l'energia di frattura coesiva, G_c, con quella di deformazione per attrito, G_f, si osserva che quest'ultima è circa un ordine di grandezza maggiore dell'energia di frattura coesiva, G_c.

Tabella 2 riepiloga le equazioni interpolanti delle risposte sperimentali descritte nei diagrammi di Figura 9, Figura 11-Figura 15.
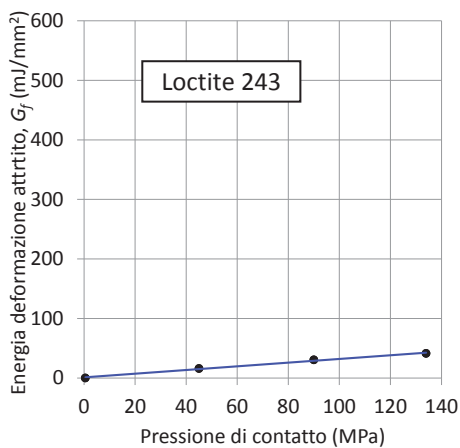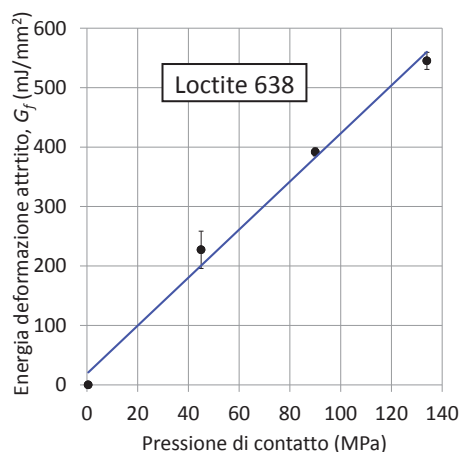
Figura 15. Energia di deformazione per attrito, G_f, per adesivo anaerobico Loctite 243 (a) ed adesivo anaerobico Loctite 638 (d).

Tabella 2. Equazioni dei parametri caratteristici della curva tensione tangenziale – scorrimento relativo (pressione p in MPa).

Risposta	Loctite 243	Loctite 638
Rigidezza, k (MPa/mm)	$k = 22.6p + 1138.8$	$k = -0.5p^2 + 83.0p + 163.0$
Tensione tangenziale massima, τ_R	$\tau_R = 0.3p + 6.1$	$\tau_R = 0.4p + 16.0$
Incremento tensione tangenziale, $\Delta\tau$ (MPa)	$\Delta\tau = 0.2p + 5.8$	$\Delta\tau = 0.1p + 15.8$
Coefficiente d'attrito, μ	$\mu = -0.0002p + 0.10$	$\mu = -0.0005p + 0.34$
Energia di frattura coesiva, G_c (mJ/mm^2)	$G_c = 0.3p + 0.2$	$G_c = 0.4p + 1.5$
Energia di deformazione per attrito, G_f (mJ/mm^2)	$G_f = 0.3p + 1.2$	$G_f = 4.2p + 0.1$

6. CONCLUSIONI

Il lavoro ha esaminato sperimentalmente il comportamento fino a completo collasso di interfacce ibride forzate e incollate con adesivo anaerobico. Si è impiegato a tal fine un provino cilindrico incollato testa a testa su un'area anulare. Due sono le variabili considerate: il tipo di adesivo anaerobico (Loctite 243 e Loctite 638) e la pressione nominale di contatto (su quattro livelli fino a 134 MPa). Le curve del momento torcente in funzione dell'angolo di rotazione, quest'ultimo misurato installando un encoder direttamente sul provino, hanno mostrato un ottima ripetibilità. I risultati sperimentali evidenziano la sostanziale superiorità di prestazioni da parte dell'anaerobico forte (Loctite 638) rispetto a quello debole (Loctite 243) sia in termini di resistenza statica a taglio, sia nella risposta post-elastica. Queste curve, inoltre, confermano che l'energia di deformazione spesa per portare a completo collasso l'interfaccia è somma di un contributo coesivo e di uno dovuto all'attrito, entrambi dipendenti linearmente dalla pressione.

BIBLIOGRAFIA

[1] Haviland, G.S. 1986, *Machinery adhesives for locking, retaining and sealing*, ed. Marcel Decker, New York.

[2] Dragoni E., and Mauri, P., 2011, "Science of friction-adhesive joints", in da Silva L.F.M., Pirondi, A, and Öchsner, A. (Eds.), *Hybrid Adhesive Joints*, 1st ed., Springer Berlin Heidelberg, Berlin, pp. 211-226.

[3] Sekercioglu, T., Gulsoz, A., and Rende, H., 2005, "The effects of bonding clearance and interference fit on the strength of adhesively bonded cylindrical components", *Mater. Des.*, **26**, pp. 377–81.

[4] Sekercioglu, T., 2005, "Shear strength estimation of adhesively bonded cylindrical components under static loading using the genetic algorithm approach", *Int. J. Adhes. Adhes.*, **25**, pp. 352–357.

[5] Sekercioglu, T., and Meran, C., 2004, "The effects of adherend on the strength of adhesively bonded cylindrical components", *Mater. Des.*, **25**, pp. 171-175.

[6] Aronovich, D.A., Murokh, A.F., Sineokov, A.P., and Khamidulova, Z.S., 2008, "Study of the Properties of Anaerobic Adhesives Cured in Cylindrical Joints", *Polymer Science*, **1**, pp. 260-265.

[7] O'Reilly, C., 1990, "Designing bonded cylindrical joints for automotive applications", Paper 900776, in Proceedings of SAE Intl Congress and Exposition, Detroit, 26th Feb - 2nd Mar.

[8] Croccolo, D., De Agostinis, M., and Vincenzi, N., 2010, "Static and dynamic strength evaluation of interference fit and adhesively bonded cylindrical joints", *Int. J. Adhes. Adhes.*, **30**(5), pp. 356-366.

[9] Croccolo, D., De Agostinis, M., and Vincenzi, N., 2012, "Design and optimization of shaft–hub hybrid joints for lightweight structures: Analytical definition of normalizing parameters", *International Journal of Mechanical Sciences*, **56**, pp. 77–85.

[10] Dragoni, E., and Mauri, P., 2002, "Cumulative static strength of tightened joints bonded with anaerobic adhesives", *Proc. Inst. Mech. Eng. (Part L)*, **216**, pp. 9-15.

[11] Dragoni, E., and Mauri, 2000, "Intrinsic static strength of friction interfaces augmented with anaerobic adhesives", *Int. J. Adhes. Adhes.*, **20**, pp. 315-321.

[12] E. Dragoni, 2003, "Fatigue testing of taper press fits bonded with anaerobic adhesives", *J. Adhes.*, **79**, 729-747.

[13] Castagnetti, D., and Dragoni, E., 2013, "Experimental assessment of a micro-mechanical model for the static strength of hybrid friction-bonded interfaces", *The Journal of Adhesion*, **89**(8), pp. 642-659.

[14] Castagnetti, D., and Dragoni, E., 2012, "Predicting the macroscopic shear strength of adhesively-bonded friction interfaces by microscale finite element simulations", *Computational Material Science*, **64**, pp. 146-150.

[15] Castagnetti, D., and Dragoni, E., 2014, "Adhesively-bonded friction interfaces: Macroscopic shear strength prediction by microscale finite element simulations", *International Journal of Adhesion and Adhesives*, **53**, 57-64.

[16] Alfano, G., and Sacco, E., 2006, "Combining interface damage and friction in a cohesive-zone model", *Int. J. Numer. Meth. Engng.*, **68**, 542–582.

[17] Alfano, G., Marfia, S., and Sacco, E., 2006, "A cohesive damage–friction interface model accounting for water pressure on crack propagation", *Comput. Methods Appl. Mech. Engng.*, **196**, pp. 192–209.

[18] Oinonen, A., and G. Marquis, G., 2011, "Shear decohesion of clamped abraded steel interfaces reinforced with epoxy adhesive", *Int. J. Adhes. Adhes.*, **31**, 550-558.

[19] Oinonen, A., G. and Marquis, G., 2011, "A parametric shear damage evolution model for combined clamped and adhesively bonded interfaces", *Engng. Fracture Mech.*, **78**, pp. 163-174.

[20] Halling, J., 1976, *Introduction to tribology*, Ed. Wykeham Publications.

[21] www.hengstler.de

[22] www.ni.com/products/

[23] www.ni.com/labview/

[24] Loctite 222, TDS, http://65.213.72.112/tds5/docs/243-IT.PDF (2009).

[25] Loctite 638, TDS, http://65.213.72.112/tds5/docs/638-IT.PDF (2009).

MODELING AND OPTIMIZATION OF THE SANDWICH BEAM SPECIMEN IN THREE-POINT BENDING FOR ADHESIVE BOND CHARACTERIZATION

Eugenio Dragoni
Department of Engineering Sciences and Methods
University of Modena e Reggio Emilia
E-mail: eugenio.dragoni@unimore.it

Hal F. Brinson
Professor Emeritus
Department of Mechanical Engineering
University of Houston
E-mail: hbrinson@uh.edu

Abstract. *Standard tests for adhesive bond characterization suffer for several deficiencies. The simplest specimens to make and test are lap joint geometries (e.g. single, double, symmetric, etc.) that generate complex stress distributions with irregularities and even singularities of the stress state. Those with the stress state closer to pure shear (e.g. napkin ring or Arcan) are difficult to make and require special test fixtures. This paper examines the stress state in the adhesive of a simple beam specimen obtained by bonding two flat plates one upon the other and loading the final sandwich in three-point bending. An elementary theory is used to optimize the specimen for in-situ measurements of either shear strength or shear modulus of the adhesive. The accuracy of the model is validated with finite element analyses, showing good agreement between the analytical and finite element model and also providing suggestions for the best geometry to be adopted for practical implementation of the test.*

Keywords: adhesives, bonded beam, bending, shear strength, shear modulus, optimization.

1. INTRODUCTION

Proper design of bonded joints requires reliable information on the mechanical properties of the adhesive in specific application conditions. When adhesives are tested in bulk (neat resin), the measured constitutive properties may not be representative of those in bonded state because the important effect of the adhesive-adherend interface on adhesive response is lost. All bond properties are affected but the influence on strength is especially significant [1]. Furthermore, not all adhesive products can be cast as bulk specimens.

Well established tests coupons that include information on the condition of the interface are single, double or other lap specimen configurations [2,3]. Though simple to make and test, these geometries have complex bond stress distributions and generate both normal and shear stresses that vary from point to point [4,5]. Stress singularities at re-entrant corners and at points of material discontinuity are also an issue [6] that undermine the meaning of these tests for providing genuine strength properties of the adhesive [7-9].

Efforts over the years have been devoted to the development of specimen geometries in which only a single pure shear stress state exists. A notable example in this category is the napkin ring torsion test, either in the standard flat-on-flat configuration [10] or in the cone-

on-flat modification [11], which ensures a near-uniform shear stress on the adhesive. A butt-bonded beam under antisymmetric bending producing a state of simple shear over the bondline was proposed by Wycherley et al. [12] as an adaptation of the famous shear test for metals due to Iosipescu [13]. A uniquely shaped specimen to measure shear stress using an axial tension test machine was introduced by Arcan and coworkers [14]. The only measurements needed in Iosipescu and Arcan tests for shear modulus and shear strength determination are the applied load, the dimensions of the adhesive layer and the relative displacement between the adherends along the bondline. However, elaborate fixtures are needed for proper loading and very precise notches (Iosipescu) and groves (Arcan) must be machined in the specimens to ensure uniformity of stresses and removal of singularities [15]. Also, the measurement of the relative displacement across the adhesive layer is not a simple task and generally requires special gauges to be performed. For these reasons, use of these specimens is generally confined to research environments.

Aimed at providing a simple method for routine measurement of adhesive properties, in the late 80s Moussiaux, Cardon and Brinson introduced a bonded double cantilever beam specimen [16], which develops a pure shear stress in the adhesive layer. With this easy to make specimen, adhesive properties (shear strength and shear modulus) can be obtained from a standard three-point bend test using the direct readings of force and displacement supplied by the testing machine. With fixed-fixed boundary conditions, the sandwich specimen can also be used in dynamic mechanical thermal analysis (DMTA) systems to obtain viscoelastic shear properties under a range of temperatures and adhesive-adherend interface conditions [17-19].

The basic theory providing the stress distribution in the adhesive and the overall sandwich beam deflection was provided in [16] and further elaborated in [17,18] for different constraint conditions. The theory in this form was assessed in [20] for the beam compliance by means of finite element analyses, showing that it tends to overestimate the beam stiffness especially for low-modulus adhesives and thin adherends. Hunston and coworkers [19] applied the original theory for analyzing the viscoelastic properties of rubbery and glassy adhesives and found encouraging results. A sensitivity analysis of the beam stiffness on the shear modulus of the adhesive was also carried out. An interesting refinement of the theory was proposed by Brinson and coworkers in [21] and used to interpret the results from DMTA testing.

Most papers available on the bonded sandwich beam focus on the determination of the adhesive shear modulus, while the adhesive shear strength is much disregarded. Further, a comprehensive analysis of the merits and the limitations of the test to get information on a wide range of adhesive properties is missing. Using the equations available in [21], this paper aims at optimizing the geometry of the sandwich beam in view of the property to be measured (modulus or strength). The optimization procedure disclosed identifies the sandwich beam dimensions which maximize either the uniformity of stresses over the bondline or the sensitivity of the test to the adhesive shear modulus (it is shown that the two conditions cannot be achieved simultaneously). Numerical example are provided, together with finite element analyses of case studies which verify the accuracy of the theory and suggest how to carry out the actual test so that the theoretical predictions are actually met.

2. ANALYTICAL MODEL

Figure 1 shows schematically the deformation of the sandwich beam produced by three-point bending. That the adhesive layer is subjected to a state of stress is easy to visualize if the two beams are loaded in the same manner but without an adhesive layer. Each would

then be independent of the other and would deform such that the tensile deformation of the bottom of the top adherend would be exactly equal and opposite the compressive deformation of the top of the bottom adherend. Should an adhesive less stiff than the adherends be placed in between (as depicted in Fig. 1), a pure shear deformation would result in the bondline. If an adhesive as stiff as the adherend material were used, the entire sandwich would deform as a single beam with height equal to the sum of the adherends and of the adhesive layer.

Several theories with different degrees of sophistication exist that can provide the stresses and the displacements arising in the sandwich beam [22-24] loaded as in Fig. 1. Developed as a refinement of the original theory by Moussiaux [16], the analytical results referenced by Brinson [21] is particularly attractive as an optimization tool for its simplicity and completeness. Figure 2 shows the essential assumptions behind Brinson's theory [21], with the free body diagrams illustrating the stress states on the adhesive layer and on the top and bottom adherends at a section distant x from the center section of the beam. The adherends develop axial constant stresses, σ_N, linear bending stresses, σ_b, and parabolic shear stresses, τ, which are all functions of x. The shear stresses at the bottom face of the upper adherend and the shear stresses at the top face of the lower adherend are equal and coincide with the shear stress, $\tau(x)$, acting on the adhesive layer. Each adherend is assumed to share one half of the total tip load, P. The thickness of the adhesive layer, t_a, is assumed to be small with respect to the thickness, h, of the adherends.
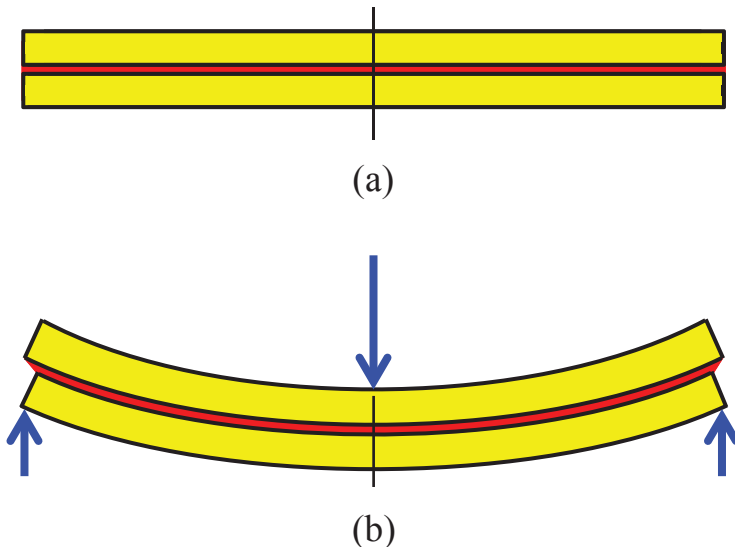

(a)

(b)

Figure 1. Schematic of the sandwich beam in the undeformed (a) and deformed (b) configurations.
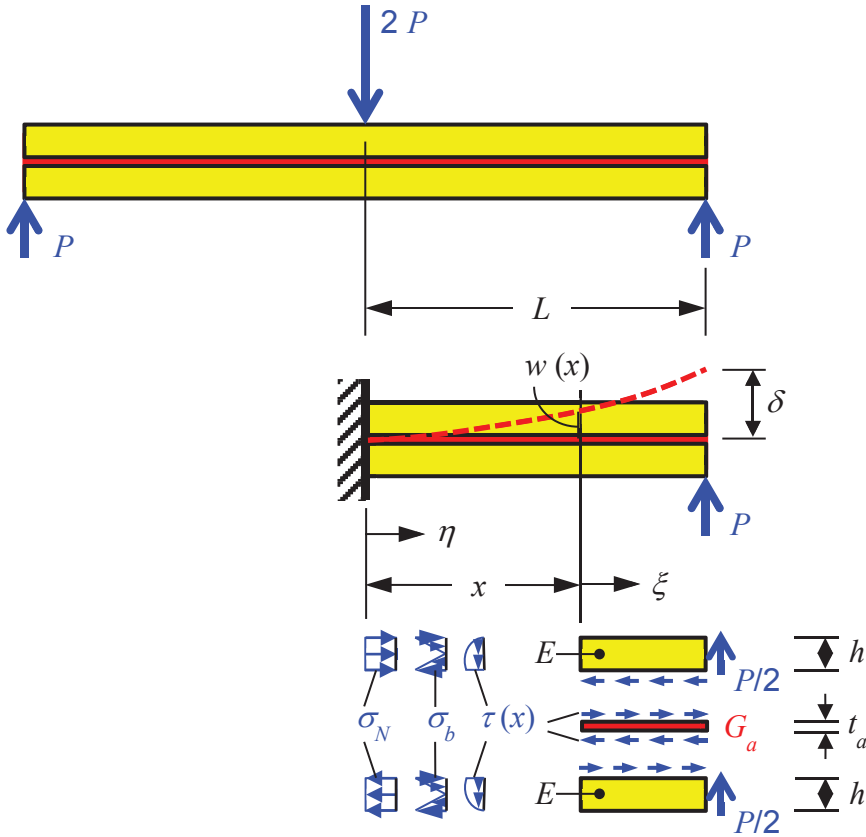
Figure 2. Bonded sandwich beam and free body diagrams of individual elements with corresponding stress states.

By forcing continuity at the centerline of the adhesive in Fig. 2, the original results by Moussiaux are obtained [16]. Instead, if continuity is enforced at the interface between adherend and adhesive, the following equations for adhesive shear stress along the length of the beam, $\tau(x)$, and tip deflection, δ (see Fig. 2), are found [21]:

$$\tau(x) = \tau_0 \left\{ 1 - \cosh\left[\alpha_L \left(\frac{x}{L} \right) \right] + \tanh \alpha_L \sinh\left[\alpha_L \left(\frac{x}{L} \right) \right] \right\} \tag{1}$$

and

$$\delta = \delta_0 \left[1 + 9 \left(\frac{\alpha_L - \tanh \alpha_L}{\alpha_L^3} \right) \right] \tag{2}$$

where:

$$\alpha_L = \sqrt{8\frac{(L/h)^2}{(t_a/h)}(G_a/E)} \tag{3}$$

$$\tau_0 = \frac{3P}{4bh} \tag{4}$$

$$\delta_0 = \frac{PL^3}{2Ebh^3} \tag{5}$$

The still unpublished derivation of the above equations (1) and (2) is presented in detail in Appendix 2. Parameter α_L in (3) measures the relative stiffness between the bond and the beam: for $\alpha_L \to 0$ (G_a/t_a very low), the sandwich beam behaves as two independent beams; for $\alpha_L \to \infty$ (G_a/t_a very high), the sandwich beam behaves as a single homogeneous beam (see Discussion). Figure 3 plots the shear stresses from (1) along the beam axis for a selection of values of the parameters α_L. Figure 4 plots the tip displacement (2) as a function of α_L in the range 0.01-100.
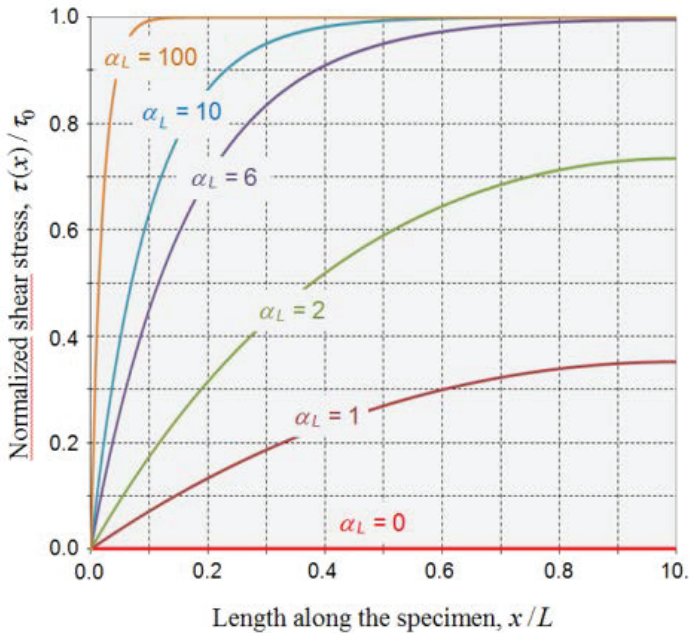

Figure 3. Distributions of shear stresses over the bondline for a selection of values of the relative adhesive stiffness.
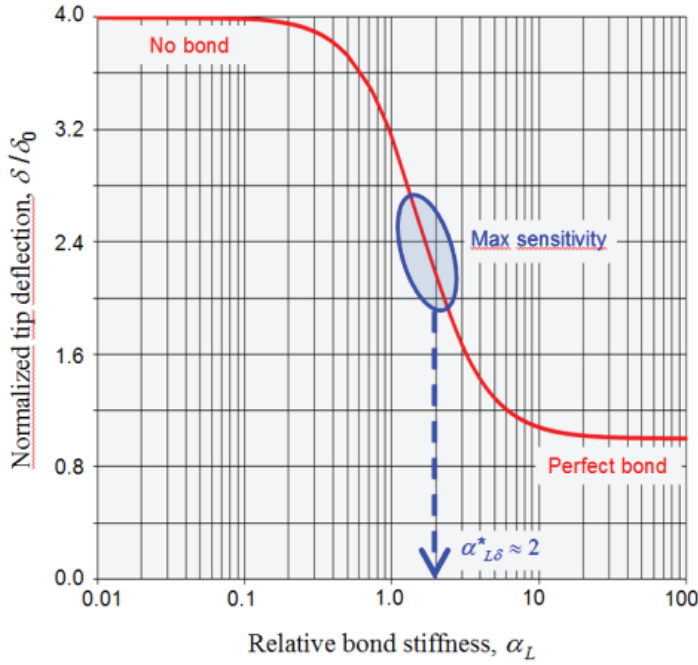
Figure 4. Curve of the normalized tip deflection of the bonded beam as a function of the relative adhesive stiffness.

3. STRESS OPTIMIZATION

Equation (1) and Fig. 3 show that the higher α_L the more uniform the shear stress over the beam span. The maximum shear stress, τ_{max}, occurs at the end point of the sandwich beam where $x = L$:

$$\tau_{max} = \tau(x)\big|_{x=L} = \tau_0 \left(1 - \cosh \alpha_L + \tanh \alpha_L \sinh \alpha_L\right) \tag{6}$$

The maximum value of the bracketed term in (6) is 1 and is achieved whenever $\alpha_L \geq 5.35$. Above this threshold of α_L the maximum shear stress in the bond, $\overline{\tau}_{max}$, is independent of the adhesive properties and amounts to:

$$\overline{\tau}_{max} = \tau_{max}\big|_{\alpha_L \geq 5.35} \approx \tau_0 = \frac{3P}{4bh} \tag{7}$$

From (1) it is easily seen that for $\alpha_L = 10$ about one half of the beam length is subjected to a stress greater than 99% of the maximum stress (7). In order to ensure a

264

significant uniformity of stresses in the adhesive layer, the sandwich beam adopted for shear strength characterization should satisfy the condition:

$$\alpha_L \geq \alpha_{L\sigma}^* = 10 \tag{8}$$

Stress constraint

Equating the maximum stress (7) to the critical shear stress of the adhesive, $\tau_{a\,cr}$, gives the load P_{cr} producing failure of the adhesive as:

$$P_{cr} = \frac{4}{3} bh\,\tau_{a\,cr} \tag{9}$$

For large values of α_L satisfying (8), the maximum expected stress in the adherends, σ_{max}, coincides with the maximum bending stress in the homogeneous beam (perfect adhesion between the adherends) is given by:

$$\sigma_{max} \approx \frac{PL}{\dfrac{b(2h)^2}{6}} = \frac{3}{2}\left(\frac{PL}{bh^2}\right) \tag{10}$$

Combining (9) and (10) gives the maximum stress in the adherends, $\sigma_{max\,cr}$, when the adhesive attains the critical stress:

$$\sigma_{max\,cr} = \sigma_{max}\big|_{P=P_{cr}} = 2\tau_{a\,cr}\left(L/h\right) \tag{11}$$

The stress (11) cannot exceed the admissible stress, σ_{adm}, of the adherends in order to keep the deformation within the elastic limit. Letting $\sigma_{max\,cr} \leq \sigma_{adm}$ and using (11) gives:

$$\frac{L}{h} \leq \left(L/h\right)_\sigma = \frac{1}{2}\left(\frac{\sigma_{adm}}{\tau_{a\,cr}}\right) \tag{12}$$

Deflection constraint

Whenever Eq. (8) is satisfied, the bracketed term in (2) is nearly unity and the tip deflection of the sandwich coincides with δ_0. Combining (5) and (9) gives the maximum displacement of the sandwich, $\delta_{0\,cr}$, when the adhesive attains the critical stress:

$$\delta_{0\,cr} = \delta_0\big|_{P=P_{cr}} = \frac{2}{3}L\left(\frac{\tau_{a\,cr}}{E}\right)\left(L/h\right)^2 \tag{13}$$

from which:

$$\frac{\delta_{0\,cr}}{L} = \frac{2}{3}\left(\frac{\tau_{a\,cr}}{E}\right)(L/h)^2 \tag{14}$$

The ratio $\delta_{0\,cr}/L$ in (14) cannot exceed a predefined limit value, $(\delta_{0\,cr}/L)_{lim} \approx 0.1 \div 0.2$, in order to maintain the deformations within the range of geometrical linearity. Letting $\delta_{0\,cr}/L \leq (\delta_{0\,cr}/L)_{lim}$ and using (14) gives:

$$\frac{L}{h} \leq (L/h)_\delta = \sqrt{\frac{3}{2}\left(\frac{E}{\tau_{a\,cr}}\right)(\delta_{0\,cr}/L)_{lim}} \tag{15}$$

Optimal sandwich design for stress uniformity

The optimal sandwich for maximum stress uniformity must simultaneously satisfy conditions (3), (8), (14) and (15). Letting $(L/h)_{max} = \min\{(L/h)_\sigma ; (L/h)_\delta\}$, with $(L/h)_\sigma$ and $(L/h)_\delta$ given by (14) and (15), a simple optimization procedure is as follows:

a) Set $\quad \alpha_{L\sigma}^* = 10$

b) Choose $\quad \alpha_L \geq \alpha_{L\sigma}^*$

c) Calculate $\quad (L/h)_{max} = \min\left\{\frac{1}{2}\left(\frac{\sigma_{adm}}{\tau_{a\,cr}}\right); \sqrt{\frac{3}{2}\left(\frac{E}{\tau_{a\,cr}}\right)(\delta_{0\,cr}/L)_{lim}}\right\}$

$$\tag{16}$$

d) Choose $\quad L/h \leq (L/h)_{max}$

e) Calculate $\quad (t_a/h)_{max} = 8(G_a/E)\left(\frac{L/h}{\alpha_L}\right)^2$

f) Choose $\quad t_a/h \leq (t_a/h)_{max}$

where Step e) derives from (3) solved for t_a/h.

4. COMPLIANCE OPTIMIZATION

Figure 4 shows that for $\alpha_L < 0.2$ and $\alpha_L > 10$ the normalized tip deflection, δ/δ_0, is constant. This means that in these ranges of α_L the deflection of the sandwich, δ, is not

affected by the shear modulus, G_a, upon which α_L depends once the beam material (E) and geometry (b, L, h) have been fixed. In order to resolve the adhesive properties from the beam displacement, parameter α_L must fall in the range of maximum sensitivity shown with the shaded ellipse in Fig. 4. The value of α_L for which the derivative of the curve in Fig. 4 is maximum is $\alpha_L \approx 1.2$, which is too low for optimization purposes. A convenient value still in the range of greatest sensitivity is the following:

$$\alpha_{L\delta}^* \approx 2 \tag{17}$$

The optimal sandwich for maximum compliance sensitivity must satisfy simultaneously conditions (3) and (17). The stresses in the adherends and the magnitude of the beam deflection are not a concern because they can be kept low by controlling the limiting the load, P, applied to the specimen (see Eqs. (2) and (5)). A suitable optimization procedure is as follows:

$$
\begin{array}{lll}
\text{a)} & \text{Set} & \alpha_L = \alpha_{L\delta}^* \approx 2 \\[2mm]
\text{b)} & \text{Choose} & L/h \text{ in the range } 5 \le L/h \le 10 \\[2mm]
\text{c)} & \text{Calculate} & t_a/h = 8\left(G_a/E\right)\left(\dfrac{L/h}{\alpha_{L\delta}^*}\right)^2
\end{array}
\tag{18}
$$

5. CASE STUDIES AND FINITE ELEMENT VALIDATION

Optimization examples

The optimization procedures described in Section 4 were applied to an epoxy and a polyurethane adhesive in contact either with steel or aluminium adherends. The properties of the adhesive and of the adherends are listed in Tables 1 and 2. The results of the optimization process for both stress and compliance are summarized in Table 3. For the sake of example, the following two sections present the step-by-step calculations for the epoxy/steel specimen in stress optimization and the polyurethane/steel specimen in compliance optimization.

Stress optimization. Assume for the epoxy adhesive and the steel adherends the following properties [25]: $t_a = 0.1$ mm, $G_a = 1.500$ MPa, $\tau_{a\,cr} = 40$ MPa, $E = 206$ GPa, $\sigma_{adm} = 500$ MPa. Further assume $(\delta_{0\,cr}/L)_{lim} = 0.1$ as limit relative deflection and, from (16)a and (16)b, $\alpha_L = \alpha_{L\sigma}^* = 10$ as relative adhesive stiffness. Choose from (16)c and (16)d $L/h = (L/h)_{max} = 6.25$ ($= (L/h)_\sigma < (L/h)_\delta = 27.79$). Finally, choose from (16)e and (16)f $t_a/h = (t_a/h)_{max} = 0.023$, which, for $t_a = 0.1$ mm, gives $h = 4.4$ mm and $L = 27.5$ mm as reported in Table 1.

Table 1. Elastic and mechanical properties of the adhesives used in the case studies.

Adhesive	E_a (MPa)	G_a (MPa)	v_a –	$\tau_{a\,cr}$ (MPa)
Epoxy	4,110	1,500	0.37	40
Polyurethane	568	200	0.42	10

Table 2. Elastic and mechanical properties of the adherends used in the case studies.

Adherend material	E (MPa)	G (MPa)	v –	σ_{adm} (MPa)
Steel	206,000	79,230	0.3	500
Aluminium	70,000	26,923	0.3	300

Table 3. Input and output data for the case studies considered in the validation step.

Target	Input data				Output data			
	Material system	t_a (mm)	$(\delta_{0\,cr}/L)_{lim}$ –	α_L –	L/h –	t_a/h –	h (mm)	L (mm)
Shear strength	Epoxy/Steel	0.1	0.1	10	6.25	0.023	4.4	27.5
Shear modulus	Epoxy/Aluminium	0.1	–	2	5	1.07	0.09	0.45
Shear strength	Polyurethane/Steel	2.0	0.1	10	25	0.049	40.8	1,020
Shear modulus	Polyurethane/Steel	2.0	–	2	10	0.20	10.0	100.0

Compliance optimization. Assume for the polyurethane adhesive and the aluminium adherends the following properties [25]: $t_a = 2$ mm, $G_a = 200$ MPa, $E = 206$ GPa. Set from (18)a assume $\alpha_L = \alpha_{L\delta}^* = 2$ as relative adhesive stiffness. Choose from (18)b $L/h = 10$. Finally, calculate from (18)c $t_a/h \approx 0.20$, which, for $t_a = 2$ mm, gives $h = 10$ mm and $L = 100$ mm as reported in Table 2.
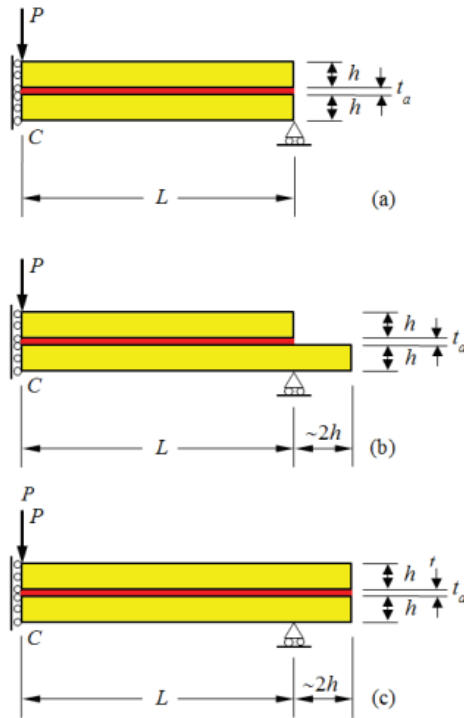
Figure 5. Sandwich beam configurations analyzed with the FE method.

Finite Element validation

The two specimens described in the former sections were analyzed using the LUSAS Finite Element (FE) system. For each specimen, the three specific geometries shown in Fig. 5 were considered: a specimen long exactly L (Fig. 5a); a specimen with upper adherend of length L and longer lower adherend (Fig. 5b); a specimen with both adherends longer than L (Fig. 5c). The geometry in Fig. 5a was made to reproduce exactly the geometric conditions of the analytical model (Section 2). The geometries in Fig. 5b,c were meant to see the effects of the extensions of the sandwich beyond the supports that are needed in practice.

In all models, the parts were discretized using quadratic plane stress elements with the elastic properties listed in Tables 1 and 2 and thickness of 1 mm. Two elements were placed through the thickness of the adhesive and 44 elements through the thickness of each adherend. The bonding length L between the supports was divided into 275 elements (for both adhesive and adherends). The length of the extensions in Figs. 5b,c was divided into 88 elements in the epoxy/steel specimen and into 55 elements in the polyurethane/steel specimen. All divisions were uniform without space grading, resulting in nearly square elements with a maximum aspect ratio of 2. The applied load was $P = 100$ N for all models. The left border of the models in Fig. 5 was restrained in the horizontal direction to enforce symmetry about the centerline of the specimen. The bottom node of the lower adherend at distance L from the centerline was restrained vertically to simulate a concentrated support.
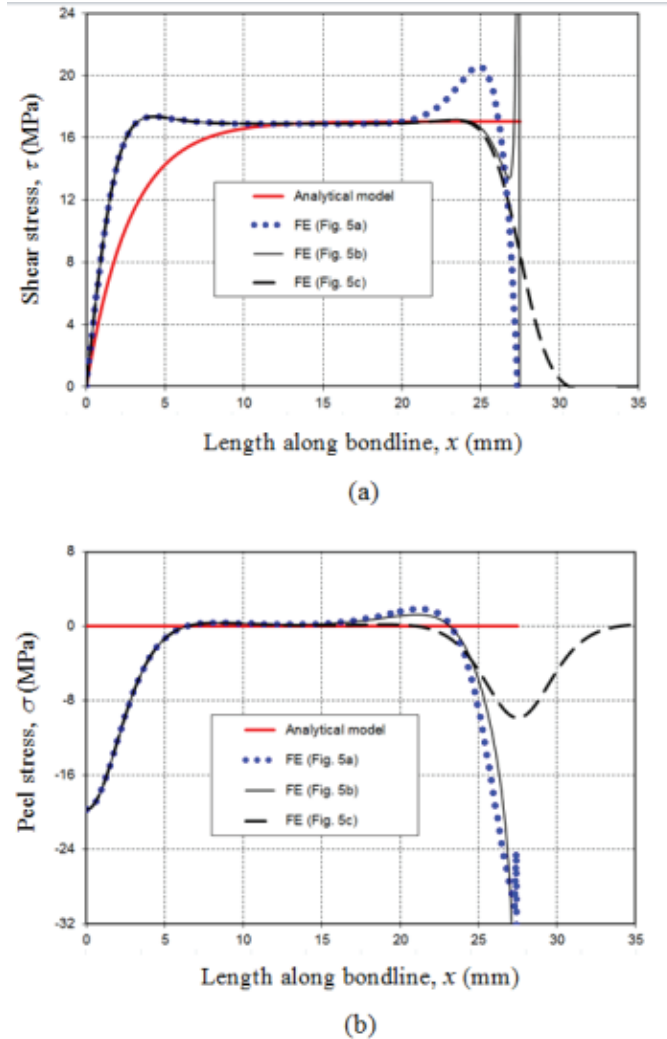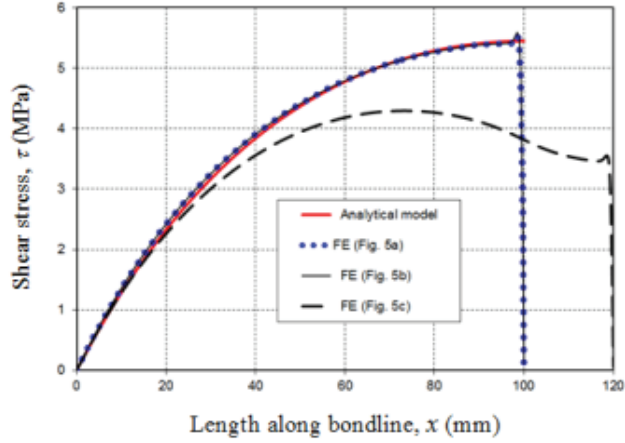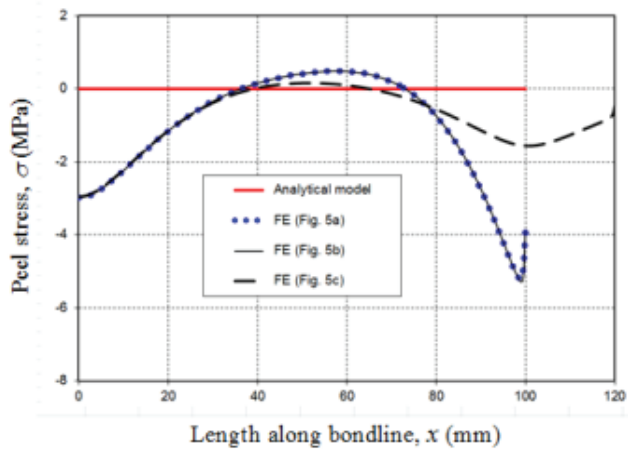
Figure 6. Analytical and FE adhesive stresses in the for various configurations of the epoxy/steel specimen: (a) shear stresses, (b) peel stresses.

The FE stress read along the midline of the adhesive layer are reported in Figs. 6 for the epoxy/steel specimen and in Fig. 7 for the polyurethane/steel specimen. Figures 6a and 7a refer to the shear stresses, Figs 6b and 7b contain the peel stresses (i.e. the stresses normal to the plane of the adhesive). All charts contain three FE stress curves corresponding to the three geometries in Fig. 5 and a fourth curve corresponding to the analytical model (Eq. (1) for the shear stresses and zero for the peel stresses, which are not contained in the theory). Table 4 compares the theoretical displacement (2) with the FE displacements measured at the bottom center point C of the models in Fig. 5.

Figure 7. Analytical and FE adhesive stresses in the for various configurations of the polyurethane/steel specimen: (a) shear stresses, (b) peel stresses.

Table 4. Comparison between theoretical and FE deflections of the beams in Fig. 5.

Material system	Specimen dimensions			Deflection δ (mm)			
	t_a	h	L	Theory	FE models		
	(mm)	(mm)	(mm)	Eq. (2)	Fig. 5a	Fig. 5b	Fig. 5c
Epoxy/Steel	0.1	4.4	27.5	0.064	0.066	0.062	0.062
Polyurethane/Steel	2.0	10.0	100.0	0.53	0.46	0.45	0.41

6. DISCUSSION

Equations (7) tells that for large values of α_L, i.e. for a stiff adhesive (G_a/t_a large in Eq. (3)), the maximum stress in the beam is τ_0, given by (4). This is the maximum shear stress that would occur in a solid homogeneous beam of thickness $2h$. Likewise, for large α_L the bracketed term in the Eq. (2) goes to unity (see also Fig. 4) and the tip deflection becomes δ_0, Eq. (5). Again, this is the tip deflection as for the solid homogeneous beam. When α_L tends to zero (very soft adhesive, G_a/t_a large in Eq. (3)), the bracketed term in the stress function (1) vanishes and the tip deflection (2) becomes $4\delta_0$, which is the deflection of each adherend under the end load $P/2$. In other terms, the sandwich beam behaves as the sum of the two adherends deforming independently of each other.

Table 3 shows that only two out of the four specimens designed for the different adhesive-adherend combinations have reasonable dimensions: epoxy/steel for strength measurement and polyurethane/steel for shear modulus determination. The other two solutions are either too big (polyurethane/steel for strength measurement) or too small (epoxy/aluminium targeted at shear modulus).

In general, for strength measurements, in which high values of α_L are needed, Eq. (16)e tends to produce unacceptably low values of $(t_a/h)_{max}$ for soft rubbery adhesives (G_a/E low). Since the adhesive thickness t_a is high for these adhesives, the value of h (and, consequently, of L) tends to be too high. Stiff glassy adhesives, with G_a/E high, have an advantage in this respect. By contrast, for the measurement of the shear modulus, in which relatively low values of α_L are requested, Eq. (18)c produces unacceptably high values of t_a/h for stiff glassy adhesives (G_a/E high). Since the adhesive thickness t_a is low for these adhesives, the value of h (and, consequently, of L) tends to be too low. Soft rubbery adhesives, with G_a/E low, have an advantage in this field. Table 3 also shows that, both for glassy and rubbery adhesives, the optimal dimensions of the sandwich specimen are quite different according as to whether the shear strength or the shear modulus of a specific adhesive is to be measured. In other words, a universal geometry does not exist, which can capture both properties equally well for any given adhesive.

Figures 6a and 7a show that the general trend of the shear stress from the FE models is close to the analytical predictions. This is especially true in Fig. 7 for the polyurethane/steel specimen with the geometries in Figs. 5a and b. The geometry in Fig. 5c produces a deviation from the analytical stresses for the polyurethane/steel specimen (dashed curve in Fig. 7a). This is because the bonded part of the specimen extending outside of the support adds a constraint to the center parts of the adherends, which cannot deform as freely as in the regular geometries (Figs. 5a and b).

From Fig. 7 we see that for the epoxy /steel specimen, the geometry in Fig. 5c enhances the stress distribution (dashed line) by eliminating the spurious stress peaks at the right end of the bondline. For the geometry in Fig. 5c the shear stress goes smoothly to zero at the end of the specimen, starting from the maximum constant value achieved in the center part of the bondline. Stress singularities that might occur at the adhesive/adherend interface at the beginning of the bondline are also moved to a region where the stress is nearly zero.

The FE curves in Figs. 6b and 7b show that the adhesive is subject to compressive normal stresses at the center ($x = 0$) and at the end points of the adhesive layer. These stresses are produced by the fact that the center load and the reaction of the end support are applied to only one of the adherends so that a mismatch between the transverse deflections arises locally. The analytical model misses this effect because the end load P and the center constraint are applied separately to the adherends (see Fig. 2). While the compressive

stresses are only a minor nuisance in specimens as in Fig. 7b which is aimed at shear modulus determination, they are of greater concern for strength measurements as in Fig. 6. This is because the compressive stresses introduce biaxiality in the state of stress, especially at the end points of the bondline where the maximum shear stress takes place and failure of the adhesive is most likely to initiate. This can have an effect on the measured properties of the adhesive due to the strength-enhancing mechanism played by the applied pressure on the shear properties of polymers in general [26] and adhesives [27-30]. Fig. 6b shows that the end compressive stress is much reduced by the specimen geometry in Fig. 5c. Because of this effect and due to a better uniformity of shear stresses, the specimen geometry in Fig. 5c is to be recommended for strength measurements. Conversely, the geometry in Fig. 5b is preferable as a practical means to measure the shear modulus of the adhesive.

Table 4 shows that the overall analytical deflection of the beam agrees favorably with the FE results for both material systems. For the epoxy/steel specimen the error is within 3% of the FE values. In the polyurethane/steel specimen the analytical model overestimates the FE deflection by about 18 % for the recommended geometry in Fig. 5b. The greater error for the polyurethane/steel system is imputable to the thicker adhesive layer ($t_a = 2$ mm) which is not as negligible with respect to the adherends ($h = 10$ mmm) as the analytical model assumes. Due to the thicker adhesive, the overall thickness of the sandwich is appreciably higher than $2h$, contributing to a higher bending stiffness than assumed by the theory (see the comments in Appendix 2 after Eq. (A5)).

While good results between the present analytical model and FE analysis has been demonstrated, it is acknowledged that Moussiaux [16] and Fior [31] also have shown good correlation between a slightly different analytical model and other FE models. In summary, despite its simplicity, the analytical model appears to be a reliable optimization tool for the bonded sandwich beam specimen aimed at routine measurements of either shear strength or shear modulus.

7. CONCLUSIONS

Using the empirical relationships provided by the ISO 76 standard, the internal dimensions of tapered roller bearings are optimized for maximum static load capacity. The bearing system investigated comprises two identical bearings undergoing whatever combination of radial and axial forces. Assuming that the radial force is applied at equal distance from the bearings of the pair, the closed-form optimization process leads to the following results:

- the static load capacity increases linearly with the filling ratio (number of rollers divided by the maximum number which can fill the bearing) and the aspect ratio (ratio of roller length to mean roller diameter of rollers) and goes up with the square of the pitch diameter of the roller set;
- given the ratio of axial to radial force, global optima exist for the contact angle and the pitch ratio (ratio of roller diameter to pitch diameter) which maximize the static load capacity;
- the bearing proportions at the global optima are too sturdy (contact angles greater than 60 degrees, pitch ratios equal to or greater than 0.5) to be used in practice;
- if the pitch ratio is constrained to stay below reasonable limits (≤ 0.25), an optimal contact angle exists which maximizes the static load capacity, regardless of the actual size and proportions of the bearing;

- the results of the optimization are conveniently summarized by a general table and a few simple equations that can be followed step-by-step to design the optimal bearing that suits any given application;
- the design procedure can either be used to design custom-made bearings (where the geometrical freedom can be exploited to the full) or to identify the best bearing from the manufactures' catalogues.

REFERENCES

[1]   Peretz, D., 1978. "Shear Stress-Strain Characteristics of Adhesive Layers". *J Adhes*, **9**(2), pp. 115–122.

[2]   ASTM Standard D1002-10, Standard Test Method for Apparent Shear Strength of Single-Lap-Joint Adhesively Bonded Metal Specimens by Tension Loading (Metal-to-Metal). ASTM International, West Conshohocken, PA, DOI: 10.1520/D1002-10, www.astm.org.

[3]   ASTM Standard D3528-96(2008) Test Method for Strength Properties of Double Lap Shear Adhesive Joints by Tension Loading. ASTM International, West Conshohocken, PA, DOI: 10.1520/D3528-96R08, www.astm.org.

[4]   Goland, M., and Reissner, E., 1944. "The stresses in cemented joints". *J Appl Mech*, **11**, pp. A17–A27.

[5]   Chalkley, P., and Rose, F., 2001. "Stress analysis of double-strap bonded joints using a variational method". *Int J Adhes Adhes*, **21**(3), pp. 241–247.

[6]   Groth, H.L., 1988. "Stress singularities and fracture at interface corners in bonded joints". *Int J Adhes Adhes*, **8**(2), pp. 107–113.

[7]   Anderson, G.P., Bennett, S.J., and DeVries, K.L., 1977. *Analysis and Testing of Adhesive Bonds*. Academic Press, New York:.

[8]   ASTM Standard D4896-01(2008)e1 Standard Guide for Adhesive-Bonded Single Lap-Joint Specimen Test Results. ASTM International, West Conshohocken, PA, DOI: 10.1520/D4896-01R08E01, www.astm.org.

[9]   Kinloch, A.J., 1987. *Adhesion and Adhesives: Science and Technology*. Chapman and Hall, New York.

[10] ASTM Standard E229-97, Standard Test Method for Shear Strength and Shear Modulus of Structural Adhesives. ASTM International, West Conshohocken, PA, DOI: 10.1520/E0229-97, www.astm.org.

[11] Grant, J.W., and Cooper, J.N., 1987. "Cone-and-plate shear stress adhesive test". *J Adhes*, **21**(2), pp. 155–167.

[12] Wycherley, G.W., Mestan, A., and Grabovac, I., 1990. "A Method for Uniform Shear Stress-Strain Analysis of Adhesives". *J Test Eval*, **18**(3), pp. 203–209.

[13] Iosipescu, N., 1967. "New accurate procedure for single shear testing of metals". *J Mater*, **2**(3), pp. 537–566.

[14] Weissberg, V., and Arcan, M., 1988. "A Uniform Pure Shear Testing Specimen for Adhesive Characterization", ASTM-STP 981, Adhesively Bonded Joints: Testing, Analysis and Design, W. S. Johnson, Ed., pp 28-38.

[15] Cognard, J.Y., Sohier, L., and Davies P., 2011. "A modified Arcan test to analyze the behavior of composites and their assemblies under out-of-plane loadings". *Compos Part A - Appl S*, **42**(1), pp. 111–121.

[16] Moussiaux, E., Cardon, A.H., and Brinson, H.F., 1987. "Bending of a Bonded Beam as a Test Method for Adhesive Properties". In Cardon AH et al., editors, Mechanical Behavior of Adhesive Joints (Euromech Colloquium 227), Paris: Pluralis, 1987, p. 1. Also: Moussiaux E. Bending of a Bonded Beam as a Test Method for Adhesive Properties. M. S. Thesis Virginia Tech, June.

[17] Li, C., Dickie, R.A., and Morman, K.N., 1990. "Dynamic Mechanical Response of Adhesively Bonded Beams: Effect of Environmental Exposure and Inter-facial Properties". *Polym Eng Sci*, **30**(4), pp. 249–255.

[18] Morman, K.N., Li, C., Zhang, F., and Dickie, R.A., 1992. "Determination of the Complex Shear Modulus of Structural Adhesives Using a doubly Clamped Sandwich Beam". *Exp Mech*, **32**(2), pp. 124–131.

[19] Hunston, D., Miyagi, Z., Schultheisz, C., and Zaghi, S., 2003. "The Sandwich Bending Specimen for Characterizing Adhesive Properties". *Mech Time-Depend Mat*, **7**, pp. 71–88.

[20] He, J., Chiang, M.Y.M., and Hunston, D.L., 2001. "Assessment of Sandwich Beam in Three-Point Bending for Measuring Adhesive Shear Modulus". *J Eng Mater Technol - T ASME*, **123**, pp. 322–328.

[21] Brinson, H.F., Dickie, R.A., and DeBolt, M.A., 1995. "Measurement of Adhesive Bond Properties Including Damage by Dynamic Mechanical Thermal Analysis of a Beam Specimen". *J Adhes*, **55**, pp. 17–30.

[22] Adams, D., and Weinstein, A.S., 1975. "Flexural Stiffness of Sandwich Beams". *J Eng Mat Technol – T ASME*, pp. 264–270.

[23] Krajcinovic D. Sandwich Beams with Arbitrary Boundary Conditions. *J. Eng. Ind. – T ASME* 1975;97:873–880.

[24] Sharma, R., and Rao, D.K., 1982. "Static Deflections and Stresses in Sandwich Beams Under Various Boundary Conditions". *J Mech Eng Sci*, **24**(1), pp. 11–20.

[25] de Castro San Román, J., 2000. "Experiments on Epoxy, Polyurethane and ADP Adhesives". Appendix A - Technical Report n° CCLab2000.1b/1, CCLAB, Ecole Polytechnique Federale de Losanne.

[26] Bridgman, P.W., 1952. *Studies in large plastic flow and fracture*. McGraw-Hill, New York.

[27] Schlimmer, M., 2004. "Anstrengungshypothese für Metallklebverbindungen". *Materialwiss Werkst*, **13**, pp. 215–21.

[28] Dragoni, E., and Mauri, P., 2000. "Intrinsic static strength of friction interfaces augmented with anaerobic adhesives". *Int J Adhes Adhes*, **20**, pp. 315–21.

[29] Dragoni, E., and Mauri, P., 2002. "Cumulative static strength of tightened joints bonded with anaerobic adhesives". *Proc Inst Mech Eng - Part L*, **216**, pp. 9–15.

[30] Castagnetti, D., and Dragoni, E., 2013. "Experimental assessment of a micro-mechanical model for the static strength of hybrid friction-bonded interfaces". *J Adhes*, **89**, pp. 642–59.

[31] Fior, V., and Brinson, H.F., 1988. "A Beam Test for Adhesives". VPI-E-88/21/CAS/ESM 88-8, July.

APPENDIX I

Notation

b	Width of beam
C_a	Correction factor for the deflection of the sandwich beam
L	Half length of the sandwich beam
$(L/h)_{max}$	Minimum between $(L/h)_\delta$ and $(L/h)_\sigma$
$(L/h)_\delta$	Limit aspect ratio to avoid excessive deformation of the sandwich
$(L/h)_\sigma$	Limit aspect ratio to avoid overstress of the adherends
E, G	Young's modulus and shear modulus of the adherends
E_a, G_a	Young's modulus and shear modulus of the adhesive
h	Thickness of the adherends
I	Bending moment of inertia of the section of each adherend ($= bh^3/12$)
P	Transverse force acting on beam ends
P_{cr}	Transverse force producing failure of the adhesive
t_a	Thickness of the adhesive layer
$(t_a/h)_{max}$	Max allowed relative thickness of bondline for stress optimization
u_a, u_b, u_s	Axial displacements of adherends and adhesive the interface
$w(x)$	Transverse deflection of beam at position x
x	Distance from beam centre along the beam axis
α_L	Relative stiffness of the adhesive layer
$\alpha_{L\delta}^*$	Optimal value of α_L for measurement of the adhesive shear modulus
$\alpha_{L\sigma}^*$	Threshold value of α_L for bond stress optimization
$\gamma_a(x)$	Shear deformation of the adhesive layer
δ	Centre deflection of the sandwich beam

δ_0	Centre deflection of the homogeneous beam
δ_{0cr}	Centre deflection of the homogeneous beam under force P_{cr}
$\left(\delta_{0cr}/L\right)_{lim}$	Limit relative deflection acceptable for the sandwich beam
η, ξ	Dummy coordinates used for integration with respect to x
ν	Poisson's ratio of the adherends
ν_a	Poisson's ratio of the adhesive
σ_{adm}	Admissible working stress of the adherends
σ_{max}	Maximum bending stress in the adherends
σ_{maxcr}	Maximum bending stress in the adherends under force P_{cr}
$\tau(x)$	Shear stress in the adhesive layer
τ_{acr}	Critical stress of the adhesive
τ_0	Maximum shear stress in the homogeneous beam
τ_{max}	Maximum shear stress in the adhesive layer
$\overline{\tau}_{max}$	Limit value of the maximum shear stress in the adhesive layer

APPENDIX 2

Stresses

Elementary beam theory gives the following equation for the deflections of the top or bottom adherend in Fig. 2:

$$EI\frac{d^2w(x)}{dx^2} = \frac{P}{2}(L-x) - \frac{bh}{2}\int_x^L \tau(\xi)\,d\xi \tag{A1}$$

where $w(x)$ is the transfer deflection of each adherend, b is the beam width, I is the flexural moment of inertia of the section of each adherend and ξ is an integration length with origin at $x = 0$.

From Fig. 2 it is clear that an arbitrary point on the bottom surface of the top adherend undergoes a displacement due to beam bending, u_b, and a displacement due to the tensile axial load induced in the bottom adherend by the adhesive shear stress, u_a. Continuity of displacements at the top adherend/adhesive interface requires that the sum of these two displacements equal the shear displacement, u_s, of the top surface of the adhesive or:

$$u_b + u_a = u_s \tag{A2}$$

in which the component displacements are given by:

$$u_b = u_b(x) = \frac{h}{2}\frac{dw(x)}{dx} \tag{A3}$$

$$u_a = u_a(x) = -\frac{1}{Eh}\int_0^x \int_x^L \tau(\xi)\,d\xi\,d\eta \tag{A4}$$

$$u_s = u_s(x) = -\frac{t_a}{2}\gamma_a(x) = \frac{t_a}{2}\frac{\tau(x)}{G_a} \tag{A5}$$

It is appropriate to point out here that the continuity condition enforced by Eq. (A2) is different than that used by Moussiaux [16]. In the above, the continuity is requested at the adherend/adhesive interface while [16] enforced continuity at the midplane of the adhesive layer. Further, [16] defined the adhesive thickness as $2t_a$ instead of t_a. With the indicated modifications, the resulting equations for shear stress in the adhesive layer and for beam deflections given in the following development are less cumbersome to utilize than those of Moussiaux. The value of the shear stress or the beam deflection for a specific set of dimensions and properties will be virtually the same as that given by [16] provided the inclusion of half the thickness of the adhesive does not appreciably alter the beam moment of inertia.

Note should also be taken that there is a contribution to beam deflection caused by the vertical shear stresses in each adherend and this effect has been neglected in Eq. (A2). However, the specimen length appropriate for the determination of adhesive shear properties would, of necessity, be such that shear deflections would be negligible. On the other hand, the shear warping of the cross-section would mean an increase in adhesive shear stress and strain.

Substituting equations (A3), (A4), and (A5) into (A2) gives:

$$\frac{h}{2}\frac{dw(x)}{dx} - \frac{1}{Eh}\int_0^x \int_x^L \tau(\xi)\,d\xi\,d\eta = \frac{t_a}{2}\frac{\tau(x)}{G_a} \tag{A6}$$

Differentiating (A1) once, (A6) twice and combining the final expressions results in the following differential equation for the shear stress in the adhesive:

$$\frac{d^2\tau(x)}{dx^2} - \frac{G_a}{t_a E}\left(\frac{bh^2}{2I} + \frac{2}{h}\right)\tau(x) = -\frac{h}{2t_a}\frac{G_a}{EI}P \qquad \text{A7)}$$

The boundary condition at the fixed end in Fig. 2 is $\left(dw/dx\right)\big|_{x=0} = 0$ and when substituted into the compatibility equation, (A6), gives $\tau(x=0) = 0$ (for $x = 0$ the integral in (A6) vanishes). The boundary condition at the free end is $\left(d\tau/dx\right)\big|_{x=L} = 0$ (in $x = L$ the bending moment is zero). Using these boundary conditions, letting $I = bh^3/12$ and regrouping the constants as in (3) and (4), integration of (A7) gives the shear stress in the adhesive as shown by Eq. (1).

Deflections

Displacements can be found by substituting the shear stresses (1) into (A1) and performing the indicated integration, which gives:

$$EI\frac{d^2w(x)}{dx^2} = \frac{P}{2}(L-x) - \frac{3P}{8}\left\{(L-x) + \frac{L}{\alpha_L}\left[\sinh\left(\alpha_L\frac{x}{L}\right) - \tanh\alpha_L\cosh\left(\alpha_L\frac{x}{L}\right)\right]\right\} \qquad \text{A8)}$$

Integrating (A8) twice and using the conditions that both the slope and deflection at the fixed end are zero yields:

$$w(x) = \frac{1}{2}\frac{PL^3}{3EI}\left(\frac{3Lx^2 - x^3}{2L^3}\right)C_a \qquad \text{A9)}$$

with:

$$C_a = \frac{1}{4} - \frac{9}{2}\left(\frac{L^3}{3Lx^2 - x^3}\right)\left[\frac{\sinh\left(\alpha_L\frac{x}{L}\right) - \tanh\alpha_L\cosh\left(\alpha_L\frac{x}{L}\right) - \left(\alpha_L\frac{x}{L}\right) + \tanh\alpha_L}{\alpha_L^3}\right] \qquad \text{A10)}$$

The first term in equation (A9) is the usual elementary solution for the deflection of a beam of height h with end load of $P/2$, i.e. the deflection of the top adherend if there were no adhesive. The correction factor C_a in (A9) takes into account the effect of the adhesive on the adherends in Fig. 2. When the adhesive shear modulus is zero, $\alpha_L = 0$, the Factor C_a is zero and the deflection given is the same as would be obtained for the top adherend acting alone. If the adhesive shear modulus is the same as that for the adherend, the solution for a monolithic beam of depth $(2h)$ is obtained. Letting $I = bh^3/12$ and rearranging, Eqs. (A9) and (A10) give for $x = L$ the end deflection (2).

INDICE DEGLI AUTORI

Finito di stampare
nel Luglio 2015 da
Global Print - Gorgonzola (MI)

In questo volume sono raccolte le memorie presentate in occasione della "Ottava Giornata di Studio Ettore Funaioli", che si è svolta il 18 luglio 2014 presso la Scuola di Ingegneria e Architettura dell'Alma Mater Studiorum – Università di Bologna. La Giornata è stata organizzata dagli ex allievi del Prof. Funaioli con la collaborazione del DIN – Dipartimento di Ingegneria Industriale e della Scuola di Ingegneria e Architettura dell'Alma Mater Studiorum – Università di Bologna, e con il patrocinio dell'Accademia delle Scienze dell'Istituto di Bologna e del GMA – Gruppo di Meccanica Applicata.

Questo volume è stato stampato con il contributo di G.D S.p.A.

Alm@DL